

UNIVERSITY OF BIRMINGHAM

The Formation of Superparamagnetic Zeolite Hybrid Materials Through a Multistep Process

By

Daniel Peter Smith

Supervisors: Dr Joseph Hriljac

Professor Paul Anderson

A thesis submitted to The University of Birmingham for the degree of Doctor of Philosophy

The School of Chemistry
College of Engineering and Physical Sciences
The University of Birmingham
December 2021

UNIVERSITY OF
BIRMINGHAM

University of Birmingham Research Archive

e-theses repository

This unpublished thesis/dissertation is copyright of the author and/or third parties. The intellectual property rights of the author or third parties in respect of this work are as defined by The Copyright Designs and Patents Act 1988 or as modified by any successor legislation.

Any use made of information contained in this thesis/dissertation must be in accordance with that legislation and must be properly acknowledged. Further distribution or reproduction in any format is prohibited without the permission of the copyright holder.

Abstract

The development of superparamagnetic hybrid zeolites would allow for easier solid-liquid separations by magnetic methods to use, for example, in the remediation of nuclear waste. The aim of this thesis is to develop and test an optimised route to achieve this.

The work presented starts by building upon the literature to develop and optimise the aqueous ion exchange of transition metals (Fe^{2+}, Co^{2+}, Ni^{2+}, Mn^{2+}, Zn^{2+}) in zeolites A, X and Y using just one step. Then a method of developing magnetic particles which are encapsulated within a vitreous aluminosilicate matrix made from the exchanged zeolites has been developed. The method has been optimised for zeolites A, X and Y using different transition metals. These materials recorded magnetic moments of up to 65.78, 55.95 and 50.05 emu/g of magnetic material for zeolites A, X and Y respectively. The use of a digestion or milling prior to the zeolite synthesis provided the means to reduce particle size and overcome differences in solubility to facilitate nucleation. Finally, several novel synthesis methods for creating a superparamagnetic form of zeolites A, X, Y and chabazite using the vitreous matrix have been developed with magnetic moments of 12.2 emu/g recorded. The final, magnetised zeolites are shown to ion exchange with no reduction in measured capacity.

Acknowledgments

Firstly, I would like to thank my supervisors Dr Joe Hriljac and Prof Paul Anderson, without whom this work would not have been possible. I would like to express my thanks for their continued support, mentorship, and the many opportunities that I have been afforded throughout this project. Thanks also to the School of Chemistry and the ESPRC for funding this project.

I would like to thank Christopher Omatsola-Morgan in Materials and Metallurgy for his help in collecting the magnetic data, without him a chapter of this thesis would not have been possible. The analysis presented in this thesis would not have been possible without the staff who maintain or have maintained the instruments used, provided training and assistance so I would like to thank Dr Louise Male (PXRD), Dr Jackie Deans (XRF & PXRD), Dr Tzu Chen (PXRD), Mr Paul Stanley (SEM), Dr Chen Huang (STEM) and Mr Norman Day (ICP-MS).

I would also like to acknowledge the many colleagues past and present who have made level 5 a relaxed and enjoyable place to work. Dr Daniel Parsons for his help and support throughout my PhD. Thanks to Dr Abbey Jarvis and Dr Lauren Dackcombe for their moral support and discussion around food and the excessive amounts of coffee that were consumed over the last few years. Thanks to Alex Sargent for completing the preliminary experiments for the nickel systems during his master's project. Thanks also to Dr Antony Nearchou, Josh Deakin, Mark Stockham, Matthew James, James Reed, Beatrice Browning and everyone else for providing the laughs and good times over the past few years whether it be in the office, the lab or the pub.

Finally, I would like to thank those in my personal life. A special thanks to my parents for their unwavering support and endlessly funding my endeavours. Thanks to my girlfriend Rosy for her help and support during the preparation of this thesis, hopefully I can repay the favour in a few years' time. Thanks also to my friends for their support and encouragement throughout this whole process.

Contents

Abstract 2

Acknowledgments 3

Contents 5

List of Figures 12

List of Tables 20

List of abbreviations 22

Chapter 1: Introduction 25

1.1. The nuclear industry 25

1.2. An introduction to zeolites 29

1.2.1. Zeolite structures and their nomenclature 29

1.2.2. Basic structure of zeolites 30

1.2.3. Properties of zeolites and their applications 31

1.2.4. Zeolite A (LTA) 36

1.2.5. Zeolites X and Y (FAU) 38

1.2.6. Chabazite (CHA) 40

1.2.7. Aqueous ion exchange of TM in zeolites 42

1.2.8. Thermal decomposition of zeolites 43

1.3. Magnetic materials 46

1.3.1. Magnetic spinels and their structure 46

1.3.2. The synthesis of magnetic spinels 48

1.3.3. Magnetically altered zeolites 49

1.4. The aim of this thesis 54

1.5. References 55

Chapter 2: Experimental 63

2.1. Synthesis techniques 63

2.1.1. Hydrothermal synthesis 63

2.1.2. Ion exchange 64

2.1.3. Solid state ion exchange 65

2.2. Instrumentation and characterisation techniques 67

2.2.1. Crystallography and X-ray diffraction 67

2.2.2. X-ray fluorescence 78

2.2.3. Raman spectroscopy 83

2.2.4. Thermogravimetric analysis and mass spectrometry 85

2.2.5. Mössbauer spectroscopy 86

2.2.6. Magnetic measurements 91

2.2.7. Scanning electron microscopy 100

2.2.8. Scanning transmission electron microscopy 103

2.2.9. Inductively coupled plasma mass spectrometry and inductively coupled plasma optical emission spectroscopy 105

2.4. Experimental procedures 107

2.4.1. Zeolite A....107
2.4.2. Zeolite X....107
2.4.3. Zeolite Y....108
2.4.4. Chabazite....109
2.4.5. Transition metal ion exchange procedure....110
2.4.6. Solid state exchange....110
2.4.7. Matrix digestion....111
2.4.8. Secondary synthesis....112
2.4.9. Ion exchange and ICP-MS procedure....114
2.5. References....115
Chapter 3: Ion exchange of *d*-block cations in Zeolite A, X and Y....118
3.1. Introduction....118
3.1.1. Transition metal ion exchange in zeolite A....121
3.2. Experimental....124
3.2.1. Contact time....124
3.2.2. Initial concentration and solution temperature....124
3.3. Initial exchange analysis....127
3.4. Influence of time on divalent transition metal cation exchange in zeolite A 129
3.4.1. The influence of time on iron(II) cation exchange in zeolite A....129
3.4.2. The influence of time in cobalt(II) cation exchange in zeolite A....135
Timeframe selection for Co(II) in zeolite A....138

3.4.3. The influence of time in manganese(II) cation exchange in zeolite A ..138

3.4.4. The influence of time on nickel(II) cation exchange in zeolite A 141

3.4.5. The influence of time on zinc(II) cation exchange in zeolite A 145

3.5. Raman spectroscopy.....149

3.5.1. Raman spectroscopy of zinc exchanged zeolite A.....149

3.5.2. Raman spectroscopy of cobalt exchanged zeolite A 151

3.5.3. Raman spectroscopy of manganese exchanged zeolite A 152

3.5.4. Raman spectroscopy of nickel exchanged zeolite A.....153

3.5.5. Raman spectroscopy of iron exchanged zeolite A.....154

3.5.6. Conclusion of a Raman spectroscopy study of transition metal exchanged zeolite A.....155

3.6. Concentration and temperature.....156

3.6.1. The influence of temperature and concentration on iron(II) cation exchange 156

3.6.2. The influence of temperature and concentration on cobalt(II) cation exchange 159

3.6.3. The influence of temperature and concentration on manganese(II) cation exchange 161

3.6.4. The influence of temperature and concentration on nickel(II) cation exchange 163

3.6.5. The influence of temperature and concentration on zinc(II) cation exchange 166

3.7. Discussion of divalent ion exchange in zeolite A 169

3.8. Ion exchange in zeolites X and Y 172

3.9. References 174

Chapter 4: The synthesis of superparamagnetic materials using transition metal exchanged zeolites 177

4.1. Introduction 177

4.2. An investigation into the effect of the anion 179

4.2.1. Cobalt(II)-A with iron(III) nitrate 179

4.2.2. Iron(II)-A with iron(III) nitrate 181

4.2.3. Cobalt(II)-A with iron(III) chloride 182

4.2.4. Iron(II)-A with iron(III) chloride 184

4.2.5. Conclusion of the anion effect 185

4.3. Removal of the hematite impurity 187

4.4. Analysis and identification of the magnetic phase 191

4.4.1. Identification of the magnetic spinel in the cobalt(II) system 191

4.4.2. Identification of the magnetic spinel in the iron(II) system 197

4.2.3. Confirmation of the identity of magnetic phases 204

4.2.4. Variable temperature XRD 205

4.5. Production of magnetic materials using transition metal exchanged zeolite A 210

4.5.1 Manganese(II) exchanged zeolite A 210

4.5.2. Nickel(II) exchanged zeolite A 211
4.5.3. Zinc(II) exchanged zeolite A 213
4.6. Magnetic behaviour of the matrix materials 215
4.6.1. Iron(II)-iron(III) matrix materials 217
4.6.2. Cobalt(II)-iron(III) matrix materials 220
4.6.3. Manganese(II)-iron(III) matrix materials 221
4.6.4. Nickel(II)-iron(III) matrix materials 222
4.6.5. Zinc(II)-iron(III) matrix materials 223
4.6.6. Conclusion of the magnetic behaviour of the matrix materials 223
4.6.7. Optimisation in zeolite X and Y 225
4.7. Production of magnetic materials using sodium zeolite A 227
4.7.1. Cobalt(II) one-step synthesis 228
4.7.2. Iron(II) one-step synthesis 232
4.8. Overall section conclusion 237
4.9. References 240
Chapter 5. Superparamagnetic zeolite hybrids 243
5.1. Introduction 243
5.2. Synthesis and characterisation of zeolite A hybrids 244
5.3. Magnetic characterisation of zeolite A hybrids 258
5.5. Zeolite A Hybrids and their ion exchange capabilities 261
5.6. Synthesis and characterisation of zeolite X hybrids 265

5.7. Magnetic characterisation of zeolite X hybrids 271

5.8. Ion exchange capabilities of zeolite X hybrids 273

5.9. Synthesis and characterisation of zeolite Y and chabazite hybrids 276

5.10. Conclusion 279

5.11 References 280

Chapter 6. Summary and further work 281

6.1. Summary 281

6.2. Further work 288

List of Figures

Figure 1 Acid sites within zeolites *34*

Figure 2 A Sodalite cage (β-cage). The main building unit of LTA. *37*

Figure 3 The LTA structure. *37*

Figure 4 Double-6-rings which create a hexagonal prism in the FAU structure. *39*

Figure 5 FAU structure. *39*

Figure 6 CHA structure. *41*

Figure 7 Access to the t-cha cage is provided by the 8-membered ring. This ring combined with double-6-rings creates the CHA structure. *42*

Figure 8 Crystal structure of a spinel originated along the (111) plane. *47*

Figure 9 Schematic depicting one possible route for magnetisation of a zeolite. *52*

Figure 10: Depiction of a unit cell *68*

Figure 11 The different types of lattice centring *68*

Figure 12: Energy level diagram of a copper atom *71*

Figure 13: Scattering of X-rays from adjacent planes' *73*

Figure 14: P-XRD pattern showing the main components. *75*

Figure 15 Depicting Rayleigh, Stokes, and anti-Stokes scattering processes in Raman spectroscopy. *84*

Figure 16 Schematic depicting the decay of 57Co. *86*

Figure 17 Example Mössbauer spectrum for an identical emitting and absorbing nuclei in the same environment. *89*

Figure 18 An example of quadrupole splitting. *90*

Figure 19 An example of magnetic splitting in a Mossbauer spectrum. *91*

Figure 20 An illustration to represent the effect of diamagnetic and paramagnetic materials on magnetic flux density. *92*

Figure 21 Illustrating the different spin orientations for each type of magnetism. *94*

Figure 22 Schematic to describe the different sections of a Hysteresis loop. At points B and E, magnetic susceptibility 'X' is at its greatest. Points C and F provide information relating to a material's residual magnetism, the point at which the curve passes through the Y-axis. Points D and G is the point of intercept on the X-axis and is a measure of a ferromagnetic sample's ability to withstand an external magnetic field. The presence and shape of a hysteresis loop provides information relating to the magnetic behaviour. 96

Figure 23 Schematic depicting the different interactions high energy electrons can have with a solid sample. 100

Figure 24 Schematic of a scanning electron microscope. 102

Figure 25 Schematics depicting the differences between TEM and STEM. 104

Figure 26 Transition metal salt used for ion exchange and their pH ranges at the concentrations used 126

Figure 27: Comparison of the Na^{+} and Co^{2+} zeolite A X-ray diffraction patterns before optimisation. The pattern for Co(II)-A has been offset by 8000 counts. 128

Figure 28 Time-based uptake kinetics of Fe(II) in zeolite A using 0.25 M iron(II) chloride at 25˚C over a 24-hour time frame. Element ratios are calculated from WD-XRF data from dried powders in pellet form. The size of the error bars reflects a 10% error commonly associated with XRF of pellets. 130

Figure 29 X-ray diffraction patterns produced by Fe(II) exchanged zeolite A at 25 ˚C when using 0.25 M iron(II) chloride solution. a) was taken after 1 hour and then subsequent patterns until h) after additional 1 hours increments, i) is after 24 hours. 131

Figure 30 Time-based uptake kinetics for zeolite A using 0.25 M iron(II) sulphate at 25˚C over a 24-hour time frame. Element ratios are calculated from WD-XRF data from dried powders in pellet form. The size of the error bars reflects a 10% error commonly associated with XRF of pellets. 132

Figure 31 X-ray diffraction patterns produced during Fe(II) ion-exchange into zeolite A using 0.25 M iron(II) sulphate at 25˚C. a) was taken after 1 hour and then subsequent patterns until h) after additional 1 hours increments, i) is after 24 hours. 133

Figure 32: Time-based uptake kinetics for zeolite A using 0.25 M cobalt(II) nitrate solution at 25˚C over a 24-hour time frame. Element ratios are calculated from WD-XRF data from dried powders in pellet form. The size of the error bars reflects a 10% error commonly associated with XRF of pellets. 135

Figure 33: X-ray diffraction patterns produced by Fe(II) exchanged zeolite A at 25 ˚C when using 0.25 M cobalt(II) nitrate a) was taken after 1 hour and then subsequent patterns until h) after additional 1 hour increments, i) is after 24 hours. *137*

Figure 34: Time-based uptake kinetics of Mn(II) in zeolite A using 0.25 M manganese(II) chloride at 25˚C, over a 24-hour timeframe. Element ratios are calculated from WD-XRF data from dried powders in pellet form. The size of the error bars reflects a 10% error commonly associated with XRF of pellets. *139*

Figure 35: X-ray diffraction patterns produced during Mn(II) ion-exchange into zeolite A using 0.25 M manganese(II) chloride at 25˚C, over a 24 hour time period. a) was taken after 15mins, d) after 1 hour, k) after 8 hours and finally l) after 24 hours. *140*

Figure 36: Time-based uptake kinetics for zeolite A using 0.25 M nickel(II) nitrate solution at 25˚C over a 24-hour time frame. Symbol size has been selected to represent the size of the error bars. Element ratios are from WD-XRF data from dried powders in pellet form. *142*

Figure 37: X-ray diffraction patterns produced during Ni(II) ion-exchange into zeolite A using 0.25 M nickel(II) nitrate at 25˚C, over a 24-hour time period. a) was taken after 15mins, d) after 1 hour, k) after 8 hours and finally l) after 24 hours. *144*

Figure 38: Time-based uptake kinetics of Zn(II) in zeolite A using 0.25 M zinc(II) chloride at 25˚C, over a 24-hour time frame. Element ratios are calculated from WD-XRF data from dried powders in pellet form. The size of the error bars reflects a 10% error commonly associated with XRF of pellets. *146*

Figure 39: X-ray diffraction patterns produced during Zn(II) ion-exchange into zeolite A using 0.25 M $ZnCl_2$ at 25˚C, over a 24 hour time period. a) was taken after 15mins, d) after 1 hour, k) after 8 hours and finally l) after 24 hours. *148*

Figure 40 Raman spectrum of Zn(II)-A and Na(I)-A using a 532nm green laser at 10% power for 10 accumulations with 10 second exposure for direct comparison. *150*

Figure 41 Raman spectrum of Zn(II)-A and Na(I)-A focused around the in 100 to 200 cm^{-1} region. *150*

Figure 42 Raman spectra produced by Na(I) zeolite A and Co(II) exchanged zeolite A after 24 hours contact with 0.25 M $FeCl2{\cdot}4H_2O$ at 65˚C using a 532nm green laser using 10% power with an exposure time of 10 seconds for 10 accumulations. *151*

Figure 43 Raman spectrum of Mn(II)-A and Na(I)-A using a 633nm red laser at 10% power for 10 accumulations with 10 second exposure for direct comparison. *152*

Figure 44 Raman spectrum of Ni(II)-A and Na(I)-A using a 532nm green laser at 10% power for 10 accumulations with 10 second exposure for direct comparison. *153*

Figure 45 Raman spectrum produced by Fe(II) exchanged zeolite A after 24 hours contact with 0.25 M $FeCl2{\cdot}4H_2O$ *at 55˚C using a 532nm green laser.* *155*

Figure 46 X-ray diffraction patterns from temperature-based uptake kinetics of Fe(II) in zeolite A when using 0.25 M iron(II) chloride salt solutions at different temperatures for 24 hours. *158*

Figure 47 X-ray diffraction patterns from temperature-based uptake kinetics of Co(II) in zeolite A when using 0.25 M cobalt(II) nitrate salt solutions at different temperatures for 24 hours. *160*

Figure 48 X-ray diffraction patterns from the study of temperature-based uptake of Mn(II) using zeolite A when in a 0.25 M manganese(II) chloride salt solution at different temperatures for 24 hours. *162*

Figure 49 X-ray diffraction patterns from temperature-based uptake kinetics of Ni(II) using zeolite A when in a 0.25 M nickel(II) nitrate salt solution at different temperatures for 24 hours. *165*

Figure 50 X-ray diffraction patterns from temperature-based uptake kinetics of Zn(II) using zeolite A when in a 0.5 M $ZnCl_2$ *salt solution at different temperatures for 24 hours.* *168*

Figure 51 XRD pattern of cobalt(II)-A heated at different temperatures in 1:1 (Fe^{3+}:Co^{2+}) *ratio with iron nitrate under atmospheric conditions.* *180*

Figure 52 XRD patterns of iron(II)-A and iron nitrate in a 1:1(Fe^{3+}:Fe^{2+}) *ratio heated at different temperatures under a nitrogen atmosphere.* *181*

Figure 53 XRD patterns of cobalt(II)-A and iron(III) chloride in a 1:1(iron:cobalt) ratio heated at different temperatures under atmospheric conditions. *183*

Figure 54 The effect of the anion on phase formation across a range of synthesis temperatures. *183*

Figure 55 XRD patterns of iron(II)-A and iron(III) chloride in a 1:1(Fe^{3+}:Fe^{2+}) *ratio heated at different temperatures under a nitrogen atmosphere.* *184*

Figure 56 XRD patterns of cobalt(II)-A and iron(III) chloride in a 2:1(Fe^{3+}:Co^{2+}) *ratio heated at different temperatures under a nitrogen atmosphere.* *188*

Figure 57 The effect of temperature and salt ratio on phase formation displayed as a ratio of cobalt spinel to hematite. Black circles represent a synthesis temperature of 600˚C, white circles 800˚C and black triangles 1000˚C. 189

Figure 58 High resolution SEM image of Co-A post synthesis with iron(III) chloride. 192

Figure 59 High resolution SEM image of Co-A post synthesis which depicts the aggregation of the magnetic particles within the recrystalised zeolite matrix. 193

Figure 60 STEM image of cobalt(II)-iron(III) matrix made at 1000˚C using cobalt(II)-A and iron(III) chloride. The elemental mapping area highlighted. Elemental Mapping images collected over the highlighted area. 194

Figure 61 Raman spectrum of the glassy matrix material produced by heating cobalt(II) zeolite A with iron(III) chloride in a 2:1 (iron:cobalt) ratio at 1000˚C under nitrogen. 197

Figure 62 Raman spectrum of a Fe^{3+}/Fe^{2+} sample made using iron(III) chloride and iron(II) zeolite A in a 2:1 (Fe^{3+}:Fe^{2+}) ratio, heated to a 1000˚C in a nitrogen atmosphere. 199

Figure 63 ^{57}Fe Mössbauer spectrum recorded at 298 K from iron(II) zeolite A thermally decomposed in a 1:2 molar ratio with iron(III) chloride at 1000˚C. 201

Figure 64 ^{57}Fe Mössbauer spectrum recorded at 298 K from Co(II) zeolite A thermally decomposed at 1000˚C in a 1:2 molar ratio with iron(III) chloride. 202

Figure 65 TGA/DTA curves of a matrix synthesis. The blue curve relates to TG% (mass loss), the purple to DTA and red corresponds to temperature. 205

Figure 66 VT-XRD scans from the 250˚C to 950˚C experiment. The temperature range shown is 350 to 500˚C as this contained the areas on interest. The Mn(II)-A and iron(III) chloride system was used in this experiment. .. 207

Figure 67 VT-XRD scans from the 400˚C to 600˚C experiment. The Mn(II)-A and iron(III) chloride system was used in this experiment. 208

Figure 68 VT-XRD scans from the 750˚C to 875˚C experiment. The Mn(II)-A and iron(III) chloride system was used in this experiment. 209

Figure 69 XRD patterns of manganese(II)-A and iron(III) chloride in a 2:1(Fe^{3+}:Mn^{2+}) ratio heated at 1000˚C under a nitrogen atmosphere. 211

Figure 70 XRD patterns of nickel(II)-A and iron(III) chloride in a 2:1(Fe^{3+}:Ni^{2+}) ratio heated at 1000˚C under a nitrogen atmosphere. 212

Figure 71 XRD patterns of zinc(II)-A and iron(III) chloride in a 2:1(Fe^{3+}:Zn^{2+}) ratio heated at 1000˚C under a nitrogen atmosphere. *214*

Figure 72 Example VSM curve *216*

Figure 73 The magnetic responses produced by the magnetic products of the 2:1 iron(III) chloride to Fe (II) zeolite A series. Black circles were from samples heated at 800˚C and the white circles were at 1000˚C. *217*

Figure 74 The magnetic responses produced by the occlusion products when using iron(III) chloride to iron(II) zeolite A ratios of 0.5:1,1:1 and 2:1 using a synthesis temperature of 1000˚C. Black circles represent the data from the 0.5:1 ratio, white circles 1:1 and black triangles 2:1 ..... *219*

Figure 75 The magnetic responses produced by the occlusion products when using iron(III) chloride to cobalt(II) zeolite A ratios of 0.5:1,1:1 and 2:1 using a synthesis temperature of 1000˚C. Black circles represent the data from the 0.5:1 ratio, white circles 1:1 and black triangles 2:1. ..... *221*

Figure 76 The magnetic responses produced by the occlusion products when using iron(III) chloride to manganese(II) zeolite A ratios of 0.5:1,1:1 and 2:1 using a synthesis temperature of 1000˚C. Black circles represent the data from the 0.5:1 ratio, white circles 1:1 and black triangles 2:1. ..... *222*

Figure 77 The magnetic responses produced by the occlusion products when using iron(III) chloride to nickel(II) zeolite A ratios of 0.5:1,1:1 and 2:1 using a synthesis temperature of 1000˚C. Black circles represent the data from the 0.5:1 ratio, white circles 1:1 and black triangles. *223*

Figure 78 XRD patterns resulting from a solid-sate exchange of Na (I) A with cobalt(II) chloride and iron(III) chloride in a 2:1:0.5(Fe^{3+}:Co^{2+}:Na^{+}) ratio heated at different temperatures under a nitrogen atmosphere. *229*

Figure 79 The magnetic responses produced by the one-step synthesis products when using A cobalt(II) chloride and iron(III) chloride in a 2:1:0.5 (Fe^{3+}:Co^{2+}:Na^{+}) ratio which were heated at different temperatures under a nitrogen atmosphere. Black circles represent the data from the 800 ˚C and the white circles 1000˚C. *231*

Figure 80 XRD patterns resulting from a solid-sate exchange of Na (I) A with iron(II) chloride and iron(III) chloride in a 2:1:0.5(Fe^{3+}:Fe^{2+}:Na^{+}) ratio heated at different temperatures under a nitrogen atmosphere. *234*

Figure 81 The magnetic responses produced by a solid-sate exchange of Na(I) A with iron(II) chloride and iron(III) chloride in a 2:1:0.5 (Fe^{3+}:Fe^{2+}:Na^{+}) ratio heated at 1000˚C under a nitrogen atmosphere. Black circles represent the data without magnetic content accounted for and the black triangles does account for the magnetic content. *235*

Figure 82 The effect of increasing the synthesis time when using materials with significantly different solubilities in the synthesis of superparamagnetic zeolite A hybrids. 244

Figure 83 Depicting the size of the matrix material before and after digestion in NaOH. Left hand image is prior digestion. Right hand image is post digestion. 246

Figure 84 Powder X-ray diffraction patterns of superparamagnetic zeolite A hybrids made as a function of NaOH (24-hour crystallisation time), using a 20% matrix content. A standard form of zeolite A has been added for comparison. 248

Figure 85 SEM images of zeolite A created using a magnetic matrix digested at different NaOH concentrations. a) 1M, b) 1.25M and c) 1.5M. 249

Figure 86 Powder X-ray diffraction patterns of superparamagnetic zeolite A hybrids made using different amounts of magnetic matrix. A standard form of zeolite A has been added for comparison. 251

Figure 87 SEM back scattered image to investigate the topology and metal oxide distribution of zeolite A made using 20% (0.2:1)matrix content alongside standard reagents. 252

Figure 88 SEM back scattered image to investigate the topology and metal oxide distribution of zeolite A made using 50% (0.5:1)matrix content alongside standard reagents. 253

Figure 89 SEM back scattered image to investigate the topology and metal oxide distribution of zeolite A made using 100% (1:1)matrix content alongside standard reagents. 253

Figure 90 A selection a STEM images of zeolite A formed using a Fe(II) Fe(III) matrix. One containing red letters to depict points at which EDX analysis was performed to identify regions of interest. 254

Figure 91 STEM image of 1:1 zeolite A hybrid with the EDX spectrum area highlighted with the corresponding elemental compositions. 256

Figure 92 TGA and DTA curves of a zeolite A hybrid with maximum magnetic loading. The blue curve relates to TG% (mass loss), the purple to DTA and red corresponds to temperature. 257

Figure 93 Magnetic response of the hybrid zeolite A using different manganese(II)-iron(III) matrix to product loadings. 259

Figure 94 A comparison of the Cs^+ uptake in the magnetised and un-magnetised forms of zeolite A when using a Mn(II) Fe(III) matrix. RSDs are included but are too small to be seen. 262

Figure 95 A comparison of the Sr^{2+} uptake in the magnetised and un-magnetised forms of zeolite A when using a Mn(II) Fe(III) matrix. *263*

Figure 96 XRD pattern of zeolite X made using a milled matrix. A pattern of Na-X has been included for comparison. *268*

Figure 97 An SEM image of a zeolite X hybrid made using milled matrix in a 0.25:1 ratio under standard synthesis conditions. *269*

Figure 98 XRD patterns of zeolite X hybrids made using different amounts of matrix content. A standard form of zeolite X has been added for comparison. *270*

Figure 99 Magnetic response of the hybrid zeolite X using different amounts nickel(II)-iron(III) matrix alongside standard synthesis reagents. *272*

Figure 100 A comparison of the Cs+ uptake in the magnetised and un-magnetised forms of zeolite X when using a Ni(II) Fe(III) matrix. RSDs are included but are too small to be seen. *274*

Figure 101 A comparison of the Sr^{2+} uptake in the magnetised and un-magnetised forms of zeolite X when using a Ni(II) Fe(III) matrix. *275*

Figure 102 A diagram of an example flow system trialled using the novel exchange materials. *289*

List of Tables

Table 1 Stability data for zeolites A, X and Y.[59] 44

Table 2 Decomposition products of zeolites at specified temperatures.[60,61,62,64] 44

Table 3: The seven crystal systems 69

Table 4 Mössbauer active isotopes and their properties.[20] 87

Table 5 Magnetic susceptibility of iron oxides.[28] 99

Table 6 Structural properties of the divalent d-block metals used during the series of ion exchange studies. ... 121

Table 7 Exchanging cations and colour of zeolites after successful exchange. 127

Table 8 The effect of temperature and concentration on Fe^{2+} cation exchange in zeolite A 157

Table 9 The effect of temperature and concentration on Co^{2+} cation exchange in zeolite A 159

Table 10 The effect of temperature and concentration on Mn^{2+} cation exchange in zeolite A 161

Table 11 The effect of temperature and concentration on Ni^{2+} cation exchange in zeolite A. 163

Table 12 The effect of temperature and concentration on Zn^{2+} cation exchange in zeolite A. 167

Table 13 Summary of zeolite A's optimised exchange conditions and the associated exchange outcomes 171

Table 14 Summary of zeolite X's optimised exchange conditions and the associated exchange outcomes 172

Table 15 Summary of zeolite Y's optimised exchange conditions and the associated exchange outcomes 173

Table 16 Raman activities of the possible phases present in the cobalt(II)-iron(III) matrix. 196

Table 17 Raman activities of the possible phases present in the iron(II) iron(III) matrix. 198

Table 18 ^{57}Fe Mössbauer parameters recorded at 298 K from iron(II) zeolite A thermally decomposed at 1000˚C in a 1:2 ratio with iron(III) chloride. 200

Table 19 ^{57}Fe Mössbauer parameters recorded at 298 K from Co(II) zeolite A thermally decomposed at 1000˚C in a 1:2 ratio with iron(III) chloride. 203

Table 20 Summary of the magnetic moments produced by the matrix materials made using transition metal exchanged zeolite A 224

Table 21 Summary of the magnetic moments produced by the matrix materials made using transition metal exchanged zeolite X 225

Table 22 Summary of the magnetic moments produced by the matrix materials made using transition metal exchanged zeolite Y *226*

Table 23 A direct comparison of the magnetic behaviour of the one and two-step synthesis methods *232*

Table 24 A summary of the magnetic moments for the zeolite A hybrid materials. *260*

Table 25 A comparison of Cs^+ and Sr^{2+} uptake in the magnetised and non-magnetised forms of zeolite A. *264*

Table 26 Experimental digestion and subsequent synthesis conditions to produce zeolite X hybrid materials. . *266*

Table 27 The magnetic moments of zeolite Y and Chabazite hybrid materials synthesised with different magnetic loadings. *277*

Table 28 A comparison of Cs^+ and Sr^{2+} uptake in the magnetised zeolite Y hybrids and their non-magnetised counterpart. *278*

Table 29 A comparison of Cs^+ and Sr^{2+} uptake in the magnetised chabazite hybrids and their non-magnetised counterpart. *278*

List of abbreviations

AC – Alternating Current

ADF – Annular Dark Field

BET – Brunauer Emmett Teller

BFD – Bright Field Detector

BS – Back Scattered

CHA – Chabazite

DC – Direct Current

DI – DeIonised

DTA – Differential Temperature Analysis

D4R – Double-4-Ring

D6R – Double-6-Ring

EDX – Energy Dispersive-X-Ray spectroscopy

ED-XRF – Energy Dispersive-X-Ray Fluorescence

EFG – Electric Field Gradient

FAU – Faujasite

FCC – Fluid Catalytic Cracking

HAADF – High Angle Annular Dark Field

HDPE – High Density PolyEthylene

HLW – High Level Waste

ICP – Inductively Coupled plasma

ICP-MS – Inductively Coupled Plasma-Mass Spectrometry

ICP-OES – Inductively Coupled Plasma-Optical Emission Spectrometry

ILW – Intermediate Level Waste

KCPS – Kilo Counts Per Second

LLW – Low Level Waste

LTA – Linde Type A

MR – Membered Ring

MS – Mass Spectrometer

M/Z – Mass to Charge

PPB – Part Per Billion

PPM – Part Per Million

PPT – Part Per Trillion

PSD – Position Sensitive Detector

RPM – Revolutions Per Minute

SE – Secondary Electron

SEM – Scanning Electron Microscope

SIXEP – Site Ion Exchange Effluent Plant

STEM – Scanning Transmission Electron Microscope

T_B – Temperature Boiling

TEM – Transmission Electron Microscope

TGA – Thermal Gravimetric Analysis

TM – Transition Metal

VSM – Vibrating Sample Magnetometer

VT-XRD – Variable Temperature-X-Ray Diffraction

W/V – Weight by Volume

WD-XRF – Wave Dispersive-X-Ray Fluorescence

XRD – X-Ray Diffraction

1D – 1 Dimensional

3D – 3 Dimensional

Chapter 1: Introduction

1.1. The nuclear industry

Nuclear power is a low-carbon and efficient method of boiling water to create steam which turns a turbine and produces electricity. Nuclear power plants split uranium atoms to create large amounts of energy through a process known as nuclear fission. Nuclear power offers an energy production method that can help mitigate climate change as the power plants do not produce greenhouse gases or introduce any combustion by-products into the atmosphere which is one of the main issues associated with fossil fuels. The energy from fossil fuels has three main consequences: accidents, air pollution and greenhouse gas emissions. Accidents: these happen during the mining and extraction of the fuel, during the transport of the materials and during the construction of the power plant. Air pollution: the burning of fossil fuels and the production of air pollutants kills approximately 5 million people per year. Greenhouse gas emissions: fossil fuels are the main source of greenhouse gases with a report written in 2018 finding that fossil fuels accounted 87% of all global CO_2 emissions.

The introduction of nuclear power has helped elevate the two main issues associated with the industry by displacing fossil fuels. Nuclear energy typically emits a very small amount of CO_2 per unit of energy produced and there is a significant reduction in the air pollution contributions.. Nuclear energy does not involve combustion, therefore, it does not produce air pollutants during energy formation which is why nuclear power is commonly promoted to be a desirable alternative to fossil fuels.[1] However, H-3 and

C-14 are emitted from the power plant during the re-fueling process. Nuclear power currently only supplies around 10% of the world's electricity.[2]

Unfortunately, the public opinion of nuclear energy is a negative one. This is thought to stem from disasters such as Chernobyl and Fukushima. These large-scale disasters resulted in several countries either halting or restricting their nuclear programmes. However, a comparison of the death tolls from fossil fuels and nuclear power including the aforementioned disasters, showed that nuclear power has a much lower death rate per year.[3] Countries such as Russia, France, China, United States and the UK have invested significantly in their nuclear energy programmes to shift their energy supply towards nuclear as it is available on demand similar to fossil fuels whereas renewables such as wind cannot constantly supply energy to meet an ever increasing energy demand.

Nuclear energy, like many other sources of energy, generates waste effluent during energy production. The effluent created by the nuclear industry poses significant health risks to humans as well as to the environment due to the harmful radioactivity. Each radionuclide has a half-life, the time taken for half of the atoms to decay hereby losing half of its radioactivity. Radionuclides with longer half-lives are typically alpha and beta emitters, this makes handling them easier as they do not require shielding or cooling. Those with shorter half-lives typically emit the more harmful gamma rays. In time all radioactive nuclides decay into non-radioactive elements, the less radioactive the isotope, the slower the decay.

Radioactive waste may be classified as either low-level (LLW), intermediate-level (ILW) or as high-level (HLW).[4] LLW waste has a radioactive content of ≤4 GBq/t of

alpha activity or ≤12 GBq/t of beta-gamma activity. LLW is typically generated by hospitals, industry and the nuclear fuel cycle. To reduce its volume, the waste is often incinerated prior to disposal.[4] LLW is said to comprise 90% of the overall waste volume but it only accounts for <1% of the radioactivity of all the radioactive waste.[4]

ILW is considerably more radioactive than LLW, with this level of waste generating heat. However, it is not enough heat energy for it to be considered an issue during the selection of the storage or disposal facility. ILW is commonly contaminated materials from decommissioning a primary reactor circuit, chemical sludges, or resins. Prior to disposal ILW might be solidified in bitumen or concrete. ILW accounts for 7% of the overall waste volume and for 4% of the radioactivity of all the radioactive waste.[4]

HLW accounts for the remaining 95% of the radioactivity. This produces vast amounts of heat energy during decay which is sufficient to increase its own temperature and that of its surroundings. Therefore, HLW must be shielded and cooled significantly. There are two main types of HLW: spent fuel removed from a reactor and separated fission product waste from the reprocessing of used fuel. HLW contains both long- and short-lived components; the amount of time it will take for the waste to become non-hazardous depends on the type of radionuclides present and whether short-lived fission products can be separated from long-lived isotopes of actinides or ^{135}Cs (half-life of $3x10^6$ years), ^{137}Cs (half-life of 30.1 years) or ^{90}Sr (half-life of 28.8 years).

Technological advancements are required to constantly enhance the measures that are in place to minimise the toxicity and reduce the volume of the radioactive waste before storage or disposal. The treatment of liquid effluent typically involves several steps, such as, precipitation, distillation, filtration, evaporation, acid digestion, solvent

extraction, wet oxidation and/or ion exchange.[5] Using inorganic exchange agents such as zeolites is widely considered the most efficient ion exchange method especially from an industrial viewpoint because of their low material cost, commercial availability, diverse structures and compositions. Zeolitic materials have been comprehensively investigated as they have been shown to tolerate the severe conditions of nuclear sites, which produce significant amounts of heat and radiation. Zeolites are also highly compatible with cement and glass matrices that are used in the immobilisation of radioactive waste.[6]

1.2. An introduction to zeolites

A Swedish mineralogist, Axel Cronstedt, discovered the first known zeolite, Stilbite in 1756.[7] He observed the evolution of water upon heating to such an extent that they appeared to boil, and thus they were named zeolites. The name zeolite is derived from two Greek words *'zeos'* meaning to boil and *'lithos'* a stone which loosely translated to boiling stone.

1.2.1. Zeolite structures and their nomenclature

Zeolites are hydrated, crystalline, microporous materials made from elements such as aluminium, oxygen and silicon. Even today zeolites are one of the most recognised branches of microporous materials. The general structure of a zeolite is shown in Formula 1 and it can be split into 3 main parts. Firstly, $M^{m+}_{x/m}$ where *m* refers to the charge on the extra framework cations. Secondly, *n* is the amount of sorbed water per formula unit. Finally, the main part of the framework $[Al^{3+}_{x}\ Si^{4+}_{1-x}\ O_2]$ where *x* is the proportion of tetrahedral sites occupied by aluminium. The framework structure is made up of TO_4 tetrahedra. T can be either or Al with $[AlO_4]^{-5}$ or Si in the form $[SiO_4]^{-4}$. Both the silicate and aluminate tetrahedra are linked through an oxygen atom resulting in the formation of a three-dimensional framework. However, Löwenstein's rule states that Al-O-Al connections cannot occur in zeolite structures due to increased charge repulsion, therefore, the Si/Al ratio can never be less than one.[8]

$$M^{m+}_{x/m}\ [Al^{3+}_{x}\ Si^{4+}_{1-x}\ O_2]\ n\ H_2O$$

Formula 1 General elemental formula of a zeolite

There are currently 235 registered frameworks with a further 59 additional frameworks pending approval. Approximately 40 of those frameworks have been found to occur naturally in volcanic rocks and oceanic sediment, due to the high temperatures and pressures.[9] Examples include chabazite, mordenite and clinoptilolite; the rest of the registered frameworks have been made synthetically. The first definitive zeolite synthesis was accomplished by R.M. Barrer in 1948, which included a synthetic analogue of mordenite and a novel synthetic zeolite which was later discovered to be the KFI framework.[10] Each of the frameworks registered have been assigned their own unique three letter code to help identify them more easily. Linde type A for example has the code LTA.[11] Porous materials can also be broken up into groups depending on their pore size. Frameworks that consist of pore diameters up to 20 Å are defined as microporous materials. Materials that have a pore size >20 Å but <200 Å are categorised as mesoporous, whilst those materials with pores >200 Å are categorised as macroporous.[7]

1.2.2. Basic structure of zeolites

Although Formula 1 describes the stoichiometry of a zeolite, it gives no indication of its structure. The main framework is built up from corner-sharing TO_4 (T=Si or Al) tetrahedra, which allows for the formation of ring structures. These structures are more commonly referred to as secondary building units.

A zeolite's structural framework is typically described by the number of secondary building units that make up that given structure i.e. LTA is made up of 8, 6 and 4 membered rings (MR). The size of the rings is conventionally described by the number of T atoms within the ring, as opposed to the total number of atoms. These rings can

link together to form more complex units such as alpha/beta cages or chains. It is the variation in ring size and different connectivity between the corner-sharing tetrahedra which allows zeolites to form such a wide array of topologies.

1.2.3. Properties of zeolites and their applications

There are several methods of modifying a zeolite to alter its properties, the simplest is changing the silicon to aluminium (Si/Al) ratio. The Si/Al ratio can be altered prior to the synthesis and is an important factor when determining the application, as the Si/Al ratio directly impacts the amount of non-framework cations and their positions within the structure. Zeolites with low silica/high alumina content develop a high field gradient because of the number of cationic charges within in the framework. These charges directly affect the surface of the framework as it becomes selective towards polar and polarisable molecules. This selectivity provides the basis for their application in purification and drying.[12] Zeolites with a Si/Al ratio of 3 to 4 exhibit characteristic changes in acid and thermal stability compared to low silica materials. Their unique properties allow them to act as adsorbents, catalysts or ion-exchange materials.[12]

Low silica and intermediate level zeolites have a heterogeneous hydrophilic surface by nature but those with high silica ratios have a more homogenous nature exhibiting hydrophobic, organophilic selectivity. They have weak interactions with water and other polar molecules but strongly adsorb less polar organic molecules. As a result, they are mainly used in molecular sieving applications because of the difference in their surface characteristics.[12] Zeolites with a high Si/Al ratio also display an even higher thermal stability and a stronger resistance to acidic conditions compared to their

counterparts. These are desirable properties which have forced using post synthetic methods.[13]

1.2.3.1 Aqueous ion exchange

The existence of [AlO_4] tetrahedra in the zeolite structure results in the framework having a negative charge because of the charge deficiency of Al^{3+}. This negative charge can be balanced by the presence of non-framework cations (commonly alkali metals) which reside in the pores and channels of the zeolite. These cations are loosely bound to the framework oxygens but are highly mobile so can readily exchange with other cations. The exchangeable nature of the non-framework cations allows the zeolite properties to be tuned via aqueous ion exchange, enabling the selectivity of zeolite sorbents and regulation of the molecular sieving behaviour.

Ion exchangers by definition are insoluble materials that contain exchangeable anions and/or cations. Materials that are capable of both anionic and cationic exchange are referred to as amphoteric ion exchangers. The first reported cation exchanger was in 1858, but it was not commercially exploited until the 1900s. It was observed that the sodium form of zeolite A could be employed as a water softener as the Na^+ ions readily exchanged with Ca^{2+} ions which are responsible for ‘hard water’. As with most exchange reactions the whole process can be completely reversed. Sodium zeolite A can be regenerated by exposing it to a sodium salt solution.[14]

Zeolites are also used in the nuclear industry. Spent nuclear fuel is removed from the reactor where it is then temporarily stored under water in ‘ponds’. Pond storage is used to allow cooling prior to dry storage or re-processing. During the storage period there is a build-up of fission products; usually this is radioisotopes of ^{137}Cs and ^{90}Sr. This

contaminated waste is classified as ILW and is managed via the waste hierarchy [12] The Sellafield plant and National Nuclear Laboratory have successfully employed a naturally occurring zeolite, known as Clinoptilolite, from California to remove the Cs^{+} and Sr^{2+} isotopes from waste liquid effluents as part of the SIXEP process; this will be discussed in more detail later in this thesis. Using zeolites for this application is seen as an attractive proposition for both storage and disposal as it has been shown to significantly reduce the volume of waste.[12]

1.2.3.2. Catalysis

Ion exchange is not only a desired property for use in a variety of applications, but it is commonly exploited in the preparation of zeolites for applications in catalysis. Zeolites containing transition metals are well established as heterogenous catalysts for industrial processes. The position that the transition metals occupy is of high interest to those developing an understanding of the catalytic properties.[15]

Different forms of zeolites can be conditioned so that non-framework cations can be in the form of protons, leading to the formation of Brønsted acid sites (donates protons) or may be altered again to provide a Lewis acid sites (accepts electrons), thus providing the basis for a diverse array of catalysis (Figure 1).[14,16]

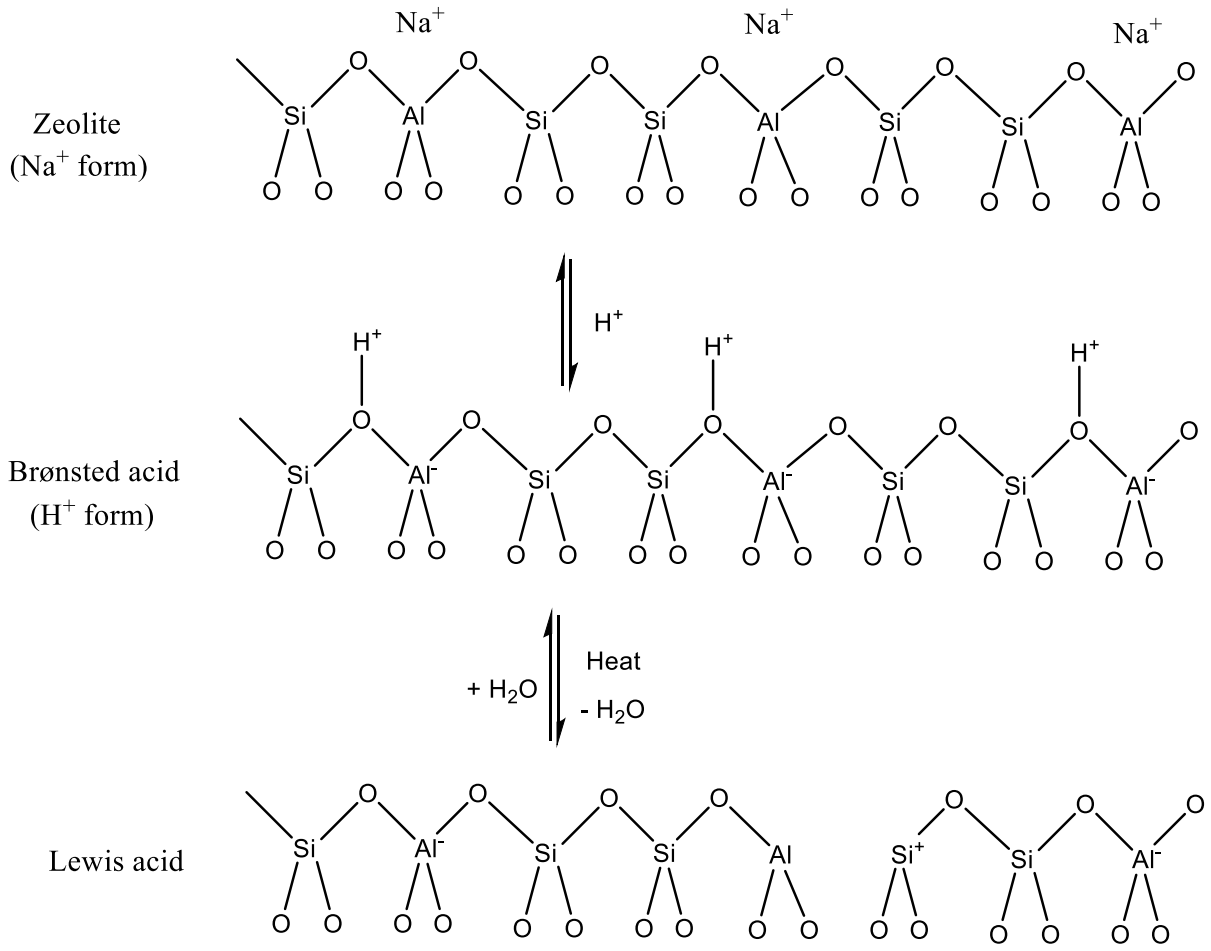


Figure 1 Acid sites within zeolites

Zeolites are considered ideal candidates for catalysis as they have a large surface area provided by the framework cavities, a property which is not exhibited by traditional catalysts. Zeolites exhibit 3 main catalytic properties: reactant shape-selectivity, transition state-selectivity and product shape-selectivity. These can prove extremely effective for selective diffusion of chemical reactions within and outside of the active sites.[12,17,18]

Industry has many uses for zeolites, but perhaps the main innovation was in 1962 when synthetic analogues of faujasites were introduced into Fluid Catalytic Cracking (FCC) of heavy petroleum distillates. Before their introduction, the traditional route

used a range of complex free radical reactions to obtain lighter distillate products. After their introduction, there was an increase in the yield of gasoline which is the most valuable product. This increase could be due to the synthetic zeolite being 10^4 orders of magnitude more active than the traditional amorphous silica-alumina catalysts. This was attributed to a higher number of active sites within the framework.[17] The two main zeolites used in Fluid Catalytic Cracking are Zeolite-USY and ZSM-5. Due to the starting materials being relatively low cost and the advantage of being able to recover and recycle the catalyst relatively easily, they have saved the petrochemical industry Trillions of pounds since they were first introduced.[19,20]

1.2.3.3. Molecular sieves

The interstitial sites of the zeolite contain non-framework cations and water molecules. Removal of these water molecules has little to no effect on the overall framework structure. However, dehydration creates empty voids where molecules other than water can be adsorbed. This process is known as ‘sorption’ as the zeolite is said to ‘sorb’ molecules into the frameworks’ voids. When the molecules are ‘sorbed’ to the ‘host’ framework they are described as ‘guests’ as they can be removed again. Removal of water can be more difficult in some zeolites than in others. This is caused by a positive correlation between the energy required for water diffusion and the framework density.[12,21]

Pore size, and the ability to alter it, is one of the most valuable properties of a zeolite. The size of the pore is dependent on the size of the oxygen window, this affects what can pass through. The silicon-oxygen ring can be 8, 10 or 12-membered having typical sizes of ~4.5 Å, ~6.3 Å and ~8.0 Å, respectively. Depending on the location of the

cation within the pore this can create a partial barrier to the pores, resulting in a reduction of accessibility. Therefore, ion exchanging zeolites is one of the preferential ways of tailoring pore sizes, as depending on which cation resides within the pore will determine the amount of space it takes up, hereby tailoring the sieving behaviour.[21] An alternative method of changing pore size is by manipulating the Si/Al ratio. If there is a decrease in the amount of Si, there is an increase in the size of each unit cell, due to difference in bond lengths of Al-O (1.75 Å) and Si-O (1.61 Å).[22]

1.2.4. Zeolite A (LTA)

Zeolite A, also termed Linde Type A (LTA), is a synthetic zeolite with the idealised formula of $Na_{12}[Si_{12}Al_{12}O_{48}]\cdot 25\ H_2O$. LTA adopts the cubic space group *Fm-3c*, where *a* is approximately 24.6 Å.[23] The main building unit of the LTA structure is the sodalite cage (also known as β-cage), which is comprised of 4 and 6-ring sub-units (Figure 2). These sodalite cages are then joined by double-4-rings (D4R) to create a larger supercage (or α-cage) as depicted in Figure 3. The supercage has the largest pore size in zeolite A through the 8MR (shown in red on Figure 3) with a diameter of ~4.1 Å and an internal diameter of ~11.4 Å.[24] The sodalite cage has an internal diameter of ~6.4 Å and pore size of ~2.5 Å. In zeolite A there are three sets of equivalently occupied cation sites. The first set contains 8 sodium ions which are in the plane of 6-ring. The second site contains 3 ions, these are in the 8-ring and the third set contains only 1 ion situated in the 4-ring, totalling 12 sodium ions per unit cell.[25]

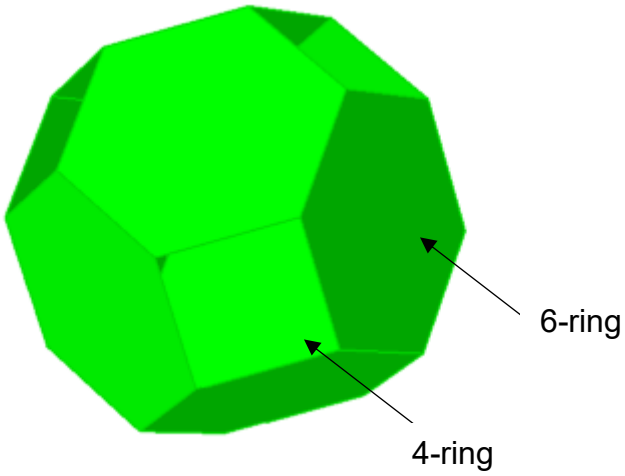


Figure 2 A Sodalite cage (β-cage). The main building unit of LTA.

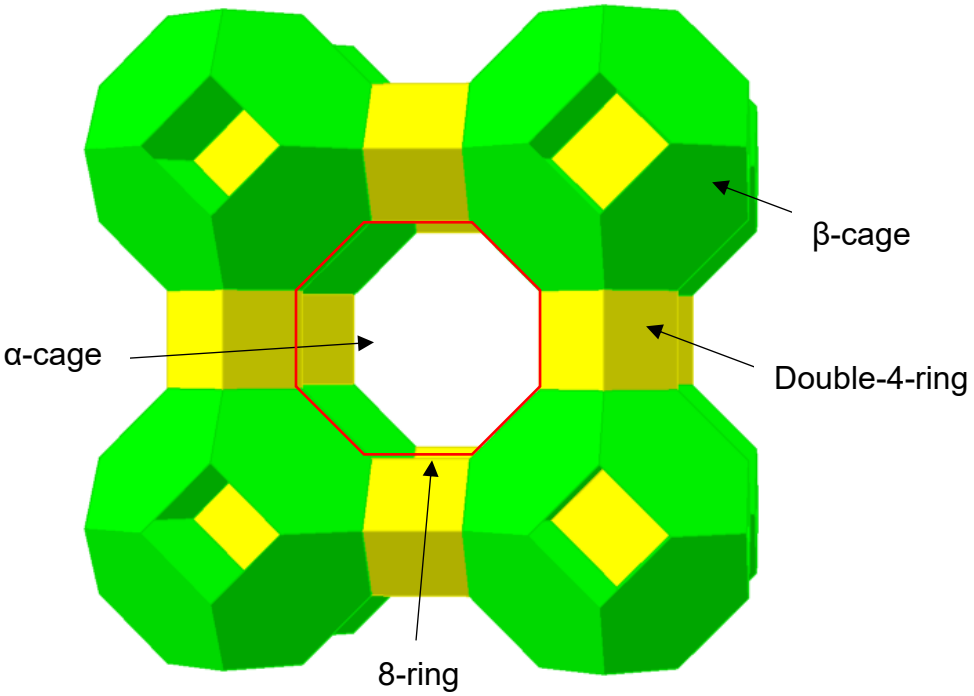


Figure 3 The LTA structure.

LTA may also be described as a primitive cubic array of sodalite cages which can be described using the space group *Pm-3m*, where *a* ≈12.3 Å.[23] Typically LTA is described using the *Pm-3m* space group, however, *Fm-3c* is considered a more accurate representation. The ideal Si/Al ratio for zeolite A is 1, as this is the maximum aluminium content permitted by Löwenstein's rule. However, zeolites with the LTA topology have a different name of ZK4 if the ratio is >1.[26] The high ion exchange capacity of LTA enabled by its high aluminium content and its preference for divalent metal cations resulted in its selection for use as a water softener as described previously.

1.2.5. Zeolites X and Y (FAU)

Zeolite X together with zeolite Y belongs to the family of zeolites with the faujasite (FAU) structure. Natural faujasite is a rare mineral, but the synthetic counterparts termed Linde X and Linde Y are widely used in catalysis and ion exchange. Both zeolite X and Y adopt the same space group of *Fd-3m* where *a* equals 25 Å and 24.6 Å, respectively.[23] The only way to differentiate between zeolite X and Y is by their Si/Al ratio, as X typically ranges from 1 to 1.5 and zeolite Y from 1.5 to 3.

The main building unit of FAU is a sodalite cage, however, these cages are then joined by a double-6-ring prism (D6R) (Figure 4) as opposed to a D4R in LTA. This difference in connectivity creates the larger supercage depicted in Figure 5. In FAU, the supercage has an internal diameter of ~13 Å with pore openings of ~8 Å. The internal diameter of the sodalite cages are the same as described previously, however, the internal pore window is now a 6MR as opposed to a 4MR.[27]

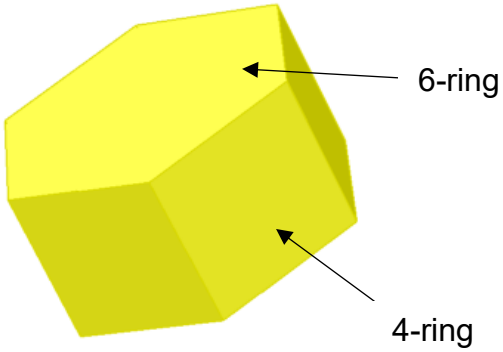


Figure 4 Double-6-rings which create a hexagonal prism in the FAU structure.

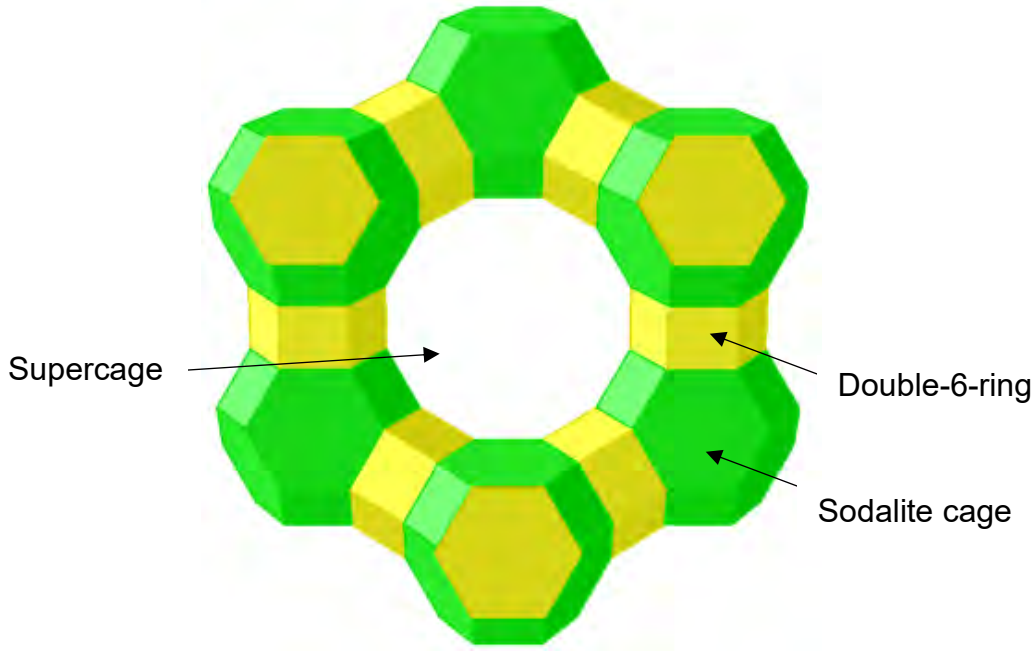


Figure 5 FAU structure.

The ideal composition of zeolite X is $Na_{86}[Si_{106}Al_{86}O_{384}]\cdot 264\ H_2O$, which means there are 86 exchangeable cations. 16 of them can be found either in the hexagonal prisms (D6R), where 1 sodium ion is present in the 16 prisms per unit cell or 2 in each of the 8 sodalite cages. For ion exchange purposes this discrepancy is not considered important.[27] 32 of the sodium ions are located in the plane of the 6-rings which connect the supercage and the sodalite cages. The remaining 38 ions are located on the equivalent crystallographic positions or in constant motion within the large cavities and cannot be located by X-ray based techniques.[27]

The ideal composition of zeolite Y is $Na_{56}[Si_{136}Al_{56}O_{384}]\cdot 250\ H_2O$, therefore 56 exchange cations. As Linde Y and Linde X have the same structure, they therefore have the same cation sites. In zeolite Y, 16 of the sodium ions are located in either the hexagonal prisms or sodalite cages and the remaining 40 are in the larger cavities.

The combination of large pore windows and void volumes within the FAU 3-dimensional (3D) framework makes it one of the most open of all currently known frameworks, making this structure ideal for its applications as an ion exchanger or in catalysis and sorption.[28]

1.2.6. Chabazite (CHA)

Chabazite is a natural zeolite that adopts the space group *R-3m* which is a trigonal space group where $a \approx 13.7$ Å and $c \approx 14.8$ Å.[23] The Si/Al ratio can vary from 2 to 3 but the idealised formula is $K_2[Si_4Al_2O_{12}]\cdot 6H_2O$.[29] Chabazite also possesses a 3D structure which contains large ellipsoidal cages (6.7 x 10 Å) which have been built from D6R's stacked in an ABCABC type sequence as shown in Figure 6.[30] These cages can be assessed by 8MR windows (3.8 x 3.8 Å); this can be seen more clearly in Figure

7.[31] The high silica version of CHA has attracted great interest for a variety of applications because of its acidic and thermal stability. Although chabazite has a relatively small aluminium content compared to the other zeolites, it is still used in ion exchange applications having shown suitable selectivity for both Cs^{+} and Sr^{2+}, whose isotopes are of concern as discussed in section 1.1. Other applications include separation of gaseous mixtures and conversion processes, such as methanol to olefins.[32]

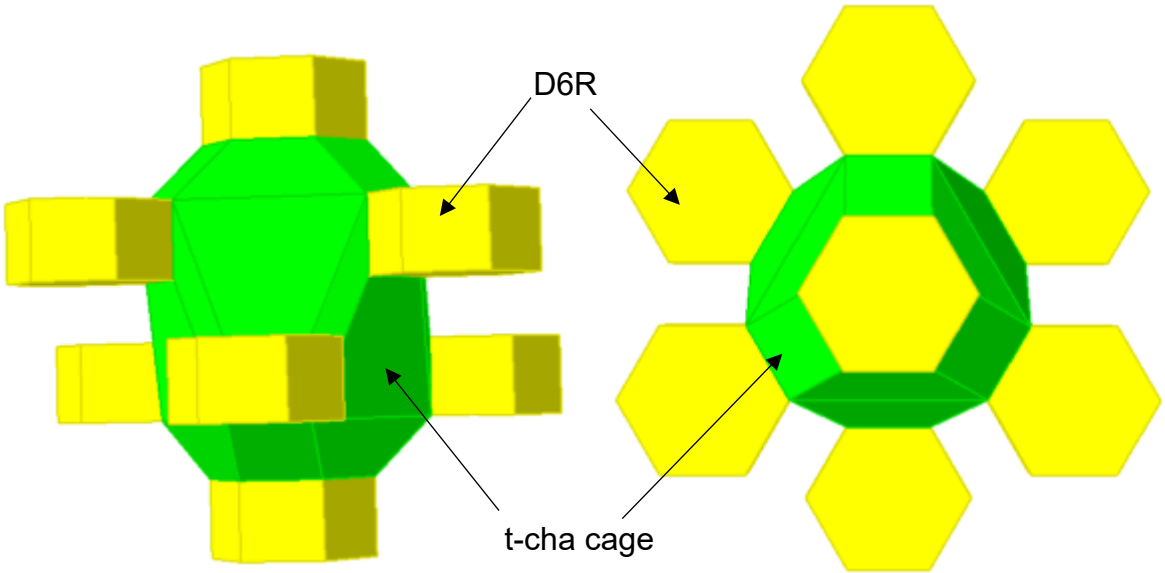


Figure 6 CHA structure.

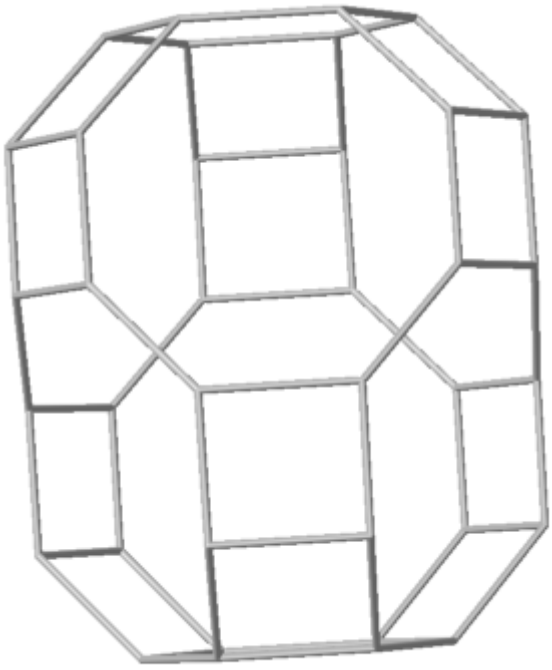


Figure 7 Access to the t-cha cage is provided by the 8-membered ring. This ring combined with double-6-rings creates the CHA structure.

1.2.7. Aqueous ion exchange of TM in zeolites

A large amount of research has been undertaken to help develop and further the understanding of ion exchange, especially for the aqueous ion exchange of transition metals (TM) in zeolites A, X and Y. [15,33-58]

Their relatively large pores, channels and cages result in unopposed exchange with little to no damage of the zeolitic structure. However, all three of the zeolites are different either in structure or composition. These differences are reflected in their aqueous ion exchange behaviours. The exchangeable cations of the parent zeolite are located in different sites in A and X, and these sites are accessed by windows of different sizes. Therefore, larger cations will only have access to certain sizes within a

given zeolite. However, ions or molecules that are too large to pass through the rings in zeolite A might be able to in zeolites X and Y.

The difference in ion exchange behaviour is not only dependent upon cation size, but also upon the zeolites' preferences. If there are several species present in an exchange solution, zeolites demonstrate a preference for one particular ion over another. This is termed as an 'ion selectivity sequence' and has been calculated using isotherms to determine the Gibbs function for the exchange equilibria of various metal species. Therefore, this can help predict how certain species may exchange under proposed conditions.

The current research that has been completed on the TM-exchange of zeolites focuses on achieving a high level of exchange through multiple ion exchanges. However, given that several of the metals are carcinogenic, carrying out multiple ion exchanges produces a large volume of aqueous waste. Given the application of these materials it seems counterintuitive to reduce one type of waste by increasing another. Therefore, the ion exchange chapter presented later (3) focuses on optimising the level of loading that can be achieved in just one exchange hereby limiting the amount of waste produced.

1.2.8. Thermal decomposition of zeolites

Later in this thesis the decomposition products of zeolites that have been ion-exchanged with several transition metals is examined. Therefore, it is important to explore the stabilities and reaction products of the zeolites (A, X and Y) used in this scheme of work. All of the zeolites investigated remained stable upon dehydration, without damaging the structure at temperatures of up to 400°C. Work initially described

by D. W. Breck provided the necessary information to determine when the zeolites were dehydrated to a constant mass and the temperatures that were required to initiate decomposition (Table 1).[59] The abbreviation cation-A (Na-A) refers to the zeolites' exchangeable cation.

Table 1 Stability data for zeolites A, X and Y.[59]

Zeolite framework	Dehydration (°C)		Decomposition (°C)
	Start	Finish	
Na-A	25	300	≥860
Na-X	50	350	≥772
Na-Y	100	400	≥793

The data compiled in Table 1 were collected using a combination of differential temperature analysis (DTA) and thermogravimetric analysis (TGA). The DTA curves of all the zeolites displayed endothermic reactions with an associated mass loss (dehydration) and a subsequent exothermic reaction with no mass loss (decomposition). The work showed that although zeolite Y requires a higher dehydration temperature it does not have the highest stability. Decomposition of zeolites and their reaction pathways has been extensively researched.[60,61,62,63,64] A summary of this for zeolites A,X and Y can be found in Table 2.

Table 2 Decomposition products of zeolites at specified temperatures.[60,61,62,64]

Zeolite framework	800-900°C	~900°C	>1000°C
Na-A	Amorphous silica	Carnegieite and nepheline	Nepheline
Na-X	Amorphous silica	Carnegieite, coesite and amorphous silica	Nepheline and trace amounts of cristobalite
Na-Y	Amorphous aluminosilicate phases	No new identifiable phases	Mullite, cristobalite and trace amounts of carnegieite

Table 2 suggests that the elemental composition of the zeolite directly affects the decomposition products. The sodium form of zeolite A decomposes into one phase, nepheline ($NaAlSiO_4$), which effectively consumes all the original components (assuming the Si/Al is 1). When the Si/Al is greater than 1 there is more than one phase present in the decomposed zeolites as shown by Na-X and Na-Y. For example, zeolite X decomposes into a carnegieite (a polymorph of nepheline) and coesite (SiO_2). Above 1000°C carnegieite and coesite undergo structural alterations to become nepheline and cristobalite (SiO_2), respectively. In zeolite Y the higher silica content suppresses the formation of silica phases at the lower temperatures before transforming into mullite, cristobalite and carnegieite at elevated temperatures.

1.3. Magnetic materials

There are five different types of magnetic behaviour: diamagnetism, paramagnetism, ferromagnetism, antiferromagnetism and ferrimagnetism. Materials that exhibit diamagnetism and paramagnetism are generally considered to be 'nonmagnetic' as they only exhibit magnetisation when in the presence of a magnetic field.[65,66] It is ferromagnetism and ferrimagnetism that are of high interest when synthesising nanoparticles. If the nanoparticles are small enough, they can exhibit superparamagnetism, which means the nanoparticles can be magnetised, demagnetised and re-magnetised simply by applying, removing and reapplying a magnetic field. This means that magnetism can be manipulated as required, which is ideal for a remediation application. A more detailed explanation of the types of magnetism and superparamagnetism is given in section 2.2.6.

1.3.1. Magnetic spinels and their structure

The synthesis of magnetic materials in the nanodomain has been intensively studied due to the mesoscopic properties of particles of quantum dimensions located in the transition region between bulk solids and atoms.[67] Magnetic spinels often contain trivalent iron alongside various divalent cations (Co, Ni, Zn) and are referred to as spinel ferrites. Magnetic nanoparticles of spinel ferrites have been of great interest for those addressing the relationships between structure (Figure 8), crystal chemistry and their resultant magnetic properties.[68] Spinel ferrites are mixed valence oxides where oxygen anions create a close-packed cubic array. The metal cations randomly occupy one-eighth of the tetrahedral (**A**) sites and half of the octahedral (**B**) interstices. They have a general formula of $[Me_{(1-x)}Fe_x]^A\ [Me_xFe_{(2-x)}]^B\ O_4$, where Me is a divalent cation

(Mn, Zn, Ni, Co, Fe) that shares the **A** and **B** site occupancies with trivalent Fe cations. *x* can be defined as an inversion parameter which allows for three structural possibilities: (1) if $x = 0$ this produces a *normal* spinel e.g. $ZnFe_2O_4$; (2) $x = 1$ produces an *inverse* spinel e.g. Fe_3O_4 or $CoFe_2O_4$; (3) when $0 < x < 1$ cations are distributed across both sites producing a *partially inverted* spinel e.g. $MnFe_2O_4$ where $x = 0.2$.[67] Mixed ferrites can be synthesised where different divalent cations coexist within the same structure.[69] This array of possibilities creates an opportunity to tailor the properties of the structure.[70] The preparation and characterisation of spinel ferrite nanoparticles drew a lot of attention as they displayed superparamagnetism.[67] The possibility of tuning the magnetic properties of a ferrite spinel by altering the divalent cation or the arrangement of the metals is considered to be one of the main advantages of using ferrites.[70,71]

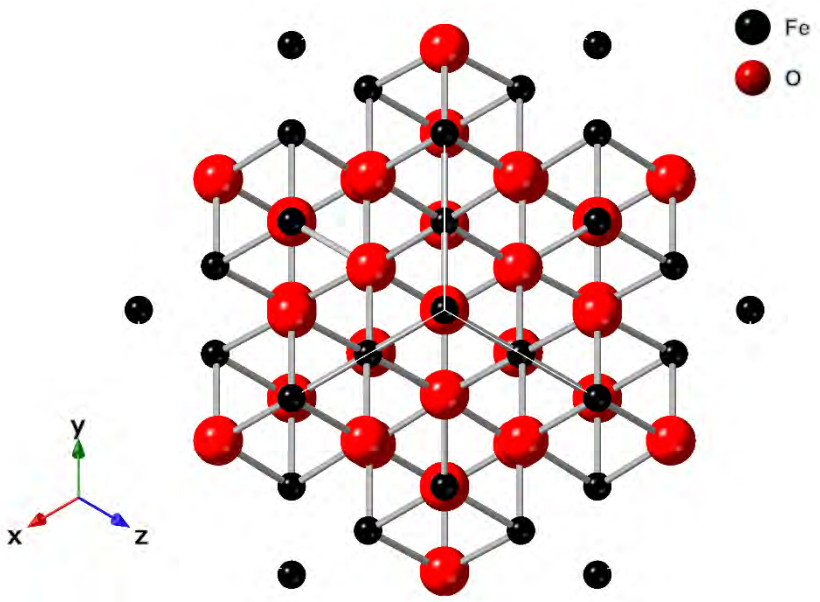


Figure 8 Crystal structure of a spinel originated along the (111) plane.

1.3.2. The synthesis of magnetic spinels

There are different methods for preparing magnetic nanoparticles, but co-precipitation is the archetypal route. This method commonly uses two water-soluble metals that are co-precipitated by a base. The reaction itself has very little control over the size and shape of the particles. The main drawbacks of this route are low crystallinity and consequently less significant magnetic properties.[72]

An alternative method uses different decomposition routes but most commonly a wet approach. This is based upon decomposing metal organic precursors in solvents with a high boiling temperature (T_B), typically a coating agent will also be present. The most common organic precursors are metal acetylacetonates or oleates. The decomposition produces highly crystalline particles close to the monodisperse limit with notable magnetic properties. This method can be tuned to create differently shaped nanoparticles. However, the reaction conditions must be in strict correspondence with a reported growth model.[72]

A large number of protocols are based on solvothermal methods in aqueous conditions, more commonly known as hydrothermal synthesis. Preparation can be carried out in both single and mixed solvent systems. Solvothermal synthesis is often conducted under elevated pressures which can be maintained under supercritical conditions. Particles formed this way usually have good crystallinity and in certain cases are comparative to nanoparticles formed via the decomposition route.[72]

The sol-gel process is a technique that has been used to prepare Fe_3O_4, γ-Fe_2O_3, $CoFe_2O_4$ and $NiFe_2O_4$ all of which have been reported to have good magnetic properties. The most common strategy is to grow the nanoparticles in a porous silica

matrix. This has been shown to produce well developed nanoparticles that are deeply embedded in the matrix. This route, however, does require the gel to be annealed and the particle size is directly affected by the annealing temperature.[72]

1.3.3. Magnetically altered zeolites

Several methods are currently used to create magnetically modified zeolites. One of the main methods used involves the decoration of zeolite surfaces with magnetic metallic nanoparticles (Fe or Co).[73,74,75,76,77] Another popular method involves the insertion of metal cations into the zeolite structure followed by a second synthesis in which the magnetic particles are developed.[78,79,80,81] The final method commonly used is the direct addition of magnetic nanoparticles into the starting gel before crystallisation.[82,83,84,85] Each of these methods has its advantages and disadvantages which will be explored throughout this section. There are also more elaborate routes such as sintering in an inert atmosphere of silica-coated Fe_3O_4 and zeolite particles[86] or the microwave-assisted reaction of suspensions of Fe_3O_4 and zeolite particles.[87] However, these methods are much more difficult to achieve and cannot be readily scaled up in comparison to the other methods presented.

1.4.3.1. Surface decoration

Decoration of the external zeolite surface is the most commonly used method of magnetisation. Magnetisation can be achieved by using one of these methods; via a coprecipitation or several thermal treatments.[73] As surface decoration had been so successful, it led to the development of a patent, which involved the modification of

natural zeolites using colloidal magnetite particles.[74,75] The particles would then directly attach to the external surface of the zeolite.

Coprecipitation is a facile and convenient method for synthesising magnetic nanoparticles as discussed previously. The morphology, size, and composition of the magnetic nanoparticles are dependent upon the temperature, pH, the Fe^{2+}/Fe^{3+} ratio, the type of salt used (nitrates, chlorides or sulphates) and ionic strength of the solution.[88] This allows for a high level of control when synthesising magnetic nanoparticles. Therefore, use of coprecipitation was considered the simplest way to magnetise a zeolite. However, use of direct precipitation on the external zeolite surface was found to significantly reduce accessible surface area.

An alternative surface decoration method that deviated slightly from the ones described previously, looked to create magnetic particles in three different steps. First, the incorporation of iron(III) into the sodium form of zeolite Y via $Fe(NO_3)_3 \cdot 9H_2O/NaNO_3$ melt exchange reaction. This was preferred to aqueous exchange as the latter was found to break down the framework.[76] The insertion was followed by exposure of the iron(III) containing zeolite to vapours of formic acid (HCOOH), where formic acid acts as a reducing agent. Finally, calcination at 400°C in air was performed.[77] This synthetic pathway leads to the aggregation of maghemite (γ-Fe_2O_3) nanoparticles (>100 Å) that are grafted onto the external surface of the zeolite. Omission of the reduction step resulted in the formation of a non-magnetic phase, commonly hematite (α-Fe_2O_3).[74] The authors demonstrated that the magnetic properties of the material, the size of the particles and the crystallinity of the host framework were influenced by the iron(III) content: the greater the iron content the greater their tendency to form larger aggregates. Although this provided more intense

magnetic properties, the crystallinity of the zeolite suffered.[74] This synthetic pathway demonstrated a greater degree of control in terms of particle size than the alternative method but, due to the size of the maghemite particles (>100 Å), they are likely to be ferromagnetic. For maghemite to be superparamagnetic they must be <10 Å.

All methods presented above are successful in the development of magnetised zeolites. However, the route of surface decoration can potentially lead to surface fouling which may result in a reduction in ion exchange properties. As the particles are merely precipitated on the external surface, it also raises questions related to their mechanical strength/stability in the application of choice.

1.4.3.2. Formation within the structure

It was hoped the issues relating to the previous method could be solved by a different route commonly used for zeolite magnetisation. This route aims to develop magnetic nanoparticles in the zeolite itself rather than on the external surface. It is suggested that the framework of the zeolite may be able to control particle size. This is possible via several different routes.

One possibility is via stepwise synthesis which involves a solid state exchange or occlusion reaction, followed by a reduction of the cations to their metallic state.[74,78] During this type of synthesis, solid state ion exchange and salt occlusion can often occur together. This means that as well as the desired cations, the anions of the metal salt are also introduced into the framework. However, the cation and anion do not always reside in the same region of the structure as it was found that the cobalt was occluded in the sodalite cage but the anions remained in the supercage.[78] The dissolution of the occluded salt had arisen because of the large electrostatic fields

existing within the host structure. Following successful metal loading, the cobalt containing zeolite was then heated under hydrogen to reduce the oxide to its element state to form the desired metal nanoparticle. These particles then migrate from the sodalite cages to the supercage and form aggregates, which may not be advantageous as the formation of these aggregates depending upon their size could block the pore network which would inhibit further ion exchange.[78] After reduction, metal particles form which are said to be in the size range of 150-250 Å, and are likely to be ferromagnetic. The proposed formation scheme is shown in Figure 9. Magnetic susceptibility measurements suggested that CoO particles were not formed but rather Co_3O_4.[80]

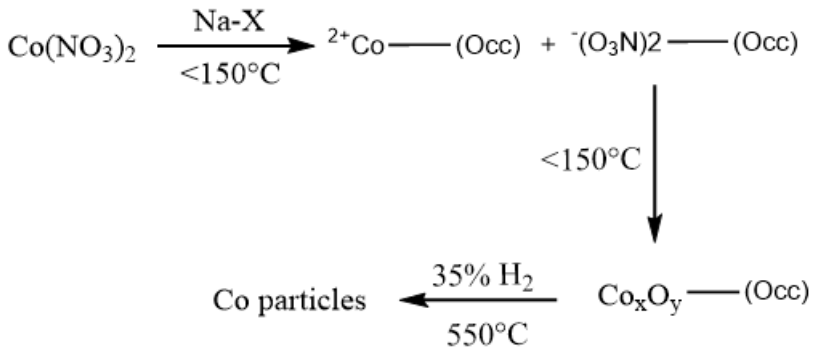


Figure 9 Schematic depicting one possible route for magnetisation of a zeolite.

These particles (150-250 Å) are too big to be accommodated within the small pores or even the supercage. This suggested the synthesis could not control particle size, which is of great importance when attempting to create superparamagnetic materials. A series of TEM experiments showed that some of the metal cations contained within the zeolite cages were not reduced to their metallic state. TEM images showed that the particles which were reduced were contained within the aluminosilicate structure. Containment of these particles resulted in local damage to the structure. This type of

damage is likely to affect the ion exchange capabilities of the zeolite, which again made this method unsuitable given the application.[89]

In the late 1990s, researchers from Hungary attempted to form Fe nanoparticles in zeolites X and Y. Iron was introduced via ion exchange, with the result being 5 wt % after 24 hours. Following the exchange, sodium azide was employed to reduce iron to its elemental state. The authors' analysis demonstrated the ability to create very small nanoparticles (<10 nm), but the reduction, which required the use of the acutely toxic and quite unstable NaN_3 is unlikely to be viable on an industrial level.[81]

Although this set of methods have been successful in creating nanoparticles within the zeolite, besides the possible inhibition of their ion exchange properties, they would not meet the requirements needed for an industrial application, as the reduced metal aggregates are not protected and therefore can be readily oxidised. In the laboratory, these zeolites could be handled within a glovebox but on an industrial level, this would not be possible, with rapid oxidation shortening the life cycle of the material.[86]

1.4.3.3. Direct synthesis inclusion

The final method is the inclusion of magnetic nanoparticles in synthesis gels. This route allows the synthesis to follow the traditional zeolite method before including premade metal nanoparticles into the mixture before crystallisation. This method was found to be successful for the synthesis of magnetic zeolite P, as the crystallinity of the zeolite was shown to be unaffected by the addition of the nanoparticles. SEM analysis found that the zeolites had near-perfect morphology with the nanoparticles detected by surface-based characterisation. The authors proposed that the zeolite building blocks grew around the nanoparticles and trapped them within their core, therefore cannot be

detected by surface-based analysis but can be via X-ray diffraction.[82] The nanoparticle loading was <3 wt%, therefore, the magnetic susceptibility values were minimal. However, the ion exchange properties remained unaffected. This method was developed further using the sodium form of zeolite A. This created a magnetic form of zeolite A using the same magnetic precursor, but the product had a significantly stronger magnetic susceptibility. They achieved a maximum nanoparticle loading of 4.7% and reported a removal efficiency of over 95% for Cu^{2+} and Pb^{2+}.[83] Given the level of loading reported, the ion exchange properties are relatively unaffected. This route demonstrated the ability to create a sufficiently strong magnetic product whilst maintaining most of its ion exchange properties. Therefore, an adaptation/combination of the gel inclusion and pore formation methods could be the most promising avenue for increasing the magnetic loading whilst maintaining the ion exchange properties.

1.4. The aim of this thesis

Using zeolites in the remediation of Cs^{+} and Sr^{2+} from liquid wastes has been shown to offer a dependable clean-up method whilst also being cost effective.[90] This led to BNFL Ltd developing the 'site ion exchange effluent plant' (SIXEP) in 1984. This process uses two columns packed with the natural zeolite clinoptilolite, to remediate the alkaline pond waters and other legacy aqueous waste streams if they are high pH. The SIXEP plant is comprised of settling tanks, sand bed filters, a carbonation tower and two ion exchange columns/beds. The contact time for the effluent in the process is approximately 8 minutes, due to the high flow rate used.[91]

It is proposed that materials developed in this thesis could be used in certain situations when a large process similar to SIXEP cannot, i.e. size restrictions or a disaster similar

to Fukushima where the erection of something similar to the SIXEP process might not be initially possible.[92] This thesis aims to not only create new materials for ion exchange but also to create a novel method that can be used to magnetise different synthetic analogues of zeolites. This thesis focuses on zeolites A, X and Y as commonly used in the ion exchange application. By incorporating a magnetic component into the zeolite, it allows for easier solid-liquid separations by merely applying a magnetic field.

1.5. References

1 H. Ritchie and M. Roser, Nuclear Energy, https://ourworldindata.org/nuclear-energy, (accessed 15 July 2021).

2 World Nuclear Association, *World Nuclear Performance Report 2021*, 2021.

3 H. Ritchie, What was the death toll from Chernobyl and Fukushima?, https://ourworldindata.org/what-was-the-death-toll-from-chernobyl-and-fukushima, (accessed 15 July 2021).

4 Radioactive Waste Management, https://world-nuclear.org/information-library/nuclear-fuel-cycle/nuclear-wastes/radioactive-waste-management.aspx, (accessed 15 July 2021).

5 V. Natarajan, M. Karunanidhi and B. Raja, *Environ. Sci. Pollut. Res.*, 2020, **27**, 29812–29823.

6 S. Kwon, C. Kim, E. Han, H. Lee, H. S. Cho and M. Choi, *J. Hazard. Mater.*, 2021, **408**, 124419.

7 P. A. Wright, *Microporous Framework Solids*, RSC Publishing, Cambridge, 2007.

8 W. Loewenstein, *Am. Mineral.*, 1954, **39**, 92–96.

9 E. Czárán, *React. Kinet. Catal. Lett.*, 1991, **45**, 161–163.

10 I. Petrov and T. Michalev, *Synthesis of Zeolite A: A Review*, Semantic Scholar, 2012.

11 IZA Website, http://www.iza-online.org/, (accessed 10 July 2021).

12 A. Dyer, *An Introduction to Zeolites as Molecular Sieves*, Wiley, 1991.

13 F. Ragon, B. Campo, Q. Yang, C. Martineau, A. D. Wiersum, A. Lago, V. Guillerm, C. Hemsley, J. F. Eubank, M. Vishnuvarthan, F. Taulelle, P. Horcajada, A. Vimont, P. L. Llewellyn, M. Daturi, S. Devautour-Vinot, G. Maurin, C. Serre, T. Devic and G. Clet, *J. Mater. Chem. A*, 2015, **3**, 3294–3309.

14 E. M. Flanigen, in *Reaction Kinetics & Catalysis Letters*, Elsevier Science Publisher, Amsterdam and New York, 2nd edn., 2001, vol. 45, pp. 11–35.

15 S. M. Seo, W. T. Lim and K. Seff, *Microporous Mesoporous Mater.*, 2013, **170**, 67–74.

16 Simmance K, University College London, 2011.

17 E. M. Flanigen, *Pure Appl. Chem.*, 1980, **52**, 2191–2211.

18 V. M. Sousa Aguiar E, Mota A, *J. Mol. Catal. A Chem.*, 1996, **104**, 265–272.

19 M. M. Mori N, Nishiyama S, Tsuruya S, *Appl. Catal.*, 1991, **74**, 35–55.

20 J. P. Martens JA, *J. Mol. Catal.*, 1993, **78**, 47–52.

21 X. Ruren, P. Wenqin, Y. Jihong, H. Qisheng and C. Jieshen, in *Chemistry of Zeolites and Related Porous Materials*, John Wiley & Sons, Ltd, Chichester, UK, pp. 1–18.

22 J. B. Jones, *Acta Crystallogr. Sect. B Struct. Crystallogr. Cryst. Chem.*, 1968, **24**, 355–358.

23 C. Baerlocher, D. H. Olson and L. B. McCusker, *Atlas of Zeolite Framework Types*, Elsevier, 2007.

24 A. Julbe and M. Drobek, in *Encyclopedia of Membranes*, Springer Berlin Heidelberg, Berlin, Heidelberg, 2016, pp. 2055–2056.

25 M. Meyer, C. Leiggener and G. Calzaferri, *ChemPhysChem*, 2005, **6**, 1071–1080.

26 R. T. Rigo, C. Prigol, Â. Antunes, J. H. Z. dos Santos and S. B. C. Pergher, *Mater. Lett.*, 2013, **102**–**103**, 87–90.

27 H. S. Sherry, *J. Phys. Chem.*, 1966, **70**, 1158–1168.

28 A. Julbe and M. Drobek, in *Encyclopedia of Membranes*, Springer Berlin Heidelberg, Berlin, Heidelberg, 2016, pp. 2059–2060.

29 T. Sano, in *Encyclopedia of Membranes*, Springer Berlin Heidelberg, Berlin, Heidelberg, 2016, pp. 360–362.

30 J. Cejka, H. van Bekkum, A. Croma and F. Schueth, *Introduction to Zeolite Molecular Sieves*, Elsevier Science Inc., 3rd edn., 2007.

31 N. Yamanaka, M. Itakura, Y. Kiyozumi, Y. Ide, M. Sadakane and T. Sano,

Microporous Mesoporous Mater., 2012, **158**, 141–147.

32 A. Dyer and M. Zubair, *Microporous Mesoporous Mater.*, 1998, **22**, 135–150.

33 S. . Ouki and M. Kavannagh, *Water Sci. Technol.*, 1999, **39**, 115–122.

34 B. BiŠKUP and B. SubotiĆ, *Sep. Sci. Technol.*, 2000, **35**, 2311–2326.

35 S. Ahmed, S. Chughtai and M. A. Keane, *Sep. Purif. Technol.*, 1998, **13**, 57–64.

36 A. Al-Haj Ali and R. El-Bishtawi, *J. Chem. Technol. Biotechnol.*, 1997, **69**, 27–34.

37 M. A. Keane, *Colloids Surfaces A Physicochem. Eng. Asp.*, 1998, **138**, 11–20.

38 M. Ahmed and S. Ahmed, *Science (80-.).*, 1996, **212**, 269–280.

39 H. Leinonen and J. Lehto, *Waste Manag. Res.*, 2001, **19**, 45–57.

40 A. Langella, M. Pansini, P. Cappelletti, B. De Gennaro, M. De' Gennaro and C. Colella, *Microporous Mesoporous Mater.*, 2000, **37**, 337–343.

41 J. Rubio and F. Tessele, *Miner. Eng.*, 1997, **10**, 671–679.

42 J. S. Kim and M. A. Keane, *J. Colloid Interface Sci.*, 2000, **232**, 126–132.

43 N. Salmon, *Angew. Chemie Int. Ed. 6(11), 951–952.*, 2013, 1–9.

44 A. Dyer and T. Shaheen, *Sci. Total Environ.*, 1995, **173**–**174**, 301–311.

45 S. M. Seo, W. T. Lim, N. H. Heo and K. Seff, *J. Porous Mater.*, 2014, **21**, 869–882.

46 C. Weidenthaler and W. Schmidt, *Chem. Mater.*, 2000, **12**, 3811–3820.

47 M. Majdan, S. Pikus, M. Kowalska-Ternes, A. Gładysz-Płaska, P. Staszczuk, L.

Fuks and H. Skrzypek, J. Colloid Interface Sci., 2003, **262**, 321–330

48 D. Bae and K. Seff, *Microporous Mesoporous Mater.*, 1999, **33**, 265–280.

49 K. Seff, *Acc. Chem. Res.*, 1976, **9**, 121–128.

50 P. E. Riley, K. B. Kunz and K. Seff, *J. Am. Chem. Soc.*, 1975, **97**, 537–542.

51 W. V. Cruz, P. C. W. Leung and K. Seff, *J. Am. Chem. Soc.*, 1978, **100**, 6997–7003.

52 S. B. Jang, M. S. Jeong, Y. Kim and K. Seff, *J. Phys. Chem. B*, 1997, **101**, 9041–9045.

53 T. Blake, 1973, 382–383.

54 D. Bae and K. Seff, *Zeolites*, 1996, **17**, 444–446.

55 N. H. Heo, W. Cruz-Patalinghug and K. Seff, *J. Phys. Chem.*, 1986, **90**, 3931–3935.

56 S. M. Seo, W. T. Lim and K. Seff, *J. Phys. Chem. C*, 2012, **116**, 13985–13996.

57 W. V. Cruz, P. C. W. Leung and K. Seff, *Inorg. Chem.*, 1979, **18**, 1692–1696.

58 M. Trgo, J. Perić and N. V. Medvidović, *J. Hazard. Mater.*, 2006, **136**, 938–945.

59 D. W. Breck, *Zeolite Molecular Sieves: Structure, Chemistry, and Use*, Wiley, New York, 1974.

60 C. Kosanovic, B. Subotic and I. Smit, *Thermochim. Acta*, 1998, **317**, 25–37.

61 T. Palenta, S. Fuhrmann, G. N. Greaves, W. Schwieger and L. Wondraczek, *J. Chem. Phys.*, 2015, **142**, 084503.

62 R. Schollner, H. Siegel and W. Schmitz, *Cryst. Res. Technol.*, 1981, **16**, 385–389.

63 N. Y. Usachev, E. P. Belanova, I. M. Krukovsky, S. A. Kanaev, O. K. Atal'yan and A. V. Kazakov, *Russ. Chem. Bull.*, 2003, **52**, 1940–1949.

64 L. Ding, H. Yang, P. Rahimi, O. Omotoso, W. Friesen, C. Fairbridge, Y. Shi and S. Ng, *Microporous Mesoporous Mater.*, 2010, **130**, 303–308.

65 V. Marghussian, *Magnetic Properties of Nano-Glass Ceramics*, 2015.

66 E. A. Boudreaux and L. N. Mulay, *Theory and Applications of Molecular Paramagnetism*, John Wiley & Sons Inc, 1976.

67 D. S. Mathew and R.-S. Juang, *Chem. Eng. J.*, 2007, **129**, 51–65.

68 M. A. Baqiya, A. Taufiq, Sunaryono, K. Ayun, M. Zainuri, S. Pratapa, Triwikantoro and Darminto, in *Magnetic Spinels - Synthesis, Properties and Applications*, InTech, 2017.

69 E. Rios, J.-L. Gautier, G. Poillerat and P. Chartier, *Electrochim. Acta*, 1998, **44**, 1491–1497.

70 O. F. Odio and E. Reguera, in *Magnetic Spinels - Synthesis, Properties and Applications*, InTech, 2017.

71 J. Mohapatra, A. Mitra, H. Tyagi, D. Bahadur and M. Aslam, *Nanoscale*, 2015, **7**, 9174–9184.

72 B. Pacakova, S. Kubickova, A. Reznickova, D. Niznansky and J. Vejpravova, in *Magnetic Spinels - Synthesis, Properties and Applications*, InTech, 2017.

73 D. Feng, C. Aldrich and H. Tan, *Hydrometallurgy*, 2000, **56**, 359–368.

74 A. B. Bourlinos, R. Zboril and D. Petridis, *Microporous Mesoporous Mater.*, 2003, **58**, 155–162.

75 V. A. Nikashina and B. F. Myasoedov, in *Natural Microporous Materials in Environmental Technology*, Springer Netherlands, Dordrecht, 1999, pp. 335–343.

76 L. N. Mulay, D. W. Collins, A. W. Thompson and P. L. Walker, *J. Organomet. Chem.*, 1979, **178**, 217–226.

77 A. Stein, G. A. Ozin and G. D. Stucky, *J. Am. Chem. Soc.*, 1990, **112**, 904–905.

78 I. Hussain, I. Gameson, P. A. Anderson, M. Slaski, P. P. Edwards and A. Dyer, *J. Chem. Soc. - Dalt. Trans.*, 1996, 775–781.

79 F. J. Lázaro, J. L. García, V. Schünemann, C. Butzlaff, A. Larrea and M. A. Zal/uska-Kotur, *Phys. Rev. B*, 1996, **53**, 13934–13941.

80 P. A. Anderson, R. G. Bell, C. R. A. Catlow, F. L. Chang, A. J. Dent, P. P. Edwards, I. Gameson, I. Hussain, A. Porch and J. M. Thomas, *Chem. Mater.*, 1996, **8**, 2114–2120.

81 K. Lbdrl, H. K. Beyerl, G. Onyestyhk, B. J. Jiinsson, L. K. Varga and S. Pronier, *Acta Metall.*, 1999, **59773**, 155–158.

82 J. Cao, X.-W. Liu, R. Fu and Z. Tan, *Sep. Purif. Technol.*, 2008, **63**, 92–100.

83 H. Liu, S. Peng, L. Shu, T. Chen, T. Bao and R. L. Frost, *Chemosphere*, 2013, **91**, 1539–1546.

84 L. C. A. Oliveira, D. I. Petkowicz, A. Smaniotto and S. B. C. Pergher, *Water Res.*, 2004, **38**, 3699–3704.

85 I. W. Nah, K. Y. Hwang, C. Jeon and H. B. Choi, *Miner. Eng.*, 2006, **19**, 1452–1455.

86 J. Dong, Z. Xu and S. M. Kuznicki, *Adv. Funct. Mater.*, 2009, **19**, 1268–1275.

87 M.-E. Kouli, G. Banis, P. Tsarabaris, A. Ferraro and E. Hristoforou, *J. Magn. Magn. Mater.*, 2018, **465**, 692–699.

88 S. Laurent, D. Forge, M. Port, A. Roch, C. Robic, L. Vander Elst and R. N. Muller, *Chem. Rev.*, 2008, **108**, 2064–2110.

89 I. Hussain, I. Gameson, P. A. Anderson, M. Slaski, P. P. Edwards and A. Dyer, *J. Chem. Soc. - Dalt. Trans.*, 1996, 775–781.

90 D. V Marinin and G. N. Brown, *Waste Manag.*, 2000, **20**, 545–553.

91 A. Dyer, J. Hriljac, N. Evans, I. Stokes, P. Rand, S. Kellet, R. Harjula, T. Moller, Z. Maher, R. Heatlie-Branson, J. Austin, S. Williamson-Owens, M. Higgins-Bos, K. Smith, L. O'Brien, N. Smith and N. Bryan, *J. Radioanal. Nucl. Chem.*, 2018, **318**, 2473–2491.

92 J. Lehto, R. Koivula, H. Leinonen, E. Tusa and R. Harjula, *Sep. Purif. Rev.*, 2019, **48**, 122–142.

Chapter 2: Experimental

2.1. Synthesis techniques

2.1.1. Hydrothermal synthesis

All the zeolites prepared and described throughout this thesis were produced via hydrothermal synthesis. Hydrothermal synthesis involves the application of heat and high pressure to a reaction slurry. For zeolites, this involves a reaction between aqueous silicates and aluminates which combine to create a homogenous gel. This gel is the product of a co-polymerisation reaction between the silicate and aluminate ions. This generally requires a high pH, therefore it is common practice to use metal hydroxides to provide this change in pH. However, if the desired zeolite has a high silicon content an organic base is preferred as it produces a lower pH.[1,2]

The type of zeolite created is heavily dependent on the synthesis temperature, the pressures generated within the reaction container and the time frame over which the conditions are maintained. The properties of zeolites can also be manipulated by adjusting the ratio of silicate to aluminate ions. Zeolite A and zeolite X have similar preparation and synthesis conditions. Zeolite A (LTA) generally has a Si/Al ratio of 1 and zeolite X (FAU) has a ratio that can vary from 1 up to 1.5. Therefore, during the synthesis of zeolite X it is common for zeolite A to be an impurity. However, if the silicate content is increased this slows down the formation of the zeolite A impurity. With any hydrothermal synthesis there is a fine balance between purity and crystallinity. If the gel formed is not homogeneous, there is a greater chance of impurities or if the gel is not heated for long enough, the zeolite will not fully form and

therefore the overall crystallinity will be reduced. Conversely, if the synthesis conditions are maintained for too long then phases can condense. For example, zeolite X would transition to zeolite A then into sodalite and finally into high density zeolite P. Varying the silicate and aluminate source is another possible way of manipulating the zeolite crystallinity and morphology. Aging solutions prior to heating has also been shown to be effective for the production of highly crystalline materials. This method was used in this project to produce zeolite Y. Although the hydrothermal process appears simplistic, the processes that control formation are not. Hydrothermal synthesis remains the most common method for zeolite formation, however, new synthetic pathways are being developed, such as microwave radiation.[3]

2.1.2. Ion exchange

The main theory behind ion exchange within zeolites has already been discussed in the introduction, therefore this section will investigate current experimental methods and how the factors involved help or hinder the exchange process.

As mentioned during chapter 1, the aluminium content of a zeolite provides a negative charge to the framework. The greater the aluminium content, the greater the negative charge, thus requiring a greater number of counter ions to balance it. Generally, these counterions are present in numbers equal to that of the aluminium.

The phrase ‘ion exchange’ most commonly relates to the aqueous exchange of metal cations in solution. Ion exchange can also refer to the exchange of metal cations outside of solution. However, this is more commonly referred to as solid state ion exchange.

In this case, the ion exchange is performed by dissolving a metal salt in a polar solvent, such as water. This solution can be heated and/or agitated throughout the duration of the exchange. Heating the solution is not a requirement, however, as will be shown throughout this thesis, heating allows the exchange to proceed at an increased rate and can result in higher levels of exchange. The choice solvent is always water, but solution conditions are important and should be selected according to which zeolite is undergoing the aqueous ion exchange. Highly acidic (pH < 2) conditions are unsuitable as they are likely to result in irreversible damage to the zeolite framework, regardless of the silicon to aluminium ratio. Metal acetates have been shown not only to act as an ion exchange reagent but can also act as a buffer during the exchange. Therefore, when highly crystalline materials are desired, acetates are a strong candidate.

2.1.3. Solid state ion exchange

A solid state ion exchange is the exchange of cations by a solid medium. Salt occlusion is a slightly different method of introducing metal cations into zeolitic structures. Occlusion refers to the trapping of a salt i.e. the anion and cation. In practice occlusion and exchange occur together in the same experiment, but an occluded zeolite contains extra cations balanced by the respective number of anions. Solid state methods have a distinct advantage over aqueous ion exchange: they can negate some of the charge balancing required in aqueous ion exchange unless occlusion occurs. This is particularly useful if a large amount of metal content is loaded into a low aluminium containing zeolite. This may also be useful when attempting to load additional cations post aqueous ion exchange. Secondly, this method has a greater potential to form nanoparticles in fewer steps.

The possible production of nanoparticles can be broken down into two simultaneous steps. Step one is the occlusion process itself and the second step is the development of the occlusion products; these can be metal or metal oxide particles in the nano domain. [4]

2.1.3.1. Multi-metal solid state ion exchange

Multi-metal aqueous ion exchange has complicated thermodynamics. If performed on zeolites it is limited by their need for charge balancing, therefore it is not commonly used for this purpose. By performing the multi-metal ion exchange via a solid-state route, exchange levels greater than full exchange can be achieved. Full exchange is considered to be the charge balancing equivalent but solid state ion exchange can add more cations than that, as the charge balancing limitation is overcome by introducing charge balancing anions (salt occlusion). Typically, the zeolite sample is heated under vacuum with the required amount of metal salts. High temperatures are usually required to allow the salts to become mobile. A vacuum is used to ensure that any gases produced do not remain trapped within the zeolite. A potential problem of utilising this technique, instead of sequential aqueous ion exchange followed by salt occlusion, is that the initial cation can remain present in the reaction mix. However, this problem can be avoided if an ammonium containing zeolite is used as the starting material, as the ammonium will decompose during the heating process.

If the aim of the exchange is to occlude only the metals and not to generate any oxides, then the amount of each salt used would be an important consideration. As the aim of this project was to create metal oxide nanoparticles with the greatest loading possible, this was not an issue.

2.2. Instrumentation and characterisation techniques

2.2.1. Crystallography and X-ray diffraction

Crystallography and X-ray diffraction are two of the most important investigative tools for a solid-state chemist. X-ray diffraction provides structural information at an atomic level whilst crystallography allows one to demonstrate how the atoms are arranged in solids.

2.2.1.1. Fundamentals of crystallography

If a solid is described as ‘crystalline’ this is referring to the periodic arrangement that the atoms adopt in a three-dimensional lattice. This arrangement is defined as a unit cell, which is the smallest repeatable unit that exhibits the symmetry of the crystal structure. By using the unit cell and translational symmetry, the entirety of the crystal lattice can be created. The unit cell has three different axes (*a, b, c*), and three different angles (*α, β, γ*), which are known as the lattice parameters; together these can be used to easily define any unit cell (see Figure 10). [5]

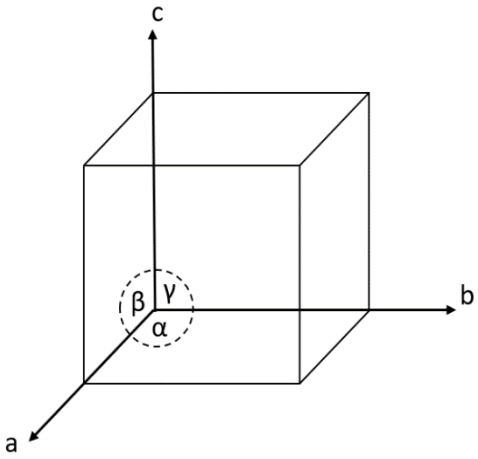
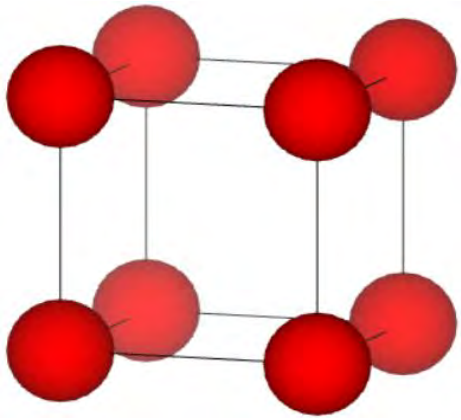
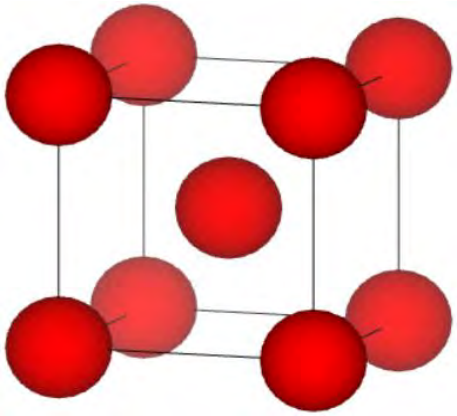


Figure 10: Depiction of a unit cell

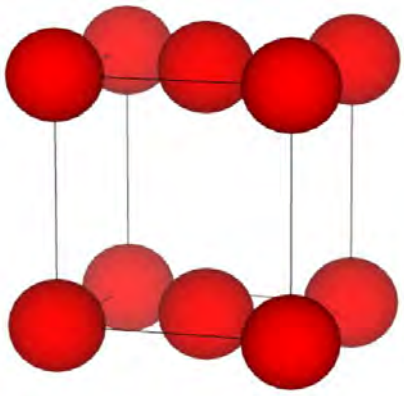
Unit cells can have four different types of lattice centring (C, P, I and F) as described by Figure 11.



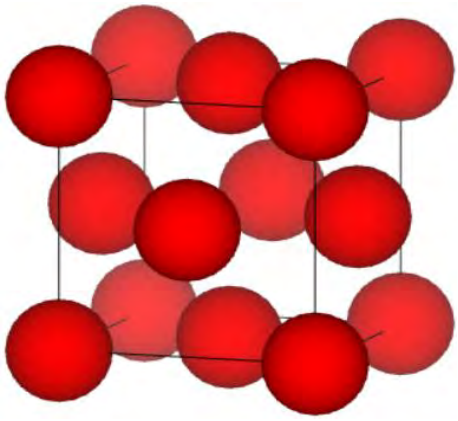
Primitive (**P**) lattice



Body-centred (**I**) lattice



Base-centred (**C**) lattice



Face-centred (**F**) lattice

Figure 11 The different types of lattice centring

The unit cell can adopt one of seven different crystal systems shown in Table 3.

Table 3: The seven crystal systems

Unit cell dimensions	Crystal system	Symmetry elements
a = b = c; α = β = γ = 90˚	Cubic	Four three-fold axis
a = b = c; α = β = γ ≠ 90˚	Trigonal	One three-fold axis
a = b ≠ c; α = β = γ = 120˚	Hexagonal	One six-fold axis
a = b ≠ c; α = β = γ = 90˚	Tetragonal	One four-fold axis
a ≠ b ≠ c; α = β = γ = 90˚	Orthorhombic	Three perpendicular two-fold axis
a ≠ b ≠ c; α = γ = 90˚ β ≠ 90˚	Monoclinic	One two-fold axis
a ≠ b ≠ c; α ≠ β ≠ γ ≠ 90˚	Triclinic	None or an inversion centre

A combination of these systems and lattice centrings creates 14 different lattice types, which are commonly referred to as the Bravais lattices. These 14 lattices show the intrinsic symmetry of each of the unit cells by identifying points of symmetry that are equivalent. These points are known as lattice points, with any atom located on said lattice point being identical to that on any other lattice point. [5]

The positions of the atoms within any unit cell are denoted using fractional coordinates with respect to the axis of the unit cell. By including the atoms in a unit cell, additional symmetry operations are created (screw and glide planes) and must be taken into consideration. The 32 crystallographic point groups along with the 14 Bravais lattices combine to create 230 different space groups which can be used to characterise any given crystal structure. [6,7] These crystals scatter X-rays which provides the basis for X-ray diffraction.

2.2.1.2. Miller indices

To help with the visualisation of the lattice, imaginary crystallographic planes can be used to divide up a unit cell and create a reference point to which the atoms within the crystal structure can be referred to. The crystallographic planes extend out of the unit cell periodically throughout the crystal structure. The planes are characterised using three separate integers known as Miller indices which are denoted (*hkl*). Depending upon the symmetry shown by the crystal system, certain lattice planes can be equivalent, such as (*100*), (*001*) and (*010*) in a cubic system. [5] Parallel planes have the same Miller indices with the distance between the planes perpendicularly denoted as the d-spacing (d_{hkl}). For a given set of (*hkl*), the d-spacing can be calculated if the unit cell parameters are known. Equation 1 shows how to calculate the d-spacing for an orthorhombic system:

$$\frac{1}{d_{hkl^2}} = \frac{h^2}{a^2} + \frac{k^2}{b^2} + \frac{l^2}{c^2}$$

Equation 1 d-spacing equation for an orthorhombic system.

The equation becomes more complex for systems with lower symmetry (e.g. triclinic) or simplifies for systems of higher symmetry (e.g. cubic).

2.2.1.3. Generation of X-rays

In most laboratory diffractometers X-rays are generated by accelerating electrons towards a target metal anode in a high energy beam. Typically, this target is made of either copper or cobalt. The accelerated beam causes electrons from the core orbitals of the metal target to be ejected. For copper, electrons can move from M and L orbitals

into the vacant K orbital to produce K_β and K_α radiation, respectively. The difference in orbital energy causes different X-rays to be emitted as shown in Figure 12.

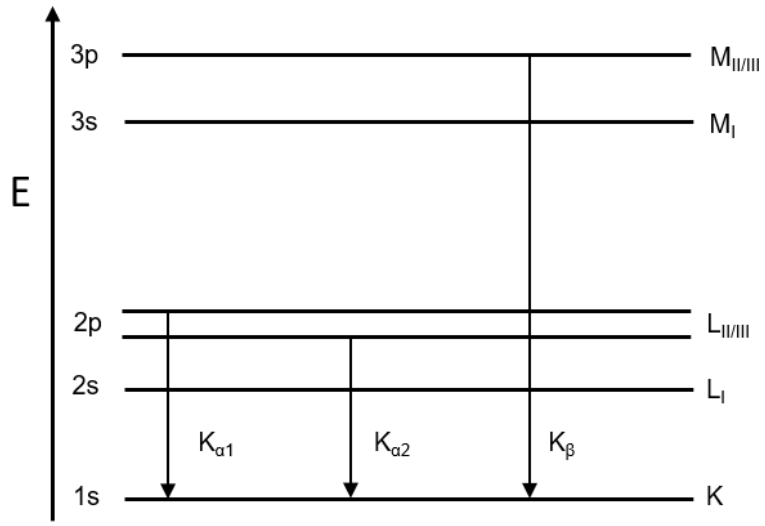


Figure 12: Energy level diagram of a copper atom

The energy of the electronic transition is a fixed value therefore a characteristic spectrum is generated for each element. The spin multiplicity of copper in the L orbital causes two separate transitions which results in two different X-ray wavelengths, known as $K_{\alpha1}$ and $K_{\alpha2}$ radiation. During the characteristic X-ray generation, background X-rays are also produced in the process when the high-speed beam of electrons is slowed rapidly upon collision with the target anode. These X-rays are known as bremsstrahlung X-rays.[8,9]

2.2.1.4. Monochromation of X-ray radiation

Monochromation is commonly required to produce a single wavelength of radiation which is then used for X-ray diffraction. Radiation generated from the X-ray source contains a wide spectrum of X-rays due to the various electronic transitions that can

occur. Monochromators are introduced to select the desired part of the X-ray spectrum, which is the $K_{\alpha 1}$ radiation for a copper source. Laboratory diffractometers commonly use two different types of monochromator, either a Crystal or Göbel Mirror. Crystal monochromators use single crystals of germanium or silicon at a particular orientation (111). Therefore, the resulting X-rays transmitted satisfy the Bragg equation (2.2.1.6). Göbel Mirror monochromators use crystals of multiple layers that are constructed in a parabolic shape. This causes the divergent beam to intercept the crystal at various points and focus into a single wavelength beam.

2.2.1.5. Fundamentals of X-ray diffraction

X-ray diffraction (XRD) is considered to be one of the most powerful investigative tools for characterisation of crystalline materials. This technique focusses X-rays onto a crystal; they are then scattered by the atomic electrons within the crystal. The scattered X-rays are detected in different directions and in varying intensities. X-rays have a wavelength of approximately 1 Å ($1x10^{-10}$ m), which is comparable to the distance between atoms within a crystal lattice. As a result of this similarity, interference between scattered X-rays can occur. Interference can be constructive where wave planes add together to give an overall higher intensity or destructive where the waves cancel out. This is dependent on the phase relationship of the two waves. If two waves of the same intensity travelling on the same directional path are not in-phase with one another, the waves destructively interfere with one another. This means that the amplitudes of the two waves cancel each other out, with no net intensity in an XRD pattern. These waves are said to have a phase shift $\delta\psi$ equal to 1. If the waves are in-phase with one another, they will combine constructively, increasing the overall

intensity of the wave and creating a peak in the resultant XRD pattern when this happens over the entirety of the crystal. These waves are said to have a phase shift $\delta\psi$ equal to 0. Waves scattered by atoms at different positions will also have a phase shift and will therefore arrive at the detector separately. Therefore, information about atomic positions can be determined from the measured intensities.

2.2.1.6. Bragg's law

In order to derive Bragg's law, it is assumed that X-rays behave like visible light and that they reflect off the planes in the lattice. However, unlike visible light, X-rays partially penetrate the X plane and can also be reflected by the planes below e.g. Y, which is parallel to the one penetrated originally as shown in Figure 13.

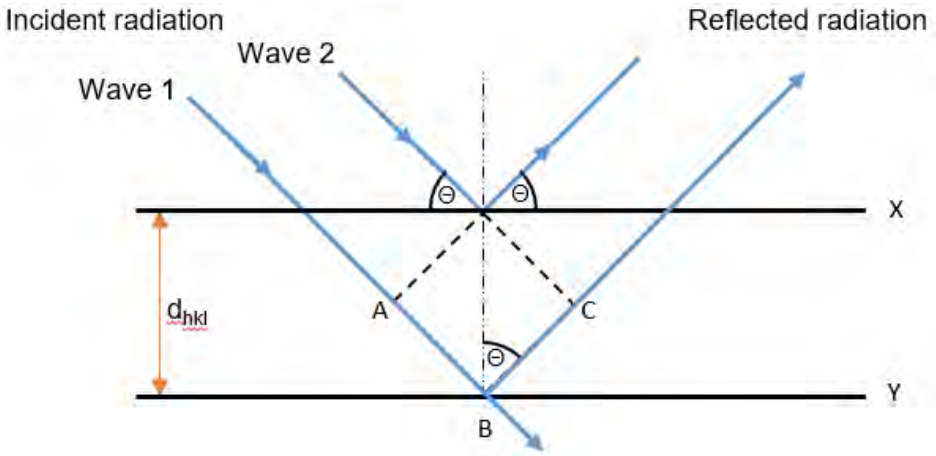


Figure 13: Scattering of X-rays from adjacent planes'

This means that wave 1 will have to travel a greater distance (AB+BC) than wave 2 before the reflection occurs. Therefore, waves scattered by parallel planes reach the detector with a phase shift. If these two planes are aligned as shown in Figure 13 then the distance 'ABC' is equal to a whole number of wavelengths ($n\lambda$), in this case the

incident X-rays will be in-phase resulting in constructive interference. This relationship is described mathematically in these equations.[8]

If

$$n\lambda = (AB + BC)$$

therefore

$$(AB + BC) = (d \sin\theta + d \sin\theta)$$

Then

$$n\lambda = (d\,\mathrm{Sin}\theta + d\,\mathrm{Sin}\theta) = 2d\,\mathrm{Sin}\theta \text{ (Bragg's Law)}$$

For any values where nλ is not an integer, there is destructive interference.

In powder diffractometry, X-rays irradiate the sample with a monochromatic beam at an incident angle of θ as depicted in Figure 13. The detector is therefore positioned at 2θ with respect to the incident beam. The powdered sample contains crystallites that are randomly orientated, therefore certain crystallites satisfy the requirements for Bragg's law. By moving the detector through a specified range of 2θ and using a scintillation counter, the relative intensities of the diffracted waves can be measured. The results are commonly displayed by plotting relative intensities against the values of 2θ but if necessary, Bragg's law can be used to convert positions of 2θ to the distances between the planes (d).[8]

2.2.1.7. What information does PXRD provide?

Every crystalline solid has its own characteristic powder pattern that can be used to identify the phases present within the sample. XRD patterns can be broken down into 4 main components as outlined in Figure 14.

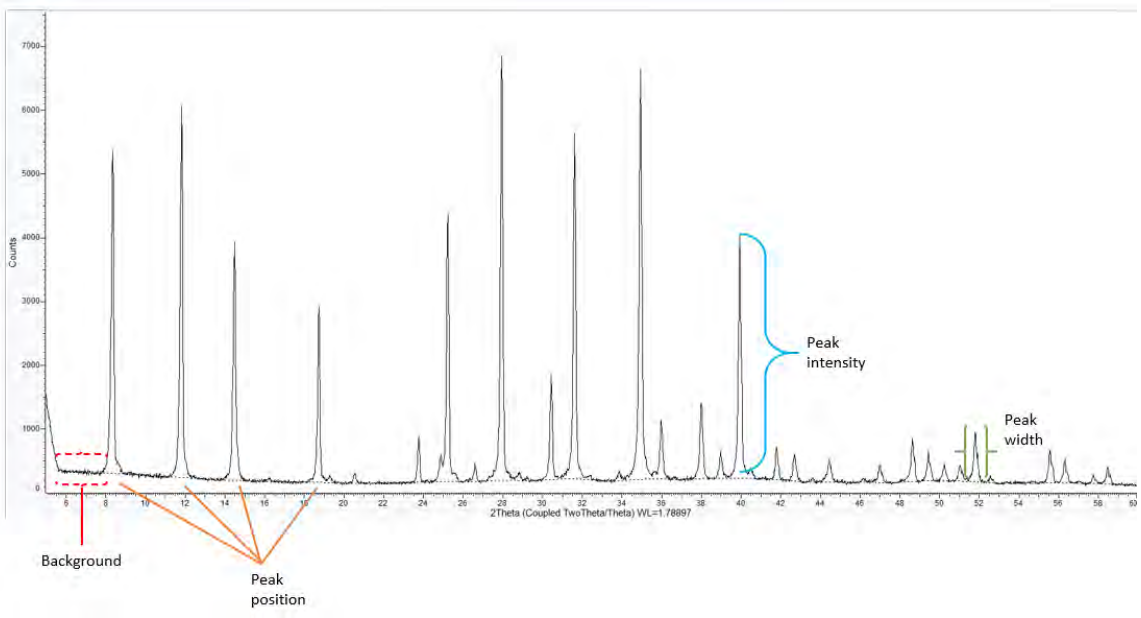


Figure 14: P-XRD pattern showing the main components.

Peak positions are determined by several different factors such as the shape, size and symmetry of the unit cell (for the reasons discussed previously when deriving Bragg's law). Peak positions are directly influenced by the distance (*d*) between parallel planes within a unit cell. The wavelength of X-ray radiation (λ) used also determines peak position. Therefore, if the radiation was changed from copper to cobalt this will result in a peak shift in 2θ. However, this can be avoided by plotting d-spacings instead of 2θ if required to convert data from two different X-ray sources. The instrumentation used

also has a contribution to the peak position, through a sample height displacement or zero point error.

Peak intensities provide information about the atoms within a unit cell in terms of atomic position, type of atoms and thermal motion of the atoms. Instrumental factors again have an impact on the overall intensity. These factors include the intensity of the X-ray source, the type of detector used, and the properties associated with these detectors. There are also experimental factors that affect the peak intensities, such as the data collection time and the scattering ability of the sample.

The background of a powder X-ray diffraction pattern is the result of a combination of instrumental and experimental effects, such as detector noise and the sample holder used. The sample itself also contributes towards the background pattern if an amorphous phase is present or through X-ray absorbance, fluorescence, and Compton scattering. These will be explored in greater detail during the X-ray fluorescence (XRF) and Raman sections.

The size and shape of the crystallites being characterised can have significant effects on the shape and intensity of the diffraction peaks. For crystals that have morphologies of platelet or needles, preferred orientation is an issue which is usually overcome by grinding the sample into a homogenous powder.[8] Peak shape is related to the size of the crystallites, with smaller crystallites resulting in broadening of the diffracted peaks. There is a relationship between crystallite size and peak width that is described in the Scherrer equation shown in Equation 2 where D_{hkl} is the crystallite size in the direction perpendicular to the lattice planes, *hkl* is the Miller indices of the planes

analysed, K is the crystallite-shape factor, λ is the X-ray wavelength, B_{hkl} is the width (full width half maximum) of the diffraction peak in radians and θ is the Bragg angle.[10]

$$D_{hkl} = \frac{K\lambda}{(B_{hkl}\, Cos\theta)}$$

Equation 2 Scherrer equation

2.2.1.7. Rietveld and Pawley refinements

A more detailed method for analysing a powder diffraction pattern is by completing a Rietveld refinement. The Rietveld refinement method developed in the 1960's is used to solve structures by starting with a structural model and refining the model by minimising the difference between the calculated and experimental diffraction patterns. The starting structural models contain information concerning the lattice parameters, occupancies, atomic positions and thermal motion. This model is used in conjunction with a least-squares mathematical method to allow the development of a diffraction pattern that is similar to that of the sample.[11]

Several years later, after the development of the Rietveld refinement, a new technique known as a Pawley refinement was devised. This allowed the unit cell parameters of a crystalline solid to be calculated. This technique still uses the least squares method, but it does not use a structural model to calculate the intensities. Instead, it refines the cell parameters until it closes matches that of the observed intensity.

2.2.1.8. X-ray diffraction instrumentation and configurations

Within this thesis, all laboratory powder diffraction collected at room temperature was collected using a Bruker D2 diffractometer which used cobalt $K_{\alpha1}$ and $K_{\alpha2}$ radiation (l = 1.788965 Å and 1.792850 Å). The diffracted Co K_{β} radiation (l = 1.620790 Å) was removed by a Ni filter. The diffraction data were collected by a LYNXEYE_XE_T detector (PSD) (1D mode) across a 2θ range of either 5-60° or 10-60° with a step size of 0.29.

All variable temperature powder diffraction data were collected on a Bruker D8 diffractometer fitted with an Anton Paar variable temperature sample stage. This diffractometer used copper $K_{\alpha1}$ and $K_{\alpha2}$ radiation (l = 1.5406 Å and 1.5444 Å) with the diffracted K_{β} radiation (l = 1.3922 Å) removed by a Ni filter. The diffraction data were collected by a Solid-state LynxEye position sensitive detector (PSD) with a 3° electronic window across a specified 2θ range of 10-60° with a step size of 0.29.

2.2.2. X-ray fluorescence

X-ray fluorescence spectroscopy (XRF) is a non-destructive analytical technique that is used to determine the elemental composition of a sample. The sample is bombarded with an X-ray beam, causing the sample to emit characteristic X-rays. These are then measured to determine the elements present and their given concentrations. An X-ray can ionise an atom provided that the energy of the incident X-ray exceeds that of the ionisation energy.[12]

In this technique core electrons are ejected from orbitals within the atom upon bombardment of the sample with high energy X-rays. To re-stabilise the electronic configuration, an electron from a higher energy orbital must move to fill the core orbital. Quantum mechanical selection rules state that only transitions that cause a change in the orbital angular momentum are allowed. [9,13]

The allowed and most probable transactions are usually noted using the Siegbahn notation; K_α corresponds to the transition from $2p_{x/y}$ to 1s, K_β corresponds to 3p to 1s and L_α is the 3d to 2p transition. K_α transitions give rise to lines with different energies $2p_{x/y}$ to 1s ($K_{\alpha1}$) and $2p_z$ to 1s ($K_{\alpha2}$).[14] The ratio of alpha and beta lines can be used to determine the thickness of the layer (Critical depth). The relative intensity of these lines will change by differing amounts depending upon the absorbance of the different layers (Critical and penetration depth). Mass absorption coefficients can be calculated and are known for each element line. Therefore, variations from the expected α:β ratios can be used to calculate layer thickness.

After stabilisation there are two possible processes that occur, either an X-ray with a characteristic wavelength (due to energy difference between the higher energy orbital and core orbital) is detected. Or alternatively, the characteristic X-ray transfers to a different electron within the atom. The resulting photoelectron is then emitted from the atom, this is a phenomenon termed the Auger effect.[9]

Fluorescence yield is the term used to describe the probability of X-ray emission occurring due to ionisation of the atom, rather than the Auger effect occurring. Fluorescence yield increases with atomic number, therefore sodium is the lightest

element that routine XRF spectroscopy can be performed upon due to the very low fluorescence yields of light elements.[9,12]

XRF spectrometers are built from 4 up to 8 primary components depending upon the detection system in place. Spectrometers are termed energy dispersive (ED) or wavelength dispersive. ED-XRF spectrometers comprise 4 components: an excitation source, a primary filter, a vacuum seal and a detector. WD-XRF spectrometers are comprised of 8 components: a rhodium anode target, a primary filter wheel, a vacuum seal, collimators, analyser crystals, a scintillation detector and a flow proportional detector. The analytical performance of each XRF spectrometer is determined by its detector which is characterised by the resolution in energy and the maximum count rate. In ED-XRF systems the detector always observes the whole spectrum, but with modern SDD detectors only able to handle 100-500 kcps (kilo counts per second), the sensitivity of ED-XRF is limited by the maximum count rate of the detection system. In WD-XRF spectrometers, detectors view only the wavelength selected handling between 1000-2000 kcps. Typically, the power of the X-ray tube is the sensitivity limitation rather than the detector.

In WD systems, X-rays emitted from the sample are separated by the wavelength of the scattered X-rays that interfere constructively prior to detection. While the sample is of fixed position, the angles of the detector and analyser crystals can be altered to comply with Bragg's law so that only particular wavelengths are measured. Only X-rays that satisfy Bragg's law can be reflected constructively. In contrast, ED systems detect emitted X-rays directly with a semi-conducting detector, commonly Si(Li). Semi-conducting detectors convert the X-ray energy into an electrical pulse, with the energy of this pulse being proportional to the intensity.[12,13,14,15]

ED and WD XRF spectrometry allow for both qualitative and quantitative analysis of a sample's composition. For qualitative analysis, elements are identified by their presence in the XRF spectrum due to their characteristic emission lines. In quantitative analysis, the relative integrated peak intensities (I_R) from the resultant spectrum are related to the weight fraction of an element (C) by two key factors: the instrument factor (K) and the matrix factor (M).

Equation 3 $$C = I_R \times K \times M$$

These key factors use complex mathematical calculations to consider the impact of determined or approximated parameters on the relationship between the weight fraction (C) and the peak integral (I_R).[12] The matrix factor (M) allows for the consideration of sample dependent phenomena such as primary absorption, secondary fluorescence and secondary absorption. Primary absorption refers to the absorption of radiation directly from the X-ray source, secondary adsorption refers to fluorescence radiation from the sample that is absorbed. Secondary fluorescence refers to any excitation that occurs by fluorescence radiation from other elements present within the sample. Secondary fluorescence and secondary absorption effects are especially prevalent in samples which contain a wider range of elements. While the matrix factor models the influence of the phenomena discussed, precise matrix factors are only thought to be possible when elements with close atomic numbers are present within a system. Any inaccuracy in the matrix factor leads to an inaccuracy in the determined weight fraction.[12]

Prior to data collection there are several different ways to prepare a sample: loose powder, a pressed pellet or a fused bead. Each method has associated advantages

and disadvantages thus it is common to use a combination. Loose powder is the most common and simplest preparation method. This method uses a plastic sample cup and a thin mylar film. The main advantage of this method is retrieval of the sample post analysis. However, as there is loose packing of the powder there is a lower signal to noise ratio. If there is a distinct difference in particle size this leads to heterogeneity in the sample and this will result in the sample having a non-constant bulk density, all of which mean that loose powder commonly has issues related to the accuracy of the critical depth and poorer low angle absorption.

The pressed powder method is the second most common preparation method. Conversely to loose powder, the sample cannot be retrieved after analysis as a briquetting agent (composed of elements almost invisible to the XRF) is used to bind the sample during pellet formation. Using pressed pellets removes most of the issues associated with loose powder but still is reported to have an error of approximately 10% (as determined by Bruker at the point of sale). The pressed pellet method is preferred for lighter elements as they are not diluted significantly by the briquetting agent.

The fused bead preparation method is preferred when characterising materials composed of heavier elements, as heavier elements are not lost during the dilution which is required as part of the sample preparation. This method requires the use of a lithium borate flux, this requires greater sample dilution (10:1 flux:sample) than for a pressed pellet (5:1), therefore is unsuitable for lighter elements. Fluorescence yield increases with atomic number and the characteristic X-rays of the heavier elements propagate further, which means that they are not lost within the lithium borate flux. Formation of the fused beads requires heating of the sample to 1050 ˚C, followed by

vigorous mixing and the introduction of a releasing agent, commonly ammonium iodide. Use of a releasing agent is required to increase the surface tension which causes the bead to release upon cooling ready for analysis. However, this preparation method poses a serious health and safety risk without using a fully automated fused bead making system, therefore fused beads were not used for analysis in this thesis.

2.2.3. Raman spectroscopy

Raman spectroscopy is a spectroscopic technique based upon inelastic scattering that can help to determine the nature of the bonding within a given material. For a material to be 'Raman active' there must be a change in the polarisability as the sample vibrates. The term polarisability can be defined as the relative tendency of the molecular electron cloud to be distorted from its original shape by an external electric field. It is the symmetry of the molecule that determines which of the vibrations are 'Raman active'. Asymmetric vibrations are less intense than symmetric vibrations.[16]

In Raman spectroscopy, the sample is irradiated with a monochromatic beam of radiation, typically generated using a laser. Upon interaction with the beam, photons are absorbed, leading to the electrons transitioning into a virtual excited state. However, the excitement is temporary as relaxation occurs and photons are released. Relaxation can occur via elastic and inelastic scattering. Elastic scattering, also known as Rayleigh scattering, happens when the energy of the emitted photon is the same as the energy absorbed (Figure 15). Rayleigh scattering occurs in most cases. However, scattering can also occur inelastically. Inelastic scattering happens when the incident energy is different to that of the emitted photon. Two types of inelastic scattering can occur depending on the initial and final energy states. If the energy of

the photon absorbed is greater than that of the photon emitted, upon relaxation the molecule is promoted to a higher vibrational state. This is known as Stokes scattering (Figure 15). If the energy of the photon absorbed is less than that of the photon emitted, the molecule is demoted to a lower vibrational state. This is known as Anti-Stokes scattering (Figure 15). It is these changes in vibrational state during inelastic scattering that are detected in Raman spectroscopy. The spectrometer detects the intensity of the scattered photons and plots it as a function of wavenumber.[17]

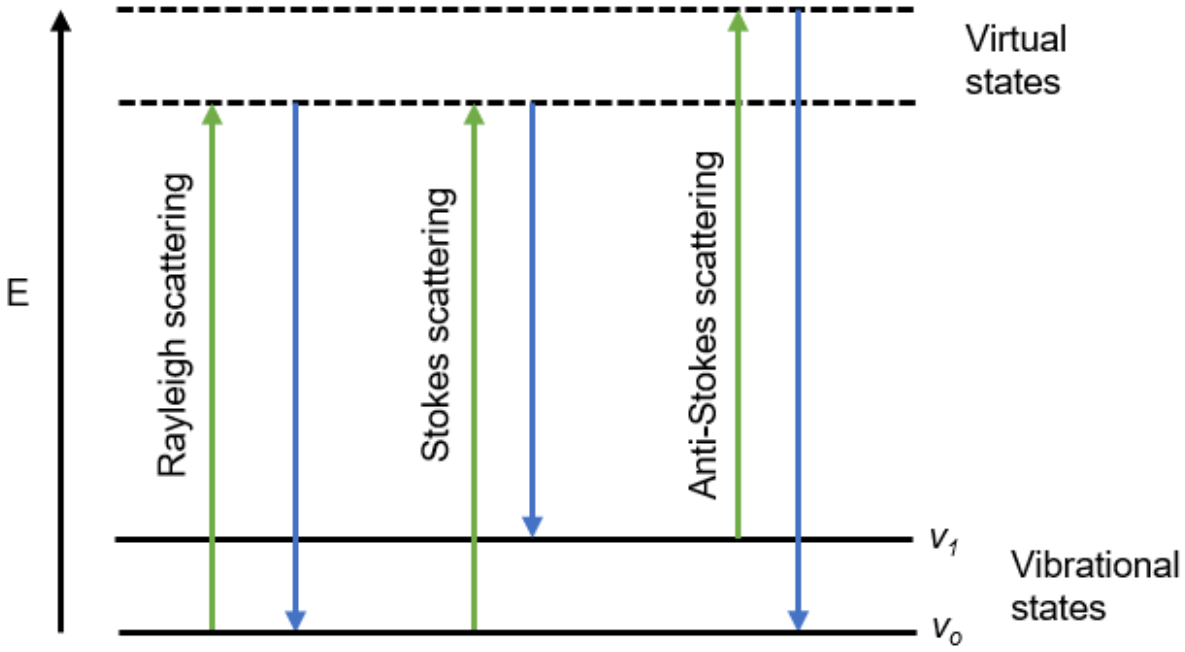


Figure 15 Depicting Rayleigh, Stokes, and anti-Stokes scattering processes in Raman spectroscopy.

The Raman spectrometer used for analysis in the thesis was a Renishaw Invia reflex microscope. Samples were irradiated using either a 532 nm or 633 nm laser which had been focused using a working distance of 20x objective lens. This creates a spot size of approximately 60 μm; the beam power used was sample dependent.

2.2.4. Thermogravimetric analysis and mass spectrometry

Thermogravimetric analysis or TGA is a technique used to measure changes in mass with varying temperature. Experiments typically use ~20-40 mg of sample in an alumina crucible which is then placed into a sealed furnace. A TGA instrument uses a very accurate balance which is mounted inside a furnace. It records changes in mass throughout the duration of the experiment. This technique is commonly used to determine a material's thermal stability, i.e. the temperature at which the sample decomposes. The chamber is evacuated and then purged with nitrogen gas for at least three cycles. The analyser is set to heat steadily to a specified rate (10 K/min) until the desired temperature is reached. Isothermal and cooling steps can also be included if desired, however, they were not required for the work completed in this thesis.[18]

Differential thermal analysis (DTA) can run alongside TGA. DTA involves recording the difference in temperature between the crucible containing the sample and an empty reference crucible. This allows for a sample's thermal events to be detected and recorded, such as melting, phase transitions or material losses.[18]

A TGA instrument can also be connected to a mass spectrometer (MS). A MS creates positively charged ions from gases that are evolved during the experiment. These charged ions are separated using their mass/charge (m/z) ratio therefore, mass loss can be attributed to a specific species. A more detailed introduction to mass spectrometry can be found in section 2.2.9.

2.2.5. Mössbauer spectroscopy

Mössbauer spectroscopy is a versatile technique that is used in several different scientific disciplines. It provides very precise information relating to a sample's structural, chemical and magnetic properties, such as the electron drawing power of electronegative groups, electron shielding, ligand bonding states and valency states.[19]

Mössbauer spectroscopy or the Mössbauer effect is the emission or resonant absorption of nuclear γ-rays where the nuclei have a recoil velocity of effectively zero, therefore is a recoil free event. Mössbauer analysis uses a radioactive source, the sample is exposed to a beam of gamma radiation, with the transmission of the beam measured. Mössbauer spectroscopy can only be performed on solid samples that have a rigid crystal lattice as this allows the nuclei in the atoms to go through a variety of energy level transitions. The nature of these energy levels is impacted (upon) by their surrounding environment, both magnetic and electronic.[20] An example of decay in a radioactive cobalt source is shown in Figure 16. This shows that ^{57}Co decays into ^{57}Fe which then decays further.

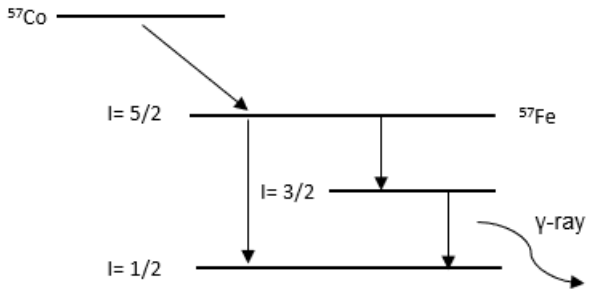


Figure 16 Schematic depicting the decay of 57Co.

During decay gamma rays are emitted, and subsequently absorbed by the sample. The energy and frequency of the gamma radiation corresponds to the transition from the ground state to an excited state of the nuclei concerned. Due to the Mössbauer effect only occurring when the absorbing and emitting nucleus exactly match, this technique is element specific and would require a different emission source for each element. However, Mössbauer is not possible for all elements as they do not have suitable emission sources. Table 4 contains several nuclei and their properties that are suitable for Mössbauer spectroscopy.[20]

Table 4 Mössbauer active isotopes and their properties.[20]

Nucleus observed	Natural abundance (%)	Ground spin state	Excited spin state	Radioisotope source
^{57}Fe	2.2	$\frac{1}{2}$	$\frac{3}{2}$	^{57}Co
^{99}Ru	12.7	$\frac{3}{2}$	$\frac{5}{2}$	^{99}Rh
^{119}Sn	8.6	$\frac{1}{2}$	$\frac{3}{2}$	^{119m}Sn
^{197}Au	100	$\frac{3}{2}$	$\frac{1}{2}$	197^{m}Pt

During an experiment, the energy of the gamma rays is modulated to achieve the required range of energies. This can be achieved by moving the position of the gamma source closer or further away from the absorber at a defined velocity as this modifies the energy by exploiting the Doppler effect. In practice this is achieved by using an oscillator with the shift in energy described in Equation 4 where *v* is velocity, *c* is the speed of light and E_γ is the unshifted γ-ray energy.

$$\text{Equation 4 } \Delta E = \left(\frac{v}{c}\right) E_\gamma$$

This information allows transmission (Counts) to be plotted against velocity (Figure 17). If the emitting and absorbing nuclei are in identical environments, only a single line will appear in the resulting Mössbauer spectrum as shown in Figure 17. However, in practice it is unlikely that the nuclei studied will be identical to the source, therefore a change in the energy of the γ-rays is required. By exploiting the doppler effect, one can sweep across a range of energies until the energy of the modulated γ-ray matches that of the absorber's nuclear transition, when a peak is record on the spectrum.[19,20]

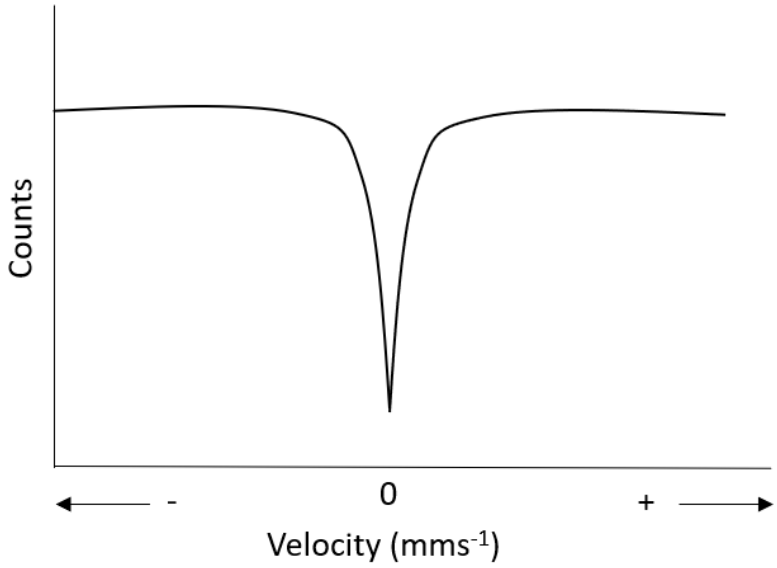


Figure 17 Example Mössbauer spectrum for an identical emitting and absorbing nuclei in the same environment.

There are typically three main components of a Mössbauer spectrum: isomer shift, quadrupole splitting and magnetic splitting. Isomer shift (δ) is reported in the spectra relative to the known absorber, with the resultant velocity either positively or negatively shifted. Isomer shift is due to the different electron charge densities between the emission source and the measured sample. Isomer shift values can be used to determine the electron drawing power of electronegative groups, electron shielding, ligand bonding states and valency states. For example, the electron configurations of Fe^{2+} and Fe^{3+} are (d^6) and (d^5), respectively. Therefore, the iron(II) ions have less s-electrons at the nucleus due to screening and thus iron(II) ions have larger positive isomer shifts compared to that of the iron(III) ions, and this provides information about oxidation states and the chemical environment as mentioned previously.

Quadrupole splitting (Δ) results in a doublet in the resultant spectra and is a result of a shift in energy levels within the nucleus which has been induced by an electric field. If

nuclei have an angular momentum quantum number I> ½ they are said to have a non-spherical charge distribution. In the presence of an asymmetric electric field the nuclear energy levels of these nuclei split. The charge distribution is described by a single quantity called the electric field gradient (EFG). This phenomenon is termed quadrupole splitting. An example of this quadrupole splitting is shown in Figure 18.

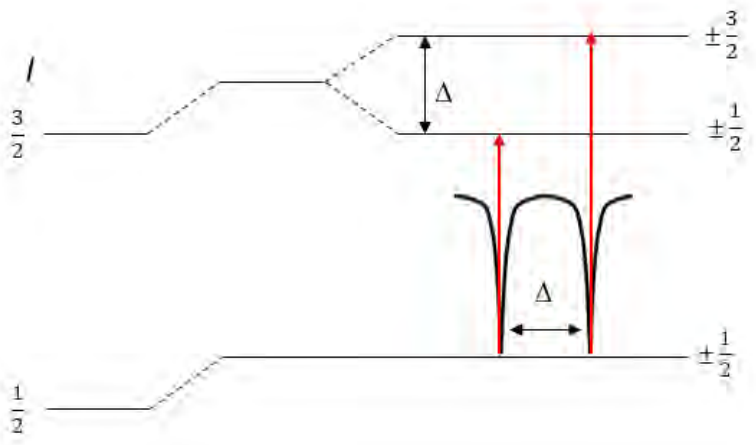


Figure 18 An example of quadrupole splitting.

The final component is magnetic splitting. In the presence of a magnetic field, the nuclear spin moment experiences a dipolar interaction with the applied field. This is known as Zeeman splitting. There are several different sources of magnetic fields that can affect the nucleus with the total effective magnetic field felt by the nuclear described by Equation 5 .The terms within the brackets are due to the atom's partially filled shells.

Equation 5 $$B_{effective} = B_{applied} + (B_{dipolar} + B_{orbitals} + B_{contact})$$

The magnetic field splits the nuclear energy levels with a spin of I into 2I+1 sub-states. For transitions to occur between ground and excited state then changes in m_I must be

1 or 0. This leads to 6 possible transitions for a 3/2 to 1/2 transition. This is illustrated as a sextet in Figure 19 with the spaces between lines proportional to $B_{effective}$.

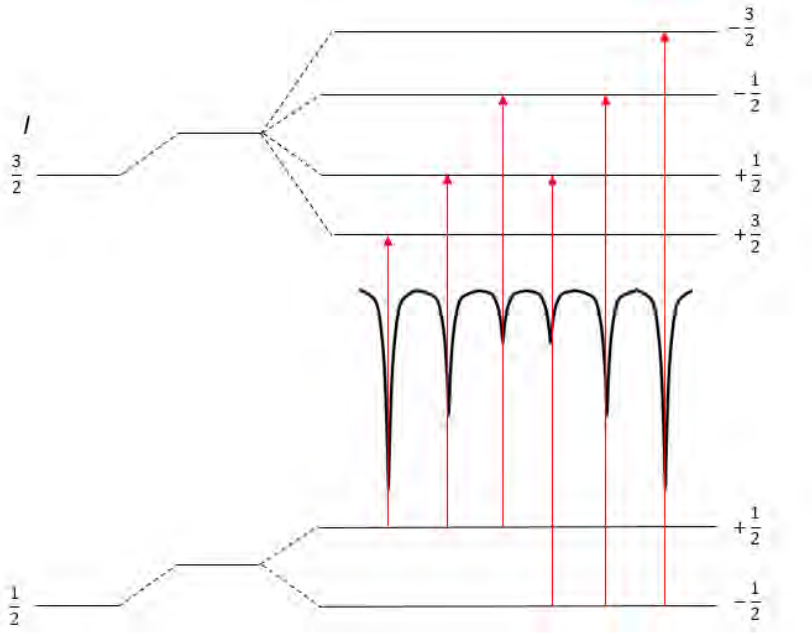


Figure 19 An example of magnetic splitting in a Mossbauer spectrum.

The Mössbauer spectroscopy performed in this project was carried out by Paul Bingham and Alex Scrimshire at Sheffield Hallam university. Interpretation of this data was carried out by myself, Prof Frank Berry and Alex Scrimshire.

2.2.6. Magnetic measurements

2.2.6.1. Magnetic behaviour

To be able to determine the behaviour of magnetic materials in a magnetic field, the types of magnetic behaviour in solids must be considered first. There are five different

types of magnetic behaviour: diamagnetism, paramagnetism, ferromagnetism, antiferromagnetism and ferrimagnetism. Typically, all forms of magnetism are the product of spin ordering of unpaired electrons. Paramagnetism is the result of the spin of unpaired electrons. This magnetism persists only in the presence of an applied field, as paramagnetic materials demagnetise upon removal of the applied field. Materials can also have a magnetic contribution from paired electrons and filled orbitals; This type of magnetism is known as diamagnetism. The magnitude is very small, and it is in the opposite direction to the applied field. Paramagnetism and diamagnetism are differentiated by the manner in which they interact with a magnetic field as shown in Figure 20.[21,22,23]

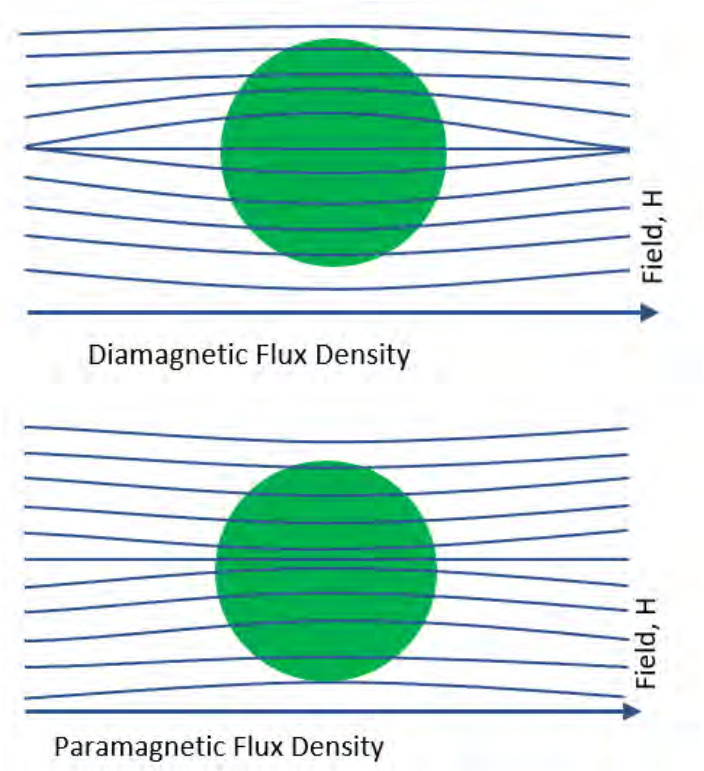


Figure 20 An illustration to represent the effect of diamagnetic and paramagnetic materials on magnetic flux density.

Figure 20 contains spheres in a magnetic field a strength ‘H’ which is depicted by lines. The spheres represent a given material. Figure 20 shows that the flux density is greater for a paramagnetic material compared to a diamagnetic one. If the representation above is under vacuum, we can therefore linearly relate the magnetic flux density ‘B’ to the applied field as shown in Equation 6 (where μ_o is the permeability of free space).[23,24,25]

Equation 6 $$B = \mu_o H$$

However, within a magnetic material the relationship between magnetic flux density ‘B’ and the field ‘H’ is more complicated as both are vector fields and can therefore at any point in time be different in both direction and magnitude. Therefore, the equation can be changed to:

Equation 7 $$B = \mu_o (H+M)$$

However, when discussing the magnetisation of a sample ‘M’ in a magnetic field, a separate term is used which is independent of the field in which the sample is placed. This is shown in Equation 8.

Equation 8 $$X = M/H$$

The equation product is referred to as a magnetic susceptibility ‘*X’* and is a measure of a sample’s overall magnetism. Different types of magnetic behaviour each have different values of magnetic susceptibility. Typically, the values of ‘*X’* obtained from samples that exhibit only diamagnetic behaviour are extremely small. The effect of diamagnetism is present in all materials, however, this effect is usually not detected if other magnetic effects from unpaired electrons are also present. As the target

compounds that will be explored later in the thesis have unpaired electrons, this next section will concentrate on these other magnetic effects.

The remaining magnetic effects can be broken down into four different groups based upon the spin orientation of the sample's free electrons.

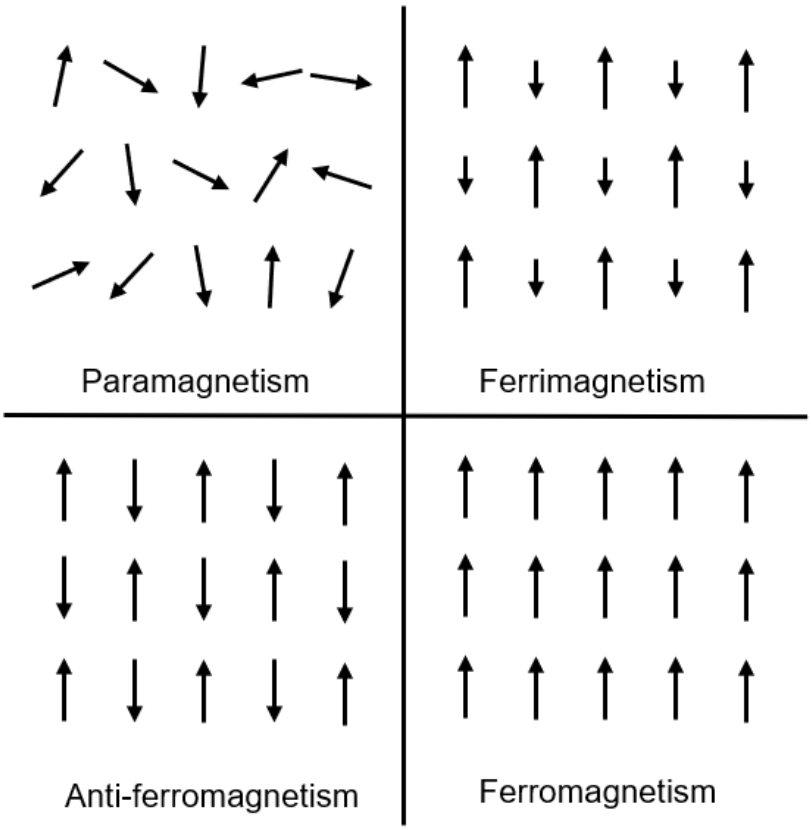


Figure 21 Illustrating the different spin orientations for each type of magnetism.

As shown in Figure 21 the spins of a paramagnetic material exhibit disorder with respect to one another. This is due to paramagnetic materials commonly having electrons that are isolated. Therefore, when exposed to a magnetic field the spins become aligned with the field. However, this alignment is opposed by the randomising effect of thermal energy, therefore, paramagnetic materials demagnetise rapidly after the applied field is removed. Both paramagnetic and diamagnetic materials are

generally considered to be nonmagnetic materials as they only exhibit magnetisation in the presence of an applied field.[25,26]

The three remaining forms of magnetism are due to spin ordering of the unpaired electrons. A ferrimagnetic system is similar to the antiferromagnetic system in that the behaviour detected is the result of opposed spin alignment. They merely differ by the way in which the opposing spins are ordered. In a ferrimagnetic system there are non-identical spins present, therefore the overall moment is unequal. Conversely, in an antiferromagnetic system there are identical spins alternating throughout and therefore there is no overall moment. The final form of magnetic behaviour is ferromagnetism. Ferromagnetic materials have a permanent magnetic moment in the absence of an applied field. Domains in the system align with the applied field. When the field is removed, sections of the domain alignment remain and can act as a permanent magnet. Ferromagnetic materials exhibit higher values of ‘X’ than the other types of magnetism mentioned.[24,25]

This next section explores the relationship between magnetic susceptibility ‘X’ and the applied field ‘H’. Figure 22 contains examples of these relationships illustrated using hysteresis loops for ferromagnetic and paramagnetic materials.

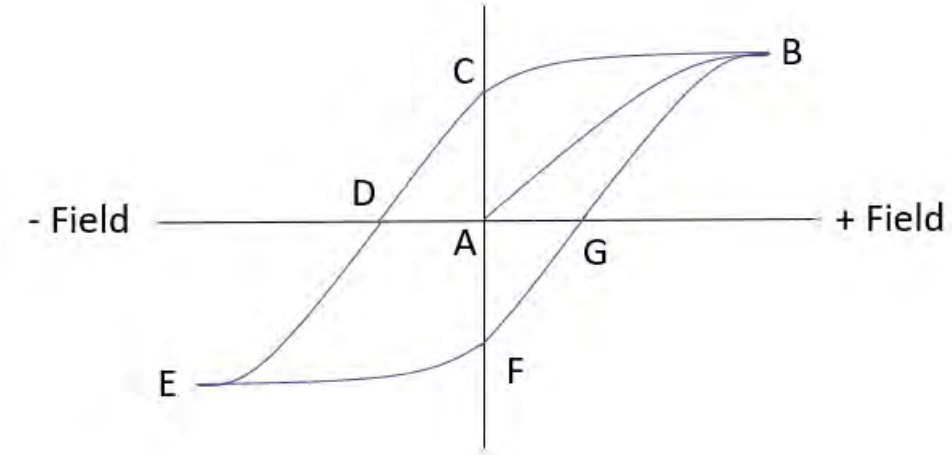


Figure 22 Schematic to describe the different sections of a Hysteresis loop. At points B and E, magnetic susceptibility ‘X’ is at its greatest. Points C and F provide information relating to a material’s residual magnetism, the point at which the curve passes through the Y-axis. Points D and G is the point of intercept on the X-axis and is a measure of a ferromagnetic sample’s ability to withstand an external magnetic field. The presence and shape of a hysteresis loop provides information relating to the magnetic behaviour.

A ferromagnetic material’s magnetic susceptibility gradually changes across the applied field. When this field is reversed, in most cases there will be a small delay which allows for a change in polarity of the material. In a paramagnetic material there is no delay, due to the random spins of the unpaired electrons having no preference to be aligned.

A hysteresis loop is generated by recording changes in the magnetic susceptibility ‘X’ as the applied field is raised and then reduced. By doing so this generates lines A-B, then B-C. At this point the applied field is then reversed and raised which creates line C-D. The applied field is then reduced back down to 0 before finally being raised in the initial direction to complete the data collection loop which is lines D-E, E-F, F-G and G-B. The results collected using this procedure provide important information about the

material characterised. At points B and E, magnetic susceptibility 'X' reaches its greatest, as all the unpaired electrons are aligned with the applied field at that level of magnetisation. This is referred to as being 'magnetically saturated'. Points C and F provide information relating to a material's residual magnetism, the point at which the curve passes through the Y-axis. Coercivity 'H_c' is the point of intercept on the X-axis and is a measure of a ferromagnetic sample's ability to withstand an external magnetic field without it becoming demagnetised (resistance to a change in applied field). When a paramagnetic material is exposed to the same field, there is no resistance therefore the line intercepts the X-axis at zero. Finally, the presence and shape of a hysteresis loop provides information relating to the magnetic behaviour of ferromagnetic and paramagnetic materials and allows for assumptions related to particle size. The width of the loop provides a value for the coercive force, this is a measure of a ferromagnetic sample's ability to withstand an external magnetic field without becoming demagnetised. The coercive force denotes whether a material is classified as a hard or soft magnet.[25]

2.2.6.2. Vibration sample magnetometry

All the magnetic data discussed later in this thesis were collected using a vibrating sample magnetometer (VSM). A VSM works on the basis that a magnetic object moved within a wire coil, generates a current. A VSM comprises two isolated units and a third part which is a control unit to link the other two. Firstly, there is a superconducting magnet, which applies the field to allow for spin alignment and therefore a magnetic susceptibility 'X' reading to be recorded. The superconducting magnet provides a variable field from 0 to 3 T. Data collected in this thesis did not exceed 2.1 T. The

second unit is a sample rod, which allows for sample movement as the rod can be vibrated at a constant rate throughout data collection. The benefit of using this type of system is that prior to collection the sample can be moved into the optimal position within the detector coil. The magnetic measurements in this thesis were collected using a two different Lakeshore machines, a Lakeshore 6300 or a Lakeshore 8300 VSM.

2.2.6.3. Superparamagnetism

Superparamagnetism is a form of magnetism that is present in ferromagnetic and ferrimagnetic nanoparticles. If the nanoparticles are small enough, magnetisation can randomly change direction as the temperature changes. Typically, the time taken between directional changes is referred to as the 'Neel relaxation time'. In the absence of an applied field, when time is used to measure the magnetisation, the time measured is much longer than that of the Neel relaxation time, therefore, the average value appears to be zero.[27] At this point, the nanoparticles are said to be in a superparamagnetic state. An applied field can magnetise the nanoparticles similar to a paramagnetic material. However, there is a huge difference in the magnetic susceptibilities with superparamagnetic materials displaying much larger readings as shown in

Table 5. Upon removal of an applied field, a superparamagnetic material will instantly demagnetise and only remagnetise if the field is reapplied. This characteristic feature is of great importance for the application of the materials in this thesis.

Table 5 Magnetic susceptibility of iron oxides.[28]

	Density (t/m^3)	Mass magnetic susceptibility ($m^3kg\ x10^{-8}$)	Type of magnetism
Hematite, α-Fe_2O_3	5.26	10 to 760	Diamagnetic
Maghemite, γ-Fe_2O_3	4.90	40,000 to 50,000	Ferromagnetic
Magnetite, Fe_3O_4	5.18	20,000 to 110,000	Superparamagnetic

Generally, any ferromagnetic or ferrimagnetic material will transition to a paramagnetic state above its Curie temperature 'T_c'. However, superparamagnetism is different as this transition occurs below T_c of the given material.[25]

When ferromagnetism was mentioned previously in section 2.2.6.1, it stated that the spins of the unpaired electrons are always aligned. However, this is not strictly true as bulk ferromagnetic materials and crystals are divided into separate magnetic domains. Within any domain the spins align but this can differ in polarity to other domains. A material is superparamagnetic if there is a single domain (composed of a single

magnetic domain). For this to be possible the nanoparticle generally has a particle size of 3-50 nm, however, this is material dependent.

2.2.7. Scanning electron microscopy

Scanning electron microscopy (SEM) is commonly used to investigate the surface of a sample using electrons, providing information relating to crystal morphology and particle size. There are several different interactions that can occur after a high energy beam of electrons is focused onto a solid sample as shown in Figure 23.

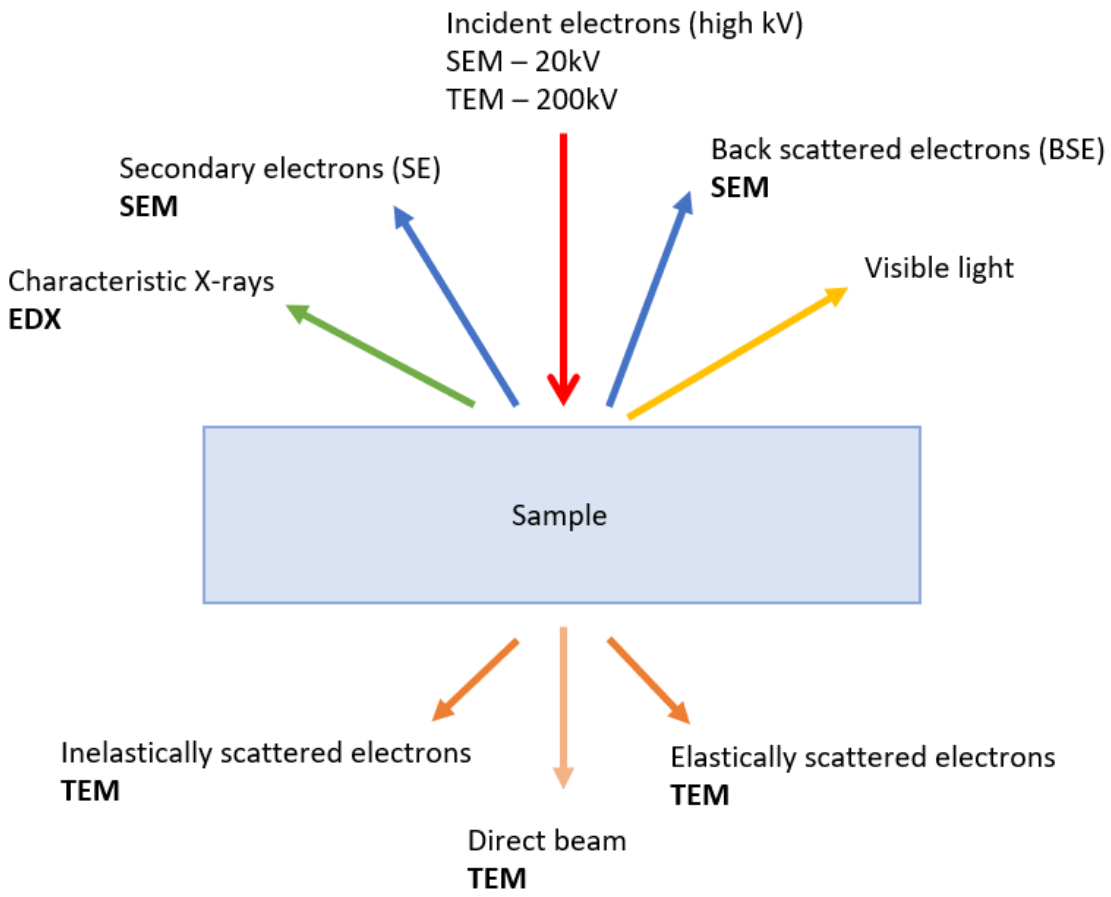


Figure 23 Schematic depicting the different interactions high energy electrons can have with a solid sample.

SEM is the simplest form of electron microscopy which detects incident electrons that have been elastically scattered, these are more commonly referred to as ‘back scattered electrons. SEM can also detect characteristic X-rays and secondary electrons, which are emitted from the surface of the sample.

These interactions allow for the production of high-resolution images on an extremely small scale (200 μm to ~1 nm). These images provide information on the composition, distribution of elements within the sample and the topography. As described previously in section 2.2.2., ionisation of the electrons in the core shell gives rise to the emission of characteristic X-rays. The proportion of elastically scattered electrons can be correlated to the atomic number of the elements present within the samples. Larger atoms with more electrons result in a greater amount of elastically scattered electrons. In the high resolution images produced by backscattered electrons, there are regions of varying brightness, with the brighter regions corresponding to areas with greater atomic numbers present compared to the darker regions of lower atomic numbers or no electron density.[29]

Secondary electron emissions from the surface of the sample produces topological images due to ionisation from the incident X-rays. Samples are often sputtered with carbon or gold (thickness <10 nm) to improve the quality of the images collected by secondary electron imaging. The surface coating prevents charging (accumulation of static fields) as this compromises the signal from the secondary electrons and ruins the image quality with bright spots.

In scanning electron microscopy, electrons are generated by an electron gun and are incident upon the sample at ~20 kV. The incident electrons are focussed using several

electromagnetic lenses including a condenser and one objective lens before being focused upon the surface as shown in Figure 24.[29]

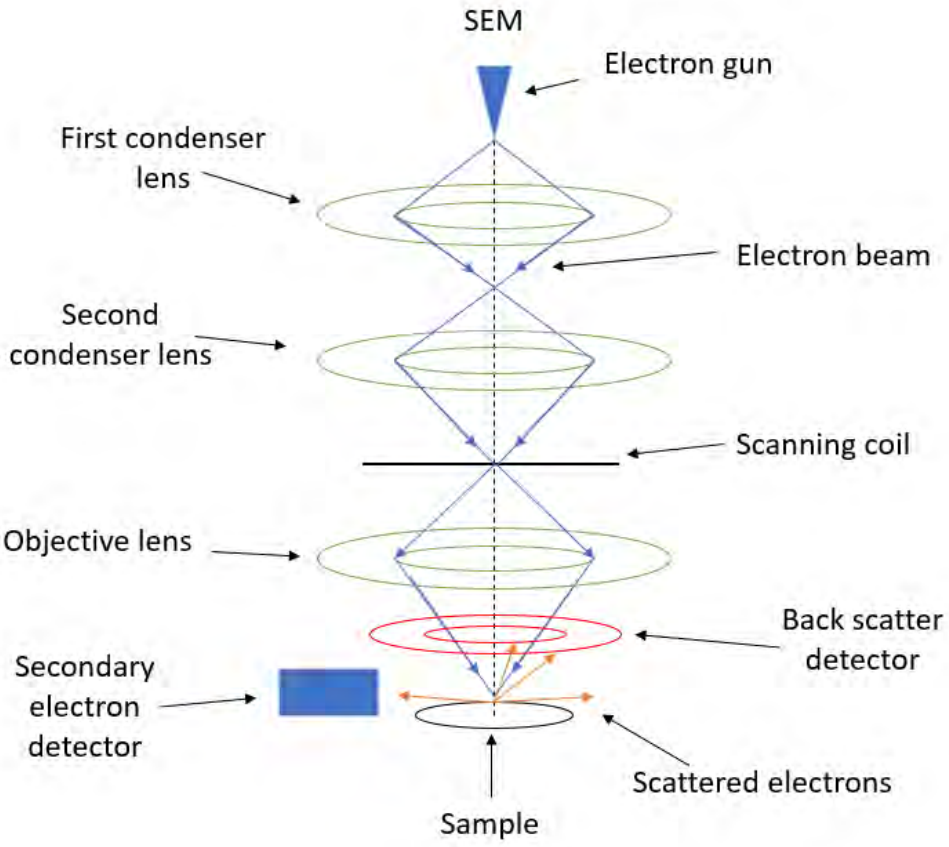


Figure 24 Schematic of a scanning electron microscope.

Electron guns used in electron spectrometers are either thermionic emission (commonly LaB_6 or W) or field emission. Thermionic emission is similar to the production of electrons within an X-ray tube a described previously in 2.2.1.3. A LaB_6 gun can produce a high brightness with a spatial resolution of 200 nm after being focused. A field emission gun applies a high electric field across a metal, which leads to tunnelling, this removes the electrons from the conduction band. Once generated, these electrons are then accelerated to create a high energy beam. The acceleration

voltage used determines the electron energy and therefore impacts upon the resolution of the resultant image. Field emission guns provide superior levels of brightness and higher spatial resolution compared to thermionic emission.[9,30]

The micrographs depicted in later chapters were collected on either a Phillips XL30 ESEM FEG microscope which is fitted with a field emission gun or a HITACHI Tabletop Microscope TM4000plus with EDS Oxford Instruments MICSF+ X-stream-2 attachment.

2.2.8. Scanning transmission electron microscopy

Scanning transmission electron microscopy (STEM) is a reversed form of transmission electron microscopy (TEM), based upon the principle of reciprocity in electron microscopy, which states that 'the elastic scattering amplitude from a source (Point X) to a detector (Point Y) is equal to that of a source at Y and a detector at X' as depicted in Figure 25.[31]

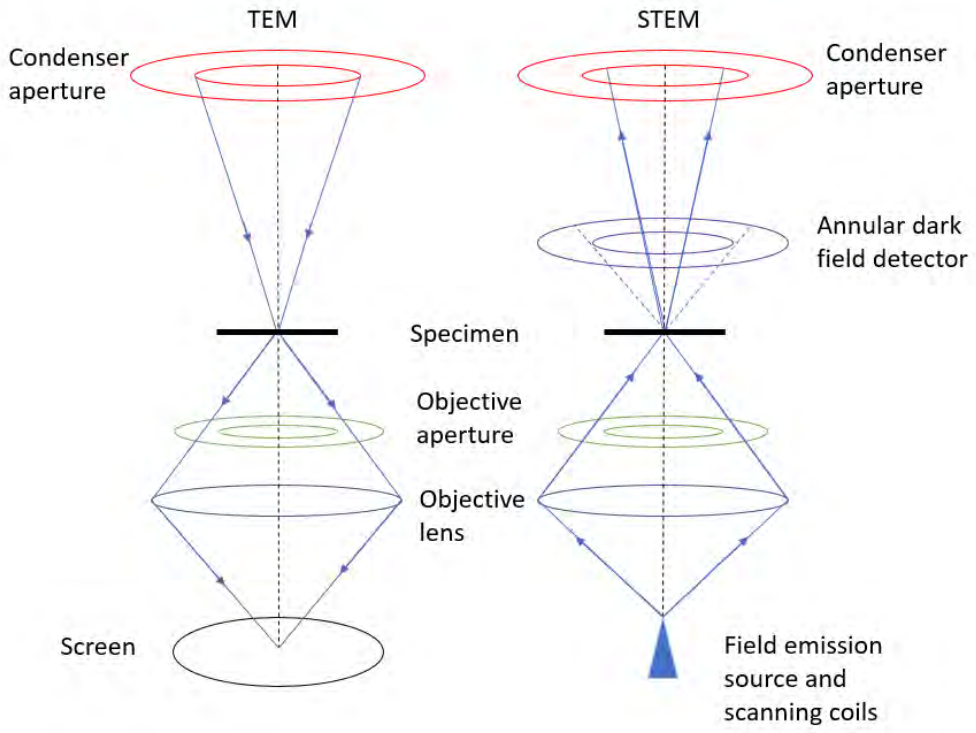


Figure 25 Schematics depicting the differences between TEM and STEM.

In STEM, a focused electron beam is scanned across the sample in a raster pattern similar to that of a SEM. However, in STEM it is the scattered and un-scattered electrons transmitted through a thin sample that are detected, as shown in Figure 23.

In a STEM the beam is moved by adjusting the scanning coils, and the objective lens is used to focus the beam. Image magnification is determined by the size of the area scanned rather than magnification by lenses. Beam size, limited by diffraction, and the aberrations of the objective lens, is the main limiting factor of resolution in a STEM. One of the distinct advantages of using STEM over TEM is that STEM can use signals that cannot be spatially correlated in TEM. Secondary electrons, characteristic X-rays, energy loss electrons and incoherently scattered electrons are examples of such signals.

In STEM the transmitted electrons are collected using three annular detectors. A bright field detector (BFD), placed on the optical axis, an annular dark field (ADF) detector and a high angle annular dark field detector (HAADF). An ADF detector creates images using electrons that have been scattered by small to medium angles. The HAADF detector detects electrons that have been scattered at high angles or incoherently. This detector system is highly sensitive to the atomic number of the atoms that have interacted with the beam, producing images where contrast is related to atomic number (Z^2). In these images, atoms with higher atomic numbers appear brighter and easier to detect than the atoms with lower atomic numbers or no electron density which appear darker.[32,33]

2.2.9. Inductively coupled plasma mass spectrometry and inductively coupled plasma optical emission spectroscopy

Inductively coupled plasma mass spectrometry (ICP-MS) and inductively coupled plasma optical emission spectroscopy (ICP-OES) are versatile techniques which are capable of elemental abundance and isotope ratio analysis (MS only). ICP-MS is widely used for trace and ultra-trace element analysis because of its high sensitivity. It allows analysis of elements at concentrations as low as 1 part per trillion (ppt) depending upon the instrument. Both ICP-MS and OES start by ionizing a sample in an inductively coupled plasma (ICP). The plasma, which is a hot gas comprising ions and free electrons, is created by applying a radiofrequency to a gas (commonly argon). This then generates an oscillating magnetic field. The ions and electrons are accelerated and deaccelerated by this field, therefore heating the plasma inductively. The hot temperature created allows for thermal ionization at the centre of the plasma.

Liquid samples are then introduced into the plasma using a nebulizer and a spray chamber, which converts the sample from a liquid into an aerosol (fine droplets) and filters out particles with a diameter >10 μm.[34,35]

ICP-OES exploits the high temperature of the plasma by exciting the electrons within the atoms which upon relaxation release a photon of characteristic wavelength that can be detected and used to quantify elemental abundance.[36] OES has limitations when analysing elements such as Cs^+ due to issues relating to the Cs^+ wavelength overlapping with several other elements of interest. Although Cs^+ has various excitation wavelengths that can be chosen, due to the concentrations used in this thesis, only the overlapping wavelength can be selected, or the detector is saturated. In ICP-OES the emission intensity is proportional to the concentration. Both forms of ICP calculate the solutions' concentrations from calibration standards of known concentrations of the element of interest.

The ICP data presented later in this thesis focused upon uptake of both Cs^+ and Sr^{2+} cations to mimic nuclear waste products. Due to limitation of ICP-OES resulting from the excitation overlapping issues explained previously, ICP-MS was used for trace elemental analysis post ion exchange. This type of ICP uses a quadrupolar filter for mass separation. Superimposed AC and DC voltages are applied across opposing rods, and the induced fields electrostatically direct the ions with respect to their m/z ratio before emerging from the quadruple filter and hitting the detector. Continuous scanning yields a mass spectrum with peaks, the heights of which are directly proportional to the number of positive ions detected for each specific mass. [34,37,38]

2.4. Experimental procedures

2.4.1. Zeolite A

The starting material of zeolite A with a chemical composition of $Na_{12}[Al_{12}Si_{12}O_{48}]\cdot 20H_2O$ (structure type LTA) was synthesised in accordance with the preparation given on the IZA website[42] using 99% reagent grade sodium hydroxide, sodium aluminate and sodium silicate pentahydrate that were purchased from VWR international. A portion of 1.6g of NaOH was dissolved in 170ml deionised water and then split into two equal amounts. To one half, 16.52g of sodium aluminate was added and then stirred until dissolved. To the other half 30.96g of sodium metasilicate pentahydrate was added with gentle heating and stirring required. Once both fully dissolved, the metasilicate solution was transferred into a 500ml HDPE bottle. Small aliquots of the sodium aluminate solution were added into the metasilicate solution followed by vigorous shaking. Once all had been added the contents were vortexed to ensure a fully homogenous gel. Crystallisation conditions were 99˚C for 5 hours. The solid product was collected via Büchner filtration and washed with deionized water until pH 7 before being dried at 70˚C overnight. Chemical composition and water content were obtained by X-ray fluorescence spectroscopy (XRF) and thermogravimetric analysis (TGA).

2.4.2. Zeolite X

The starting material of zeolite X with a chemical composition of $Na_{86}[Si_{106}Al_{86}O_{384}]\cdot 264 H_2O$ (structure type FAU) was synthesised in accordance with the preparation given

on the IZA website[42] using 99% reagent grade sodium aluminate and sodium silicate solution that were purchased from VWR international.

A portion of 2.16g of sodium aluminate was dissolved in 15ml deionised water. In a separate beaker dissolve 6.68g of sodium metasilicate pentahydrate in 10ml deionised water with gentle heating and stirring required. Once both fully dissolved, the metasilicate solution was transferred into a 500ml HDPE bottle. Small aliquots of the sodium aluminate solution were added into the metasilicate solution followed by vigorous shaking. Once all had been added the contents were vortexed to ensure a fully homogenous gel. Crystallisation conditions were 90˚C for 24 hours. The solid product was collected via Büchner filtration and washed with deionized water until pH 7 before being dried at 70˚C overnight. Chemical composition and water content were obtained by X-ray fluorescence spectroscopy (XRF) and thermogravimetric analysis (TGA).

2.4.3. Zeolite Y

The starting material of zeolite X with a chemical composition of $Na_{56}[Si_{136}Al_{56}O_{384}]\cdot 250\ H_2O$ (structure type FAU) was synthesised in accordance with the preparation given on the IZA website[42] using 99% reagent grade sodium hydroxide, sodium aluminate, sodium metasilicate pentahydrate and sodium silicate solution that were purchased from VWR international. This synthesis method used a seed and feed stock which combine to create an overall gel. **Seed gel;** A 2.035g portion of NaOH was dissolved in 9.97ml deionised water. Once dissolved a 1.045g portion of sodium aluminate was added and stirred for a minimum of 10 minutes. To this 11.36g of sodium metasilicate pentahydrate was added with gentle heating and vigorous shaking required to ensure

homogeneity. Once complete this was aged for at least 24 hours. **Feed gel;** A 0.7g portion of NaOH was dissolved in 65.48ml deionised water. Once dissolved a 6.454g portion of sodium aluminate was added and stirred for a minimum of 10 minutes. To this 71.215 of sodium silicate solution was added with vigorous shaking required to ensure homogeneity. **Overall gel;** a 8.25g portion of **seed gel** was combined with the whole **feed gel.** Once all had been added the contents were vortexed to ensure a fully homogenous gel. Crystallisation conditions were 100˚C for 24 hours. The solid product was collected via Büchner filtration and washed with deionized water until pH 7 before being dried at 70˚C overnight. Chemical composition and water content were obtained by X-ray fluorescence spectroscopy (XRF) and thermogravimetric analysis (TGA).

2.4.4. Chabazite

The starting material of chabazite with a chemical composition of $K_2[Si_4Al_2O_{12}]\cdot 6H_2O$ (structure type CHA) was synthesised in accordance with the preparation given on the IZA website[42] using potassium hydroxide (J. T. Baker reagent grade, 45% KOH solution) and (NH_4^+) zeolite Y that were purchased from Sigma Aldrich. 26.8ml of potassium hydroxide was added into 198.2ml of deionised water. To this 25g of zeolite was added and shaken for 30 seconds. Crystallisation conditions were 99˚C for 96 hours. The solid product was collected via Büchner filtration and washed with deionized water until pH 7 before being dried at 70˚C overnight. Chemical composition and water content were obtained by X-ray fluorescence spectroscopy (XRF) and thermogravimetric analysis (TGA).

2.4.5. Transition metal ion exchange procedure

The salts used and their respective cations is shown in Figure 26. This experimental method was applied to each of the zeolites for each of the cations An example for the iron(II) based exchanges is given; The Fe^{2+} containing zeolites were prepared by aqueous ion exchange using 0.25 M, 0.5 M, 1 M and 2 M $FeCl_2 \cdot 4H_2O$ salt solutions. Salts were dissolved in nitrogen-purged deionised water to help prevent the oxidation of divalent iron. For each exchange, a stoichiometric amount of zeolite was shaken in 50ml tubes within a Memmert shaking water bath in a 5× excess of metal salt to zeolite ratio. Each exchanged sample was collected by centrifugation then washed with deionised water until the washings were pH 7 and dried at 70˚C overnight. Exchange times ranged from 15 minutes up to 24 hours with samples being removed after their specified time period. To study the effect of temperature alongside concentration, a series of exchanges were conducted from 25˚C to 65˚C in 10˚C increments. Chemical compositions of the samples including cation contents were determined by WD-XRF using 13mm pressed pellets with a Bruker T8 Tiger using an 8mm detection mask. Pellets were made from thoroughly ground mixtures of 5:1 ratio sample to briquetting agent (Spectroblend 44µm powder) pressed to 8 bar.

2.4.6. Solid state exchange

2.4.6.1. Two-step solid state exchange

The solid-state exchanges were conducted under nitrogen bubbled through deionised water prior to reaching the sample. Each occlusion used starting materials with maximum M(II) exchange levels (M= Fe, Co, Mn, Ni or Zn). Occlusion molar ratios of

trivalent iron to divalent iron were 2:1, 1:1 or 0.5:1. A stoichiometric amount of $FeCl_3 \cdot 6H_2O$ and divalent metal exchanged zeolite were ground in a cold mortar and pestle before being transferred into an alumina crucible, which was then placed into a tube furnace and purged with nitrogen before being heated. The temperatures ranged from 600˚C to 1000˚C using a ramp rate of 5˚C per minute, a dwell time of 3 hours and no set cooling rate.

2.4.6.2. One-step solid state exchange

The solid-state exchanges were conducted under nitrogen bubbled through deionised water prior to reaching the sample. Each occlusion used a specified amount of zeolite with a certain amount of divalent metal. The amount of divalent metal used was calculated to replicate the level of exchange achieved during aqueous ion exchange. To this a given amount of trivalent iron salt was added. An example is as follows; 0.5g of zeolite A, 0.515g of cobalt(II) nitrate hexahydrate and 0.735g of iron(III) chloride hexahydrate were ground in a cold mortar and pestle before being transferred into an alumina crucible, which was then placed into a tube furnace and purged with nitrogen before being heated. The temperatures ranged from 600˚C to 1000˚C using a ramp rate of 5˚C per minute, a dwell time of 3 hours and no set cooling rate. This had a Na^+:Co^{2+} ratio of 1:1 and a Co^{2+}:Fe^{3+} of 1:2.

2.4.7. Matrix digestion

2.4.7.1. Zeolite A digestion

A specified amount of matrix-zeolite A was heated at 200˚C for 24 hours in a Teflon autoclave in varying concentrations of NaOH ranging from 0.1M up to 3M. (1.25M

optimal). The remaining solids were kept together post digestion as they were directly used in the secondary synthesis.

2.4.7.2. Chabazite digestion

A specified amount of matrix-zeolite Y was heated at 200˚C for 24 hours in a Teflon autoclave in 1.25 M KOH. The remaining solids and digestion liquor were kept together post digestion as they were directly used in the secondary synthesis.

2.4.8. Secondary synthesis

2.4.8.1. Zeolite A hybrid

After the specified amount matrix had undergone basic digestion in the optimised concentrations of NaOH solution in a Teflon liner, sodium aluminate and sodium metasilicate pentahydrate were added as per the standard zeolite A preparation method given in 2.4.1. The amount added is dependent upon the matrix content required. The Teflon liner was then held on a vortex mixer to ensure homogeneous distribution of the digested magnetic matrix through the aluminosilicate gel before being placed back into a 99˚C oven for 24 hours. The solid product was collected via Büchner filtration and washed with deionized water until pH 7 before being dried at 70˚C. The dried sample was then ground, any unbound strongly magnetic material was magnetically removed from the main sample by carefully bringing a magnet only as close as necessary prior to analysis.

2.4.8.2. Zeolite X hybrid

A 1g portion of matrix was dry ground at 150 rpm in a RETSCH XRD-Mill McCrone using ZrO_2 grinding media. Following this a specified amount of the ground matrix was added to a synthesis gel as per the standard zeolite X preparation in section 2.4.2. The amount added was dependent upon the matrix content required i.e. 50% (0.5:1). The resultant gel was then held on a vortex mixer to ensure homogeneous distribution of magnetic matrix through the aluminosilicate gel before being placed into a 90˚C oven for 24 hours. The solid product was collected via Büchner filtration and washed with deionized water until pH 7 before being dried at 70˚C. The dried sample was then ground, any unbound strongly magnetic material was magnetically removed from the main sample by carefully bringing a magnet only as close as necessary prior to analysis.

2.4.8.3. Zeolite Y hybrid

A specified amount of ground matrix is added to the **feed gel** prior to incorporation of the **seed gel** as per the standard zeolite Y preparation method in section 2.4.3. The amount added was dependent upon the matrix content required i.e. 50% (0.5:1). The Crystallisation conditions were 100˚C for 24 hours. The solid product was collected via Büchner filtration and washed with deionized water until pH 7 before being dried at 70˚C overnight. The dried sample was then ground, any unbound strongly magnetic material was magnetically removed from the main sample by carefully bringing a magnet only as close as necessary prior to analysis.

2.4.8.4. Chabazite hybrid

After the specified amount matrix had undergone basic digestion in 1.25M KOH solution in a Teflon liner, the potassium hydroxide solution and zeolite Y were added as per the standard preparation in section 2.4.4. Crystallisation conditions were 99˚C for 96 hours. The solid product was collected via Büchner filtration and washed with deionized water until pH 7 before being dried at 70˚C overnight. The dried sample was then ground, any unbound strongly magnetic material was magnetically removed from the main sample by carefully bringing a magnet only as close as necessary prior to analysis.

2.4.9. Ion exchange and ICP-MS procedure

Approximately 0.03g of hybrid zeolite was dispersed in 15ml of exchange solution (10ppm). The amount of active zeolite was scaled with the amount of matrix for each exchange thus the uptake would be comparable. The solutions were exchanged for 24 hours at room temperature which is sufficient for equilibrium to be reached. After 24 hours the samples were centrifuged with 10ml of the supernatant removed. This was then passed through a 22µm filter into a fresh centrifuge tube and acidified with ultrapure nitric acid (2% W/V). The samples were stored in a refrigerator until the day of analysis. On the day of analysis 100µl of solution was diluted further using 9.9ml of 2% nitric acid. A calibration curve was created using elemental standards at 1, 5, 10, 50, 100 and 500ppb.

2.5. References

1 R. W. Thompson, *Verif. Synth. Zeolitic Mater.*, 2001, **2**, 21–23.

2 H. Lechert, *Verif. Synth. Zeolitic Mater.*, 2001, **2**, 33–38.

3 K. Jansen, *Verif. Synth. Zeolitic Mater.*, 2001, **2**, 39–42.

4 H. G. Karge, in *Handbook of Heterogeneous Catalysis*, Wiley-VCH Verlag GmbH & Co. KGaA, Weinheim, Germany, 2008.

5 A. R. West, *Solid State Chemistry and its Applications*, 2nd Editio., 2014.

6 U. Miller, *Inorganic Structural Chemistry*, John Wiley & Sons, Ltd, Chichester, UK, 2006.

7 S. L. J. Billinge and R. E. Dinnebier, *Powder Diffraction:Theory and Practice*, Royal Society of Chemistry, Cambridge, 2008.

8 Y. Leng, in *Materials Characterization*, Wiley-VCH Verlag GmbH & Co. KGaA, 2013, pp. 47–82.

9 Y. Leng, in *Materials Characterization*, Wiley-VCH Verlag GmbH & Co. KGaA, 2013, pp. 221–251.

10 U. Holzwarth and N. Gibson, *Nat. Nanotechnol.*, 2011, **6**, 534.

11 P. Paufler, *The Rietveld Method. International*, Oxford University Press, 1995.

12 Y. Leng, in *Materials Characterization*, Wiley-VCH Verlag GmbH & Co. KGaA, 2013, pp. 191–219.

13 C. Slater, pp. 9–45.

14 E. Margui and R. Van Griken, *X-Ray Fluorescence Spectrometry and Related Techniques*, Momentum Press, 2013.

15 R. Yerly, 2014, 16.

16 Skoog, *Fundamentals of Analytical Chemistry*, Cengage Learning, Ninth., 2013.

17 D. A. Skoog, D. M. West, F. J. Holler and S. R. Crouch, in *Fundamentals of Analytical Chemistry*, 2014, pp. 655–697.

18 Y. Leng, in *Materials Characterization*, Wiley-VCH Verlag GmbH & Co. KGaA, 2013, pp. 333–365.

19 Introduction to Mössbauer Spectroscopy, https://www.rsc.org/membership-and-community/connect-with-others/through-interests/interest-groups/mossbauer/#links, (accessed 16 March 2021).

20 C. E. Housecroft and A. G. Sharpe, *Inorganic Chemistry - Catherine E. Housecroft And Alan G. Sharpe 2nd Edition*, Pearson Education, 2nd edn., 2005.

21 K. M. Krishnan, *Fundamentals and Applications of Magnetic Materials*, Oxford University Press, 2016.

22 J. Crangle, *Solid State Magnetism*, Springer US, Boston, MA, 1st edn., 1991.

23 D. C. Jiles, *Adv. Mater.*, 1992, **4**, 378–379.

24 K. M. Krishnan, *Fundamentals and Applications of Magnetic Materials*, Oxford University Press, 2016.

25 V. Marghussian, *Magnetic Properties of Nano-Glass Ceramics*, 2015.

26 E. A. Boudreaux and L. N. Mulay, *Theory and Applications of Molecular*

Paramagnetism, John Wiley & Sons Inc, 1976.

27 V. Marghussian, *Chapter 4. Magnetic Properties of Nano-Glass Ceramics*, 2015.

28 A. Gupta and D. Yan, in *Mineral Processing Design and Operations*, Elsevier, 2016, pp. 629–687.

29 Y. Leng, in *Materials Characterization*, Wiley-VCH Verlag GmbH & Co. KGaA, 2013, pp. 127–161.

30 Y. Leng, in *Materials Characterization*, Wiley-VCH Verlag GmbH & Co. KGaA, 2013, pp. 83–126.

31 Y. Wen, T. Shang and L. Gu, *Microscopy*, 2017, **66**, 25–38.

32 D. B. Williams and C. B. Carter, *Transmission Electron Microscopy*, Springer US, Boston, MA, 2009, vol. 47.

33 J. M. Cowley, *Appl. Phys. Lett.*, 1969, **15**, 58–59.

34 F. Vanhaecke, in *Fundamentals and applications using ICP-MS*, 2012, pp. 31–75.

35 M. P. Dziewatkoski, L. B. Daniels and J. W. Olesik, *Anal. Chem.*, 1996, **68**, 1101–1109.

36 S. M. Nelms, *Inductively Coupled Plasma Mass Spectrometry Handbook*, 2009.

37 G. Nageswaran, Y. S. Choudhary and S. Jagannathan, in *Spectroscopic Methods for Nanomaterials Characterization*, 2017, vol. 2, pp. 163–194.

38 B. Pénicaut, C. Bonnefoy, C. Moesch and G. Lachâtre, *Ann. Pharm. Françaises*, 2006, **64**, 312–327.

Chapter 3: Ion exchange of *d*-block cations in Zeolite A, X and Y

3.1. Introduction

The main component of the magnetic spinels are transition metals, the preferred method of inclusion in zeolites is adsorption. There are many parameters that can impact the adsorption process of different cations on to zeolite frameworks. The most important of these can be broken down into three key criteria; 1) the zeolite itself, 2) the adsorbed ions and 3) the ion exchange conditions. Throughout this thesis, all three key criteria have been explored. The first set of parameters relate to the characteristics of the zeolite itself such as chemical composition, the internal structure of micro and macromolecular pores and average particle size. These were explored by using different zeolites with the zeolite A (LTA), zeolite X or Y (FAU) and chabazite (CHA) structures. These parameters were also explored by using zeolites of the same structure but different chemical compositions, such as FAU X and Y. The second set are linked to the characteristics of the adsorbed ions such as dehydration energies, ionic mobility, tendency to create hydrated complexes whilst in solution and the radius of the ion when hydrated. This set of parameters was explored using several different divalent metal cations. Each cation had a different tendency to hydrate whilst in solution, a different dehydration energy and a different ionic mobility. There were also differences in size of the hydrated radii, which can be important depending upon the size of the pore windows within the zeolite. The third set of parameters are related to the ion exchange conditions such as temperature, pH of the contact solution, solid to

liquid ratio, initial concentrations, the intensity of the agitation during the exchange and nature of the cation as well as the accompanying anion.[1] This set of parameters was explored by varying the temperature, initial concentrations, initial pH and accompanying anions.

To reach the desired high adsorption capacities, zeolites are usually chemically activated (conditioned). Generally, natural zeolites can be conditioned when the cations present in solution substitute for those in the zeolite structure. The hydrated cations of Na^+, K^+ and NH_4^+ are commonly used to condition natural zeolites, as they have smaller hydrated radii and lower hydration energies than $Ca^{2+}$and Mg^{2+}, thus exhibit a higher degree of availability for ion exchange. This in turn explains the increase in ion exchange ability.[2]

The adsorption behaviour of zeolitic materials/minerals follows the Brønsted and Lewis theory of acidic and basic sites that exist with the structure. Specifically, the oxygen atom in the silicon and aluminium bonded tetrahedra, which holds the negative charge of the lattice, provides the basic site of the structure which is a potential location for adsorption. Therefore, isomorphous Al for Si substitution can account for a negative charge and the lattice oxygen can behave as a proton acceptor. This is usually referred to as oxygen alkalinity and it is potentially responsible for the adsorption of metal-hydroxy species. Zeolite crystals can be shaped differently and exhibit surface imperfections, which can lead to the formation of sites with different energies. The range of these site energies will cause a nonhomogeneous distribution of adsorption of the different species.[3,4] Throughout the exchange there is a risk that the framework is weakened and therefore it is at greater risk of breakdown through agitation, which

can lead to the production of new highly reactive sites. Therefore, this mechanical effect increases the possible number of sites.

The adsorption mechanism of divalent metal cations is generally considered to occur via the following route: (1) diffusion of cations from their bulk solution onto a film that surrounds the zeolite particle; (2) diffusion through the external film; (3) diffusion through the micro or macropore network towards the absorption sites; (4) dehydration of the cations once they are in proximity of the adsorptive sites and rehydration of any counter ions; (5) the exchange of the cations as the divalent metal binds to the framework adsorption site to replace the counter ion; (6) diffusion of the counter ions back to the external solution. [1,5,6,7]

If the exchange is carried out under dynamic conditions, using a heterogenous system, the rate determining step would not be step (1) as when in solution the ions are only ever in their hydrated form. The volume of these hydrated ions is governed by the number of water molecules that surrounds the central ion while the electric charge governs the ionic radius when dehydrated. As it is thought that the hydrated ionic radius plays a role in the mobility of these ions throughout the pore networks, this would mean that any step involving diffusion from the film into the micro/macropores can be considered rate limiting. However, it should be noted that dehydrated cations have ionic movement and can travel along the framework as seen within a solid oxide ion conductor. Diffusion of counterions back to the external solution can also affect the mobility of the metal cations therefore limiting diffusion. Each of the different cations has their own hydrated ionic radii which generate different dehydration energies. The larger the hydration radii, the greater the dehydration energy which will therefore limit step 5. In a more general view, the rate limiting steps are considered to be diffusion

through the external film followed by diffusion into the pore network, then dehydration of the exchanged cations and finally binding to the adsorptive sites.[8]

The series of studies described throughout this chapter will explore the optimisation of the one contact ion exchange process using different *d*-block metals to obtain maximum cation loading, instead of using multiple ion exchanges as is commonly done in this area of research. Table 6 denotes the cations used as well as their structural properties.

Table 6 Structural properties of the divalent *d*-block metals used during the series of ion exchange studies.

Cation	Mn^{2+}	Fe^{2+}	Co^{2+}	Ni^{2+}	Zn^{2+}
d^n	d^5	d^6	d^7	d^8	d^{10}
CFSE (Dq)	0	4	8	12	0
ΔH_{hydr}(KJ mol^{-1})	-1845 [9]	-1920 [9]	-2054 [9]	-2106 [9]	-2044 [9 6]
Preferred coordination within a zeolite framework	Trigonal Bipyramidal [10 11]	Octahedral [9]	Octahedral [9]	Octahedral [9]	Tetrahedral [12]
Hydrated Radii (Å)	2.17[13]	2.10[13]	2.09[13]	2.07[13]	2.09[13]
Dehydrated Radii (Å)	0.83 [14]	0.78 [14]	0.75 [14]	0.69 [14]	0.75 [14]

3.1.1. Transition metal ion exchange in zeolite A

Ion exchange has previously been used to introduce transition metals into the framework of zeolite A.[11,14,15,16] Often, only a small fraction of the sodium cations can be replaced, with sharp upper limits previously reported.[14] Optimal loading can be achieved through multiple contacts with fresh ion exchange solutions.[14] However, this produces excessive volumes of spent ion exchange effluent on a large scale. This is undesirable if the exchanging cation is cobalt, as it is toxic towards aquatic life and a

suspected carcinogen. By optimising the one contact exchange, the volume of waste produced would be significantly reduced and allow ion exchange to be viable on an industrial scale.

Zeolites are weakly acidic in nature. Sodium cation exchangers are selective towards hydrogen based on

Equation 9.

$$(RNa + H_2O \Leftrightarrow RH + Na^+ + OH^-).$$

Equation 9 The selective exchange of hydrogen in sodium based cation exchange materials where R is any sodium based cation exchanger.

This leads to high pH values when the exchanger is equilibrated with a relatively dilute electrolyte solution. One of the main concerns during this type of ion exchange, is if the exchanging cation hydrolyses the zeolite to form for hydronium ions (H_3O^+) in neutral salt solutions or deionised water.[17] [18] If this occurs the H^+ concentration can increase by several orders of magnitude, which would promote H^+ exchange. In low silica aluminosilicate zeolites, such as LTA, H^+ exchange is especially problematic; it can lead to damage of the framework causing defects in the structure or even dealumination (Equation 10 and Equation 11).

$$(\text{-Al-OH} + H^+ \rightarrow \text{-Al-}OH_2^+)$$

Equation 10 Showing the potential effect of H+ absorption on aluminium primary building units of zeolite structures.

$$(\text{-Si-OH} + H^+ \rightarrow \text{-Si-}OH_2^+)$$

Equation 11 Showing the potential effect of H+ absorption on silicon primary building units of zeolite structures.

These types of reactions are favoured at lower pH levels with the two species formed later detaching because of their high degree of surface protonation. This in turn leads to highly polarized interatomic bonds, which facilitate the detachment of a surface level cationic group into solution. Other examples of this type of hydrolysis have been seen previously when introducing Ni(II) and Co(II). [11,14,15] The general formula of hydrolysed metal cations is $[M_mO_n(OH)_b]^{v+}$. It has been reported that these species can be exchanged into or may even form within zeolites.[19]

The general composition of zeolite A is $Na_{12}[Al_{12}Si_{12}O_{48}]\cdot 27H_2O$.[20] This means that the maximum number of divalent cations would be 6 per formula unit. As the amount of cations present is linked to the aluminium (Al) content all the consequent data is shown as a cation to aluminium ratio. The maximum exchanged cation to Al ratio for a divalent cation is 0.5. Any value greater than this will not be balanced by the framework charge and therefore will be considered as an ‘over-exchanged’ amount.[21]

3.2. Experimental

The exchanges were optimised utilizing parameters linked to the ion exchange conditions (criteria 3). The chosen parameters were contact time, solution temperature and initial concentration.

3.2.1. Contact time

Time-based kinetics were only carried out on 0.25 M solutions as these have the slowest, hence most readily measured, rates. To investigate contact time, a set of parallel experiments consisting of 12 sample tubes each containing the same amount of zeolite powder and transition metal solution of specified concentration was used. The samples were shaken at 150 revolutions per minute (RPM) within a heated water bath. The solution temperature was kept at 25˚C (±0.05˚C) for the entirety of the exchange. A sample tube was removed from the water bath, collected via Buckner filtration then washed with deionised (DI) water. Samples were taken every 15 minutes up until 1 hour and then every hour up until 8 hours and then a further sample was taken after 24 hours. Samples were dried in an oven at 70˚C prior to analysis. Exchange results presented throughout this thesis are cation ratios derived from WD-XRF data.

3.2.2. Initial concentration and solution temperature

To investigate these parameters, several sets of sequential experiments were carried out. Each set consisted of 4 sample tubes, each containing the specified amount of zeolite powder and transition metal solution of specified concentration. The samples were again shaken at 150 rpm within a heated water bath. The solution temperatures

initially started at 25˚C (±0.05˚C) and increased in 10˚C increments up to 65˚C (±0.05˚C), above that the framework was found to be destroyed except for the nickel exchange where breakdown was observed at 75˚C. The samples were removed from the water bath collected via Buckner filtration then washed with deionised (DI) water after 24 hours.

For each different transition metal exchange, the corresponding transition metal salt was used. Figure 26 shows the salts used and their pH range across the different concentrations. Initial concentrations of transition metal salt varied from 0.25 M up to a maximum of 2 M. The pH of the salts is important as the use of highly acidic salts has been shown to promote proton exchange.[22,23] This can reduce the cation exchange capacity or result in possible dealumination/desilication. However, exploratory initial exchanges found this not to be occurring and thus the mentioned salts were used for this study.

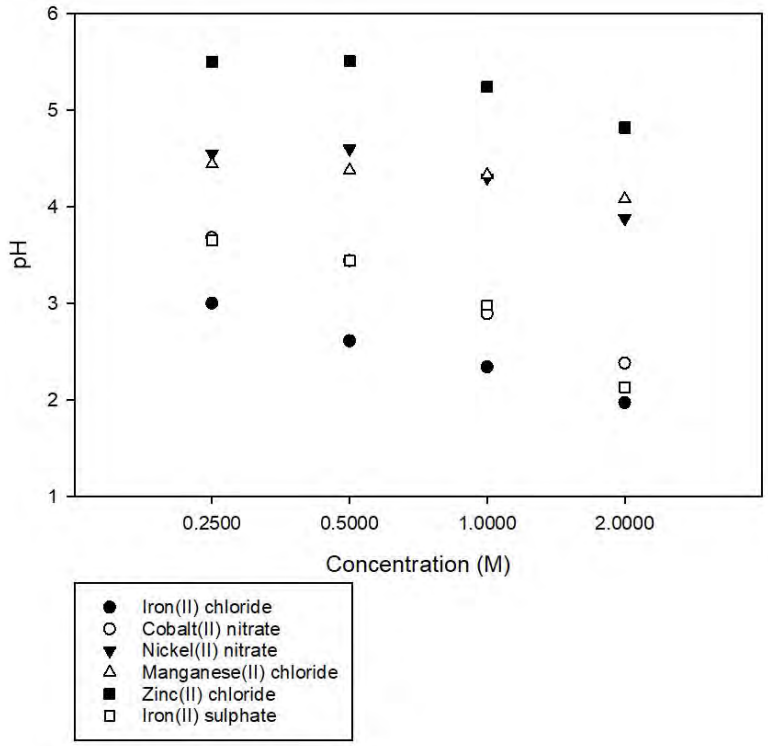


Figure 26 Transition metal salt used for ion exchange and their pH ranges at the concentrations used

3.3. Initial exchange analysis

Before the optimisation process could begin, the presence of the transition metal within the zeolite was first confirmed. An advantage of completing ion exchanges using salts that form coloured complexes with water, is that evidence of exchange is provided by colour changes to the zeolites. The standard sodium form of zeolite A, X and Y is white and after a successful ion exchange the colour changes for most metals depending upon the exchanging cation. Table 7 contains list of cations and the colours associated with a successful exchange.

Table 7 Exchanging cations and colour of zeolites after successful exchange.

Exchange cation	Exchanged zeolite colour
Fe(II)	Pale green
Fe(III)	Red
Co(II)	Pink
Mn(II)	Very pale pink/White
Ni(II)	Green
Zn(II)	White

After confirming the presence of the transition metals, powder X-ray diffraction patterns and loose powder WD XRF analysis were collected to support this. An example XRD pattern is shown in Figure 27 . A standard sodium form of zeolite A has been included for reference. Neither pattern has been rescaled so that the relative intensities can be approximately compared. It shows there is a change in the relative peak intensities, due to a change in the electron density of the cations (Co vs Na) and differences in

relative sample absorption. These differences are seen independent of the exchanging cation. The comparison for the remaining divalent cations is included in the appendix (section 3.1). The Co(II)-A pattern contains a small broad peak at 13˚ 2θ, this it thought to be from the sample holder due to insufficiently filling the holder.

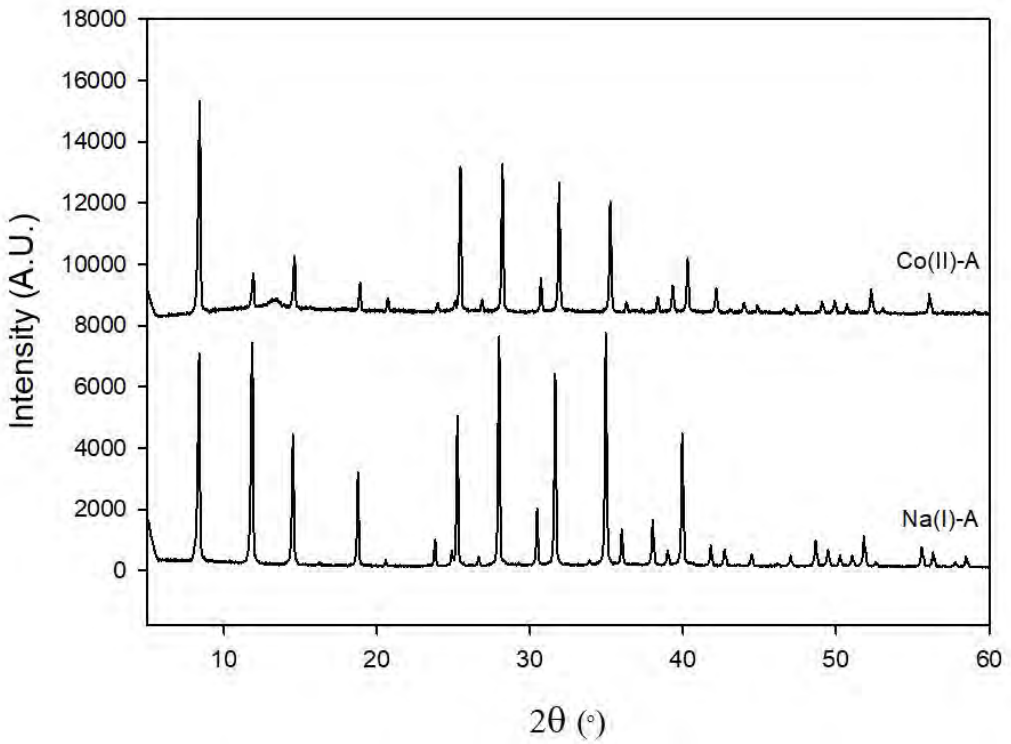


Figure 27: Comparison of the Na^{+} and Co^{2+} zeolite A X-ray diffraction patterns before optimisation. The pattern for Co(II)-A has been offset by 8000 counts.

It is interesting to note that cobalt exchanged zeolite A remains more stable upon dehydration compared to the other transition metal exchanged zeolites that were explored in this thesis. This is likely related to the ease at which cobalt decreases its coordination from octahedral to tetrahedral. Crystal field stabilisation energy considerations allow for a tetrahedral configuration in d^7 metals to occur to a greater extent than for other d^n metals.[24]

3.4. Influence of time on divalent transition metal cation exchange in zeolite A

This next section explores the optimisation of the ion exchange by investigating the parameter in criteria 3 (ion exchange conditions). The first of the parameters to be varied was contact time. Iron was chosen as the first transition metal investigated as this posed the greatest challenge due to how readily iron oxidises.

3.4.1. The influence of time on iron(II) cation exchange in zeolite A

The effect of the counter ion in the metal salt was simultaneously investigated alongside contact time. The salts chosen were iron(II) chloride and iron(II) sulphate.

3.4.1.1. Time investigation using iron(II) chloride

Figure 28 contains exchange data of zeolite A and 0.25 M iron(II) chloride up to 24 hours contact time. The results show that even after one hour the Fe/Al ratio had already exceeded the theoretical maximum, although a small amount of sodium was still detected. After 24 hours, when the Fe/Al ratio reached its maximum value, there was no sodium detected implying full exchange had been achieved. Throughout the exchange, there is more iron present than expected. Over-exchange of divalent metals has been observed before, where both excess metal and anions from solution enter the pores.[25,26] An alternative explanation for the over-exchanging iron is the formation of iron (hydroxy) oxides. This is suspected to be more plausible as the exchanged zeolite is brown rather than the expected pale green, but this will be discussed in more

detail in section 3.5.5. The Si/Al ratio started at 1.10 but appeared to remain constant suggesting that no dealumination or desilication occurred.

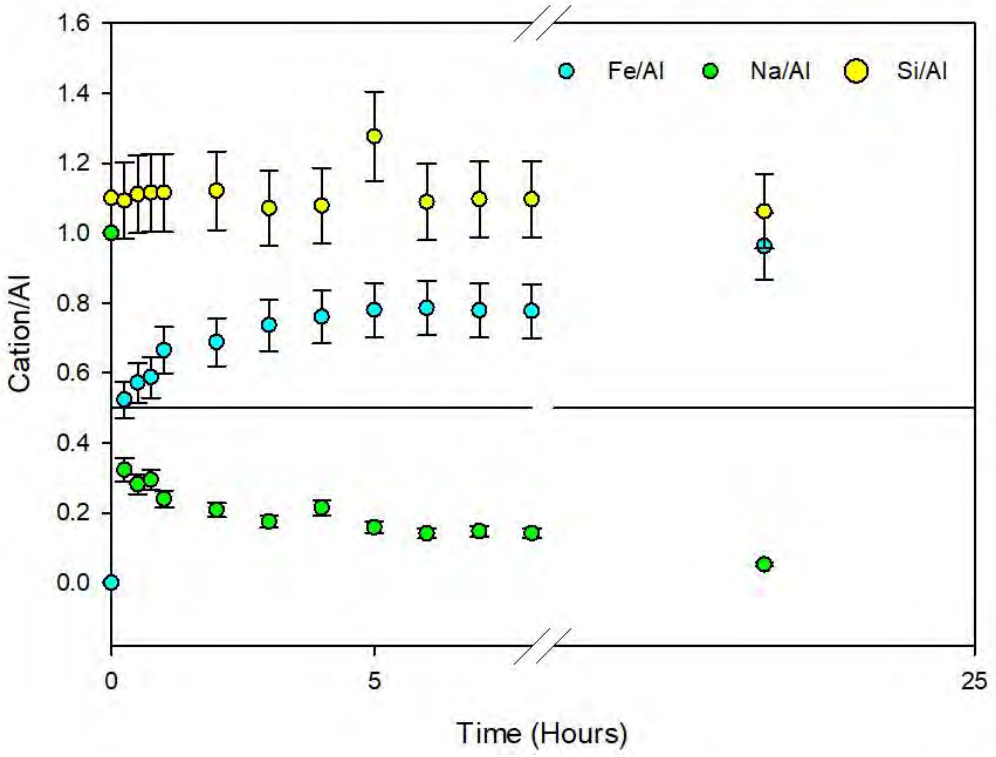


Figure 28 Time-based uptake kinetics of Fe(II) in zeolite A using 0.25 M iron(II) chloride at 25˚C over a 24-hour time frame. Element ratios are calculated from WD-XRF data from dried powders in pellet form. The size of the error bars reflects a 10% error commonly associated with XRF of pellets.

Figure 29 shows that the intensity of the XRD peaks decreased as the contact time with the salt solution increased. There were also notable changes in relative intensities and the (422) reflection at 18° 2θ was observed after 24 hours as shown in Figure 29 (i). The amount of iron loading does not appear to correlate to the appearance of this additional (422) reflection. Why this reflection appears is unknown. During the exchange, the lattice parameters varied from 12.208(1) to 12.187(1) Å which is negligible therefore this suggests the exchange is not directly affecting the structure of the framework.

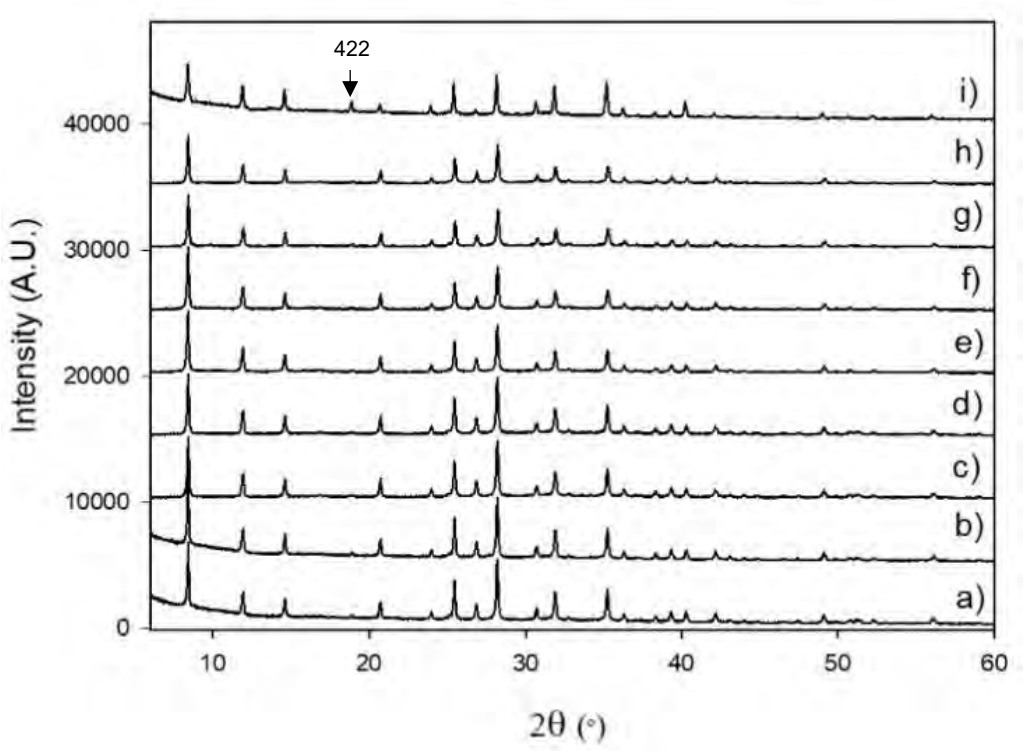


Figure 29 X-ray diffraction patterns produced by Fe(II) exchanged zeolite A at 25 ˚C when using 0.25 M iron(II) chloride solution. a) was taken after 1 hour and then subsequent patterns until h) after additional 1 hours increments, i) is after 24 hours.

3.4.1.2 Time investigation using Iron(II) sulphate

The time-based kinetic study was also completed in a 0.25 M solution of iron(II) sulphate with the results shown in Figure 30. Overall loading was similar compared to that for iron(II) chloride. There is a spike in the Fe/Al ratio after 3 hours which was coupled with a drop in Na content, but this value returned to an expected value after 4 hours, so it is believed to be an anomalous data point. The Fe/Al ratio reached a maximum again after 24 hours and is comparable to that for iron(II) chloride. No sodium content was detected after 24 hours suggesting that the zeolite was fully exchanged. The Si/Al ratio remained stable suggesting no dealumination or desilication occurred.

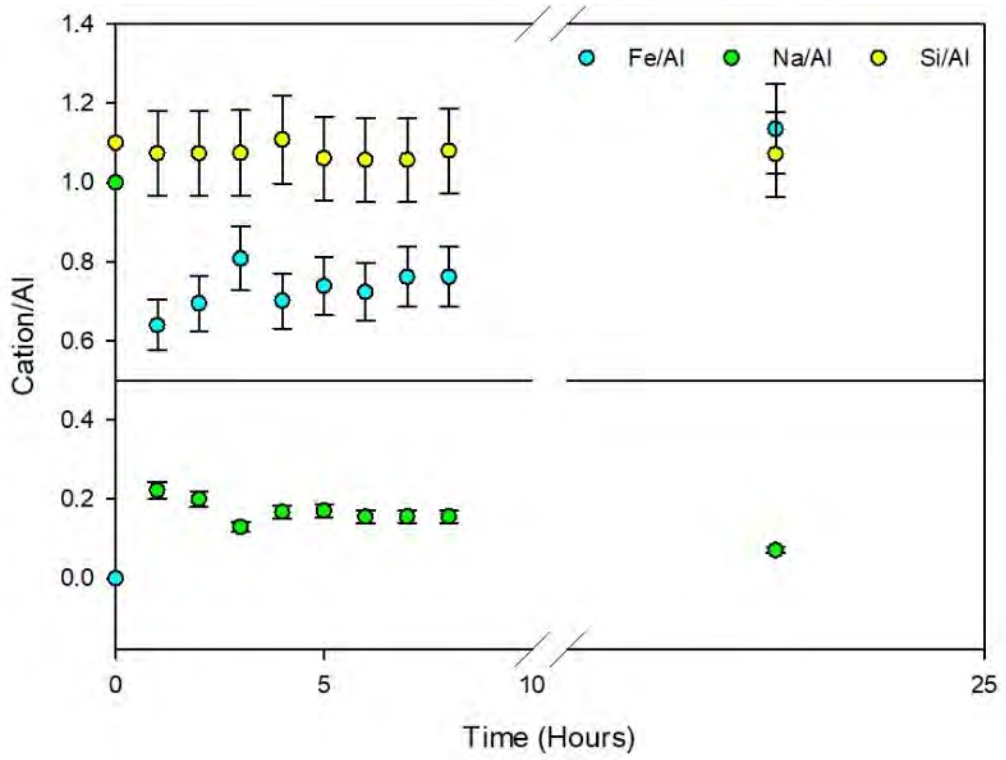


Figure 30 Time-based uptake kinetics for zeolite A using 0.25 M iron(II) sulphate at 25˚C over a 24-hour time frame. Element ratios are calculated from WD-XRF data from dried powders in pellet form. The size of the error bars reflects a 10% error commonly associated with XRF of pellets.

Figure 31 contains X-ray diffraction data from the iron(II) sulphate study. The lattice parameters were 12.211(3) Å to 12.198(3) Å. Once again, they did not change significantly during exchange. The (422) reflection at 18° 2θ was not present after 24 hours but was present in several of the other patterns. However, it was not as pronounced as in the iron(II) chloride series.

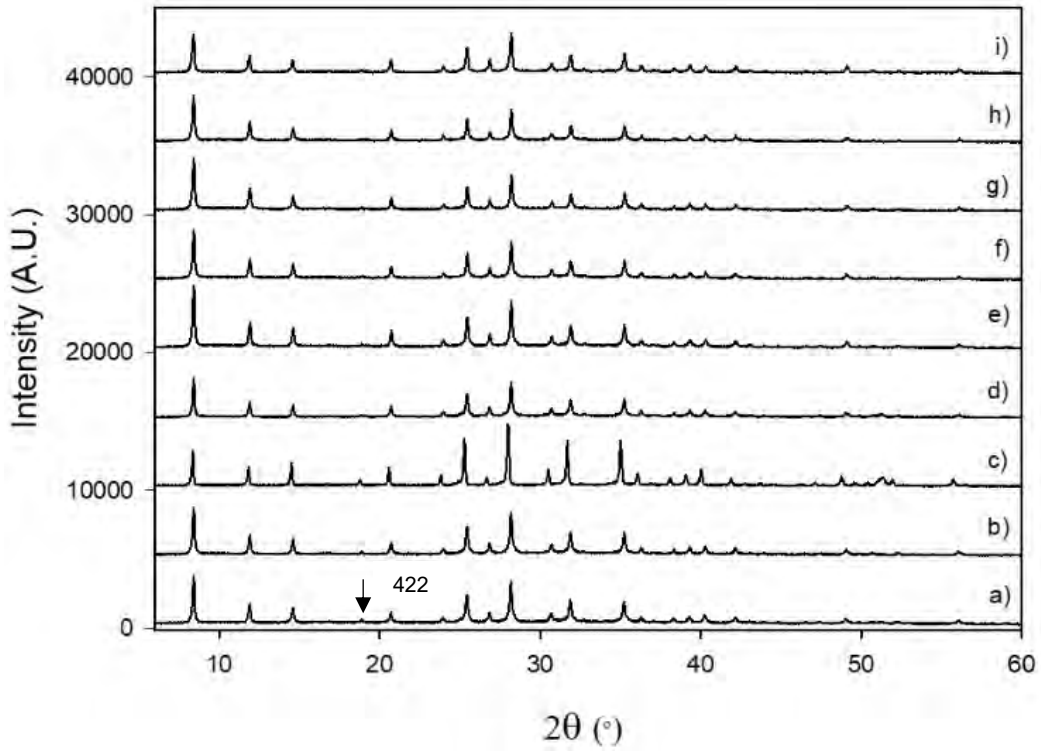


Figure 31 X-ray diffraction patterns produced during Fe(II) ion-exchange into zeolite A using 0.25 M iron(II) sulphate at 25˚C. a) was taken after 1 hour and then subsequent patterns until h) after additional 1 hours increments, i) is after 24 hours.

3.4.1.3. Effect of time on Fe(II) cation exchange

Iron appears to over-exchange regardless of the anion used. This was shown in Figure 28 and Figure 30 with greater amounts of iron detected than would be expected based upon the amount sodium detected during WD-XRF analysis. These figures also suggest that iron(II) sulphate exchange is initially more favourable. However, as the exchanges progressed the differences became negligible with both maximum Fe/Al values occurring after 24 hours.

3.4.1.4 Selection of counter ion and contact timeframe for Fe(II) exchange in zeolite A

These studies showed the anion initially influenced the uptake/kinetics but did not impact the overall level of exchange. The chloride salt was chosen for all subsequent work as changes in the X-ray diffraction patterns would be easier to observe. As the overall aim of this optimization was to maximize Fe(II) within zeolite A, the time frame for exchange was decided to be 24 hours as this had the greatest iron and lowest sodium content.

3.4.2. The influence of time in cobalt(II) cation exchange in zeolite A

The second metal investigated was cobalt. Figure 32 contains the element ratios derived from WD XRF after an ion exchange in a cobalt(II) nitrate solution for up to 24 hours.

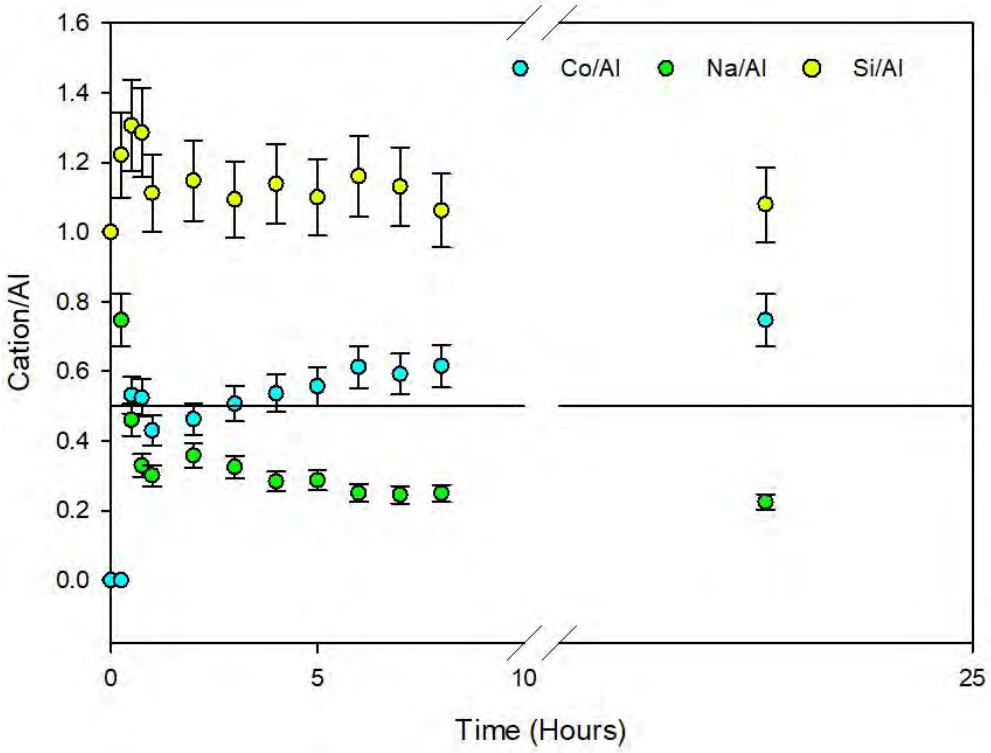


Figure 32: Time-based uptake kinetics for zeolite A using 0.25 M cobalt(II) nitrate solution at 25˚C over a 24-hour time frame. Element ratios are calculated from WD-XRF data from dried powders in pellet form. The size of the error bars reflects a 10% error commonly associated with XRF of pellets.

Figure 32 suggests that cobalt did not initially exchange as no cobalt was detected until after 30minutes. But then after 30minutes the Co/Al ratio exceeded the theoretical maximum (100% exchange). After an hour, the ratio reduced slightly to 90%. At the same point in time, the Na/Al ratio was proposed to be just below 0.4 suggesting that 40% of the original amount of sodium remained. After the exchange had exceeded 3 hours, the Co/Al ratio passed the theoretical boundary for maximum pore loading for a

second time. Throughout the whole of the exchange, small increases in the Co/Al ratio were coupled with a decrease in the Na/Al ratio. Both reached their respective maximum and minimum values after 24 hours. However, even after 24 hours the Na/Al ratio did not fall below 0.23 (23%) even though the Co/Al ratio vastly exceeded the levels expected for divalent ions.

Based upon the observations throughout the exchange, these results suggest that significant ‘over-exchange’ had been occurring. Surface precipitation was one theory explored to explain over-exchange. The initial pH of the exchange solution was acidic and could have become even more acidic during the exchange. However, at this pH it is more likely for species to redissolve than precipitate. Nevertheless, hydroxide formation was investigated. Hydroxide precipitation on the surface of the zeolite is unlikely to occur given the acidic pH of the exchange solution. However, it is possible they may occur in the pores as there is separate intrapore chemistry compared to that in the exchange solution. Hydroxide species have been observed previously by single crystal diffraction. However, as these hydroxide species are more likely to occur within the pores it would not explain why a higher than expected Co/Al ratio is observed.[25,26] If the hydroxide species were present within the pores it may result in pore blocking, this would explain why sodium never fully exchanged out.

Alongside precipitates blocking the exchange, metal ions hydration spheres are thought to be one of the main causes of slow cation exchange as it nears the exchange limit. After the outer spheres have been withdrawn, the water that remains is more energetically bound and therefore it is more difficult for the hydration sphere to be lost. This issue can potentially be overcome by increasing the temperature at which the exchange is conducted,[27] this theory is explored in greater detail in section 3.5. The

Si/Al ratio remained relatively constant indicating that there was no significant dealumination or desilication.

Figure 33 shows the X-ray diffraction patterns of zeolite A associated with the time-based exchange kinetics at 25˚C in 0.25 M cobalt(II) nitrate solution. The only visible change was the decrease in intensity as contact time with the salt solutions increased but the framework remained stable throughout with no additional reflections. Lattice parameters varied marginally from 12.259(4) to 12.204(4) Å.

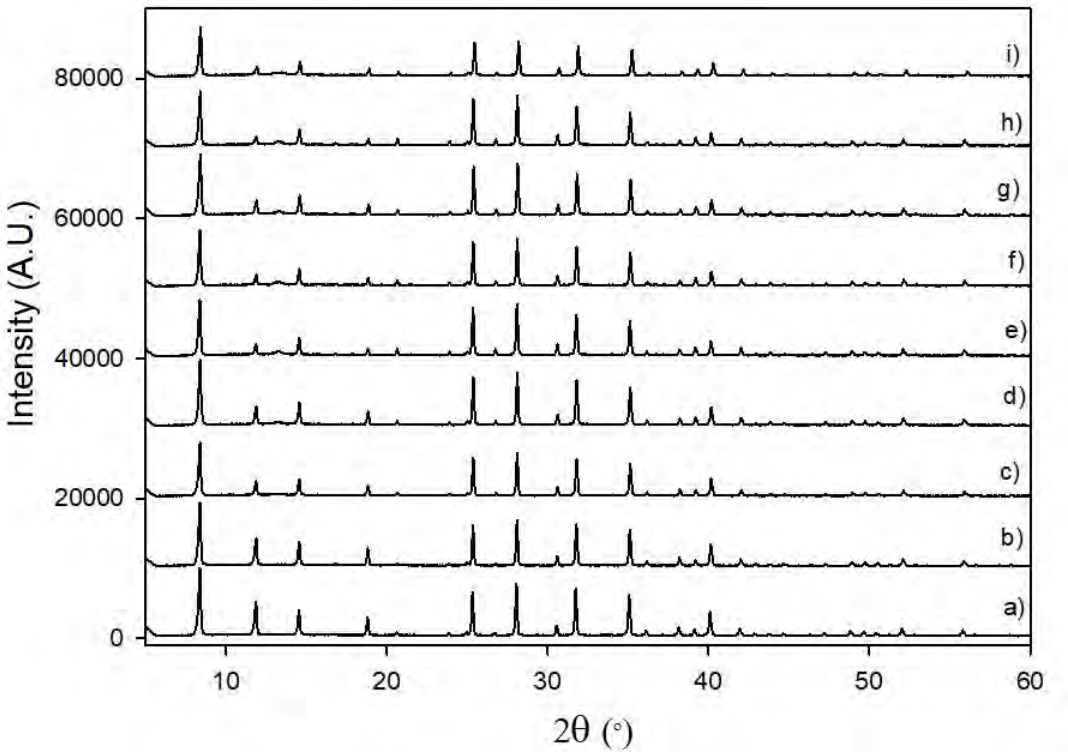


Figure 33: X-ray diffraction patterns produced by Fe(II) exchanged zeolite A at 25 ˚C when using 0.25 M cobalt(II) nitrate a) was taken after 1 hour and then subsequent patterns until h) after additional 1 hour increments, i) is after 24 hours.

Timeframe selection for Co(II) in zeolite A

This study has again shown significant levels of over-exchange occurring as was seen previously of divalent iron. Although, in this case even after 24 hours when the maximum Co/Al ratio is reported around 23% sodium remains. The corresponding XRD pattern showed that the structure remained and as the aim was to maximise cobalt content, 24 hours was again chosen as the timeframe.

3.4.3. The influence of time in manganese(II) cation exchange in zeolite A

Confirming the presence of manganese could not be done visually due to the zeolite remaining white in colour after a successful exchange. The presence can only be confirmed by WD-XRF and supported by XRD. Within zeolites, manganese can adopt a different coordination environment than Co/Fe, as it favours the trigonal bipyramidal coordination. This could be particularly important when analysing the Mn ion exchange data.

3.4.3.1. Time investigation using $MnCl_2$

Figure 34 contains the results of the time-based exchange kinetics conducted at 25˚C. The Mn/Al points in blue shows that after only 30 minutes the value had already surpassed the theoretical maximum but ~35% of the sodium remained. This again suggested that over-exchange was occurring with Mn(II) exchange being extremely favourable in dilute salt solutions at 25˚C. At the pH value measured, monovalent $Mn(OH)^+$ can form. The ion exchange of $Mn(OH)^+$, due to its small hydration radius,

can result in a higher quantity of manganese bound to the zeolite, than would be expected from ion exchange alone. The non-stoichiometric behaviour observed indicates that intraparticle adsorption could be occurring alongside ion exchange. This therefore suggests that diffusion through the zeolite is the main resistance to mass transfer of the exchanging manganese ion to the exchange site.[6]

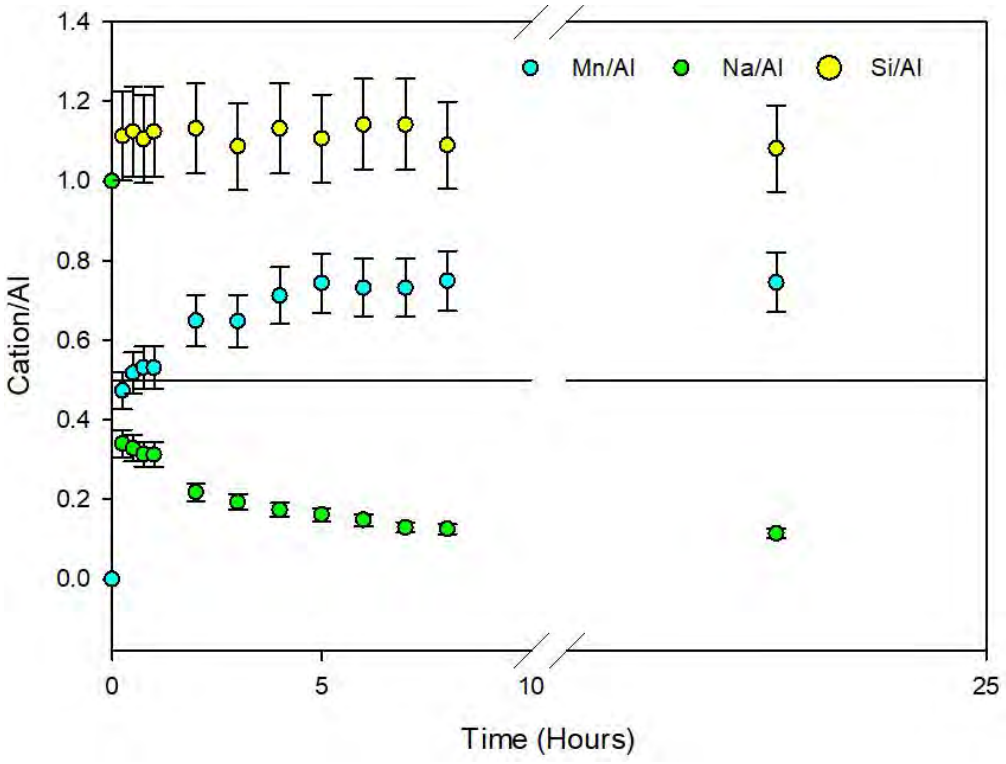


Figure 34: Time-based uptake kinetics of Mn(II) in zeolite A using 0.25 M manganese(II) chloride at 25˚C, over a 24-hour timeframe. Element ratios are calculated from WD-XRF data from dried powders in pellet form. The size of the error bars reflects a 10% error commonly associated with XRF of pellets.

Figure 35 contains the diffractions patterns related to the time-based uptake of divalent manganese. As has been shown by the other divalent metal exchanges, there is a decrease in the intensity of the reflections which occurs to a greater extent when in the solution for longer. However, the high angle peaks remain visible throughout, suggesting that these exchanges are not as damaging on the zeolite framework as the other metals have been, even with significant over-exchange occurring. This may be

related to the smaller hydrated radius of monovalent $Mn(OH)^+$ as discussed previously. As has been seen previously, after a successful ion exchange an additional reflection appears at 18˚ 2θ. Lattice parameters varied from 12.256(3) to 12.236(3) Å suggesting the exchange did not affect the structure.

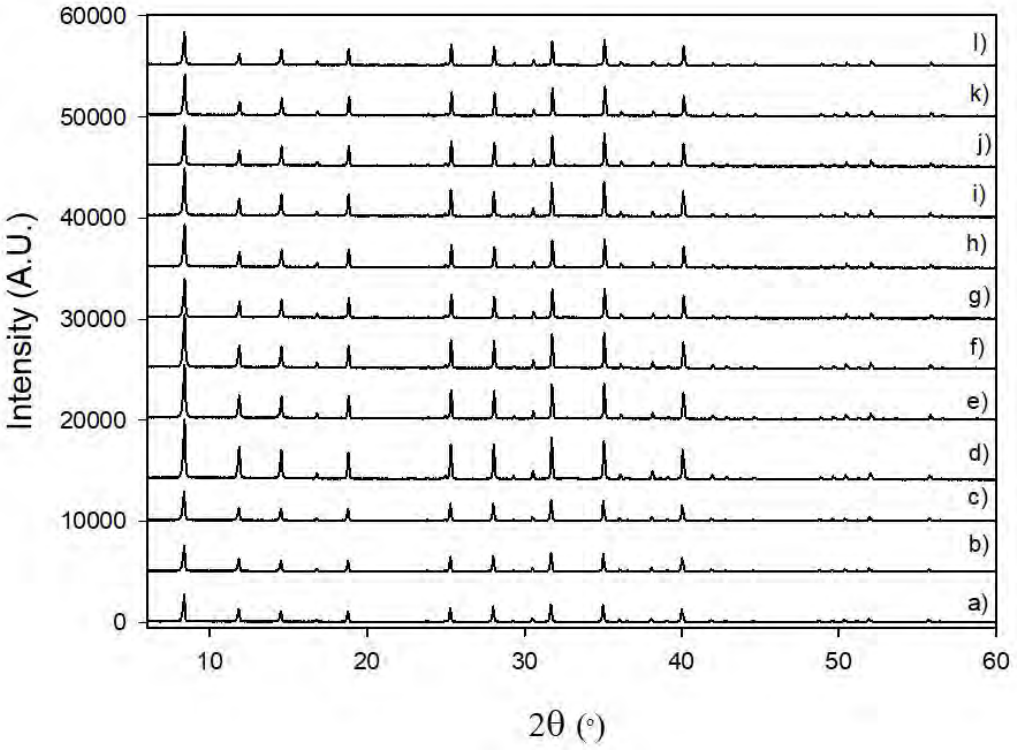


Figure 35: X-ray diffraction patterns produced during Mn(II) ion-exchange into zeolite A using 0.25 M manganese(II) chloride at 25˚C, over a 24 hour time period. a) was taken after 15mins, d) after 1 hour, k) after 8 hours and finally l) after 24 hours.

3.4.3.2. Selection of timeframe for Mn(II) in zeolite A

This study also showed high levels of over-exchange but to a lesser extent than that shown for iron and cobalt. Similarly to cobalt, the maximum cation/Al ratio is reported to be at 24 hours with approximately 18% sodium remaining. Analysis of the

corresponding XRD pattern showed this timeframe was suitable and thus 24 hours was selected as the timeframe to maximise uptake.

3.4.4. The influence of time on nickel(II) cation exchange in zeolite A

3.4.4.1. Time investigation using nickel(II) nitrate

Figure 36 shows the time-based kinetics of divalent nickel using a 0.25 M solution of nickel(II) nitrate held at 25˚C for up to 24 hours. The figure shows different trends in exchange compared to the behaviour observed for divalent cobalt and iron. The Ni/Al data illustrates that there was an initial sharp exchange in the first 15 minutes, with approximately 50% of the maximum nickel content exchanging during this time. There was shallow fall off over the next half hour. The nickel content began to increase again after an hour, followed by small incremental increases until it reached 86% exchange after 5 hours (which was the highest value achieved). After 6 hours there was a sharp decrease to ~60%, then the Ni/Al value remained around this value throughout the rest of the process. The Si/Al ratio did remain stable throughout suggesting that hydrolysis was not an issue.

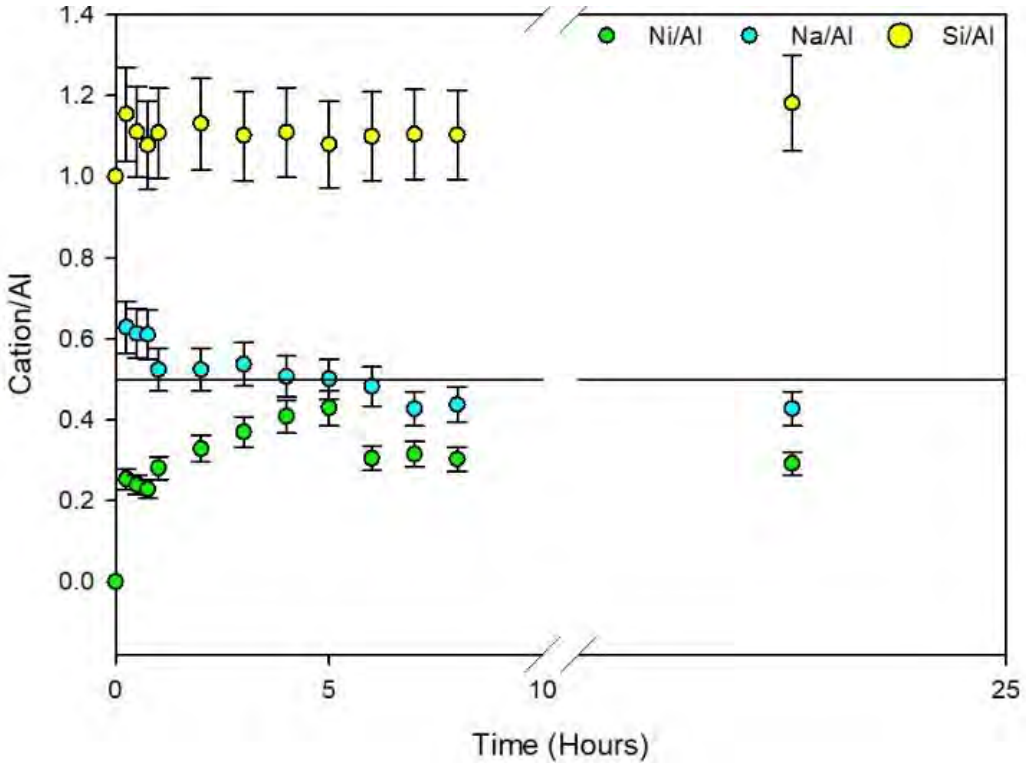


Figure 36: Time-based uptake kinetics for zeolite A using 0.25 M nickel(II) nitrate solution at 25˚C over a 24-hour time frame. Symbol size has been selected to represent the size of the error bars. Element ratios are from WD-XRF data from dried powders in pellet form.

Figure 36 suggests slower exchange kinetics were observed, compared with that of cobalt and iron at 25˚C, with several other distinct differences observed compared to the cobalt and iron studies. The most notable difference was seen in the Ni/Al values, with the exchange value remaining below 100% exchange. Furthermore, the Na/Al value remained above 50% for the majority of the exchange. As the nickel content did not exceed the theoretical maximum, it suggested that there was no over-exchange occurring. However, after 6 hours, 50% of the sodium cations remained within the zeolite when 86% nickel exchange was also observed. Therefore, a greater amount of sodium remained than would be possible if over-exchange had not occurred. After 24 hours the sodium content was reduced to 43%, this suggests nickel exchange was

less favourable over this timeframe than cobalt and iron. Lattice parameters varied from 12.295(3) to 12.457(6) Å.

The limitations shown in the nickel exchanges is either due to the sodium cations inability to exchange out into solution or the inability of the nickel cations to exchange in, even in a weakly concentrated solution. It was initially proposed that the inability to exchange was a thermodynamic issue as exchange of one smaller divalent cation for two larger monovalent cations is preferred by zeolite A. The exchangeable hydrated nickel complexes had a ΔH_{hydr} value of -2106 KJ mol^{-1} which is the most negative of all the cations that were explored during the ion exchange studies. This meant that removal of the nickel hydration spheres would require the greatest amount of energy and therefore the nickel would not be fully dehydrated suggesting it would not reach the size restricted sites of adsorption. However, the limitation in exchange was not considered to be size related as the hydrated and dehydrated radii of nickel is smaller than that of cobalt but instead may be due to Ni^{2+} preferring 4-coordination thus is less likely to occupy the same sites as Na. Another possibility is that the difference in energy required was the reason why the nickel exchange at 25˚C was less successful compared to cobalt and iron. If this reasoning outlined above is correct, by increasing the temperature of the exchange solution this would remove the limitation. The limitation of nickel exchange could also be a selectivity problem, with zeolite A previously shown to readily ion exchange with cobalt or iron.

Figure 37 shows the X-ray diffraction patterns of zeolite A associated with the time-based uptake kinetics at 25˚C in 0.25 M nickel(II) nitrate solution for up to 24 hours. The peak intensities negligibly decreased with contact time and remained stable. During divalent nickel exchange an additional reflection began to appear at around 18°

2θ. As the exchange progressed the intensity of this peak decreased and after 2 hours it was not present in any of the subsequent patterns.

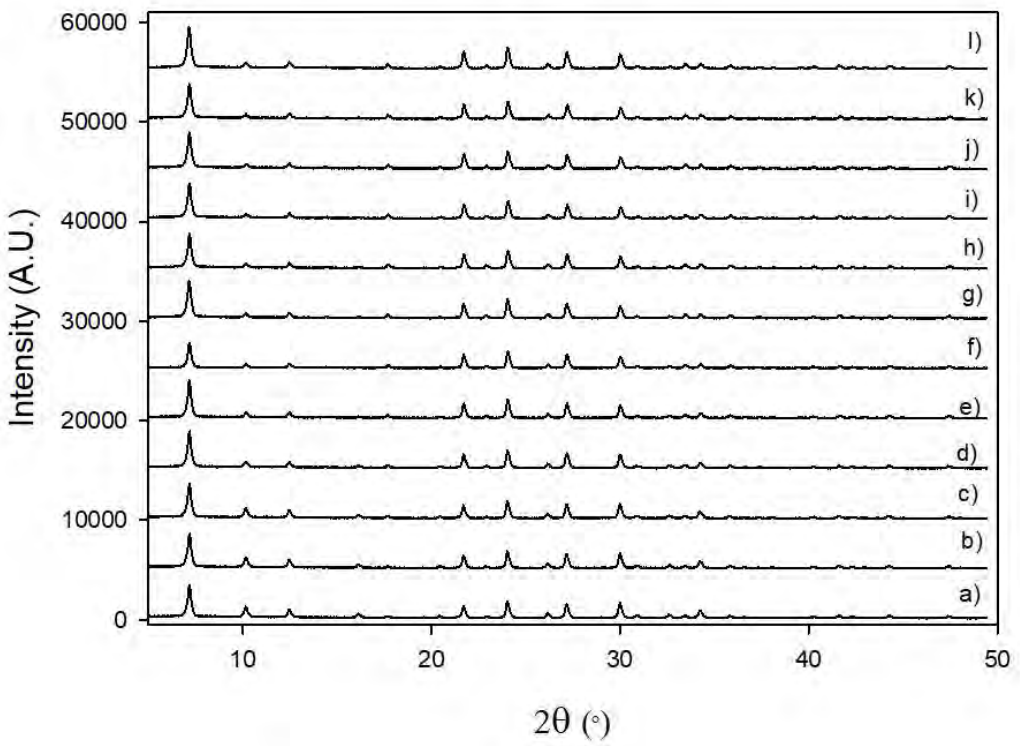


Figure 37: X-ray diffraction patterns produced during Ni(II) ion-exchange into zeolite A using 0.25 M nickel(II) nitrate at 25˚C, over a 24-hour time period. a) was taken after 15mins, d) after 1 hour, k) after 8 hours and finally l) after 24 hours.

3.4.4.2 Selection of timeframe of Ni(II) in zeolite A

This study had noticeably lower levels of over-exchange than the studies discussed previously. The maximum nickel content appeared to occur after 5 hours however, over 50% of the sodium remained. But the lowest sodium content was not until after 24 hours. The aim was to maximise nickel content which would suggest a 5-hour timeframe was optimal, however, a lower sodium content suggests a greater amount of nickel was likely to be present within the pore network. The corresponding XRD

pattern showed the structure remained and as the aim was to maximise nickel content within the zeolite, 24 hours was chosen as the timeframe.

3.4.5. The influence of time on zinc(II) cation exchange in zeolite A

The final divalent cation investigated was zinc. Similarly to manganese exchanged zeolites, zinc exchange was also unable to be confirmed visually, as the zinc exchanged zeolites are also white in colour. Instead X-ray diffraction and loose powder WD-XRF were used to confirm.

The Na/Al data presented in Figure 38 suggested that the zeolite had a preference towards zinc over the other metals investigated. During the first hour of the exchange, it appeared that there was a rapid uptake with the zinc content already exceeding 100% exchange and no sodium cations detected after 15 and 45 minutes. After an hour had elapsed, the erratic variation in cation/Al ratios settled down. After only 1 hour, approximately ~80% of the sodium had exchanged into the external solution with around ~40% of the possible zinc cations exchanging in place of them. This was the first time this behaviour had been seen in any of the ion exchanges conducted. As the exchange progressed, the zinc content increased further as more of the sodium exchanged back into the external solution. After exchanging for 24 hours, zinc exchange reached its maximum value of 92%, at this point no sodium cations were

detected therefore having an 8% discrepancy. Lattice parameters varied from 12.206(3) Å after 15 minutes to 12.133(4) Å after 24 hours.

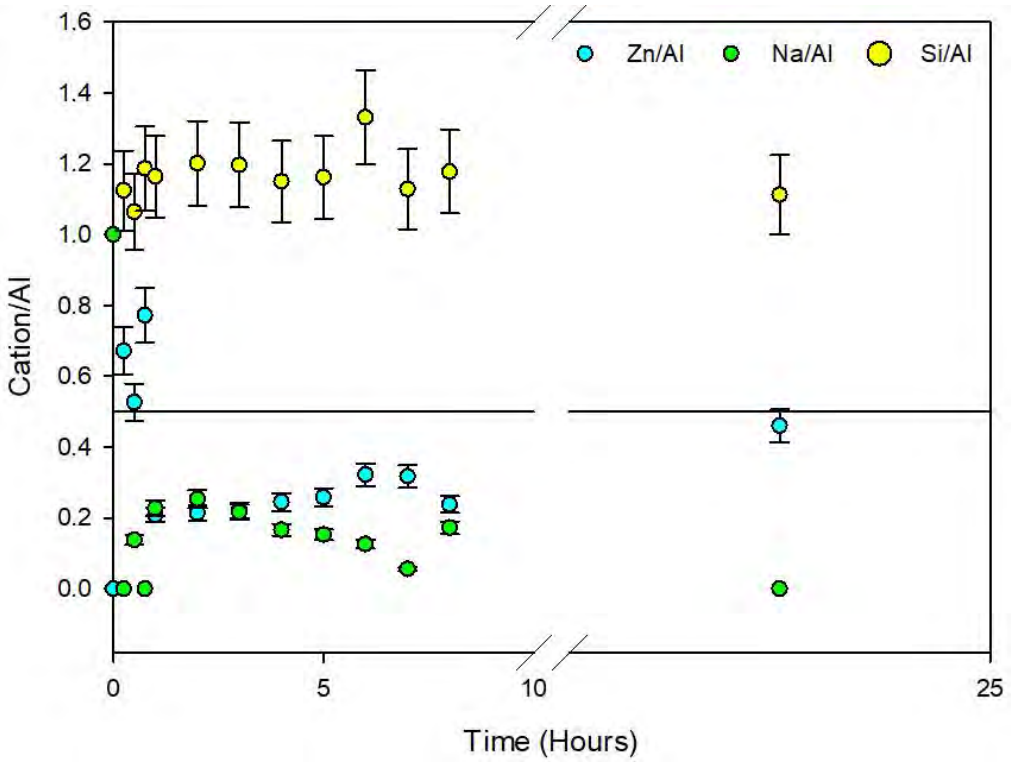


Figure 38: Time-based uptake kinetics of Zn(II) in zeolite A using 0.25 M zinc(II) chloride at 25˚C, over a 24-hour time frame. Element ratios are calculated from WD-XRF data from dried powders in pellet form. The size of the error bars reflects a 10% error commonly associated with XRF of pellets.

Using WD-XRF to determine the composition of materials that contain both zinc and sodium can be complicated and possibly misleading. To get an accurate zinc value when completing the analysis, the calculation cannot always use the k_α radiation at 8.6737 KeV but instead, the l_α radiation at 1.012 KeV can be selected to obtain the correct divergence. However, the K_α line for sodium is at 1.040 KeV which means there is significant overlap between the zinc and sodium. Before deciding on which emission line to use, the emission spectra had to be checked for overlap depending on the intensity of the emission peaks. The XRF machine has built-in analysis algorithms that deconvolute these when necessary, to obtain the most accurate value possible. This

limitation needs to be considered when interpreting the results and could explain the erratic variation in values that was seen in the first hour of exchange. The Si/Al ratio fluctuated slightly throughout with a spike seen in the sample taken after 8 hours but this did not occur again after 24 hours therefore will be taken as an experimental anomaly.

The XRD patterns of the time-based exchange in Figure 39 showed similarities to the Mn time study, as the framework remained stable throughout with no decrease in intensity or loss of high angle peaks. There was a difference in relative intensities in the 24-hour sample when compared to the other scans, this pattern was also the only one to not display the additional peak at 18˚ 2θ. However, it remained unknown whether the presence additional reflection in the XRD pattern was linked to zinc content but as the 24-hour sample had significantly more zinc content this timeframe was chosen going forward, as the aim of this study was to maximise zinc content.

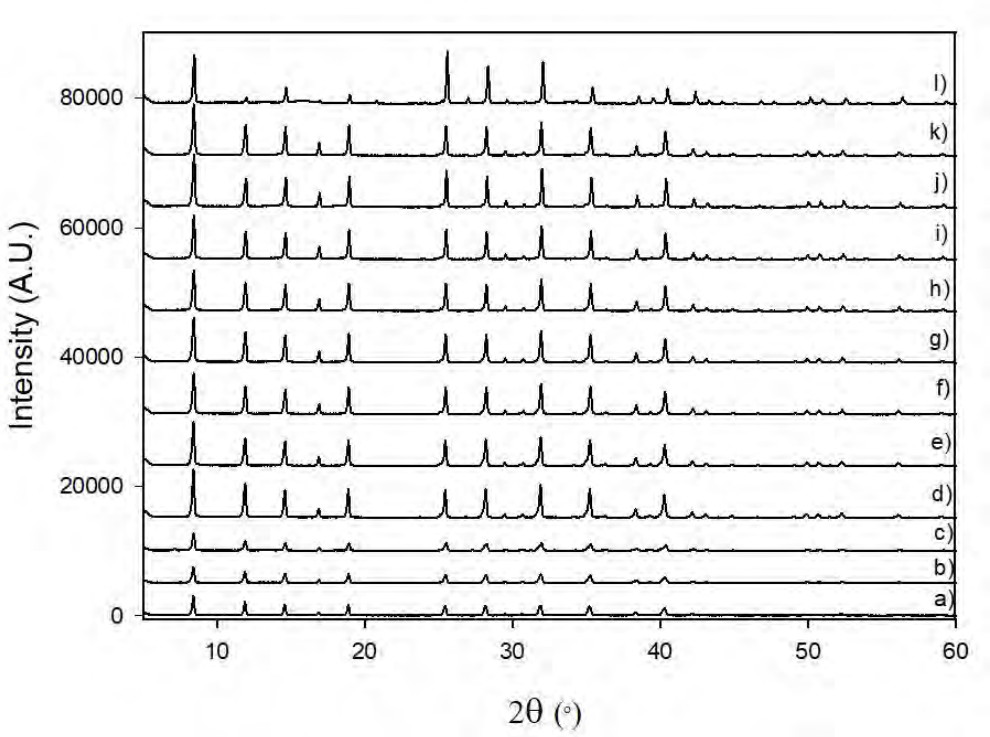


Figure 39: X-ray diffraction patterns produced during Zn(II) ion-exchange into zeolite A using 0.25 M $ZnCl_2$ at 25˚C, over a 24 hour time period. a) was taken after 15mins, d) after 1 hour, k) after 8 hours and finally l) after 24 hours.

3.5. Raman spectroscopy

The WD-XRF data presented throughout the different time studies has shown significant levels of over-exchange. Due to the nature of the exchange conditions and to maintain charge neutrality, the additional metal content could only be present within the pores or on the surface of the zeolite as certain phases. A metal oxide, metal hydroxide or metal oxyhydroxide would be the expected phases to form under said conditions. The most likely species for each divalent metal system will be discussed in this section.

By considering the mechanism of adsorption, (step 1- the diffusion of cations from their bulk solution onto a film that surrounds the zeolite particle) it was proposed that this could lead to precipitation of any additional phases on the surface. For this reason, Raman spectroscopy was chosen to inspect the surface of the exchanged zeolites. The spectra collected are shown in Figure 40 through to Figure 45. Each figure also contains a spectrum of the unexchanged sodium form of zeolite A except for Fe-A as including sodium lost the resolution required to see the peaks of interest. The sodium form was collected using the same parameters and has been provided for comparison.

3.5.1. Raman spectroscopy of zinc exchanged zeolite A

Figure 40 contains the Zn-A Raman spectrum which has peaks observed at ~590 cm^{-1}, ~800 cm^{-1} and ~1100 cm^{-1}. This spectrum clearly matches the sodium form of zeolite A. However, the small cluster of peaks below 200 cm^{-1} decreased in intensity compared to the 3 main peaks, as shown in Figure 41. The absence of any additional

zinc phases in the Raman spectrum and XRD patterns provides evidence to support the WD-XRF data that zinc was not over exchanging.

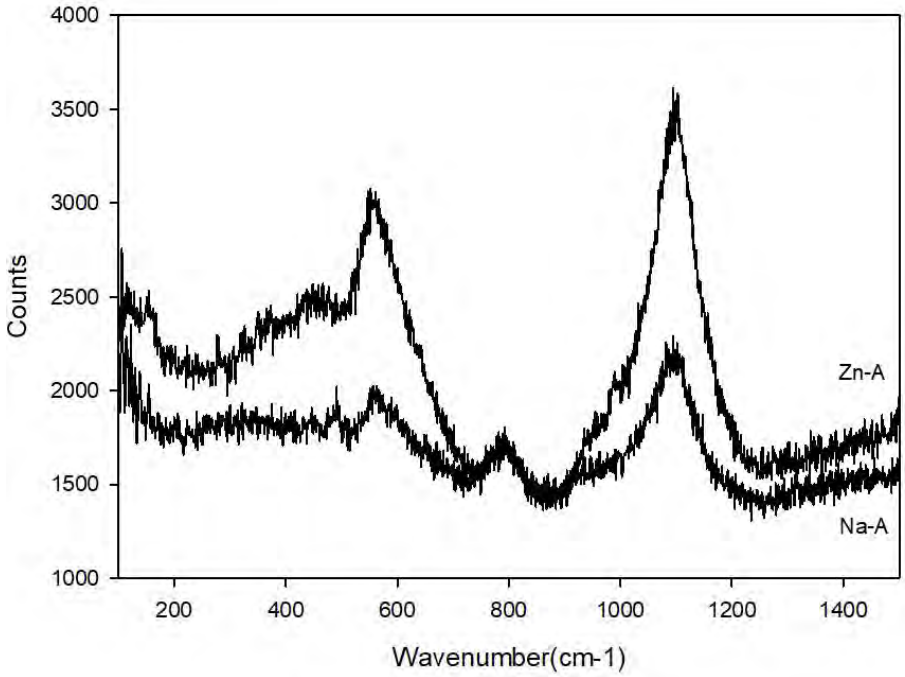


Figure 40 Raman spectrum of Zn(II)-A and Na(I)-A using a 532nm green laser at 10% power for 10 accumulations with 10 second exposure for direct comparison.

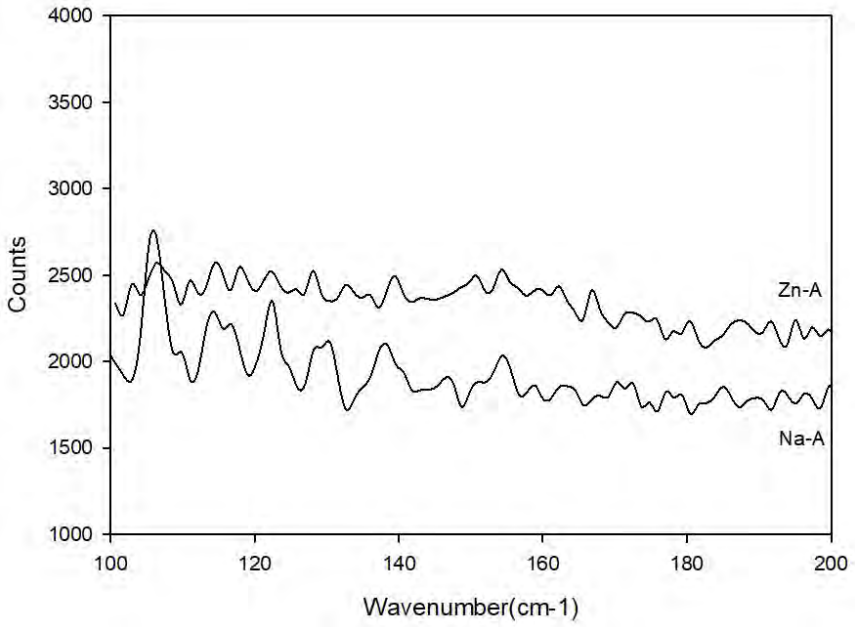


Figure 41 Raman spectrum of Zn(II)-A and Na(I)-A focused around the in 100 to 200 cm^{-1} region.

3.5.2. Raman spectroscopy of cobalt exchanged zeolite A

Figure 42 shows the Co-A spectrum compared to that of Na-A. The spectrum has small peaks in the region below 200 cm^{-1} with the more distinctive broad peaks seen at 480 cm^{-1}, 660 cm^{-1}, 797 cm^{-1} and 1094 cm^{-1}. All the peaks observed in the Co-A spectrum match to those of the sodium form of zeolite A but are less pronounced. The absence of any additional peaks associated with cobalt phases in the Raman spectrum suggests the species is not Raman active or at too low of a level to be detected. However, this does not disprove the theory that surface level precipitation can explain the surplus of Co content relative to Al.

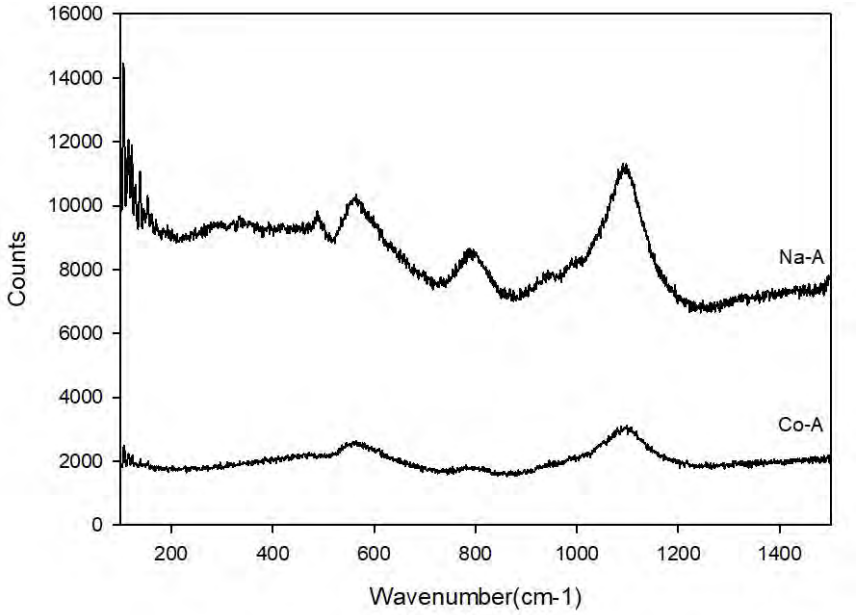


Figure 42 Raman spectra produced by Na(I) zeolite A and Co(II) exchanged zeolite A after 24 hours contact with 0.25 M $FeCl2{\cdot}4H_2O$ at 65˚C using a 532nm green laser using 10% power with an exposure time of 10 seconds for 10 accumulations.

3.5.3. Raman spectroscopy of manganese exchanged zeolite A

Figure 43 contains the Raman spectrum of Mn-A. Over-exchange may present as precipitation on the surface as described previously. Therefore Mn may present as an oxide, but, manganese oxide has three different crystal structures α-MnO_2, β-MnO_2 or γ-MnO_2, each with a unique Raman spectrum.[28,29] The spectrum was also checked against Mn_2O_3, MnOOH and $Mn(OH)_2$ but no match was found. The spectrum closely matched to α-MnO_2 however, it does not have the 3 associated peaks after 600 cm^{-1}, therefore, this suggests it does not fit to any of the manganese oxide possibilities. After comparing the peaks in Figure 43 to the values of the remaining potential precipitates, a match could not be found. It was deemed that none of the expected species had precipitated on the surface or at least not enough to be detected by Raman spectroscopy. The spectrum was compared to that of the sodium form of zeolite A, the only similarity was seen at around 1000 cm^{-1} where the broad peak had narrowed

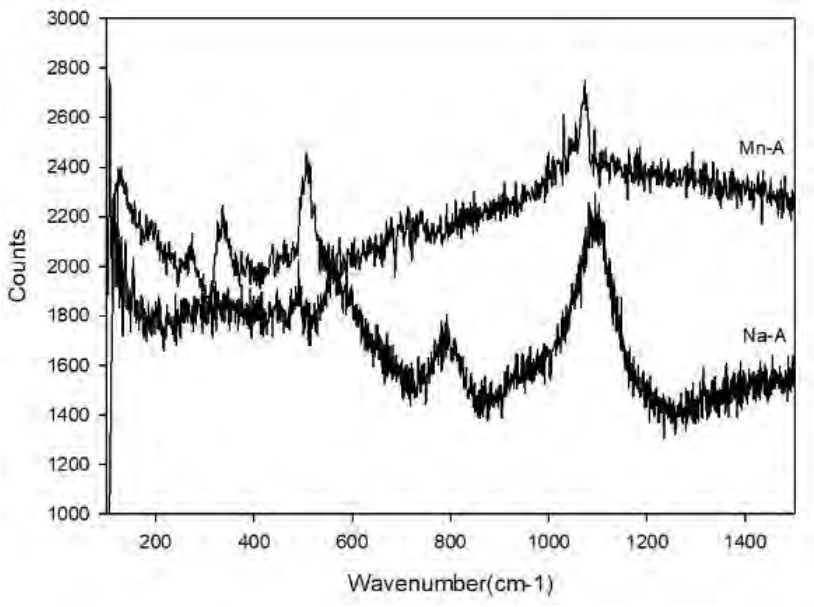


Figure 43 Raman spectrum of Mn(II)-A and Na(I)-A using a 633nm red laser at 10% power for 10 accumulations with 10 second exposure for direct comparison.

significantly. This suggested something had happened during the exchanged but could not be explained by using Raman alone.

3.5.4. Raman spectroscopy of nickel exchanged zeolite A

Figure 44 shows the Ni-A spectrum, peaks were observed at 404cm^{-1}, 501cm^{-1}, 579cm^{-1}, 694cm^{-1} and 1045cm^{-1}. Nickel oxide or nickel hydroxide are the most plausible species that could precipitate due to over-exchange. Nickel oxide would have peaks at 570cm^{-1}, 730cm^{-1}, 906cm^{-1}, 1090cm^{-1} and 1490cm^{-1}.[30] Nickel hydroxide would have peaks at 486cm^{-1}, 622cm^{-1}, 933cm^{-1}, 1098cm^{-1}, 3584cm^{-1} and 3662cm^{-1}.[31] However, the Raman peaks did not match to any of these species but instead matched more closely to Na-A but with peaks shifted and significantly reduced peak widths. This again suggested over-exchange could not be detected by Raman spectroscopy, but it does show that aqueous exchange influenced the structure.

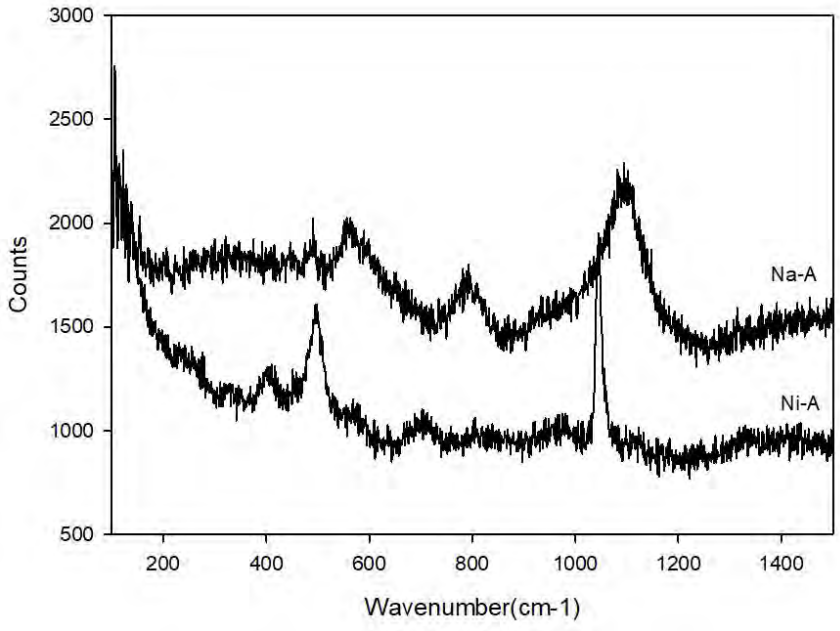


Figure 44 Raman spectrum of Ni(II)-A and Na(I)-A using a 532nm green laser at 10% power for 10 accumulations with 10 second exposure for direct comparison.

3.5.5. Raman spectroscopy of iron exchanged zeolite A

The spectrum shown in Figure 45 has peaks at 225 cm^{-1}, 295 cm^{-1}, 410 cm^{-1}, 616 cm^{-1} and a very broad one at 703 cm^{-1}.[32] These values do not match those of the sodium form of zeolite A but are consistent with 5 of the 6 peaks seen for hematite. As it is common for the 247 cm^{-1} (E_g) transition to be absent,[32] this suggests that iron may not have been divalent throughout the whole exchange and may have oxidized in part to form the oxide. However, no hematite was observed in the X-ray diffraction pattern as it is likely to be hidden by the zeolite's pattern due to the differences in the intensities. As Raman is surface sensitive, this suggests that there is a small surface coating of hematite. This would explain the brown colour seen after a successful exchange. It is also consistent with the WD-XRF data which shows a surplus of Fe relative to Al and would therefore account for some of the over-exchange observed.

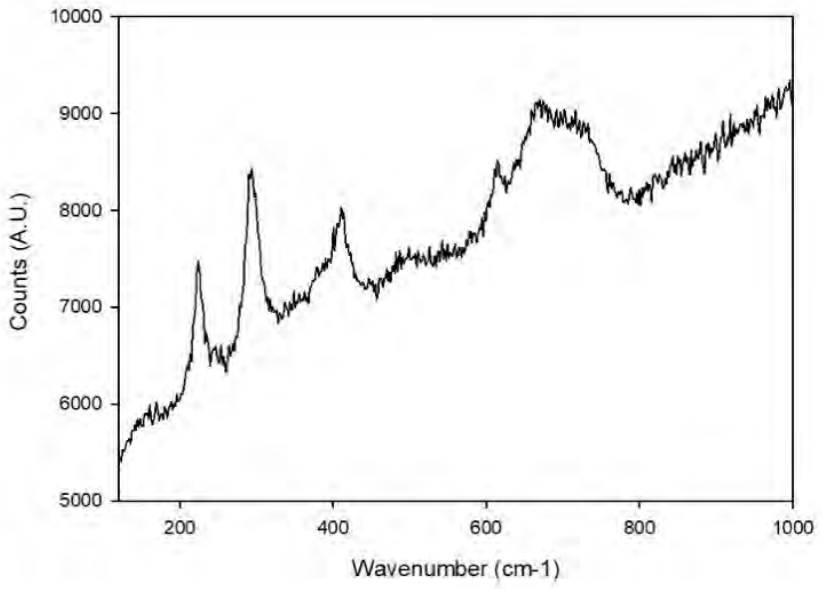


Figure 45 Raman spectrum produced by Fe(II) exchanged zeolite A after 24 hours contact with 0.25 M $FeCl2{\cdot}4H_2O$ at 55˚C using a 532nm green laser.

3.5.6. Conclusion of a Raman spectroscopy study of transition metal exchanged zeolite A

Section 3.4 demonstrated regardless of the transition metal used there was some degree of over-exchange, it was proposed that this was a result of surface precipitation. However, although Raman spectroscopy is a surface technique there was no surface precipitates detected other than for the iron exchanged zeolites which detected hematite. This is thought to be linked to how quickly iron oxidises compared to other metals studied rather than over-exchanged precipitation. Therefore, there would be greater amounts of surface iron precipitates which allows them to be detected. However, this theory is unconfirmed and it remains unknown whether the lack of detection is due to the proposed species being too low level to be detected an opposed to the species not being Raman active which is unlikely given the expected species.

3.6. Concentration and temperature

As several of the time studies showed low levels of sodium remaining after 24 hours, the effect of initial concentration and exchange temperature were investigated for further optimisation. It was proposed that this could result in greater levels of sodium exchange and thus higher metal loading. The effects of concentration and temperature were investigated simultaneously.

3.6.1. The influence of temperature and concentration on iron(II) cation exchange

The effects of temperature and concentration on divalent iron exchange over 24 hours can be seen in Table 8. Graphical representations of the data in the tables throughout this chapter for each of the cations are included in the appendix (section 3.2). Table 8 shows that when the lower concentrations were used it resulted in higher levels of divalent iron exchange at 25˚C with minimal amounts of sodium being detected. However, the overall iron content is comparable in all cases. Once the temperature was increased to 35˚C, a smaller amount of sodium was detected in all cases but a significant spike in Fe/Al ratio was seen for both 0.5 M and 1 M solutions. No such spike was seen when the temperature was increased further in any of the samples.

Table 8 The effect of temperature and concentration on Fe^{2+} cation exchange in zeolite A

0.25 M $FeCl_2$	**Fe/Al Ratio**	**Na/Al Ratio**	**Si/Al Ratio**	**0.5 M $FeCl_2$**	**Fe/Al Ratio**	**Na/Al Ratio**	**Si/Al Ratio**
25°C	0.9(6)	0.0(5)	1.0(9)	**25°C**	0.9(2)	0.0(6)	1.1(1)
35°C	0.9(9)	0.0(4)	1.0(8)	**35°C**	1.2(1)	0.0(6)	1.0(7)
45°C	1.0(6)	0.0(2)	1.0(5)	**45°C**	0.9(7)	0.0(3)	1.0(7)
55°C	1.0(6)	0.0(1)	1.0(2)	**55°C**	0.9(8)	0.0(2)	1.0(3)
65°C	1.1(8)	0.0(0)	1.0(0)	**65°C**	1.0(1)	0.0(1)	1.0(1)
1 M $FeCl_2$	**Fe/Al Ratio**	**Na/Al Ratio**	**Si/Al Ratio**	**2 M $FeCl_2$**	**Fe/Al Ratio**	**Na/Al Ratio**	**Si/Al Ratio**
25°C	0.8(8)	0.0(9)	1.0(7)	**25°C**	1.0(0)	0.1(7)	1.1(2)
35°C	1.1(9)	0.0(5)	1.1(3)	**35°C**	0.9(7)	0.1(1)	1.1(2)
45°C	0.6(8)	0.2(1)	1.2(9)	**45°C**	0.8(4)	0.1(1)	1.0(9)
55°C	0.9(9)	0.0(4)	1.1(1)	**55°C**	0.9(3)	0.1(1)	1.0(9)
65°C	1.1(4)	0.0(3)	1.0(8)	**65°C**	0.9(8)	0.0(5)	1.0(7)

Overall, the use of lower concentrations resulted in higher levels of sodium exchange out of the framework at the same temperature. The cause of this is not certain, but it is proposed that using highly concentrated solutions leads to faster over-exchange and this brings in more anions for charge balancing. Alternatively, it may be precipitation of a surface iron oxide coating described previously in section 3.5.5. Either of these would block the pore windows and/or channels and prevent the loss of sodium.

Regardless of the concentration used, the Si/Al ratio did not drastically change. This implies that even at higher temperatures there was not significant proton exchange occurring, as this would have impacted the pH and would have caused dealumination.[22] As understanding the factors that affect iron loading was the driving force of this part of the study, the Fe/Al ratio was focused on to decide the optimum conditions, as it was thought that any of the Fe(II) present could partake in the second step of the process and the differences in sodium content were negligible in certain cases. This suggested that a 0.25 M concentration would be the most favorable.

Figure 46 contains the X-ray diffraction patterns relating to the 0.25 M iron(II) chloride temperature series. It shows that as the temperature increased there was a slight reduction in overall intensity, until 65˚C where all long-range order was lost, suggesting that the zeolite framework was destroyed. As maintaining the framework structure was preferable, based upon analysis of the XRD patterns and the WD-XRF data, a concentration of 0.25 M heated at 55˚C for 24 hours was chosen as the optimum for a one contact divalent iron aqueous ion exchange.

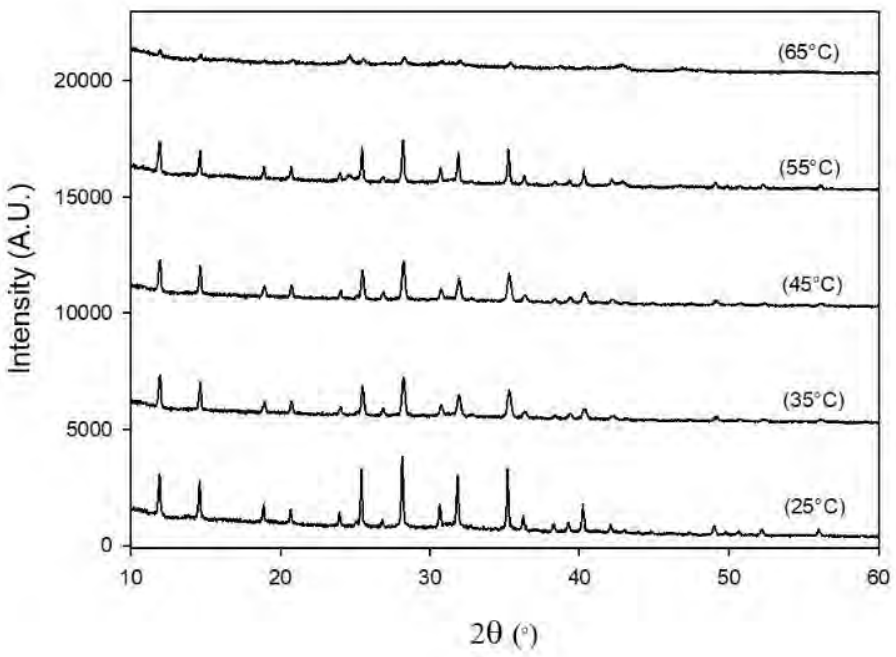


Figure 46 X-ray diffraction patterns from temperature-based uptake kinetics of Fe(II) in zeolite A when using 0.25 M iron(II) chloride salt solutions at different temperatures for 24 hours.

3.6.2. The influence of temperature and concentration on cobalt(II) cation exchange

Table 9 demonstrates the effect the temperature and concentration on divalent cobalt ion exchange over 24 hours. Table 9 showed that regardless of the concentration used, increasing the temperature of the solution resulted in an increase in the cobalt content and a decrease in the sodium content. The ion exchanges that were carried out in the more concentrated solutions had significantly less pore loading and overall cobalt content across the temperature range.

Table 9 The effect of temperature and concentration on Co^{2+} cation exchange in zeolite A

0.25 M $Co(NO_3)_2$	**Co/Al Ratio**	**Na/Al Ratio**	**Si/Al Ratio**	**2 M $Co(NO_3)_2$**	**Co/Al Ratio**	**Na/Al Ratio**	**Si/Al Ratio**
25°C	0.7(1)	0.1(8)	1.0(8)	**25°C**	0.5(8)	0.2(7)	1.0(5)
35°C	0.8(4)	0.1(3)	1.0(9)	**35°C**	0.6(8)	0.2(2)	1.1(3)
45°C	0.9(6)	0.1(1)	1.1(1)	**45°C**	0.8(1)	0.1(7)	1.0(9)
55°C	0.9(8)	0.0(9)	1.1(2)	**55°C**	0.8(7)	0.1(3)	1.0(8)
65°C	1.1(3)	0.0(5)	1.1(1)	**65°C**	0.9(6)	0.0(8)	1.0(7)
0.5 M $Co(NO_3)_2$	**Co/Al Ratio**	**Na/Al Ratio**	**Si/Al Ratio**	**1 M $Co(NO_3)_2$**	**Co/Al Ratio**	**Na/Al Ratio**	**Si/Al Ratio**
25°C	0.6(7)	0.1(9)	1.0(8)	**25°C**	0.6(5)	0.2(5)	1.1(7)
35°C	0.7(7)	0.1(5)	1.0(7)	**35°C**	0.7(1)	0.2(1)	1.0(8)
45°C	0.8(7)	0.1(3)	1.0(9)	**45°C**	0.8(5)	0.1(7)	1.1(5)
55°C	0.9(7)	0.0(9)	1.0(9)	**55°C**	0.8(8)	0.1(2)	1.1(2)
65°C	1.0(3)	0.0(4)	1.0(5)	**65°C**	0.9(3)	0.1(1)	1.1(2)

It is proposed that due to the high concentration of the solutions, significant surface aggregation occurred, this resulted in the partial blocking of the pore network therefore disabling the exchange process. This would have limited access to the pores, therefore less sodium could exchange into the external solution and more would remain within the framework. As this would also have prevented cobalt from reaching the absorption sites, it could plausibly explain why the lower Co/Al and higher Na/Al ratios occur only in the more concentrated solutions.

The less concentrated solutions showed greater levels of Na entering the external solution at similar Co/Al readings compared to their counterparts. These results would appear to back up the hypothesis proposed earlier. Every Co/Al reading exceeds the theoretical maximum suggesting there was significant over-exchange occurring, especially at elevated temperatures. Table 9 also shows that neither concentration nor temperature has an influence upon the Si/Al ratios and therefore this suggests that no significant hydrolysis occurred. Based upon the results shown in Table 9, the optimal concentration was 0.25 M as this allowed for the greatest cobalt content and the lowest sodium content. As maintaining the zeolite framework was preferred, the XRD patterns in Figure 47 had to be reviewed before deciding upon the optimal temperature. The greatest cobalt content and the lowest sodium content occurred when heating the exchanges to 65˚C and Figure 47 shows that the structure remained relatively stable when compared to its counterparts, therefore it was chosen as the optimal temperature.

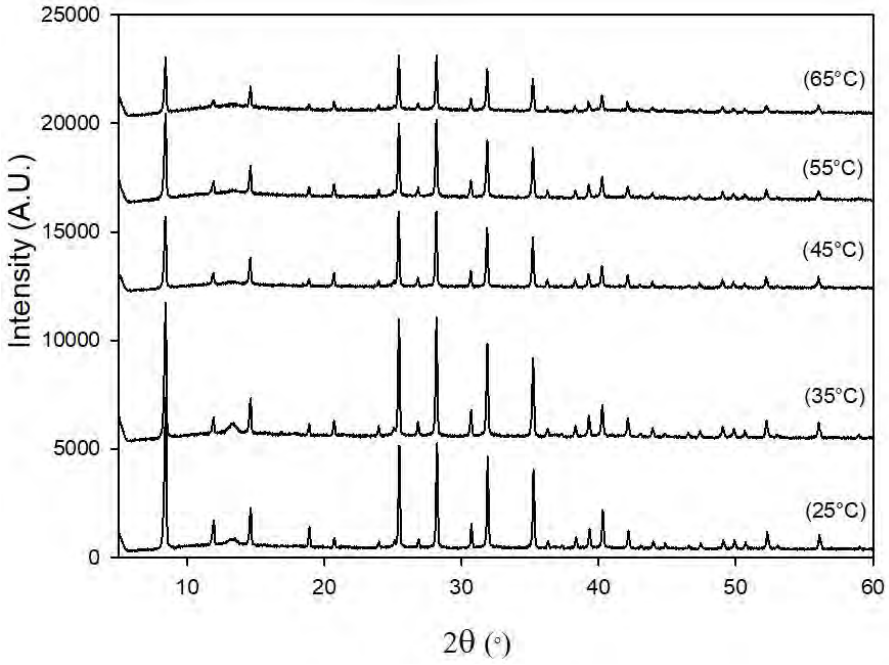


Figure 47 X-ray diffraction patterns from temperature-based uptake kinetics of Co(II) in zeolite A when using 0.25 M cobalt(II) nitrate salt solutions at different temperatures for 24 hours.

3.6.3. The influence of temperature and concentration on manganese(II) cation exchange

The results of the manganese varied temperature and concentration exchanges over 24 hours are shown in Table 10.

Table 10 The effect of temperature and concentration on Mn^{2+} cation exchange in zeolite A

0.25 M $MnCl_2$	**Mn/Al Ratio**	**Na/Al Ratio**	**Si/Al Ratio**	**0.5 M $MnCl_2$**	**Mn/Al Ratio**	**Na/Al Ratio**	**Si/Al Ratio**
25°C	0.8(2)	0.1(1)	1.1(4)	**25°C**	0.8(2)	0.1(1)	1.1(1)
35°C	0.8(2)	0.0(7)	1.1(0)	**35°C**	0.7(7)	0.1(3)	1.1(1)
45°C	0.8(3)	0.0(8)	1.1(0)	**45°C**	0.8(2)	0.1(1)	1.1(1)
55°C	0.8(4)	0.0(8)	1.0(6)	**55°C**	0.8(3)	0.0(9)	1.1(4)
65°C	0.8(7)	0.0(6)	1.1(0)	**65°C**	0.8(4)	0.0(9)	1.1(3)
1 M $MnCl_2$	**Mn/Al Ratio**	**Na/Al Ratio**	**Si/Al Ratio**	**2 M $MnCl_2$**	**Mn/Al Ratio**	**Na/Al Ratio**	**Si/Al Ratio**
25°C	0.7(3)	0.2(1)	1.1(2)	**25°C**	0.6(7)	0.2(0)	1.0(9)
35°C	0.7(1)	0.1(7)	1.0(9)	**35°C**	0.6(8)	0.1(9)	1.0(9)
45°C	0.7(2)	0.1(8)	1.1(1)	**45°C**	0.6(9)	0.2(1)	1.1(4)
55°C	0.7(5)	0.1(7)	1.1(3)	**55°C**	0.7(1)	0.2(3)	1.1(2)
65°C	0.7(7)	0.1(6)	1.1(2)	**65°C**	0.7(3)	0.2(1)	1.1(2)

As has been shown for the previous divalent cation exchanges, the lower concentrations resulted in greater manganese content and increased sodium exchange back into solution for the reasons previously discussed. Table 10 shows there was no positive correlation between Mn content and temperature. The sodium values also follow the same trend. However, this is less apparent in the 2 M study as outward exchange may have been limited for the reasons explained previously.

The main difference seen in the manganese study (Table 10) compared to the iron and cobalt studies, was the negligible effect that temperature had on increasing the manganese content. The iron and cobalt exchange data presented in

Table 8 and Table 9 showed a positive correlation between temperature and cation content. This is thought to be due to manganese having the lowest hydration energy (-

1845 kJ mol^{-1}) of all the divalent cations tested. Therefore, the higher temperatures were not required for removal of the hydration shell. Instead, the outward exchange of sodium into the external solution was determined to be the limiting factor, hence the more concentrated solutions had a greater sodium content.

The greatest cation content and sodium removal occurred during the 0.25 M series but before deciding the optimal temperature, the XRD patterns in Figure 48 needed to be reviewed. At the higher temperatures, the framework remained undamaged as the high angle peaks have little to no decrease in intensity. As the differences in Mn/Al across the temperature range were negligible, once errors were considered, it was decided that a 0.25 M solution at 35˚C held for 24 hours would be the optimum conditions for divalent manganese exchange for zeolite A.

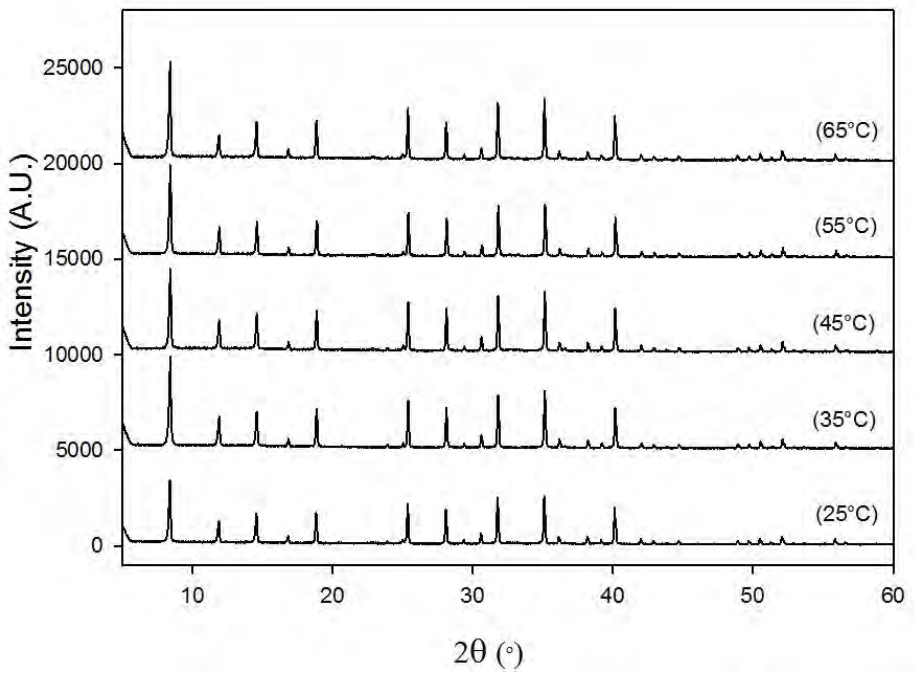


Figure 48 X-ray diffraction patterns from the study of temperature-based uptake of Mn(II) using zeolite A when in a 0.25 M manganese(II) chloride salt solution at different temperatures for 24 hours.

3.6.4. The influence of temperature and concentration on nickel(II) cation exchange

It was hoped that these studies would provide further information to explain why the exchange of monovalent sodium for divalent nickel was occurring less readily.

Table 11 showed that at 25˚C nickel loading was similarly independent of the concentration used. This was seen previously in both the cobalt and iron exchanges. The less concentrated solutions resulted in less sodium present after an exchange, implying that pore loading was more successful.

Table 11 The effect of temperature and concentration on Ni^{2+} cation exchange in zeolite A.

0.25 M $Ni(NO_3)_2$	**Ni/Al Ratio**	**Na/Al Ratio**	**Si/Al Ratio**	**0.5 M $Ni(NO_3)_2$**	**Ni/Al Ratio**	**Na/Al Ratio**	**Si/Al Ratio**
25°C	0.3(6)	0.4(1)	1.1(2)	**25°C**	0.3(6)	0.4(1)	1.0(8)
35°C	0.7(3)	0.2(5)	1.1(3)	**35°C**	0.6(6)	0.2(4)	1.1(1)
45°C	0.8(3)	0.1(7)	1.1(3)	**45°C**	0.8(7)	0.2(2)	1.1(2)
55°C	1.0(6)	0.1(2)	1.1(4)	**55°C**	1.0(7)	0.1(2)	1.0(9)
65°C	0.8(6)	0.1(4)	1.0(9)	**65°C**	0.8(3)	0.1(5)	1.1(1)
75°C	1.2(1)	0.0(4)	1.0(5)	**75°C**	1.0(7)	0.1(3)	1.0(8)
1 M $Ni(NO_3)_2$	**Ni/Al Ratio**	**Na/Al Ratio**	**Si/Al Ratio**	**2 M $Ni(NO_3)_2$**	**Ni/Al Ratio**	**Na/Al Ratio**	**Si/Al Ratio**
25°C	0.2(2)	0.4(7)	1.1(8)	**25°C**	0.3(9)	0.4(8)	1.0(8)
35°C	0.6(7)	0.2(5)	1.1(2)	**35°C**	0.5(9)	0.3(1)	1.1(6)
45°C	0.8(2)	0.1(6)	1.1(1)	**45°C**	0.7(7)	0.2(2)	1.1(1)
55°C	0.9(9)	0.1(2)	1.0(5)	**55°C**	1.0(5)	0.1(6)	1.1(2)
65°C	0.9(4)	0.1(4)	1.1(1)	**65°C**	0.8(3)	0.1(8)	1.0(9)
75°C	1.2(1)	0.0(5)	1.0(9)	**75°C**	0.9(5)	0.1(6)	1.0(6)

Once the temperature was increased, the differences began to show regardless of the concentration used. With each temperature increase, a greater amount of nickel was detected, along with a decrease in sodium content. The ion exchanges that were carried out in the more concentrated solutions had less pore loading, as more sodium remained within the zeolite framework, and had less overall nickel content across the same temperature range, compared to the lower concentrations used.

The reasoning for this behaviour has been mentioned previously in the cobalt section 3.4.2. Throughout the series of exchanges there was no notable rise/fall in sodium content, however, in 3 out of the 4 concentrations there was a significant spike in Ni/Al ratio when carried out at 55˚C. The greatest nickel and lowest sodium content occurred at 75˚C. However, if the exchanges were performed at temperatures above 55˚C this caused damage to the zeolite framework. The XRD patterns showed long rang order was lost, as shown in Figure 49.

When the exchanges were carried out at temperatures of 35˚C or above over-exchange occurred in each scenario. This suggested that increasing the temperature alleviated the limitation found in the time-based study and that the energy limitation hypothesis proposed previously could be correct. Upon reviewing the WD-XRF data and considering the damage caused to the zeolite when exchanging at elevated temperatures, it was decided that the optimum exchange was achieved by using a 0.25 M solution of nickel(II) nitrate at 55˚C for 24 hours. A concentration of 0.25 M was chosen as this series had similar exchange levels to the other concentrations used. However, the use of the lowest concentration possible is preferable as if this process was scaled up, the hazards associated with the toxic waste produced would be minimised. The temperature was chosen to be 55˚C as this had a higher nickel and lower sodium content than its counterparts and with the differences in crystallinity between the elevated temperatures negligible as shown in Figure 49.

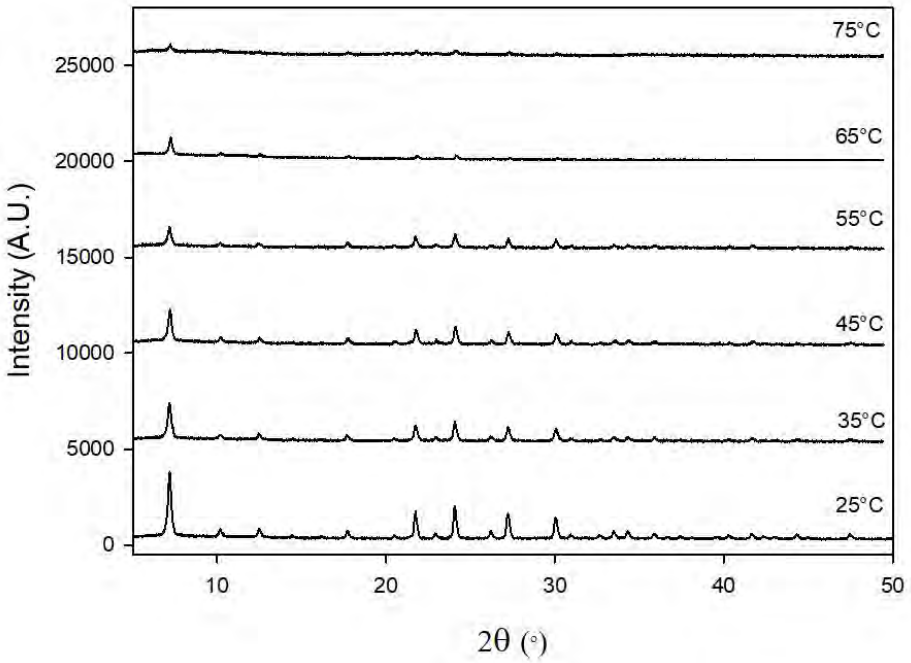


Figure 49 X-ray diffraction patterns from temperature-based uptake kinetics of Ni(II) using zeolite A when in a 0.25 M nickel(II) nitrate salt solution at different temperatures for 24 hours.

3.6.5. The influence of temperature and concentration on zinc(II) cation exchange

The final cation to be investigated was zinc. However, the time-based study found that after 24 hours there was no sodium detected within the sample, this implied that maximum divalent cation exchange had already occurred. However, it was unknown if full exchange had been achieved or the results were misleading due to limitation of the WD-XRF analysis as outlined previously. As the cobalt, iron and nickel studies have shown that by increasing the temperature the metal content can be increased further the study was carried out anyway. Although there would be no differences in sodium content there could be increased zinc content if full exchange had not actually been achieved.

The results of these studies are summarised in Table 12 below. Table 12 shows that there were significant differences compared to the cobalt, iron and nickel studies with the results more similar to those seen for manganese. Independent of the temperature and concentration used, little to no over-exchange occurred which suggests there was an additional factor that limited this exchange.

Table 12 The effect of temperature and concentration on Zn^{2+} cation exchange in zeolite A.

0.25 M $ZnCl_2$	**Zn/Al Ratio**	**Na/Al Ratio**	**Si/Al Ratio**	**0.5 M $ZnCl_2$**	**Zn/Al Ratio**	**Na/Al Ratio**	**Si/Al Ratio**
25°C	0.4(6)	0.0(4)	1.1(1)	**25°C**	0.4(4)	0.0(7)	1.1(1)
35°C	0.4(9)	0.00	1.2(4)	**35°C**	0.5(1)	0.00	1.1(5)
45°C	0.5(1)	0.00	1.1(4)	**45°C**	0.4(4)	0.00	1.3(8)
55°C	0.5(7)	0.00	1.1(9)	**55°C**	0.5(0)	0.00	1.2(1)
65°C	0.5(6)	0.00	1.1(3)	**65°C**	0.5(7)	0.00	1.1(6)
1 M $ZnCl_2$	**Zn/Al Ratio**	**Na/Al Ratio**	**Si/Al Ratio**	**2 M $ZnCl_2$**	**Zn/Al Ratio**	**Na/Al Ratio**	**Si/Al Ratio**
25°C	0.4(3)	0.0(5)	1.1(6)	**25°C**	0.4(4)	0.00	1.1(3)
35°C	0.4(3)	0.0(6)	1.3(4)	**35°C**	0.4(4)	0.00	1.1(7)
45°C	0.4(6)	0.0(3)	1.1(3)	**45°C**	0.4(5)	0.00	1.1(7)
55°C	0.5(2)	0.1(6)	1.1(8)	**55°C**	0.4(4)	0.00	1.1(3)
65°C	0.5(2)	0.00	1.1(4)	**65°C**	0.4(8)	0.00	1.0(5)

When comparing this Zn(II) ion exchange data to the other metals covered in this thesis, the absence of any over-exchange even at elevated temperatures was the main difference. The pH level of these exchanges was significantly higher than the other divalent metals, with the pH being 4.82-5.50 rather than a pH <4. It is known that between pH 4-6 ion exchange is the major mechanism of removal of zinc from aqueous solutions. The adsorption of zinc(II) ions is said to increase linearly with pH. However, upon passing pH 6 the formation of zinc hydrate begins and upon passing pH 8 formation of zinc(II) hydroxide occurs.[33] The concentration of zinc in solution is the sum of several Zn^{2+} and zinc-hydroxides species given in Equation 12.[4]

$$[Zn]_{total} = [Zn]^{2+} + [Zn(OH)]^{+} + [Zn(OH_2)]^{0} + [Zn(OH_3)]^{-} + [Zn(OH_4)]^{2-}$$

Equation 12 The concentration of zinc in solution is the sum of the possible zinc and zinc hydroxide species.

The existence of these species and the possibility of adsorption is dependent on the pH of the solution. It has been found previously that high concentrations of Zn^{2+} reside as the monovalent $[Zn(OH)]^{+}$, ionic pair $[Zn(OH_2)]^{0}$ or as ZnO clusters.[34,35,36] The

concentration of these hydroxy species can be increased by increasing the initial concentration and the pH.[30,37] Adsorption into the channels of the zeolite results in a lowered mobility and therefore can completely disable the ion exchange as appears to have happened here. Furthermore, as the formation of these particular species advances, they begin to reduce the participation of Zn^{2+} in the ion exchange and begin to heavily influence the incorporation mechanisms into the zeolite structure.

In the previous studies, the lower concentrations resulted in higher levels of exchange however in this instance this was not seen. This suggests that it was not possible for over-exchange to occur under these conditions. As the zinc contents were similar, the powder diffraction patterns were used to select the parameters that caused the least amount of degradation to the framework structure. Using a 0.5 M concentration appeared to have a less damaging effect on the framework with 35˚C chosen as the optimum conditions for maximising zinc content.

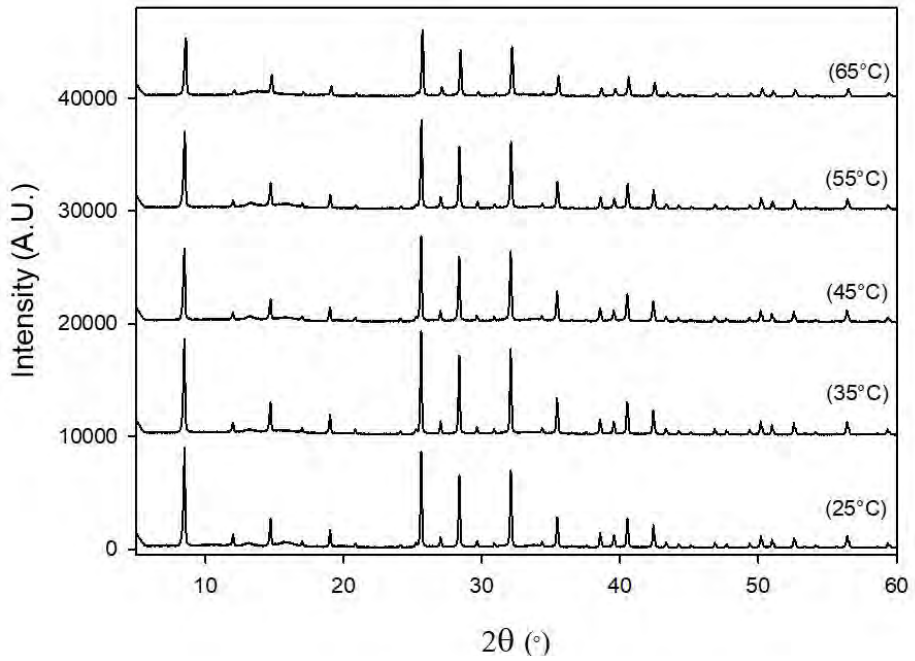


Figure 50 X-ray diffraction patterns from temperature-based uptake kinetics of Zn(II) using zeolite A when in a 0.5 M $ZnCl_2$ salt solution at different temperatures for 24 hours.

3.7. Discussion of divalent ion exchange in zeolite A

Throughout this section, divalent cation exchange for several *d*-block metals in zeolite A has been explored. Based on the results collected, optimal conditions for each cation exchange were determined and were found to be very similar. The main differences were not related to the time of the uptake as equilibrium was always reached by 24 hours, but rather the levels of uptake reached, and the levels of over exchange associated with that. The time-based studies showed that the highest levels of over-exchange were seen during the iron and cobalt exchanges. However, the level of over-exchange did not increase as significantly as it did for the nickel exchanges once the temperature was increased. This suggested the exchanges were limited for different reasons, although the systems still resulted in significant over-exchange. It is difficult to determine the reason for the over-exchange as the ion exchanges being studied are not considered a clean exchange of a divalent metal for sodium, there is more chemistry occurring or over exchange would not happen. If, surface precipitation is proposed to be the main reason, iron species can readily oxidise, precipitate, and block the pores. This would explain why it takes longer to remove all the sodium in this system. If this theory is explored further, it would explain the relative over exchange levels seen for cobalt and nickel. As cobalt can also oxidise but does so more slowly than iron and nickel can only be divalent hence displaying lower levels of ion exchange. However, a surface precipitate was only detected for the iron(II)-A system where hematite was found using Raman spectroscopy. This does not however disprove the theory for the remaining cations, it suggests that the species present is not Raman active or more likely that there was not enough to be detected.

The zinc and manganese systems were shown to have different behaviour possibly due to pH of the solutions and the species that this allows to be present in solution. At the pH used it is proposed that zinc resides as the monovalent $[Zn(OH)]^+$, ionic pair $[Zn(OH_2)]^0$ or as ZnO clusters, adsorption of these species has been shown to disable the ion exchange process and may explain why lower levels of zinc were detected. Due to the issues relating to zinc/sodium determination, WD-XRF analysis alone does not provide conclusive evidence to determine whether zinc over exchange occurs instead this would require the digestion of the exchanged sample in HF followed by the use of ICP-OES/MS for a more accurate analysis. Although manganese was also shown to have over exchanged, it is proposed to be due to monovalent $Mn(OH)^+$ forming at the pH used. Due to its smaller hydrated radius, it can result in a higher quantity of manganese bound to the zeolite than would be expected from ion exchange alone. This suggests that the pH level may be a factor for over exchange, however, this requires further work.

This chapter has shown that the exchange of manganese(II) and zinc(II) is unaffected by temperature. In the case of zinc, it was thought that the adsorption is disabled therefore, temperature is unable affect the levels exchange. In regard to manganese, it was proposed that as manganese has the lowest hydration energy (-1845 KJ mol^{-1}) it did not require additional energy provided by the increase in temperatures to remove the hydration shell. Instead, the outward exchange of sodium into the external solution was the limiting factor, thus the more concentrated solutions had a greater sodium content as a result of pore blocking. The effect of temperature and concentration has been shown to have a much larger impact upon the iron, cobalt and nickel exchanges compared to that of zinc and manganese. The temperature of the solution directly

affected the kinetic energy of the cations, hereby increasing the mobility of the cations and subsequently increasing the rate of diffusion. In a more general view, an increase in temperature resulted in higher levels of exchange. This is proposed to be due to the zeolite exhibiting a higher affinity for the metal cations and/or an increase in the number of active sites on the surface of the zeolite. At elevated temperatures zeolites have shown that the energy of the system facilitates the attachment of metals on its surface. All of which help explain why an increase in metal exchange was observed.[38]

Table 13 Summary of zeolite A's optimised exchange conditions and the associated exchange outcomes

Exchanging cation	Time frame (Hours)	Concentration (M)	Temperature (˚C)	Na/Al ratio	M^{2+}/Al ratio
Fe^{2+}	24	0.25	55	0.01	1.06
Co^{2+}	24	0.25	65	0.05	1.13
Mn^{2+}	24	0.25	35	0.07	0.82
Ni^{2+}	24	0.25	55	0.12	1.06
Zn^{2+}	24	0.5	35	0.00	0.51

3.8. Ion exchange in zeolites X and Y

The influence of time, temperature and concentration was investigated for all the cations present earlier in this thesis for zeolites X and Y. The ion exchange conditions were optimised for all the metal cations for both zeolite X and Y using the same process as was presented for zeolite A. The trends observed were similar to those presented already in this chapter albeit to a lesser extent. Therefore, the ion exchange data have not been discussed but a summary of the optimised conditions is included in the tables 14 and 15 below. The graphs representing the ion exchange data can be found in the appendix section 3.3-3.6. As cation exchange for each metal had been successfully optimised, the metal loaded zeolites could progress onto the next synthesis stage.

Table 14 Summary of zeolite X's optimised exchange conditions and the associated exchange outcomes

Exchanging cation	Time frame (Hours)	Concentration (M)	Temperature (˚C)	Na/Al ratio	M^{2+}/Al ratio
Fe^{2+}	24	0.25	55	0.16	0.92
Co^{2+}	24	0.25	55	0.22	0.69
Mn^{2+}	24	0.5	55	0.15	0.73
Ni^{2+}	24	1.0	65	0.00	0.98
Zn^{2+}	24	0.25	25	0.00	0.42

Table 15 Summary of zeolite Y's optimised exchange conditions and the associated exchange outcomes

Exchanging cation	Time frame (Hours)	Concentration (M)	Temperature (˚C)	Na/Al ratio	M^{2+}/Al ratio
Fe^{2+}	24	0.25	55	0.22	0.92
Co^{2+}	24	0.25	75	0.23	1.41
Mn^{2+}	24	0.5	25	0.25	1.08
Ni^{2+}	24	1.0	75	0.41	1.38
Zn^{2+}	24	1.0	25	0.00	1.28

3.9. References

1 L. Mihaly-Cozmuta, A. Mihaly-Cozmuta, A. Peter, C. Nicula, H. Tutu, D. Silipas and E. Indrea, *J. Environ. Manage.*, 2014, **137**, 69–80.

2 M. Sprynskyy, B. Buszewski, A. P. Terzyk and J. Namieśnik, *J. Colloid Interface Sci.*, 2006, **304**, 21–28.

3 Godelitsas. A, Charistos. D, A. . Tsipis, C. Tsipis and Fillippidis. A, *Chem. - A Eur. J.*, 2001, **17**, 3705.

4 M. Trgo and J. Perić, *J. Colloid Interface Sci.*, 2003, **260**, 166–175.

5 S. M. Robinson, W. D. Arnold and C. H. Byers, *AIChE J.*, 1994, **40**, 2045–2054.

6 M. Trgo, J. Perić and N. V. Medvidović, *J. Hazard. Mater.*, 2006, **136**, 938–945.

7 M. Kithome, J. W. Paul, L. M. Lavkulich and A. A. Bomke, *Soil Sci. Soc. Am. J.*, 1998, **62**, 622–629.

8 A. Teutli-Sequeira, M. Solache-Ríos and M. T. Olguín, *Hydrometallurgy*, 2009, **97**, 46–52.

9 B. John, *Ions in solution*, Woodhead Publishing, 1999.

10 P. E. Riley, K. B. Kunz and K. Seff, *J. Am. Chem. Soc.*, 1975, **97**, 537–542.

11 P. E. Riley and K. Seff, *J. Phys. Chem.*, 1975, **79**, 1594–1601.

12 P. E. Riley and K. Seff, *Inorg. Chem.*, 1974, **13**, 1355–1360.

13 Y. Marcus, *Chem. Rev.*, 1988, **88**, 1475–1498.

14 N. H. Heo, W. Cruz-Patalinghug and K. Seff, *J. Phys. Chem.*, 1986, **90**, 3931–

3935.

15 R. L. Firor and K. Seff, *J. Phys. Chem.*, 1978, **82**, 1650–1655.

16 H. S. Lee, W. V. Cruz and K. Seff, *J. Phys. Chem.*, 1982, **86**, 3562–3569.

17 R. P. Townsend and E. N. Coker, *Stud. Surf. Sci. Catal.*, 2001, **137**, 467–524.

18 R. P. Townsend, J. F. O'Connor and K. R. Franklin, *Adsorpt. Sci. Technol.*, 1984, **1**, 269–283.

19 C. Ronay and K. Seff, *Zeolites*, 1993, **13**, 97–101.

20 F. Collins, A. Rozhkovskaya, J. G. Outram and G. J. Millar, *Microporous Mesoporous Mater.*, 2020, **291**, 109667.

21 C. Weidenthaler, Y. Mao and W. Schmidt, in *studies in surface science and cataylsis*, 2002, vol. 142, pp. 1857–1864.

22 Z. Gao and L. V. C. Rees, *Zeolites*, 1982, **2**, 72–78.

23 R. P. Townsend and E. N. Coker, *Stud. Surf. Sci. Catal.*, 2001, **137**, 467–524.

24 In *American chemical society*, 1976.

25 D. Bae and K. Seff, *Microporous Mesoporous Mater.*, 1999, **33**, 265–280.

26 D. Bae and K. Seff, *Microporous Mesoporous Mater.*, 2000, **40**, 219–232.

27 E. GALLEI, *J. Catal.*, 1974, **33**, 62–67.

28 M. Sun, B. Lan, T. Lin, G. Cheng, F. Ye, L. Yu, X. Cheng and X. Zheng, *CrystEngComm*, 2013, **15**, 7010–7018.

29 B. S. Singu, S. E. Hong and K. R. Yoon, *J. Energy Storage*, 2019, **25**, 100851.

30 N. Mironova-Ulmane, A. Kuzmin, I. Steins, J. Grabis, I. Sildos and M. Pärs, *J. Phys. Conf. Ser.*, 2007, **93**, 012039.

31 B. Shruthi, B. J. Madhu, V. B. Raju, S. Vynatheya, B. V. Devi, G. V. Jayashree and C. R. Ravikumar, *J. Sci. Adv. Mater. Devices*, 2017, **2**, 93–98.

32 S. Das and M. J. Hendry, *Chem. Geol.*, 2011, **290**, 101–108.

33 E. G. Filatova and Y. N. Pozhidaev, *IOP Conf. Ser. Earth Environ. Sci.*, , DOI:10.1088/1755-1315/666/4/042034.

34 S. Raynes, M. A. Shah and R. A. Taylor, *Dalt. Trans.*, 2019, **48**, 10364–10384.

35 I. Pinilla-Herrero, E. Borfecchia, J. Holzinger, U. V. Mentzel, F. Joensen, K. A. Lomachenko, S. Bordiga, C. Lamberti, G. Berlier, U. Olsbye, S. Svelle, J. Skibsted and P. Beato, *J. Catal.*, 2018, **362**, 146–163.

36 S. M. T. Almutairi, B. Mezari, P. C. M. M. Magusin, E. A. Pidko and E. J. M. Hensen, *ACS Catal.*, 2012, **2**, 71–83.

37 P. Misaelides, A. Godelitsas, V. Charistos, D. Ioannou and D. Charistos, *J. Radioanal. Nucl. Chem. Artic.*, 1994, **183**, 159–166.

38 M. A. Wassel, H. A. Shehata, H. F. Youssef, A. S. Elzaref and A. Fahmy, *Int. J. Innov. Sci. Eng. Technol.*, 2016, **3**, 422–429.

Chapter 4: The synthesis of superparamagnetic materials using transition metal exchanged zeolites

4.1. Introduction

Of the five types of magnetism in solids described previously in section 2.2.6.1., it is ferromagnetism and ferrimagnetism that are of most interest for the waste remediation application. As if the ferro/ferrimagnetic nanoparticles are small enough, they are superparamagnetic, this means the particles are magnetic in the presence of a magnetic field and are paramagnetic otherwise. This effectively means that their magnetism can be tuned as required, which would be a desired characteristic given the application. Previously ferromagnetic nanoparticles have been used to magnetise zeolites. [1,2,3,4,5] Based upon the limitations of the magnetisation methods presented previously (1.4.3.) it was thought that a combination of the surface decoration, cation insertion and the direct addition of magnetic nanoparticles would create the optimal product. Given that the cation insertion method had made metal nanoparticles which could easily oxidise, a metal oxide was thought be the most suitable target. The spinel family was chosen as the ideal option as their magnetic properties can be easily tuned by incorporating different cations and spinel ferrite nanoparticles are known to display superparamagnetism.[6,7,8]

To create a superparamagnetic spinel (MFe_2O_4 where M= Co, Fe, Ni, Mn or Zn) within a TM-exchanged zeolite requires the incorporation of iron(III) followed by a thermal treatment. It is reported in the literature that zeolites remain stable up to 950˚C.[9,10,11,12] Therefore, it was hoped that by performing the reaction at temperatures lower than

950˚C, it would maintain the zeolite structure. Use of these temperatures should provide sufficient energy to introduce iron(III) ions into the zeolite and then form magnetic nanoparticles. As the target product had a formula of MFe_2O_4 it would be assumed that a molar ratio of 2:1 iron(III):M(II) would be optimal, however, 1:1 and 0.5:1 ratios were also used to account for possible variation in M(II) content within the zeolite framework across the different TM.[2] This could also be used to investigate how the iron(III) cations interact with the metal(II) cations already within zeolite or if the 'over-exchanged' metal content presented in chapter 3 was able to partake in the formation of MFe_2O_4. As a control measure exchanged zeolite A was also heated in the absence of the iron salt.

4.2. An investigation into the effect of the anion

To investigate the effect of the anion, the divalent iron and cobalt systems were chosen to introduce iron(III) using a nitrate and chloride anion. The divalent and trivalent salts were initially used in a 1:1 ratio.

The divalent cobalt reactions were conducted in a muffle furnace using a 5˚C per minute ramp rate and a 3-hour dwell period before cooling back to room temperature. The reactions were completed in air and used over a temperature range starting at 400˚C increasing in 200˚C increments up to 1000˚C. The divalent iron reactions were conducted in a tube furnace using the same heating conditions as outlined above. A tube furnace was required to create a nitrogen atmosphere as the Fe (II) present within the zeolite can easily oxidise when heated in the presence of oxygen.

First the effect of the nitrate anion was investigated. Nitrate salts are often used in salt occlusions due to their lower melting points (47.2˚C).[2] Iron(III) nitrate boils at 125˚C therefore the preliminary reactions involved heating to 90˚C. This was then held for 2 hours, allowing the salt to melt and the metal ions to insert into the zeolite before rising to the dwell temperature. However, the preliminary reactions found that holding at the lower temperature had no advantageous impact on the final phases formed therefore the reaction parameters outlined above were used.

4.2.1. Cobalt(II)-A with iron(III) nitrate

Firstly, the cobalt system reacting with the iron(III) nitrate will be discussed. Analysis of the XRD patterns in Figure 51 showed that the zeolite had fully decomposed at a much lower temperature than expected from the literature. This breakdown was

suspected to be the result of a side reaction occurring during the reaction or possibly due to the structure becoming weakened during the aqueous exchange and therefore breaking down earlier than expected. Upon increasing the temperature to 800˚C or above two new phases developed which are denoted by the red and blue asterisk. The reflections marked with a red asterisk are related to hematite (α-Fe_2O_3). The blue asterisk matches to reflection produced by both cobalt ferrite ($CoFe_2O_4$) and maghemite (γ-Fe_2O_3). They both are magnetic and have defect spinel structures, but the XRD patterns are so similar they cannot be distinguished by this technique. Identification of the specific phase will be explored later in the chapter but until it is identified the phase will be referred to as a magnetic spinel. The peak around 41˚ had a small shoulder which is thought to be due to the overlap of the peaks around that region from hematite and the unconfirmed phase.

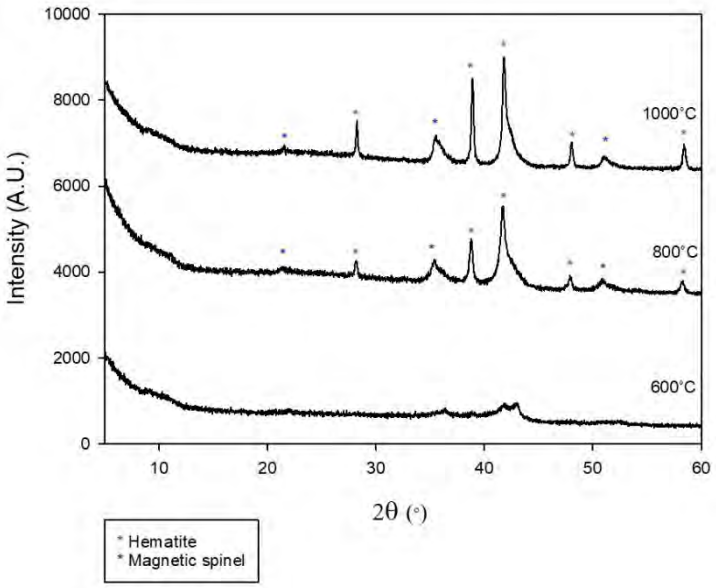


Figure 51 XRD pattern of cobalt(II)-A heated at different temperatures in 1:1 (Fe^{3+}:Co^{2+}) ratio with iron nitrate under atmospheric conditions.

Figure 51 shows that the zeolite framework is not maintained after completing this process and therefore the parent zeolite would not be available for ion exchange

post-synthesis. It was proposed that this product could be incorporated into a new second-generation zeolite that would be readily available to undergo ion exchange. This theory will be discussed in greater detail in Chapter 5.

4.2.2. Iron(II)-A with iron(III) nitrate

Analysis of the iron(II)-iron(III) system, Figure 52, showed that the zeolite broke down earlier than expected and independent of the temperature used, hematite was the only phase to form. This was not desirable as hematite is diamagnetic and therefore it is only weakly attracted towards a magnetic field. As the results showed that use of the nitrate anion created products that were not desirable, therefore, the occlusions at the other ratios (Fe^{3+}:Fe^{2+}) were not completed.

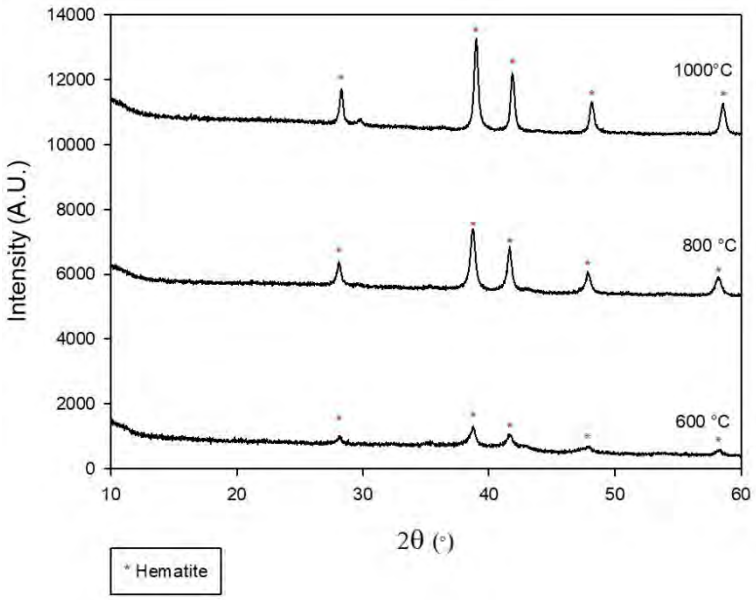


Figure 52 XRD patterns of iron(II)-A and iron nitrate in a 1:1(Fe^{3+}:Fe^{2+}) ratio heated at different temperatures under a nitrogen atmosphere.

4.2.3. Cobalt(II)-A with iron(III) chloride

The next set of reactions investigated the effect of the chloride anion in the cobalt and iron zeolite A systems. The molar ratios used were the same as in section 4.2.1. (1:1 Fe^{3+}:M^{2+}). Chloride salts are less commonly used in salt occlusions because they have greater melting (306˚C) and boiling points (316˚C) than the nitrate salts used previously.

The results of the divalent cobalt system are shown in Figure 53, at 600˚C the zeolite fully decomposed with hematite being the only product. However, by comparing the pattern of this product to that of the nitrate anion it had greater peak intensities and narrower peak shapes which suggested that use of this anion resulted in larger particle sizes. Raising the synthesis temperature to 800˚C or 1000˚C led to the formation of a second phase, these reflections related to the magnetic spinel described earlier. The weight fractions of the cobalt system for iron salts were calculated and are presented in Figure 54 (An example of this type of refinement is shown in the appendix section 4.3). This confirmed that the nitrate anion favours the formation of hematite independent of temperature.

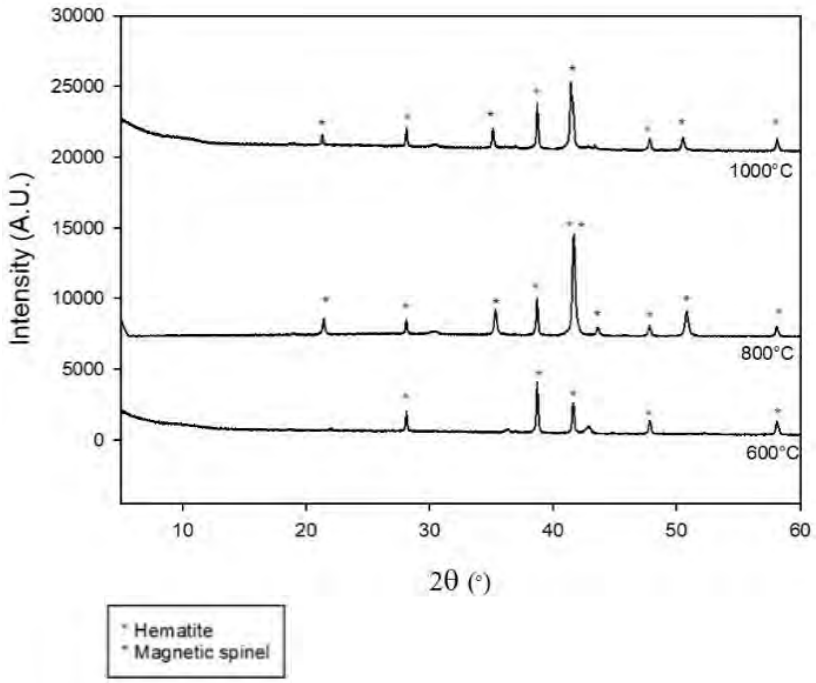


Figure 53 XRD patterns of cobalt(II)-A and iron(III) chloride in a 1:1(iron:cobalt) ratio heated at different temperatures under atmospheric conditions.

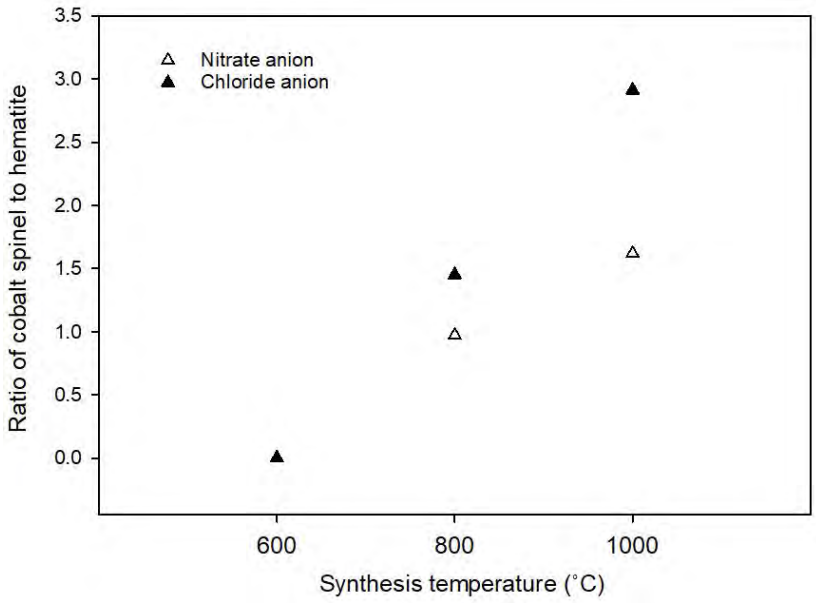


Figure 54 The effect of the anion on phase formation across a range of synthesis temperatures.

4.2.4. Iron(II)-A with iron(III) chloride

The results of the chloride anion and the divalent iron reactions are presented in Figure 55. It shows that similarly to when the nitrate anion was used, at 600˚C hematite (α-Fe_2O_3) is the only product. When the temperature was increased to either 800˚C or 1000˚C, the magnetic spinel phase appeared and became the more dominant phase. Interestingly an additional phase also appears after 800˚C, the broken zeolite framework recrystallized into mullite ($3Al_2O_3{\cdot}2SiO_2$). This reinforced the theory that this matrix material could be used as a possible silica source in a new zeolite preparation.

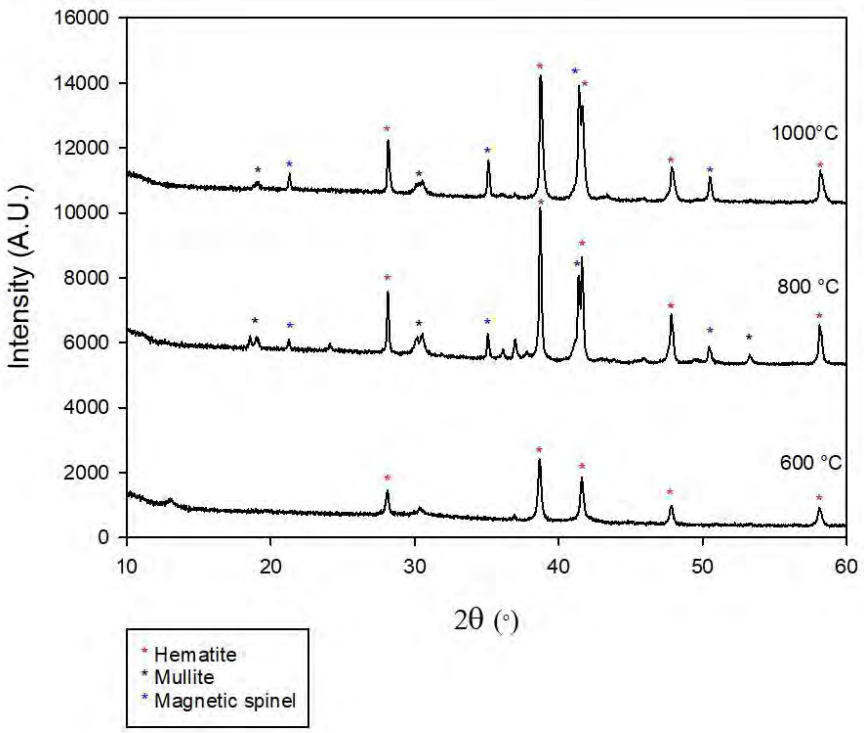


Figure 55 XRD patterns of iron(II)-A and iron(III) chloride in a 1:1(Fe^{3+}:Fe^{2+}) ratio heated at different temperatures under a nitrogen atmosphere.

4.2.5. Conclusion of the anion effect

The use of different anions led to differences in the XRD patterns in terms of relative intensities, crystallinity, phase formed, impurities and particle size. For the cobalt system, differences were seen in the peaks of Figure 51 as they were significantly broader and less intense compared to Figure 53. This indicates that smaller particles are formed when a nitrate salt is used, which is desirable when attempting to form nanoparticles. However, the XRD patterns suggested that hematite is the dominant phase rather than the desired magnetic spinel. This was confirmed by the weight fractions shown in Figure 54, this suggested the material made using iron(III) nitrate would be less desirable. At the higher temperatures this behaviour was to be expected as when nitrate breaks down, it will act as an oxidising agent. Further confirmation was provided by comparing the magnetic strength of the nitrate and chloride samples using a Nd bar magnet. The chloride samples had a significantly stronger response in the presence of the Nd bar magnet. This was contrary to expectation, as if there had been nanoparticles formed when using a nitrate salt, the magnetic response should be significantly stronger than the chloride samples.

For the iron system, the main differences came in the products, as only when using the chloride salt did anything but hematite form. This system also has reflections produced by mullite. During the synthesis, the zeolite framework decomposed into an amorphous silica phase, upon cooling this was then recrystallized into mullite. It is proposed that the nanoparticles are contained within the mullite matrix. The mullite or amorphous silica phase will be referred to as the ‘matrix’ throughout this thesis. The formation of mullite during thermal decompositions can be viewed as a positive feature, as it has previously been reported to relate to high levels of aqueous ion exchange.[12]

The recrystallisation occurring presents an opportunity, it was proposed that it could be used as a possible silica source in a new secondary zeolite preparation. This theory is explored thoroughly in chapter 5.

Further investigation found that the strength of the magnetic response of the materials made using the chloride anion improved further from 7.68 emu/g to 12.06 emu/g upon increasing the iron(III):Cation(II) from 1:1 to 2:1.

4.3. Removal of the hematite impurity

Throughout the anion investigation, it became apparent that independent of the system used there was an issue that resulted in the formation of hematite, either as an impurity or as a sole product. For example, in the cobalt(II)-iron(III) system, the 600˚C sample contained 83% hematite which was reduced to 47% in the 1000˚C sample. It is proposed that when the reaction is conducted at higher temperatures, the zeolites form a viscous glassy matrix. This allows for superior mixing of the divalent and trivalent cations before phase formation which helps prevent regions of deficiency, therefore, decreasing the amount of hematite present. However, as hematite formation occurred regardless of the temperature used it was suggested that formation was not solely due to inferior mixing and that there was another reason behind this. It was proposed in section 3.5.5. (related to iron(II) ion exchange) that hematite formed due to oxidation of iron(II). However, the formation of hematite (α-Fe_2O_3) is also possible through a conversion process from maghemite (γ-Fe_2O_3) above 450˚C.[13,14,15,16] In an attempt to reduce/remove the hematite impurity, the cobalt solid state reactions were instead completed under a nitrogen atmosphere. If hematite formation had been caused by oxidation, heating the sample under nitrogen should prevent any unwanted side reactions and minimise the amount formed. The solid state reactions that used a 2:1 iron(III) to cobalt(II) ratio were repeated under nitrogen as these products initially contained the greatest amount of hematite. The two different anions were again used to determine if the atmosphere had influenced the behaviour of the nitrate anion. The divalent iron solid state reactions were already completed under nitrogen therefore this experiment could not be applied to this system.

The most decisive results under the nitrogen atmosphere were seen for the chloride anion and are shown in Figure 56. In this case, the use of 600˚C still produced hematite as the sole product. At elevated temperatures, there were significant differences as Mullite recrystallized from the amorphous silica phase. This had previously only been seen in the iron(II)-iron(III) system. At even higher temperatures, the hematite phase was considerably reduced with the magnetic spinel becoming the dominant phase.

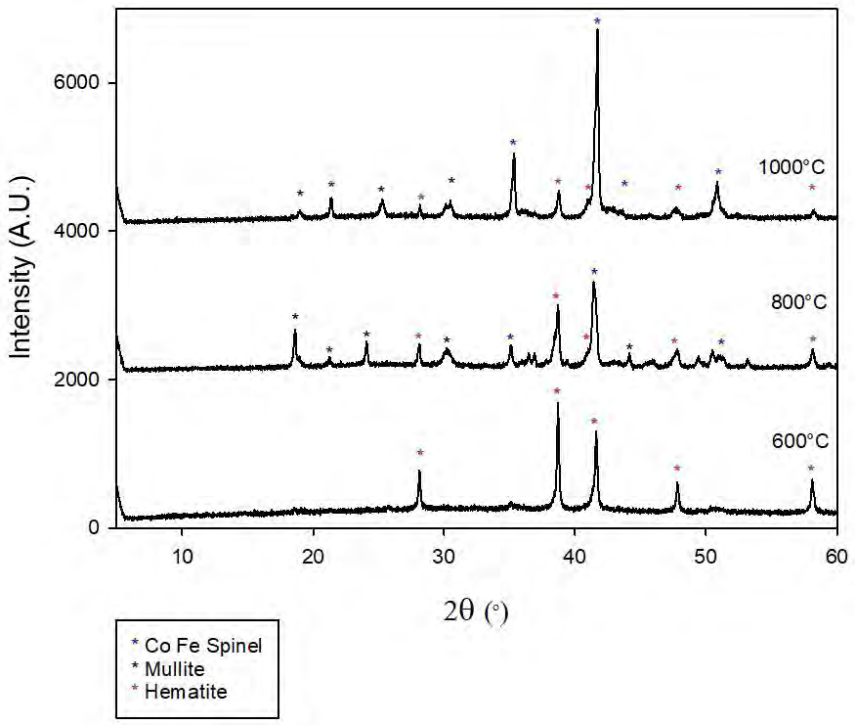


Figure 56 XRD patterns of cobalt(II)-A and iron(III) chloride in a 2:1(Fe^{3+}:Co^{2+}) ratio heated at different temperatures under a nitrogen atmosphere.

The weight fractions of the hematite and cobalt spinel were calculated for all the different synthesis conditions outlined at the beginning of the chapter to allow for complete analysis. The results of these calculations, Figure 57, showed that as the synthesis temperature and salt ratio were increased, the hematite content was significantly reduced while the cobalt spinel content increased. This suggested that increasing the temperature does allow for superior mixing as was proposed earlier,

whilst the nitrogen atmosphere prevented oxidation hereby minimising hematite formation. As for the salt ratio changes, it is proposed that the formation of hematite occurs due to a lack of divalent cobalt and is therefore unable to form cobalt spinel. The calculated cobalt content of the zeolite is determined by XRF analysis and there is approximately a 10% error associated with this measurement. Therefore, by applying the stoichiometric amount of trivalent iron based upon these approximations there could be an excess of iron that then generates additional hematite. Figure 57 also showed that the higher temperatures were needed to create the greatest amount of cobalt spinel and that the salt ratio used also had a significant effect. Therefore 1000˚C will be used to create all the magnetic materials from this point onwards.

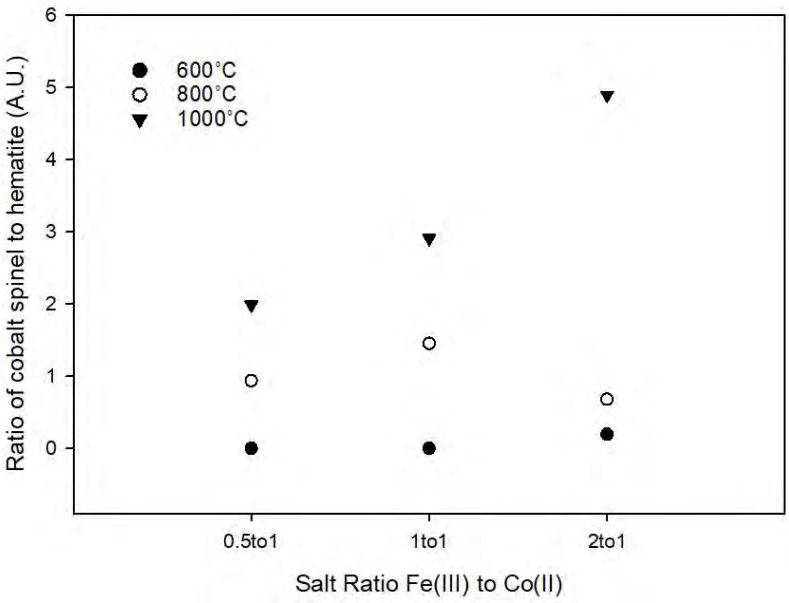


Figure 57 The effect of temperature and salt ratio on phase formation displayed as a ratio of cobalt spinel to hematite. Black circles represent a synthesis temperature of 600˚C, white circles 800˚C and black triangles 1000˚C.

There were also differences when iron(III) nitrate was used under a nitrogen-rich atmosphere. Crystallinity increased, with an order of magnitude increase in peak intensities, while peak broadening was reduced suggesting an increase in particle size. There was a change in background noise to signal ratio and a change in relative intensities between the two phases with the cobalt spinel becoming more pronounced.

A Nd bar magnet was used to visually compare the magnetic strength of the products of the different anions. Critically the nitrate sample appeared magnetically weaker than the iron(III) chloride samples made under air and nitrogen. When comparing the magnetic strength of the chloride anion, it could be seen the sample formed under nitrogen had a significantly stronger response than that of the sample made under air. Therefore, based upon this observation and the nitrogen atmosphere reducing the hematite content, the optimised solid state reactions would use a chloride salt under a nitrogen atmosphere in a 2:1 ratio of iron(III) to exchanged zeolite.

4.4. Analysis and identification of the magnetic phase

Section 4.3. showed how the hematite impurity had been minimised, however, the identity of the magnetic phase remained unknown. When using X-ray radiation, the resultant diffraction patterns of γ-Fe_2O_3 (hematite) and $CoFe_2O_4$ are nearly identical and therefore this was not suitable for phase determination. In this instance, Raman spectroscopy was employed as γ-Fe_2O_3 and $CoFe_2O_4$ have different vibrational modes.

4.4.1. Identification of the magnetic spinel in the cobalt(II) system

Before collecting Raman spectroscopic data these samples were analysed using an SEM with EDX capabilities. The high-resolution SEM images are shown in Figure 58 and Figure 59. SEM/EDX is similar to Raman in the fact that they are both surface-based techniques with limited penetration depths. SEM images showed small high contrast particles on a lower contrast Si/Al matrix. EDX analysis of these smaller particles confirmed the presence of Fe and Co. Several spots were analysed on the same crystal as well as across different particles to highlight if any regions were deficient in certain elements. Each spot confirmed that cobalt resided alongside iron. This suggested that $CoFe_2O_4$ was likely to be the magnetic product. SEM also confirmed the distribution across a range of larger particles. However, it was unknown if the smaller matrix particles also contained spinel. To explore this STEM was used.

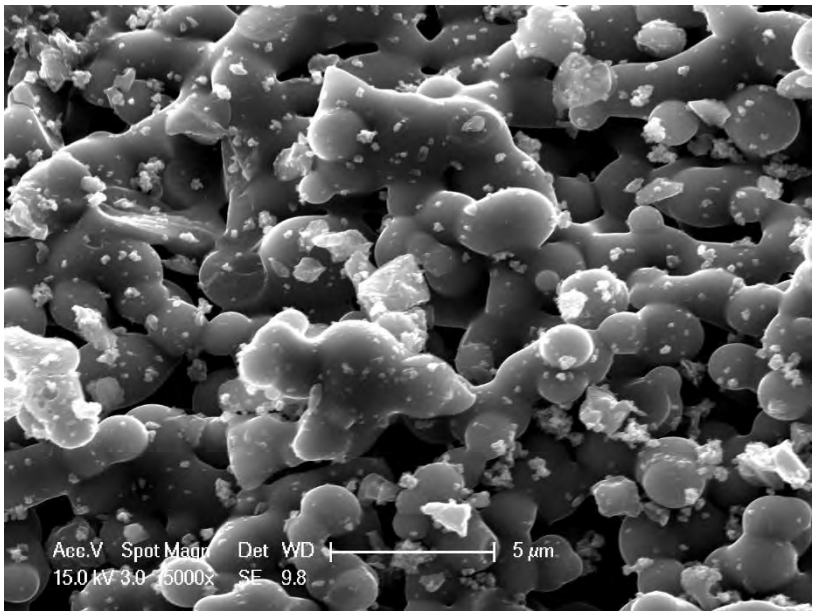


Figure 58 High resolution SEM image of Co-A post synthesis with iron(III) chloride.

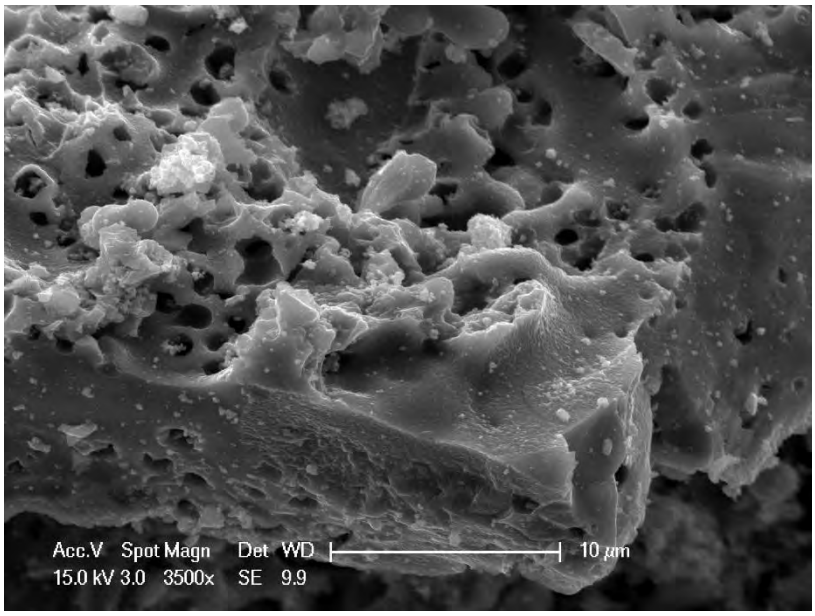


Figure 59 High resolution SEM image of Co-A post synthesis which depicts the aggregation of the magnetic particles within the recrystalised zeolite matrix.

Due to the difference in sample preparation to SEM, STEM allows very small particles to be observed and analysed. Figure 60 contains the STEM image of a cobalt(II)-iron(III) matrix and corresponding elemental images. The image at the top left of Figure 60 is a STEM image of a single matrix particle that has regions of higher and lower contrast. The image contains two highlighted boxes, one is the area of interest over which the elemental mapping with be collected. The second is for spatial drift which was required due to the high magnification used. This box covers a larger area to act as a reference, a scan of this region taken periodically. The remaining images in Figure 60 are of element maps. The bottom images are related to iron and cobalt, this graphically confirms that iron and cobalt reside beside one another. The silicon and aluminium images show differences in their levels of shading over region the spinel is. The dark regions show areas of deficiency which suggests that spinel particles are

embedded as well as on the surface. The oxygen distribution appears uniform across the surface.

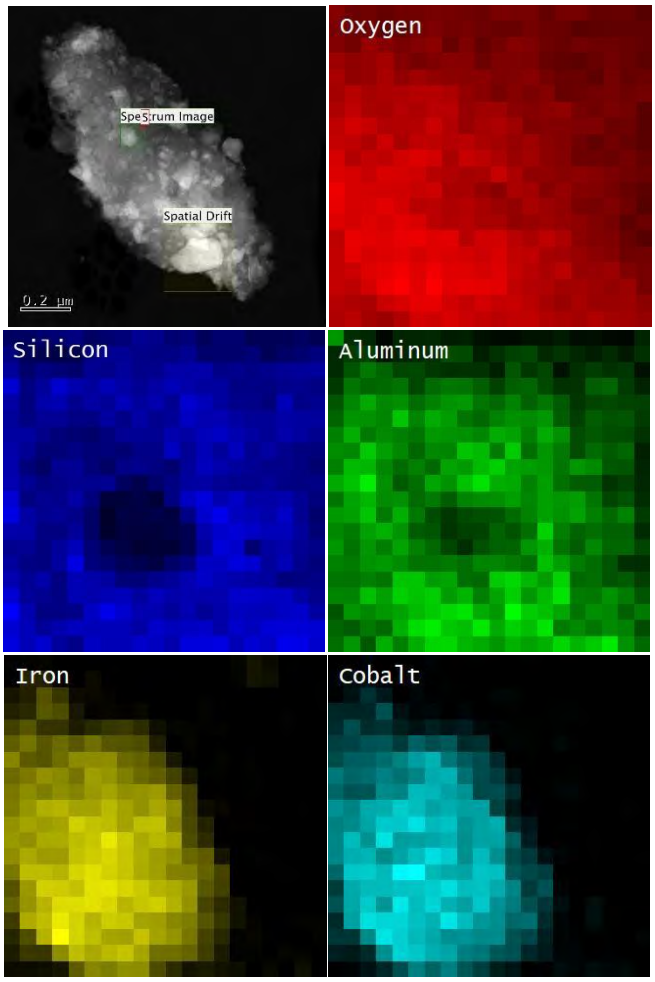


Figure 60 STEM image of cobalt(II)-iron(III) matrix made at 1000˚C using cobalt(II)-A and iron(III) chloride. The elemental mapping area highlighted. Elemental Mapping images collected over the highlighted area.

As electron microscopy had shown some of the magnetic oxide particles were trapped within the glassy matrix, it was not possible to obtain accurate size distributions. Obtaining size distributions from the particles on the surface was also not possible as matrix particles aggregated due to the nature of the synthesis as shown in Figure 59.

An alternative method was to use the Scherrer equation, the basis being that the width of a powder X-ray diffraction reflection relates to the coherent diffraction domain size. An important distinction is that this dimension is perpendicular to the diffraction plane being analysed and also it is the coherent diffraction domain size that is being estimated, rather than crystallite size.[17] Although this method does have its limitations it still can give a useful approximation. Upon applying it to one of the cobalt systems, hematite averaged a domain size of 65 nm and the spinel 59 nm. By using this estimation in conjunction with the magnetic behaviour can provide a reasonably reliable size approximation.

After electron microscopy had confirmed the whole sample contained regions of interest, the cobalt samples were analysed by Raman spectroscopy. The XRD patterns in section 4.3. (Figure 56) showed that there were three phases present: mullite, hematite and the unidentified magnetic phase. The Raman transition for each of the possible phases is shown in Table 16.

Table 16 Raman activities of the possible phases present in the cobalt(II)-iron(III) matrix.

Phase	Number of active modes	Wavenumber (cm^{-1})
Mullite	8	310, 410, 610, 710, 880, 960, 1040 and 1160 [18]
Hematite	6	225, 247, 299, 412, 497 and 619 [19,20]
Maghemite	3	350, 500 and 700 [19,20]
$CoFe_2O_4$	5	210, 310, 474, 616 and 694 [21]

The Raman spectrum collected on the cobalt(II)-iron(III) system is presented in Figure 61. The peaks at 202, 387, 503 and a broad peak from 610 to 790 cm^{-1} (centred at 736) appear in a similar region to the expected peaks of $CoFe_2O_4$.[21] However, upon comparing this pattern to pure powder of $CoFe_2O_4$, Figure 61 is slightly different. This suggested it was not $CoFe_2O_4$ or that there was small particles of the spinel which is affecting the spectrum collected, thus appearing different to a pure powder.[22]

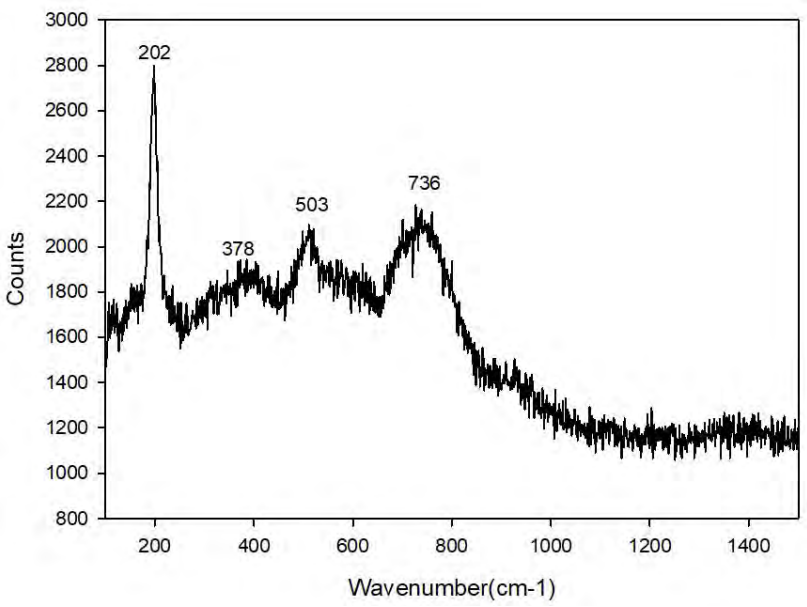


Figure 61 Raman spectrum of the glassy matrix material produced by heating cobalt(II) zeolite A with iron(III) chloride in a 2:1 (iron:cobalt) ratio at 1000˚C under nitrogen.

As Raman spectroscopy had given no further indication of the identity of the magnetic component, Mössbauer spectroscopy was required to probe the coordination environments of iron. This will be explored later in this chapter.

4.4.2. Identification of the magnetic spinel in the iron(II) system

Analysis of the XRD patterns for the iron(II)-iron(III) system suggested the formation of magnetite (Fe_3O_4), however, similarly to cobalt ferrite, magnetite is also difficult to distinguish from maghemite. However, there are several methods for distinguishing between iron oxides. Each of the iron oxides has a unique Raman and Mössbauer spectrum. As both spinel-related oxides are magnetic, a comparison of their magnetic behaviour is another possible way to distinguish between them. Magnetite exhibits superparamagnetism if the particle size is between 3-50nm whereas maghemite (γ-Fe_2O_3) is ferromagnetic unless the particle size is <10nm, then it is also superparamagnetic.[23]

SEM/EDX analysis cannot be applied to the iron(II)-iron(III) system due to EDX being unable to account for charge differences, as the energy emitted is characteristic of iron independent of charge. However, SEM and STEM was able to confirm the distribution of iron throughout the matrix via elemental mapping similar to that presented for the cobalt(II)-iron(III) system.

To investigate the sample further Raman spectroscopy was used, active transitions for the possible products outlined previously is given in Table 17.

Table 17 Raman activities of the possible phases present in the iron(II) iron(III) matrix.

Phase	Number of active modes	Wavenumber (cm^{-1})
Hematite	6	225, 247, 299, 412, 497 and 619 [19] [20]
Maghemite	3	350, 500 and 700 [19,20]
Magnetite	5 (only 4 visible)	193, 306, 538 and 668 [19,20]
FeO(OH)	5	245, 373, 522, 713 and 1303 [19,20]
FeO (Metastable below 570˚C – decomposes into hematite and magnetite)	N/A	N/A (Shows as hematite as the laser converts the magnetite)

As shown in Figure 62, the Raman spectrum matches only to that expected from hematite. However, the XRD patterns confirm an additional phase is also present. Although a second phase could not be detected by Raman spectroscopy, this could be plausibly explained. It is highly likely the iron on the surface layer will have oxidized into hematite with the magnetic phases being trapped within the bulk. As Raman spectroscopy is a surface-sensitive technique the laser may not penetrate to a sufficient depth to detect the second phase. Furthermore, if hematite were to be the only phase, it would not explain how the sample was strongly magnetic.

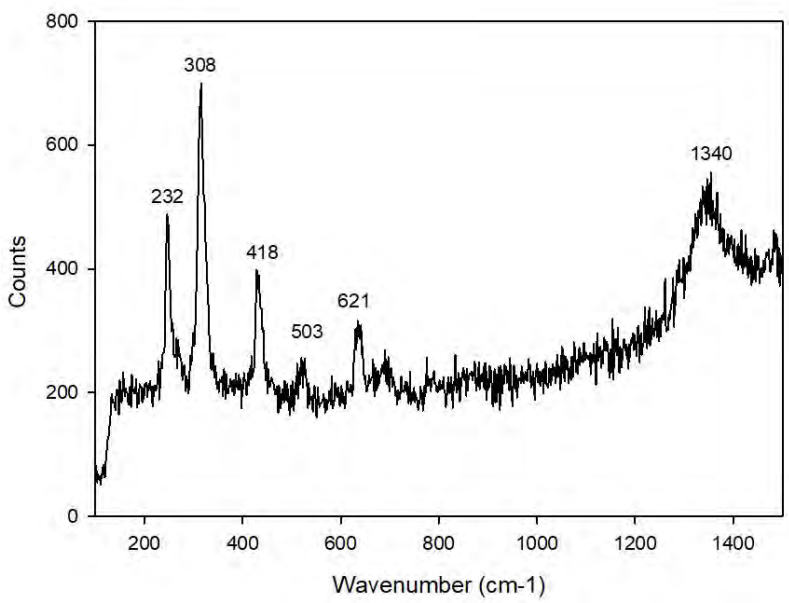


Figure 62 Raman spectrum of a Fe^{3+}/Fe^{2+} sample made using iron(III) chloride and iron(II) zeolite A in a 2:1 (Fe^{3+}:Fe^{2+}) ratio, heated to a 1000˚C in a nitrogen atmosphere.

As Raman spectroscopy had been unsuccessful in magnetic phase identification, ^{57}Fe Mössbauer spectroscopy was used instead. It is more sensitive than XRD to identify these magnetically ordered phases due to the difference in magnitude of the magnetic hyperfine fields of magnetite, maghemite and $CoFe_2O_4$. Mössbauer spectroscopy also

removes the surface limitations of Raman spectroscopy as it probes the bulk of the sample.

The ^{57}Fe Mössbauer spectrum in Figure 63 is from the 2:1 iron(III) chloride with iron(II) exchanged zeolite A which had been heated to 1000˚C. The ^{57}Fe Mössbauer parameters are collected in Table 18. The spectrum was best fitted to four components. The small doublet (δ = 0.26 mms^{-1}, $e^2qQ/2$ = 0.94 mms^{-1}) can be assigned to low-coordinate Fe^{3+}.[24] The sextet with the large magnetic hyperfine splitting (H= 51.5 T) is characteristic of hematite (α-Fe_2O_3) whereas the two sextets with H= 49.3 T and 45.8 T are characteristic of magnetite (Fe_3O_4).[25] Therefore, the magnetic phase was confirmed to be the magnetite which was the phase initially targeted.

Table 18 ^{57}Fe Mössbauer parameters recorded at 298 K from iron(II) zeolite A thermally decomposed at 1000˚C in a 1:2 ratio with iron(III) chloride.

	δ ± 0.02(mms^{-1})	**$e^2qQ/2$ ± 0.04(mms-^{1})**	**H ±0.05 (T)**	**Area ±3 (%)**
Low coordinate Fe^{3+}	0.26	0.94		5
α-Fe_2O_3	0.37	-0.10	51.5	50
Fe_3O_4	0.33	-0.06	49.3	21
	0.65	0.01	45.8	24

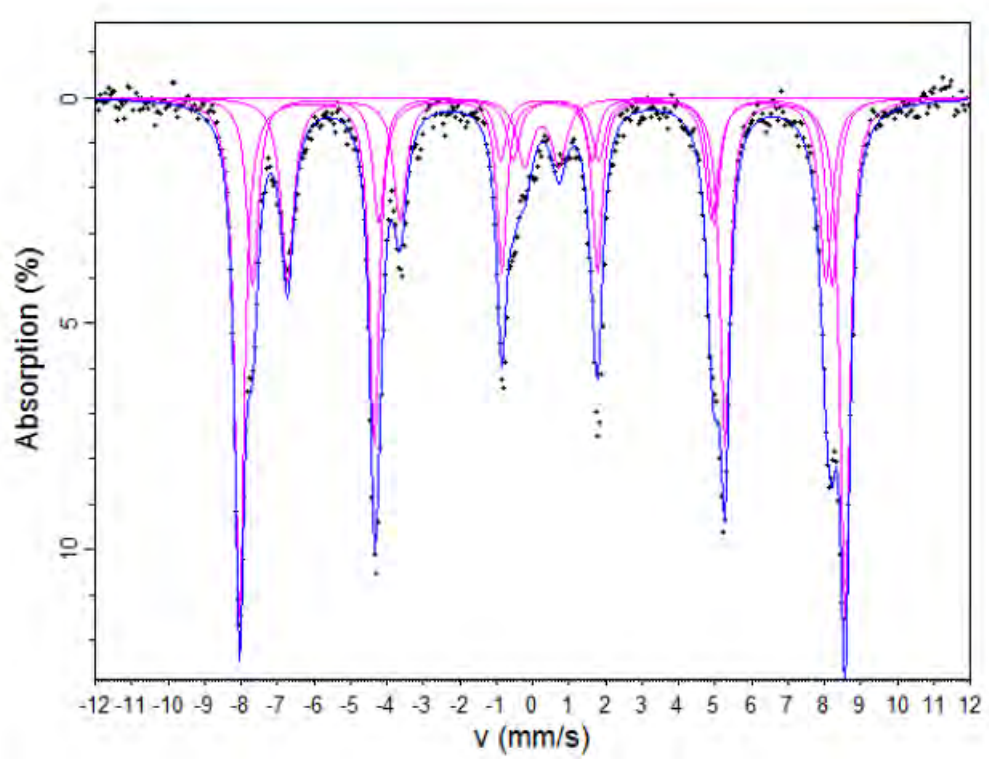


Figure 63 ^{57}Fe Mössbauer spectrum recorded at 298 K from iron(II) zeolite A thermally decomposed in a 1:2 molar ratio with iron(III) chloride at 1000˚C.

After successfully confirming the identity of the magnetic component in the iron(II)-iron(III) samples, Mössbauer analysis was then completed on the cobalt iron system. The ^{57}Fe Mössbauer spectrum recorded from the 2:1 hydrated iron(III) chloride with cobalt (II) exchanged zeolite A which had been heated to 1000˚C is shown in Figure 64 and the ^{57}Fe Mössbauer parameters are collected in Table 19. The spectrum was best fitted to four components. The small doublet (δ = 0.31 mms^{-1}, $e^2qQ/2$ = 0.92 mms^{-1}) can be assigned to low-coordinate Fe^{3+}.[24] The sextet with the large magnetic hyperfine splitting (H= 51.2 T) is characteristic of hematite (α-Fe_2O_3),[25] Whereas the two sextets with H= 49.0 T and 46.5 T can be assigned to cobalt ferrite.[26] These values are closely related to magnetite, however, due to the absence of divalent iron, it is reasonable to assume that this is cobalt ferrite. To resolve the spectrum further low temperature (5K) measurements would be required.

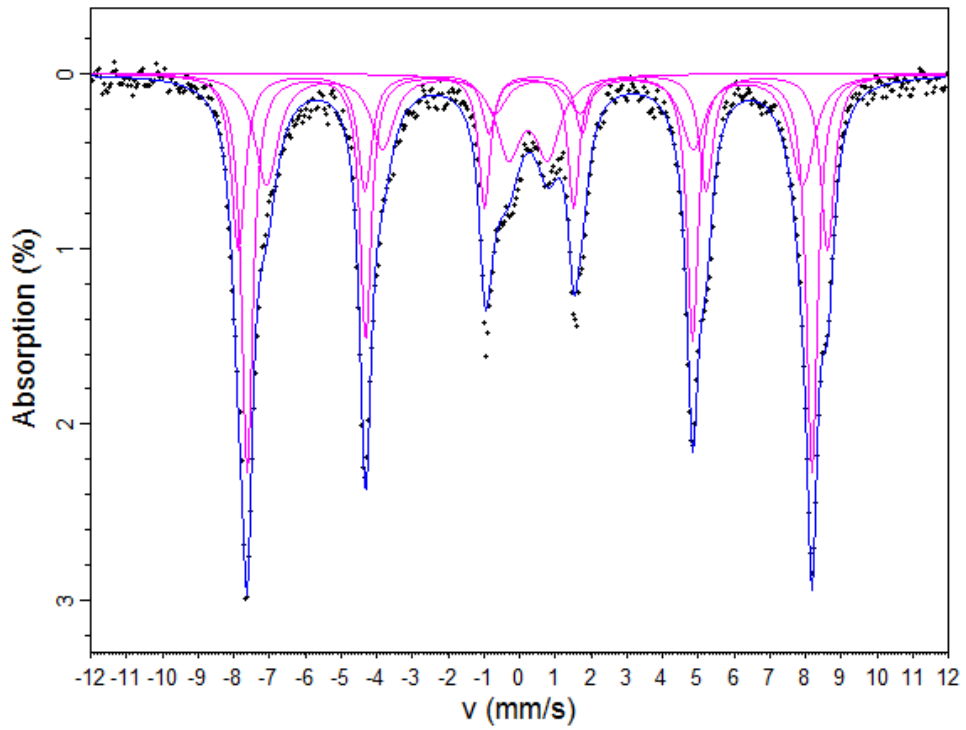


Figure 64 ^{57}Fe Mössbauer spectrum recorded at 298 K from Co(II) zeolite A thermally decomposed at 1000˚C in a 1:2 molar ratio with iron(III) chloride.

Table 19 ^{57}Fe Mössbauer parameters recorded at 298 K from Co(II) zeolite A thermally decomposed at 1000˚C in a 1:2 ratio with iron(III) chloride.

	δ± 0.02(mms^{-1})	**e^{2}qQ/2 ± 0.04(mms-^{1})**	**H ±0.05 (T)**	**Area ±3 (%)**
Low coordinate Fe^{3+}	0.24	1.093		9
α-Fe$_2$O$_3$	0.42	-0.03	51.2	23
CoFe$_2$O$_4$	0.27	0.01	49.0	43
	0.47	-0.05	46.5	25

4.2.3. Confirmation of the identity of magnetic phases

Using a combination of XRD, SEM, STEM, EDX, Raman and Mössbauer spectroscopy has allowed for full characterisation to determine the magnetic component within the matrix of both systems presented. As the characterisation confirmed the target structures of $CoFe_2O_4$ and magnetite had been successfully synthesized, this synthesis method could then be applied to the remaining transition metal exchanged forms of zeolite A synthesised in chapter 3. However, the reaction pathway was unknown. To help develop further understanding VT-XRD (performed under a N_2 atmosphere) was completed in conjunction with TGA/DTA to highlight regions of high interest.

4.2.4. Variable temperature XRD

The TGA/DTA curves in Figure 65 contain four regions of interest at approximately 200, 400, 600 and 850˚C. At 200˚C there is a loss of around 20% mass which was confirmed to be water by the mass-spectrometer. The region at 400˚C did not have an accompanying mass loss, therefore, is suspected to be the formation of hematite. The two remaining phase changes are thought to be formation of the breakdown of the zeolite structure followed by the formation of magnetic spinel.

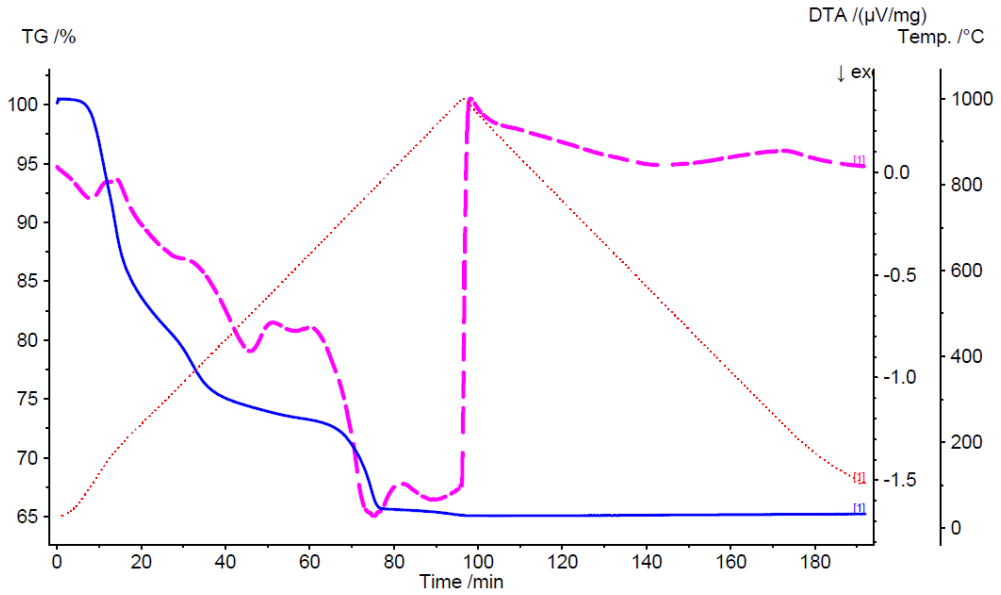


Figure 65 TGA/DTA curves of a matrix synthesis. The blue curve relates to TG% (mass loss), the purple to DTA and red corresponds to temperature.

To investigate all three of the regions highlighted by the TGA/DTA, a heating programme from 250 to 950˚C was used on the VT-XRD. The heating program ramped in 1˚C increments and held the temperature for 60 seconds before collecting diffraction data every 25˚C. This diffractometer used copper $K_{\alpha1}$ and $K_{\alpha2}$ radiation (I = 1.5406 Å and 1.5444 Å), preliminary XRD data found a 30-minute collection time sufficient for

phase detection with only a small amount of fluorescence. The 2θ range was reduced from 10-60˚ to 17-43˚ to keep the collection time as small as possible to capture the phase changes as they happened. The synthesis investigated here used Mn(II) exchanged zeolite A and iron(III) chloride. The results of the VT-XRD are shown in Figure 66.

The range of temperatures from the experiment carried out in Figure 66 ranged from 250˚C to 950˚C. However, the range in the figure is reduced from 350 to 500˚C as no peaks were seen before 350˚C and no further changes were observed in the pattern after 500˚C. The pattern at 25˚C has been included to show how the zeolite initially appeared on this diffractometer. Copper radiation was used to collect this pattern therefore the peaks will be shifted down in 2θ relative to what has been shown in the previous XRD patterns. As copper Kα radiation has a shorter wavelength than that of cobalt Kα, the reflections are shifted to a lower 2θ values.

Analysis of the XRD patterns indicated a small amount of magnetic spinel formed with the only visible peak shown with a blue asterisk. The other peaks associated with this phase would be at 18.2˚, 30.1˚ and a small peak at 37.1˚ which can be seen as a slight shoulder on the peak at 35.6˚. The peaks denoted in red are those associated with hematite and these peaks are significantly more intense. This is likely to be due to the sample holder which is made of Al_2O_3. The holder has the same space group as hematite and will therefore have reflections appear in the same 2θ position, therefore, increasing the intensity of those peaks. As the sample heats, the sample begins to constrict, this exposes the outer regions of the sample holder. As the temperature

increases so does the amount of holder exposure which in turn increases the intensity of the peaks as shown in Figure 66.

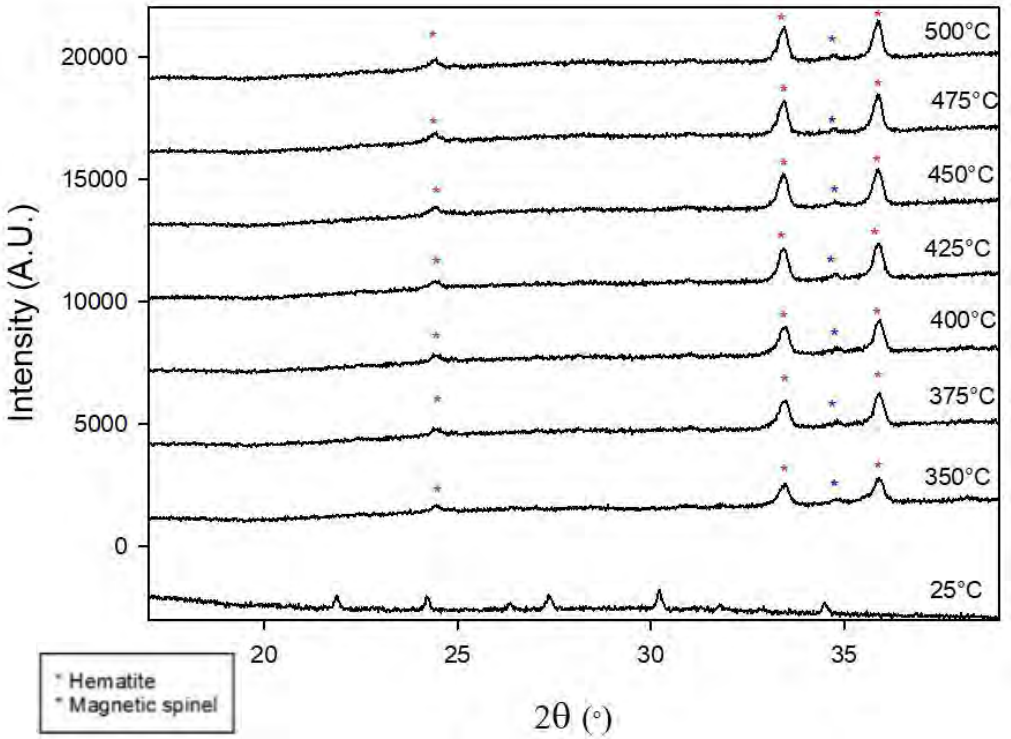


Figure 66 VT-XRD scans from the 250˚C to 950˚C experiment. The temperature range shown is 350 to 500˚C as this contained the areas on interest. The Mn(II)-A and iron(III) chloride system was used in this experiment.

The experiments ran in Figure 66 did not capture any phase changes possibly due to the range used being too large. Instead, diffraction was collected over a narrower range of 300˚C to 600˚C with data collected every 25˚C and instead used a 15-minute scan time. An additional experiment ran from 750˚C to 875˚C as it was suspected that the slow ramp to higher temperatures was favouring the formation of hematite due to poor mixing seen at the lower temperatures. The results of the two experiments are shown in Figure 67 and Figure 68 respectively. Neither Figure 67 nor Figure 68 was able to capture the phase change. However, it did suggest that the use of the lower temperatures and thus slower ramp to the higher temperatures was favouring hematite formation as Figure 68 had less hematite present than Figure 67. The peaks without

an asterisk in Figure 67 are reflections produced by α-cristobalite. The set of experiments carried out suggested that the current setup was unable to capture the data fast enough to be able to track the phase formation. To be able to view this behaviour would require synchrotron radiation however, this was not possible due to the high temperatures required.

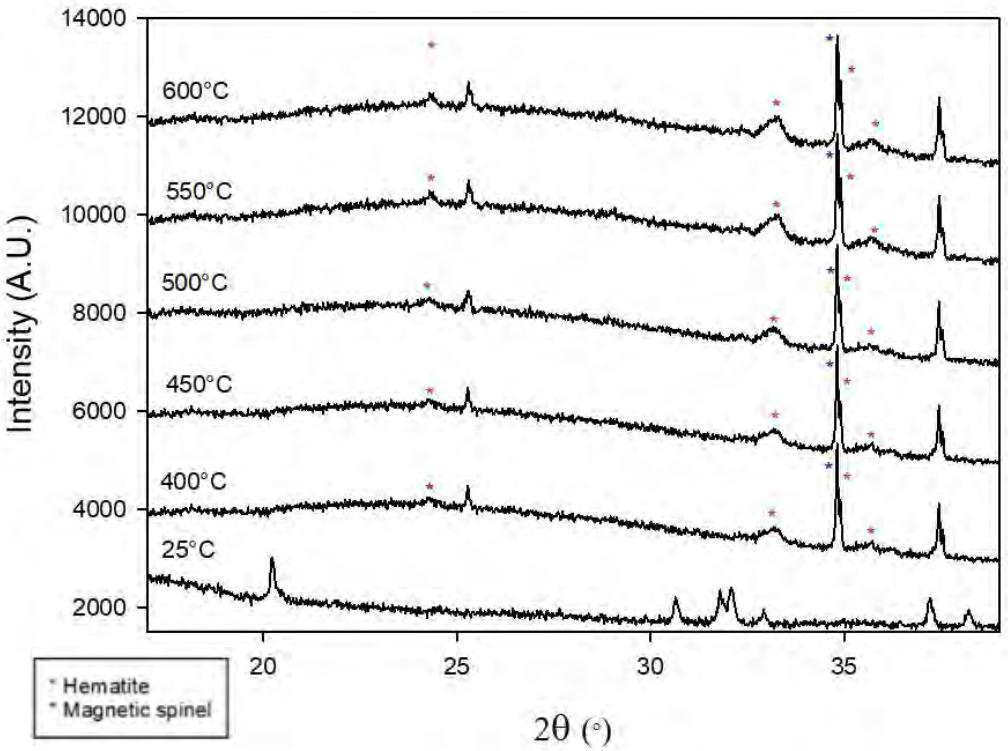


Figure 67 VT-XRD scans from the 400˚C to 600˚C experiment. The Mn(II)-A and iron(III) chloride system was used in this experiment.

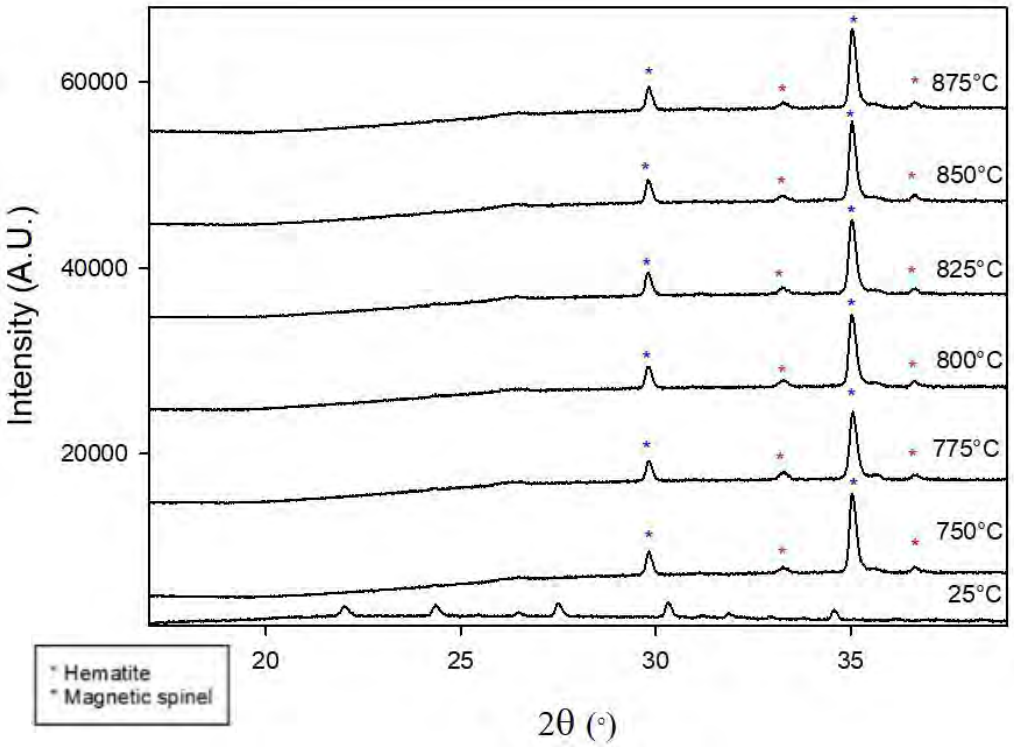


Figure 68 VT-XRD scans from the 750˚C to 875˚C experiment. The Mn(II)-A and iron(III) chloride system was used in this experiment.

4.5. Production of magnetic materials using transition metal exchanged zeolite A

As the method developed was found to create the desired product, it was applied to the remaining exchanged zeolites; manganese, nickel and zinc. These reactions were all completed using the ratios outlined in the introduction but conducted under the optimised conditions determined in section 4.3. However, only the samples made using a synthesis temperature of 1000˚C will be discussed throughout this section as using a synthesis temperature of 600˚C or 800˚C produced samples that had greater amounts of hematite impurities and therefore would have a weaker magnetic moment as had been shown previously by the weight fractions in Figure 57.

4.5.1 Manganese(II) exchanged zeolite A

Figure 69 contains the manganese(II)-A XRD patterns following the incorporation of iron(III). This indicates that when a higher salt ratio is used it favours the formation of the superparamagnetic phase ($MnFe_2O_4$) with a very small amount of hematite. This was confirmed by the manganese spinel to hematite ratios obtained from the weight fractions starting at 1.92 suggesting nearly twice as much spinel was present compared to hematite. Increasing the salt ratio to 1:1 and 2:1 increased manganese spinel to hematite ratios to 15.02 and 21.07, respectively. Although Mössbauer spectroscopy was not carried out on this material, it is reasonable to assume that the magnetic product is manganese ferrite, as this synthesis is following the procedure that was confirmed to have created cobalt ferrite and magnetite. Therefore, the optimised

conditions for synthesising manganese ferrite is a 2:1 iron(III):manganese(II) at 1000˚C under N_2.

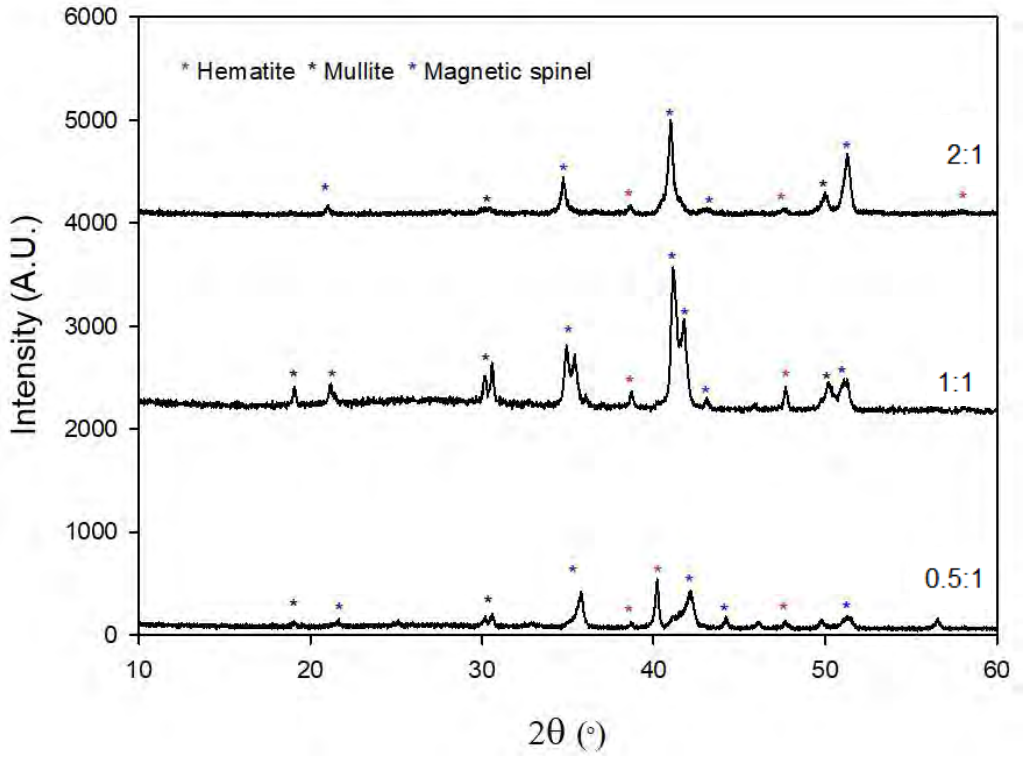


Figure 69 XRD patterns of manganese(II)-A and iron(III) chloride in a 2:1(Fe^{3+}:Mn^{2+}) ratio heated at 1000˚C under a nitrogen atmosphere.

4.5.2. Nickel(II) exchanged zeolite A

Figure 70 contains the results of the incorporation of iron(III) in nickel(II)-A. The XRD patterns showed that the 2:1 salt ratio produced the most crystalline material. However, in this scenario, it did also appear to contain the most hematite, even under a nitrogen atmosphere. This was confirmed by the weight fractions with the 2:1 sample containing 55% hematite and only 33% nickel ferrite. The 0.5:1 and 1:1 contained the same amount of nickel ferrite at 47% and varied in hematite content at 26 and 39% respectively. It must be noted that during the synthesis of these materials, there was a

suspected hairline crack in the alumina tube itself. This might therefore explain why the hematite content is above that expected from previous experiments. Therefore, these samples were remade in several furnaces prior to collection of the magnetic data. It is reasonable to assume that the magnetic product is nickel ferrite for the reasons given previously. Due to the possible leak in the alumina tube, there was no obvious optimal conditions. The only way to determine the best product is via their magnetic moment, this will be discussed in section 4.6.

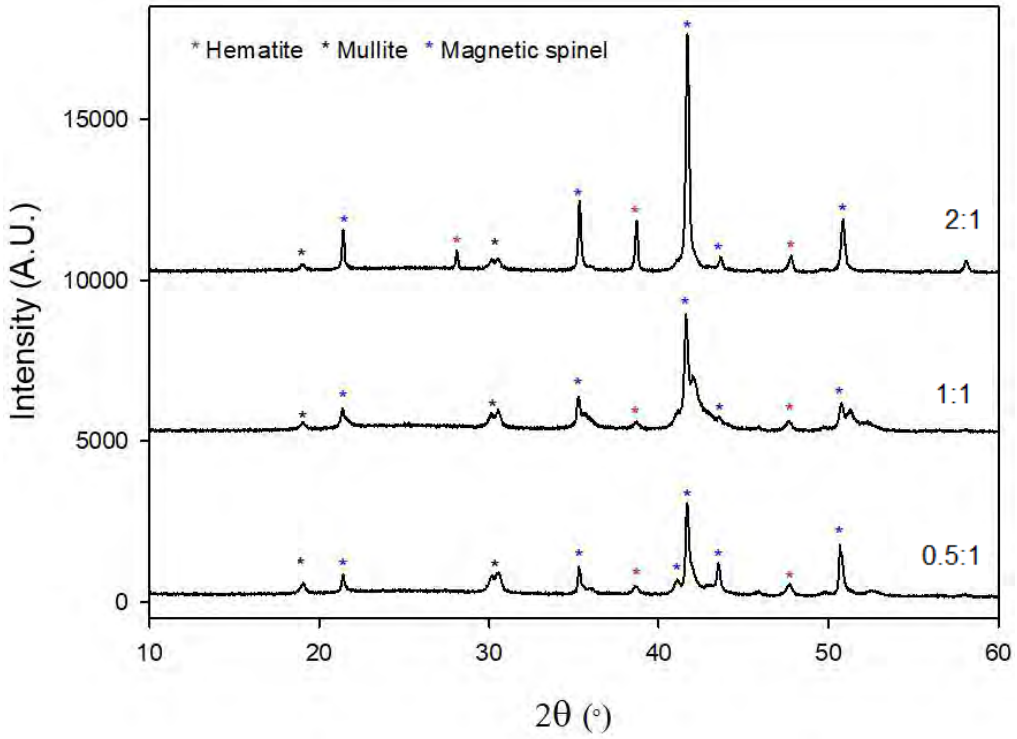


Figure 70 XRD patterns of nickel(II)-A and iron(III) chloride in a 2:1(Fe^{3+}:Ni^{2+}) ratio heated at 1000˚C under a nitrogen atmosphere.

4.5.3. Zinc(II) exchanged zeolite A

The zinc(II)-A XRD patterns presented in Figure 71 display noticeable differences to what has been presented previously for the other divalent metals. The 0.5:1 ratio had the highest zinc ferrite to hematite ratio at 2.02 which reduced to 1.38 and 0.074 for 1:1 and 2:1 respectively. When a 2:1 ratio was used hematite was still the dominant phase, this had not been observed in the other systems. This was thought to have happened due to the amount of zinc determined by XRF being incorrect. This difference is presumed to have arisen due to errors associated with measuring zinc content using XRF when sodium is present as described previously. Therefore, it would be reasonable to assume that the zinc content has been overestimated, thus creating hematite in regions that were zinc deficient. Due to this complication in the absence of an ICP-MS/OES or flame photometry it was not possible to obtain reliable information regarding zinc content therefore no further optimisation was attempted at this time. The magnetic moments of these samples would still be measured.

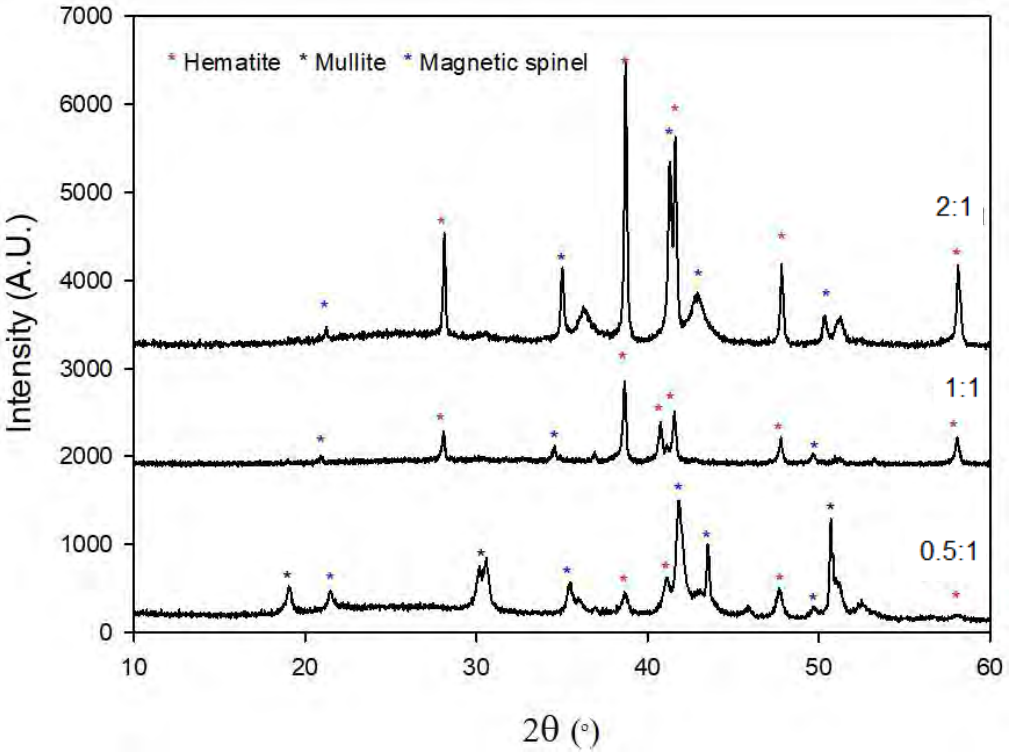


Figure 71 XRD patterns of zinc(II)-A and iron(III) chloride in a 2:1(Fe^{3+}:Zn^{2+}) ratio heated at 1000˚C under a nitrogen atmosphere.

4.6. Magnetic behaviour of the matrix materials

Vibrating sample magnetometer (VSM) measurements were used to compare the magnetic behaviour of the materials developed in sections 4.2., 4.3. and 4.5. A VSM curve provides four important pieces of information relating to the sample; magnetic saturation, residual magnetism, coercivity and the presence of a hysteresis loop. An example of these is shown in Figure 72. Magnetisation saturation is the point at which the magnetisation or the magnetic moment is at its greatest (**A** or **D**). Residual magnetism is the point at which the curve passes through the Y-axis (**B** or **E**). Coercivity is the point of intercept on the X-axis (**C** or **F**). This is a measure of a ferromagnetic samples ability to withstand an external magnetic field without becoming demagnetized. The presence and shape of a hysteresis loop (**blue curve**). The absence of a hysteresis loop is indicative of superparamagnetic materials and is therefore the most common method for confirming this type of magnetic behaviour. If a hysteresis loop is present the width of the loop provides a value for the coercive force. This value determines if the material is classified as a hard or soft magnet.

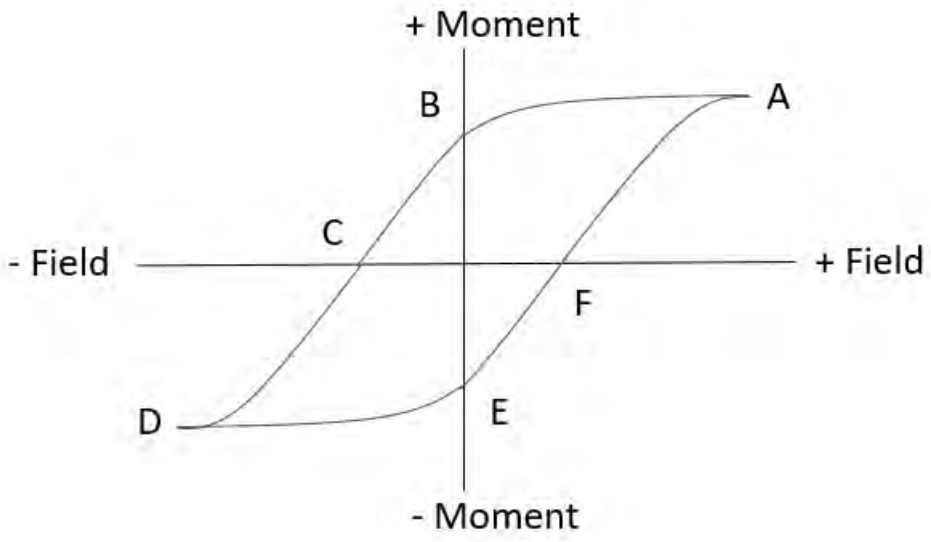


Figure 72 Example VSM curve

Three out of the four parameters are important when determining superparamagnetism. For a material to be superparamagnetic residual magnetism and coercivity values should be zero, therefore, the curve intercepts both axis at the origin. By intercepting at the origin, a hysteresis loop cannot exist here by satisfying the requirements to be superparamagnetic. Although, a specific magnetic saturation value is not required to be deemed superparamagnetic it can be of great importance depending on the application, i.e. the greater the magnetic saturation the easier magnetic separation would be under dynamic conditions.

In section 4.2.4 (the iron(II)-iron(III) system), Figure 55, showed that at elevated synthesis temperature the same phases were produced. Therefore, this set of materials were used to investigate the effect synthesis temperature had on the overall magnetism (the amount of the metal content is accounted for).

4.6.1. Iron(II)-iron(III) matrix materials

Figure 73 contains the magnetic responses of the products from the iron(II)-A 2:1 ratio series when using iron(III) chloride at 800 and 1000˚C. Neither of the samples display a hysteresis curve and both curves intercept the x-axis at zero, which allows these materials to be classed as superparamagnetic. This is consistent with the presence of magnetite nanoparticles as found in the splitting in the Mössbauer spectra. The highest value recorded and therefore the strongest magnetic response was exhibited by the sample made at 1000˚C with a reading of 26.08 (emu/g) compared to the sample made at 800˚C which had a value of 20.07 (emu/g). This suggests that the use of 1000˚C is advantageous in the synthesis of magnetic particles, this was suggested by the XRD patterns and their respective weight fractions.

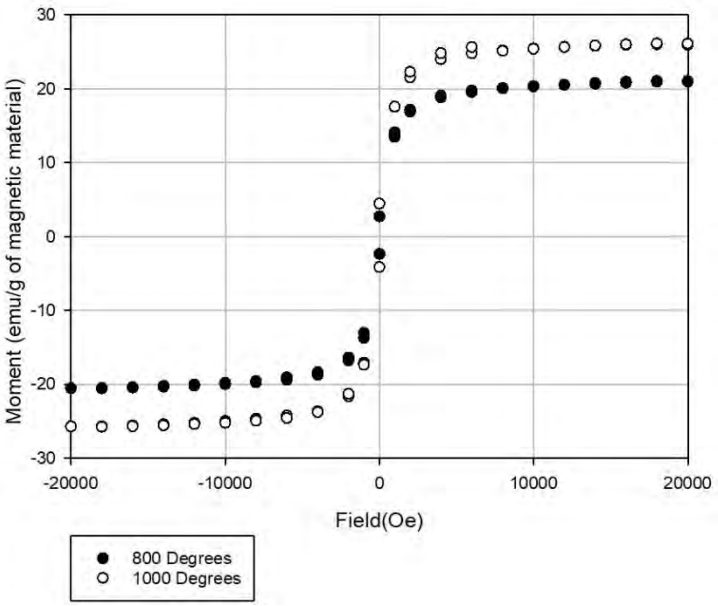


Figure 73 The magnetic responses produced by the magnetic products of the 2:1 iron(III) chloride to Fe (II) zeolite A series. Black circles were from samples heated at 800˚C and the white circles were at 1000˚C.

It was thought that based upon the weight fractions obtained from the GSAS refinements the amount of iron(III) present favoured the formation of the magnetic phases, this, in turn, affects the overall magnetism. This theory was explored further by measuring the moments of the samples which all had a synthesis temperature of 1000˚C and varied only by the amount of iron(III) salt. The results are shown in Figure 74, showing that the magnetic saturation values for the samples in the 1:1 and 0.5:1 series were less than the 26.08 (emu/g of magnetic material) produced using a 2:1 ratio at the same temperature. This was to be expected as greater amounts of magnetite should have formed. It had been proposed that increasing the iron(III) content further could increase the amount of magnetic material if more iron(II) was present than had been detected from the XRF, as a result of errors associated with this method of data collection. However, contrary to this expectation the 3:1 sample registered a moment of 7.98 (emu/g of magnetic material). This suggested there was too much iron(III) compared to the divalent iron, therefore, greater amounts of diamagnetic hematite formed resulting in a significantly weaker product.

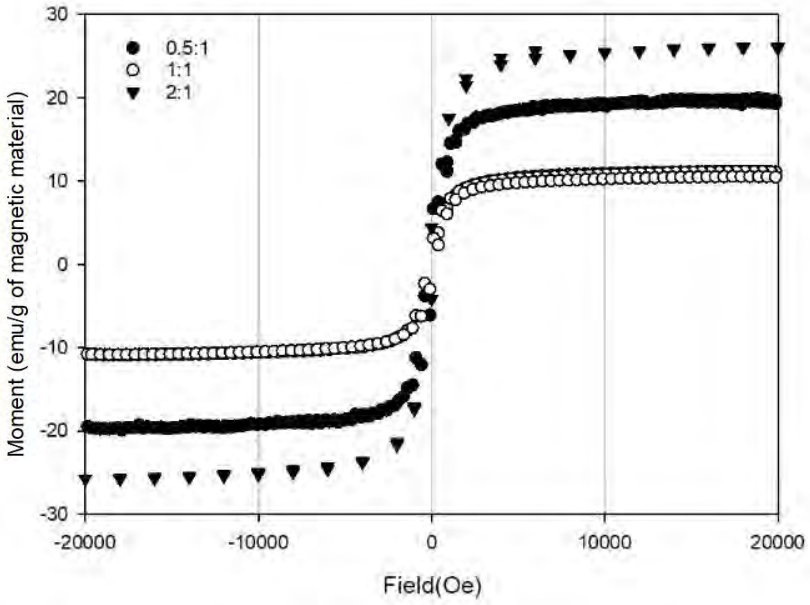


Figure 74 The magnetic responses produced by the occlusion products when using iron(III) chloride to iron(II) zeolite A ratios of 0.5:1,1:1 and 2:1 using a synthesis temperature of 1000˚C. Black circles represent the data from the 0.5:1 ratio, white circles 1:1 and black triangles 2:1

Surprisingly the 0.5:1 produced a greater magnetic moment than the 1:1 at 20.1 compared to 11.38 (emu/g of magnetic material) even though the weight fractions suggested the 1:1 sample had ten times the amount of magnetite compared to the 0.5:1. Critically, all the samples were superparamagnetic with the only difference being the strength of the magnetic moment. Therefore, the 2:1 ratio material was chosen to magnetise zeolite A in chapter 5 as it had the strongest moment. It should be noted that there is a difference in the number of data points in Figure 74 is due to the measurements being collected on two different machines.

After analysing all the VSM data related to all the transition metals and zeolite A it confirmed that using a synthesis temperature of 1000˚C created samples with the greatest magnetic moments per gram of sample. This matched the values obtained for the weight fraction. The un-presented magnetic data for the other synthesis temperatures can be found in a table in the appendix section 4.2.1. If there is no

magnetic data present for a particular sample, it can be assumed that the product was not magnetic.

4.6.2. Cobalt(II)-iron(III) matrix materials

After confirming the presence of cobalt ferrite from Mössbauer spectra, the magnetic responses of the materials made at 0.5:1, 1:1 and 2:1 ratio were collected. The results are presented in Figure 75. Neither the 0.5:1 or 1:1 sample produced a hysteresis curve, however 2:1 did, which implied the sample exhibited a small degree of ferromagnetism. This was to be expected as the use of the Scherrer equation in section 4.3. estimated that the particles were greater than 50nm and it has been reported previously that $CoFe_2O_4$ particles must be <10 nm to be superparamagnetic.[27] Therefore, the sample was deemed to be ferromagnetic and only the 0.5:1 and 1:1 samples were classed as superparamagnetic.

Although there was a small amount of ferromagnetism, the greatest magnetic moment was exhibited by the 2:1 sample at 36.5 emu/g of magnetic material. The 1:1 and 0.5:1 produced significantly lower moments at 18.7 and 16.82 emu/g of magnetic material respectively. As a superparamagnetic product was required for the application therefore to magnetise zeolite A using a cobalt iron system a 1:1 ratio needed to be chosen. Although the moment of the 1:1 sample is relatively weak compared to some of the other systems that will be presented in the thesis, it should still be sufficiently magnetic for the application. Therefore the 1:1 matrix will be used to create new magnetic secondary zeolite as presented in chapter 5.

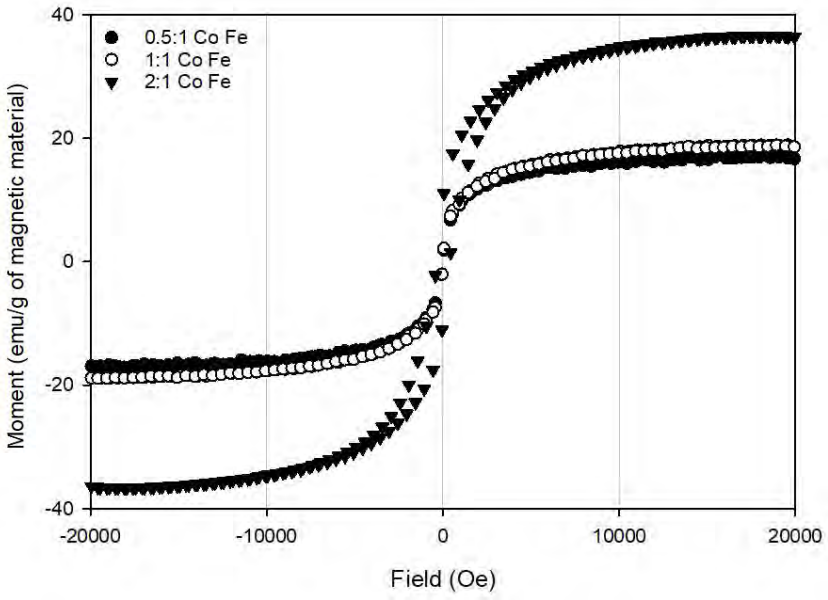


Figure 75 The magnetic responses produced by the occlusion products when using iron(III) chloride to cobalt(II) zeolite A ratios of 0.5:1,1:1 and 2:1 using a synthesis temperature of 1000˚C. Black circles represent the data from the 0.5:1 ratio, white circles 1:1 and black triangles 2:1.

4.6.3. Manganese(II)-iron(III) matrix materials

Figure 76 contains the magnetic response of the materials from the manganese iron series. Conversely to the cobalt iron materials, there was no hysteresis displayed by the 2:1 sample, it also had the greatest magnetic moment out of the samples presented thus far at 65.78 emu/g of magnetic material. Neither 0.5:1 nor 1:1 produced a hysteresis curve, but they did have one of the smallest magnetic moments of any of the zeolite A samples measured at 29.76 and 8.96 emu/g of magnetic material for 1:1 and 0.5:1 respectively. Based upon Figure 76 all samples are classed as superparamagnetic. As the 2:1 ratio had the greatest magnetic moment by a significant margin it was chosen to magnetise a zeolite A in chapter 5.

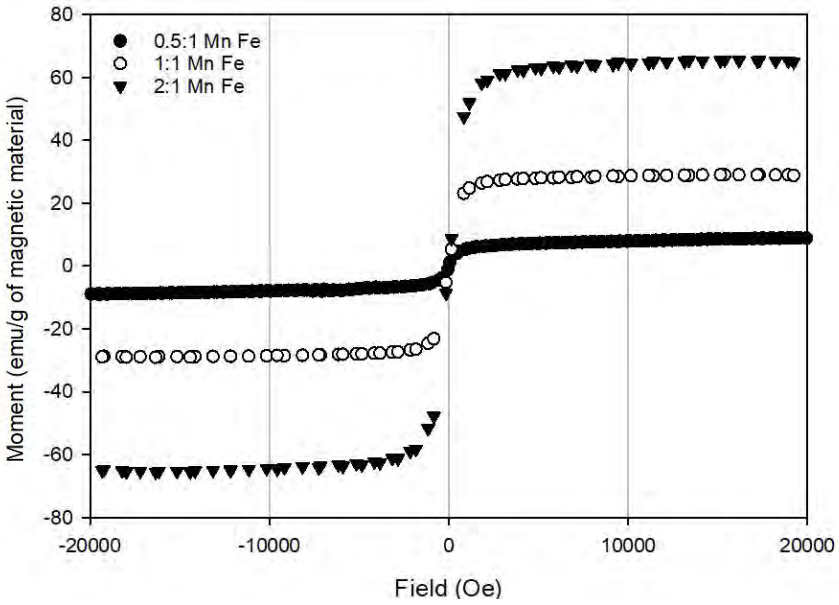


Figure 76 The magnetic responses produced by the occlusion products when using iron(III) chloride to manganese(II) zeolite A ratios of 0.5:1,1:1 and 2:1 using a synthesis temperature of 1000˚C. Black circles represent the data from the 0.5:1 ratio, white circles 1:1 and black triangles 2:1.

4.6.4. Nickel(II)-iron(III) matrix materials

Figure 77 contains the magnetic response from the nickel iron systems. None of the curves displayed hysteresis, therefore, all are superparamagnetic. The greatest moment was recorded by the 2:1 system at 26.43 emu/g of magnetic material. Samples made using a 1:1 and 0.5 ratio were significantly less at 13.43 and 9.88 emu/g of magnetic material respectively. Therefore the 2:1 ratio matrix was chosen to magnetize zeolite A in the next chapter.

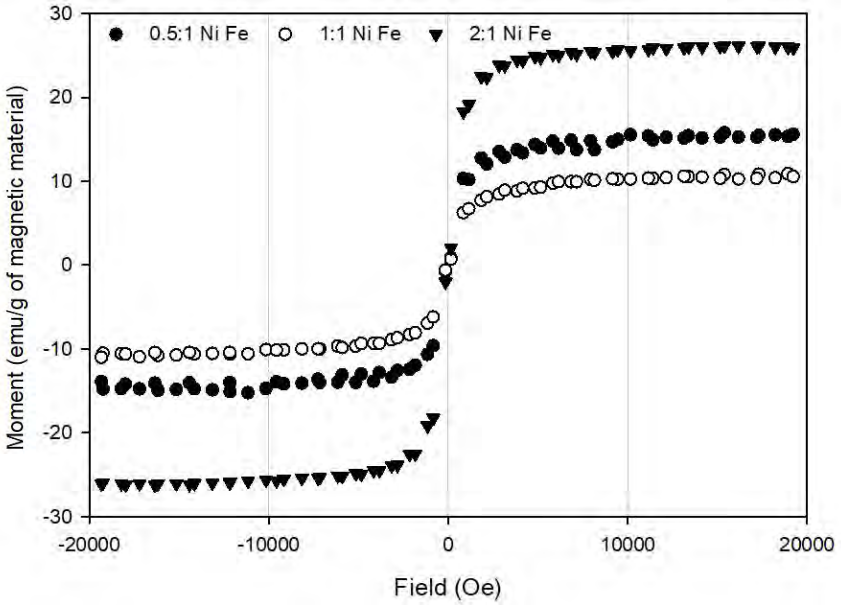


Figure 77 The magnetic responses produced by the occlusion products when using iron(III) chloride to nickel(II) zeolite A ratios of 0.5:1,1:1 and 2:1 using a synthesis temperature of 1000˚C. Black circles represent the data from the 0.5:1 ratio, white circles 1:1 and black triangles.

4.6.5. Zinc(II)-iron(III) matrix materials

All of the zinc iron materials made using Zinc(II)-A were measured, as none of the samples displayed significant magnetism >1 emu/g of magnetic material, therefore, they were not able to magnetise zeolite A for this application.

4.6.6. Conclusion of the magnetic behaviour of the matrix materials

VSM measurements were able to confirm the desired superparamagnetic behaviour for 4 out of 5 materials. Only the zinc iron system did not create a magnetic product. This was believed to have arisen from disparities between the zinc content calculated from the XRF spectrum and the true zinc content, owing to sources of error discussed

previously (3.4.5.) This was proposed to be a result of less zinc exchanging than was first thought, therefore, very little of the desired zinc ferrite forms and instead mostly hematite forms. The cobalt iron system did exhibit a small degree of ferromagnetism at the highest salt ratio which was thought to be caused by increased particle size. This synthesis method was found to create materials with significant magnetic moments up to a maximum of 65.78 (emu/g of magnetic material) registered for the manganese iron system. All of the systems presented with the exception of zinc were chosen to attempt to magnetise a fresh form of zeolite A with unaffected ion exchange abilities.

Table 20 Summary of the magnetic moments produced by the matrix materials made using transition metal exchanged zeolite A

	Exchanged transition metal				
Iron(III) chloride: transition metal exchanged zeolite	Co	Fe	Mn	Ni	Zn
0.5:1	16.82	20.10	8.96	9.88	>1
1:1	18.70	11.38	29.76	13.43	>1
2:1	36.50	26.08	65.78	26.43	>1
3:1	N/A	7.98	N/A	N/A	N/A

4.6.7. Optimisation in zeolite X and Y

The ion exchanged products of zeolite X and Y that had been optimised as part of the work in the previous chapter were subjected to the same experimental procedure as that presented for the zeolite A. An example of the XRD patterns for both systems for one of divalent metal exchanged zeolites is given in the appendix (section 4.1.) along with the graphical representations of the magnetic data of those systems (section 4.2.2. and 4.2.3.). A numerical summary of the magnetic moments recorded is given in Table 21 and 22 for zeolites X and Y respectively. If any of the systems do not have any magnetic data present, it can be assumed the products were not magnetic. The most magnetic product from each divalent/trivalent metal system was taken forward to the next stage of the synthesis.

Table 21 Summary of the magnetic moments produced by the matrix materials made using transition metal exchanged zeolite X

	Exchanged transition metal				
Iron(III) chloride: transition metal exchanged zeolite	Co	Fe	Mn	Ni	Zn
0.5:1	No data	No data	13.07	10.08	19.86
1:1	No data	No data	32.13	39.73	16.44
2:1	50.22	No data	24.82	29.86	4.49
3:1	62.59	No data	55.95	48.00	18.22

Table 22 Summary of the magnetic moments produced by the matrix materials made using transition metal exchanged zeolite Y

	Exchanged transition metal				
Iron(III) chloride: transition metal exchanged zeolite	Co	Fe	Mn	Ni	Zn
0.5:1	27.15	1.05	No data	7.88	No data
1:1	44.46	32.00	No data	15.84	No data
2:1	50.05	13.32	No data	42.51	No data
3:1	38.40	3.37	No data	27.54	No data

4.7. Production of magnetic materials using sodium zeolite A

Zeolites are usually stable to higher temperatures than exhibited during the salt occlusions. This could be caused by defects such as stacking faults in the framework that occurred during synthesis as a templating agent was not used. However, this is unlikely to be the cause given the crystallinity of the XRD patterns. An alternative explanation could be that the framework is damaged during aqueous ion exchange or possibly during the occlusion process itself.

It had been established that the desired magnetic spinels could be synthesised via a two-step process, therefore an independent investigation was started to explore if these spinels could be made in just one step. The proposed new method would act as a 'one pot' exchange in which both the di- and trivalent cations would be loaded simultaneously. This would allow the potentially damaging aqueous ion exchange to be skipped, whilst allowing for greater metal loading as the solid state synthesis can bypass the charge balancing requirement associated with aqueous exchange of Na^+. During this type of synthesis, solid state ion exchange and salt occlusion can occur together. This means that as well as the desired cations, the anions of the metal salt can also be introduced. Various cation ratios were tried in an attempt to load the highest content possible; the ratios were calculated based upon the structure target spinel. This series of reactions were also completed under a nitrogen atmosphere to reduce unwanted side products.

It was hoped that this series of work could provide a greater understanding of the solid state reactions occurring during the synthesis. If successful it would allow for direct

comparisons in magnetic behaviour to the two-step reactions, which might help optimise both synthesis methods further. This route was also proposed to help with the investigation into the effect that the over-exchanged content had on the formation of the magnetic spinel and how that influences their magnetic behaviour. As an initial starting point the divalent content was fixed and the amount of trivalent iron was varied.

The amount of cobalt introduced was calculated to replicate the level of exchange achieved during aqueous ion exchanges in chapter 3, but initially without any over-exchange. Initially, this hypothesis was investigated using the cobalt(II)-iron(III) and iron(II)-iron(III) systems, the results are shown in Figure 78 and Figure 80 respectively.

4.7.1. Cobalt(II) one-step synthesis

The data shown in Figure 78 indicated that at the lowest synthesis temperature of 400˚C, even without the possibility of damage caused by aqueous ion exchange, the zeolitic framework degraded. Previously in the two-step method, degradation was not seen until 600˚C and above. This behaviour has been proposed to be due to iron(III) chloride being a moderately strong Lewis acid. The zeolite itself contains silicon and aluminium both are commonly used as Lewis acid catalysts. This type of reaction commonly results in heterolytic bond cleavage and would plausibly explain the degradation.[28] However, it is proposed that the addition of the cobalt(II) nitrate enhanced the issue and might explain why it occurs 200˚C lower compared to the two-step method.

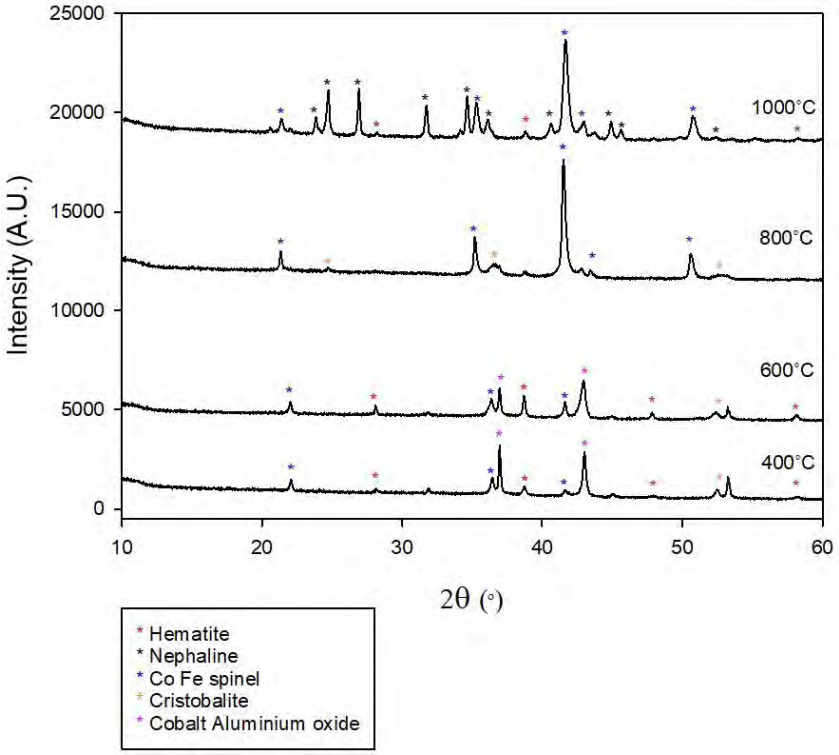


Figure 78 XRD patterns resulting from a solid-sate exchange of Na (I) A with cobalt(II) chloride and iron(III) chloride in a 2:1:0.5(Fe^{3+}:Co^{2+}:Na^{+}) ratio heated at different temperatures under a nitrogen atmosphere.

In the 400˚C and 600˚C samples, there were additional peaks seen at 43.0˚, 52.4˚ and 53.2˚ 2θ. These reflections are produced by a cristobalite (SiO_2) impurity. Cristobalite is a polymorph of silica, the cubic structure usually requires temperatures above 1500˚C to be stable. However, at ambient temperatures like the ones used here, a tetragonal phase forms instead, this is known as alpha or low cristobalite.[29] The 1000˚C sample contains several extra peaks that were not seen during the two-step exchanges, this was due to larger amounts of sodium remaining. Na(I)-zeolite A transforms into a mixture of carnegiete ($NaAlSiO_4$) and nepheline ($Na_4(Al_4Si_4O_{16})$ above 900˚C. The mixture recrystallizes into nepheline at ~1000˚C as was seen in Figure 78.[30]

Interestingly, several spinel related peaks (denoted by the blue asterisk) could be seen at lower temperatures than in the two-step method. This again confirms the theory that the higher temperatures required in the two-step route promote greater mixing of the ions, rather than being a requirement for phase formation as $CoFe_2O_4$ was shown to form at 400˚C as opposed to ≥800˚C in the two-step method. Small intensity hematite peaks were also present, suggesting that hematite occurs regardless of the ratio used and is more strongly dependent on areas of deficiency. However, these results suggest that this one-step process also made the desired cobalt ferrite with several additional phases. To determine which of the routes synthesised the most desirable material, their magnetic behaviours needed to be compared. The magnetic moments recorded for the one-step process is shown in Figure 79. The lower temperature samples were not included in the figure as they recorded significantly lower magnetic moments of 0.37 and 0.89 emu/g for 400 and 600˚C heatings, respectively, and exhibited ferromagnetism which would not have been visible if included in Figure 79. Figure 79 shows strong magnetic moments of 18.2 and 24.2 emu/g for 800˚C and 1000˚C samples respectively. Both samples exhibit superparamagnetism although there was a slight shift in the data points on the second pass through a positive field. Upon first look, it would be reasonable to assume that as these magnetic moments were greater than the 16.4 emu/g recorded for the two-step 1000 ˚C but this might not be strictly true. To determine which has the stronger magnetic moment the magnetic content of each system needs to be considered to allow for a more accurate comparison. This analysis method was applied to both sets of data with the results summarised in Table 17.

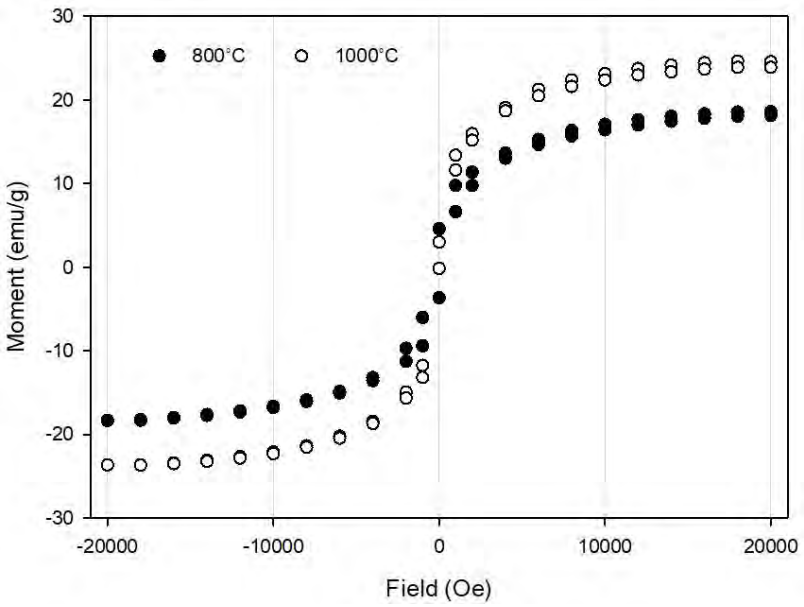


Figure 79 The magnetic responses produced by the one-step synthesis products when using A cobalt(II) chloride and iron(III) chloride in a 2:1:0.5 (Fe^{3+}:Co^{2+}:Na^{+}) ratio which were heated at different temperatures under a nitrogen atmosphere. Black circles represent the data from the 800 ˚C and the white circles 1000˚C.

Table 23 shows that the one-step method created a significantly more magnetic material at 61.4 compared to the two-step at 36.8 emu/g of magnetic material. Therefore, both materials would be taken forward to create a magnetic zeolite as it was unknown if the additional phases within the matrix could lead to issues during the secondary synthesis.

Table 23 A direct comparison of the magnetic behaviour of the one and two-step synthesis methods

Sample (Number of steps 1 or 2)	Iron content (wt%)	Cobalt content (wt%)	Total content (wt%)	Magnetic moment (emu/g)	Adjusted magnetic moment (emu/g of magnetic material)
0.5:1 (2)	16.3	18.5	34.8	5.92	16.5
1:1 (2)	21.9	16.5	38.4	7.3	18.7
2:1 (2)	32.3	12.8	45.1	16.4	36.8
800˚C (1)	23.5	15.9	39.4	18.2	47.1
1000˚C (1)	24.6	15.0	39.6	24.2	61.4

4.7.2. Iron(II) one-step synthesis

The iron(II)iron(III) system was then investigated using the one-step method. The results of this are shown in Figure 80. The pattern of the 400˚C sample was not included in this data set as only the background was detected during the scan possibly due to the only very small hematite particles forming at this time, these particles would not form sharp enough Bragg peaks to be seen above the background. The iron(II)/iron(III) system shows different synthesis behaviour to the cobalt iron system,

as use of the lower temperatures resulted in hematite as the sole product. This suggested that in the case of iron(II)-iron(III) use of lower synthesis temperatures favoured the formation of hematite as had been seen previously during the VT-XRD experiments. Upon comparing Figure 80 to Figure 55, it can be seen that during the two-step method (Figure 55) the magnetic phase formed at 800˚C alongside mullite. Whereas in this case, mullite crystallisation did not occur until a temperature of 1000˚C was used. Also present as an impurity in the 1000˚C sample was α-cristobalite which had not been seen in any of the two-step synthesis XRD patterns, except for the materials synthesised during VT-XRD characterisation. Regardless of the impurity phases hematite remained the dominant phase at 1000˚C. Therefore, it can be predicted that this material will have a weaker magnetic moment than its two-step counterpart.

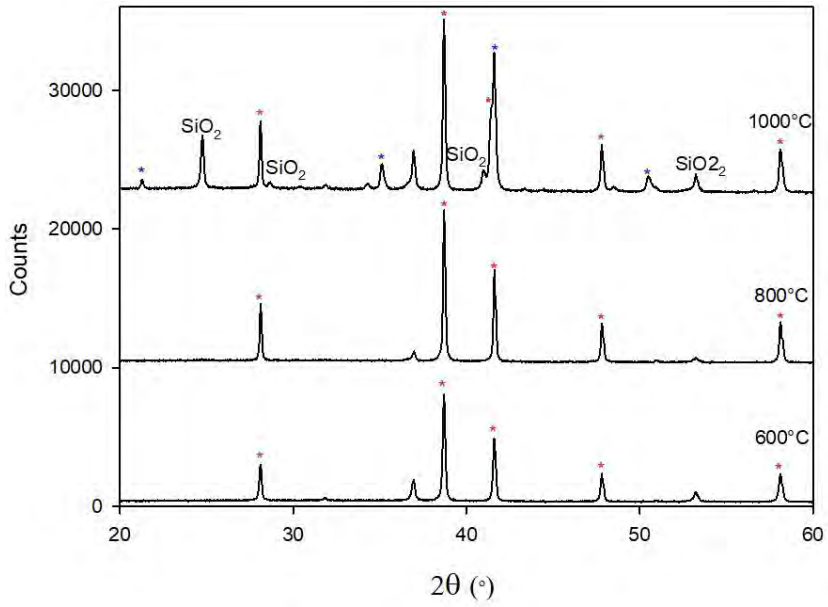


Figure 80 XRD patterns resulting from a solid-sate exchange of Na (I) A with iron(II) chloride and iron(III) chloride in a 2:1:0.5(Fe^{3+}:Fe^{2+}:Na^{+}) ratio heated at different temperatures under a nitrogen atmosphere.

Figure 81 contains the curve recorded by the one-step sample made at 1000˚C. The metal content approximation was also applied to this sample with the result is provided in the same figure. Figure 81 shows that this route can also form a superparamagnetic material. Therefore, it is proposed that the method of dispersing reactants throughout a silica matrix provides a sufficient level of particle size control, if the magnetite particles were bigger than 10 nm, they would not display superparamagnetism.

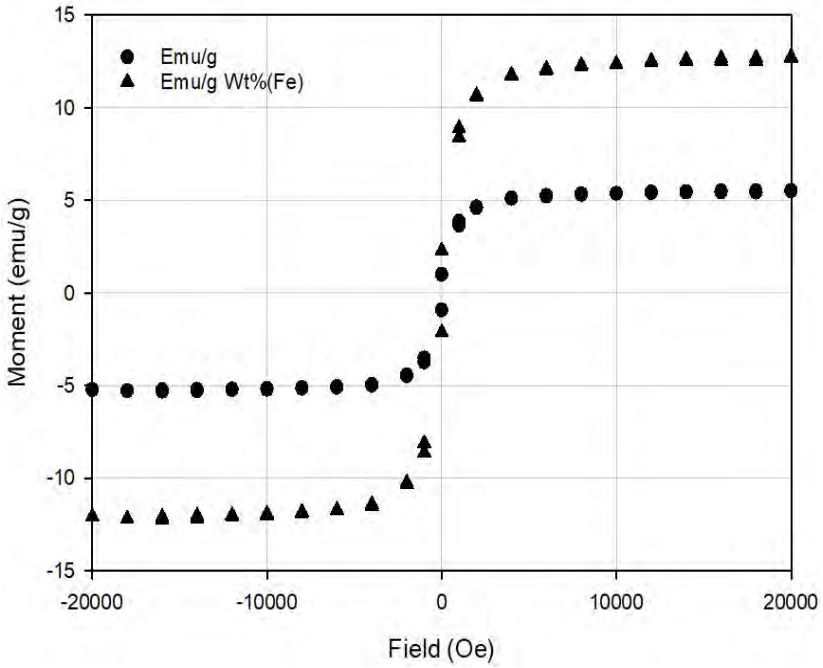


Figure 81 The magnetic responses produced by a solid-sate exchange of Na(I) A with iron(II) chloride and iron(III) chloride in a 2:1:0.5 (Fe^{3+}:Fe^{2+}:Na^{+}) ratio heated at 1000˚C under a nitrogen atmosphere. Black circles represent the data without magnetic content accounted for and the black triangles does account for the magnetic content.

The one step synthesis procedure for the iron(II)iron(III) system only created one magnetic product, therefore only this sample can be compared to the materials created using the two-step method. The one-step method created sample magnetic moment of only 5.59 emu/g, this improved to 12.67 (emu/g of magnetic material) with the magnetic content included.

However, both values are significantly smaller than those recorded for the two-step method, possibly due to how readily iron(II) oxidises. This meant that magnetite formation was unfavourable under the conditions used. As the two-step method created a material with a stronger moment only the two-step synthesis product was

taken forward to create a magnetic zeolite. The strongest moment possible was required as the moment will be reduced upon incorporation into a new secondary zeolite and in a waste remediation application, a stronger magnetic moment is preferred.

The one-step synthesis was never completed for nickel, manganese and zinc as magnetic data could not be obtained to determine if the one or two-step method was preferred due to COVID-19 restrictions.

4.8. Overall section conclusion

The work in this chapter focused on the introduction of iron(III) into the system and investigated the effect that the anion has on the phases formed. The investigation found that use of a nitrate anion appeared to favour the formation of hematite regardless of the synthesis temperature, this was to be expected as at the higher temperatures where nitrate will break down and act as an oxidising agent. A chloride anion was found to be the better of the two anions as this enabled the formation of a magnetic spinel alongside hematite. Weight fractions obtained from Rietveld refinements found that a collection of these materials contained up to 83% hematite. Hematite formation was initially proposed to have formed via a conversion process from maghemite. However, VT-XRD in conjunction with TGA/DTA found that direct synthesis of hematite occurred instead of via a conversion reaction. This suggested that it was happening due to an oxidation reaction. Therefore, the reactions were completed under nitrogen gas which reduced the hematite content significantly, facilitating the formation of increased amounts of the magnetic spinel.

Regardless of the salt ratio and temperature used the zeolite was found to break down earlier than suspected. This was initially thoughted to be due to framework defects or damage caused by ion exchange. However, it is proposed to be related to the acidity of the iron(III) salts. During the synthesis the zeolite broke down and in certain cases recrystallised, therefore, it created an aluminosilicate matrix in which the magnetic component was trapped. It was thought that this matrix could be used as a silica or alumina source for a new secondary zeolite.

A combination of techniques including powder X-ray diffraction, ^{57}Fe Mössbauer spectroscopy, Raman spectroscopy and electron microscopy provided a comprehensive characterisation of the materials, which enabled this novel preparation method to be applied to the remaining transition metal exchanged zeolites made in Chapter 3. TGA/DTA was used to highlight regions of interest during the synthesis. By using this information in conjunction with VT-XRD it was hoped that phase formation could be recorded as it happened to indicate the mechanism of the reaction. However, there were limitations related to the setup which meant that this could be fully resolved.

The magnetic behaviour of the materials was recorded using VSM. The hysteresis graphs recorded on the VSM confirmed that 4 out of the 5 systems investigated displayed superparamagnetism. The investigation of the two-step method suggested that use of a 1000˚C synthesis temperature and a 2:1 (Fe^{3+}:Cat^{2+}) salt ratio created a product with the largest magnetic moment. The zinc(II)-iron(III) system made via the two-step method was the only system in which hematite dominated regardless of the conditions used.

As the two-step preparation method had been successful a one-step method was devised. This method aimed to exchange both the di and trivalent iron simultaneously, it was hoped that this could lead to the development of a product that was more magnetic as this method would not be limited by the charge balancing requirement of aqueous ion exchange. VSM and XRD found this route was successful for the cobalt(II)-iron(III) system in the development of superparamagnetic materials which were significantly more magnetic than that made via the two-step. However, as the initial sodium cations were not removed this led to impurities such as nepheline and α-cristobalite. It was unknown how the additional phases would affect the incorporation

into the new secondary zeolite, therefore, materials from both methods were taken forward.

4.9. References

1 D. Feng, C. Aldrich and H. Tan, *Hydrometallurgy*, 2000, **56**, 359–368.

2 A. B. Bourlinos, R. Zboril and D. Petridis, *Microporous Mesoporous Mater.*, 2003, **58**, 155–162.

3 L. N. Mulay, D. W. Collins, A. W. Thompson and P. L. Walker, *J. Organomet. Chem.*, 1979, **178**, 217–226.

4 I. Hussain, I. Gameson, P. A. Anderson, M. Slaski, P. P. Edwards and A. Dyer, *J. Chem. Soc. - Dalt. Trans.*, 1996, 775–781.

5 F. J. Lázaro, J. L. García, V. Schünemann, C. Butzlaff, A. Larrea and M. A. Zal/uska-Kotur, *Phys. Rev. B*, 1996, **53**, 13934–13941.

6 D. S. Mathew and R.-S. Juang, *Chem. Eng. J.*, 2007, **129**, 51–65.

7 O. F. Odio and E. Reguera, in *Magnetic Spinels - Synthesis, Properties and Applications*, InTech, 2017.

8 J. Mohapatra, A. Mitra, H. Tyagi, D. Bahadur and M. Aslam, *Nanoscale*, 2015, **7**, 9174–9184.

9 F. E. Trigueiro, D. F. J. Monteiro, F. M. Z. Zotin and E. Falabella Sousa-Aguiar, *J. Alloys Compd.*, 2002, **344**, 337–341.

10 T. Palenta, S. Fuhrmann, G. N. Greaves, W. Schwieger and L. Wondraczek, *J. Chem. Phys.*, 2015, **142**, 084503.

11 C. Weidenthaler and W. Schmidt, *Chem. Mater.*, 2000, **12**, 3811–3820.

12 Y. L. K. Berger A S, Samsonova T I, *Russ Chem Bull*, 1978, **20**, 2015–2019.

13 E. Darezereshki, *Mater. Lett.*, 2011, **65**, 642–645.

14 C.-W. Lee, S.-S. Jung and J.-S. Lee, *Mater. Lett.*, 2008, **62**, 561–563.

15 S.-W. Cao, Y.-J. Zhu and Y.-P. Zeng, *J. Magn. Magn. Mater.*, 2009, **321**, 3057–3060.

16 T. Belin, N. Millot, N. Bovet and M. Gailhanou, *J. Solid State Chem.*, 2007, **180**, 2377–2385.

17 J. S. J. Hargreaves, *Catal. Struct. React.*, 2016, **2**, 33–37.

18 N. Bost, S. Duraipandian, G. Guimbretière and J. Poirier, *Vib. Spectrosc.*, 2016, **82**, 50–52.

19 D. L. A. De Faria, S. Venâncio Silva and M. T. De Oliveira, *J. Raman Spectrosc.*, 1997, **28**, 873–878.

20 S. Das and M. J. Hendry, *Chem. Geol.*, 2011, **290**, 101–108.

21 P. Chandramohan, M. P. Srinivasan, S. Velmurugan and S. V. Narasimhan, *J. Solid State Chem.*, 2011, **184**, 89–96.

22 D. A. Gómez, J. Coello and S. Maspoch, *Vib. Spectrosc.*, 2019, **100**, 48–56.

23 V. Marghussian, *Chapter 4. Magnetic Properties of Nano-Glass Ceramics*, 2015.

24 F. Menil, *J. Phys. Chem. Solids*, 1985, **46**, 763–789.

25 N. . Greenwood and T. . Gibb, *Mössbauer spectroscopy*, Chapman and Hall, London, 1971.

26 M. Al-Maashani, A. M. Gismelseed, K. A. M. Khalaf, A. A. Yousif, A. D. Al-Rawas, H. M. Widatallah and M. E. Elzain, *Hyperfine Interact.*, 2018, **239**, 1–8.

27 A. L. Gurgel, A. E. Martinelli, O. L. de A. Conceição, M. M. Xavier, M. A. Morales Torres and D. M. de Araújo Melo, *J. Alloys Compd.*, 2019, **799**, 36–42.

28 F. A. Carey and R. J. Sundberg, *Advanced Organic Chemistry*, Springer US, Boston, MA, 2007.

29 Mineral information:Cristobalite, https://www.mindat.org/min-1155.html.

30 C. Kosanovic, B. Subotic and I. Smit, *Thermochim. Acta*, 1998, **317**, 25–37.

Chapter 5. Superparamagnetic zeolite hybrids

5.1. Introduction

It was initially thought that a combination of the three commonly used zeolite magnetisation methods described in section 1.4 would be optimal. However, the synthesis method presented in Chapter 4 only encompassed 2 of those methods: surface decoration and the insertion of cations. However, as the zeolitic structure had broken down during the synthesis it meant that magnetic particles were contained within a vitreous aluminosilicate matrix. By including the aluminosilicate matrix in a new zeolite synthesis, the method became similar to the direct addition magnetisation method. Therefore, the synthesis method became a mixture of all three methods. It was proposed that as the magnetic particles were contained within a aluminosilicate matrix, the magnetic particles would be less likely to inhibit nucleation, resulting in a new zeolite hybrid material with a higher magnetic loading than has been reported previously.[1,2,3,4] If successful in magnetising the zeolites, it was hoped that this method would cause less surface fouling than coprecipitation whilst achieving similar levels of magnetisation. This would mean that more of the surface area is accessible therefore, the resulting zeolite should have less restricted ion exchange properties than has been observed for magnetised zeolites made via coprecipitation. The magnetic component of this method is an oxide therefore, this should create magnetic zeolites with a more stable component than those containing metal nanoparticles, therefore, prolonging the life cycle of the material.[5]

5.2. Synthesis and characterisation of zeolite A hybrids

Initially, synthesis focused on using the matrix of the one or two-step method as 20% (0.2:1) of the aluminate source with the commonly used regents. By doing so allows the magnetic content of the hybrid material to be easily interpreted post synthesis. However, using the unaltered aluminosilicate matrix directly in a standard zeolite A synthesis was unsuccessful. Certain syntheses found that the matrix particles inhibited nucleation and in those that were successful, most of the zeolite remained unmagnetised. During the initial testing, the crystallisation time was increased from 5 hours to 24 hours which made a significant difference to the crystallinity of zeolite when the matrix material was present as shown in Figure 82.

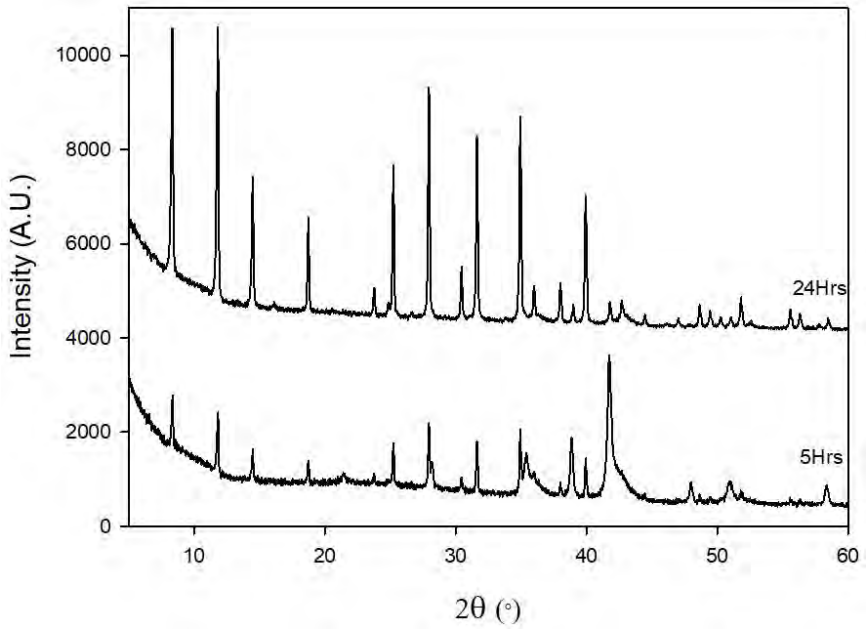


Figure 82 The effect of increasing the synthesis time when using materials with significantly different solubilities in the synthesis of superparamagnetic zeolite A hybrids.

Although increasing the synthesis time allowed for more successful nucleation with the aluminosilicate matrix material present, large parts of the zeolite remained unmagnetised as only a small amount of the zeolite was attracted towards a Nd bar magnet. Therefore, the aluminosilicate matrix needed to be altered before the synthesis. The incorporation failure was thought to stem from differences in particle size and in solubility between the aluminosilicate matrix and the reagents commonly used in zeolite synthesis. To overcome these issues the aluminosilicate matrix was subjected to basic digestion. A NaOH digestion has been used previously for dissolution of zeolites[6], therefore, using NaOH to treat the aluminosilicate matrix should reduce the particle size and overcome the solubility differences. The digestion would use a specified concentration of NaOH. These vessels would then be heated to 200˚C and kept there for 24 hours to ensure sufficient digestion had occurred.

Initial experiments used different concentrations to determine which would be the most appropriate for the synthesis and digestion. The digested material and corresponding solution were kept together post digestion as they were directly used in the secondary synthesis. The NaOH solution replaced the water. Water is usually added to hydrate the starting materials; these then combine to create a gel. NaOH was chosen as the secondary zeolite has sodium as the exchangeable cation, therefore, the use of NaOH should not have any adverse effects on the synthesis.

SEM was initially used to investigate the effect of digestion on the particle size. The changes observed in the particle size are displayed in Figure 83. The base digestion was typically only partial, but there was always a reduction in the particle size of the aluminosilicate matrix which then allowed dissolution during the main synthesis step.

Analysis of SEM images confirmed successful digestion of the aluminosilicate matrix when using concentrations between 1 and 3 M therefore, the concentration selected would be chosen depending upon how it influences the formation of zeolite A.

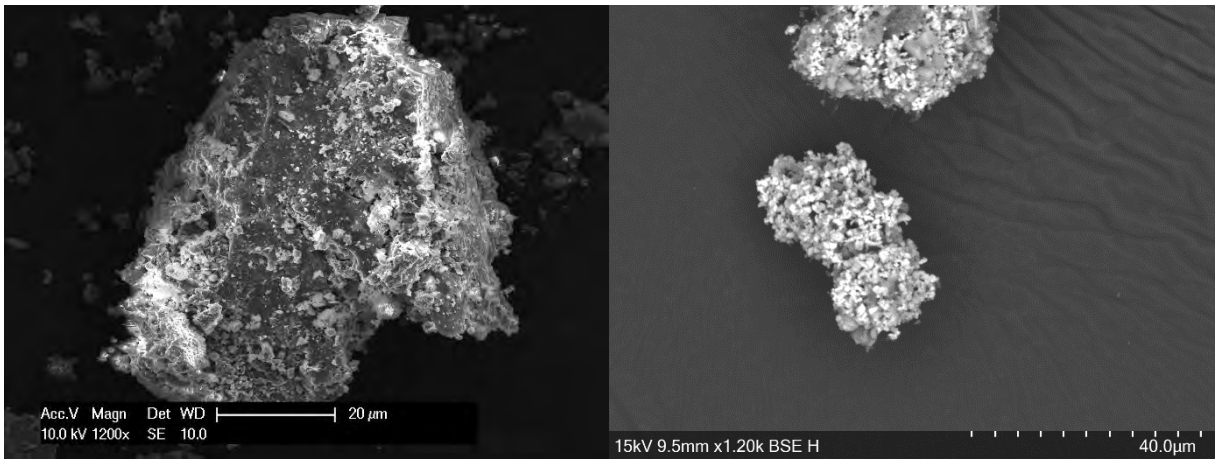


Figure 83 Depicting the size of the matrix material before and after digestion in NaOH. Left hand image is prior digestion. Right hand image is post digestion.

The high contrast spots in both images of Figure 83 correspond to regions of high transition metal content, in this case, Fe. The lower contrast regions are areas of Si and Al. The righthand image shows how the digestion broke down the larger aluminosilicate agglomerates (left hand image) into smaller ones. It was proposed that smaller particles could encourage nucleation to occur around the metal oxides rather than inhibiting it.

A standard zeolite A synthesis uses 0.6 M NaOH, however, when this concentration was used for digestion with 20% aluminosilicate matrix content (0.2:1), and a standard crystallisation time of 5 hours, only poorly crystalline zeolite A was observed. Based upon the effect of increasing time shown in Figure 82 the zeolites made using digested aluminosilicate matrix instead used a 24-hour synthesis time instead of 5. The NaOH concentrations were varied from 1 M up to a maximum of 1.5 M as concentrations greater than this began to affect the formation of the framework adversely. A separate

set of experiments found that the digestion had also been successful in reducing the particle size for the matrix made in one-step. Although the one-step aluminosilicate matrix could not be successfully incorporated into the new zeolite. It was thought that this could be related to the additional phases present in the aluminosilicate matrix as this was not an issue for the two-step aluminosilicate matrix. Therefore, the one-step aluminosilicate matrix was not used to magnetize zeolite A. The effect of changing the NaOH concentration on the zeolite A when using the two-step aluminosilicate matrix is shown in Figure 84.

Figure 84 shows the effects of the three different concentrations which initially does not appear to be too significant as the overall and relative intensities are similar. The use of 1.25/1.5 M NaOH produced a slightly more crystalline product which can be seen most notably by comparing the peak at 16.2˚. However, the differences were more significant visually, as the colour changed from white to progressively greyer/blue with increasing concentration NaOH. This suggested a greater amount of magnetic matrix had been digested and then incorporated, but not in a large enough quantity to be detected by XRD. In the presence of an Nd bar magnet, most of the sample was attracted regardless of the concentration used. This suggested the pretreatment digestion had been successful for enhancing incorporation into a new zeolite A structure.

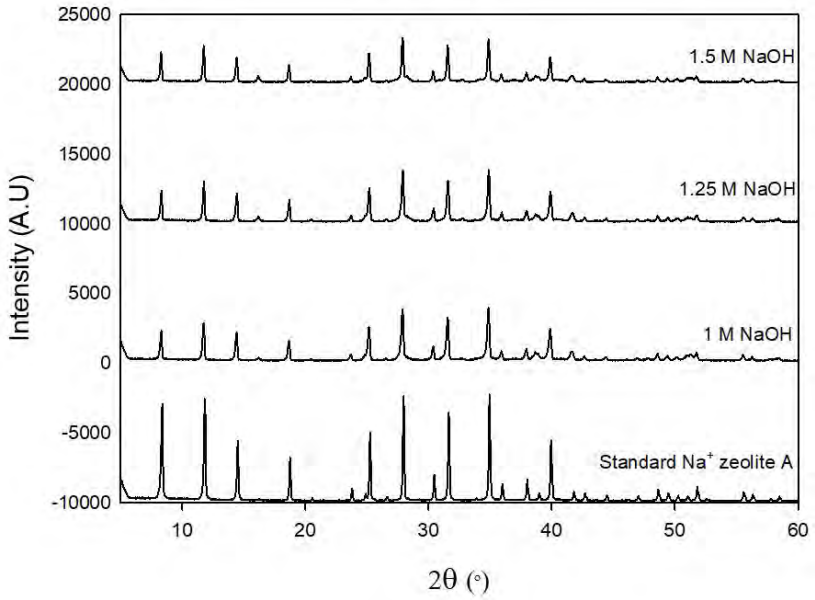


Figure 84 Powder X-ray diffraction patterns of superparamagnetic zeolite A hybrids made as a function of NaOH (24-hour crystallisation time), using a 20% matrix content. A standard form of zeolite A has been added for comparison.

To provide more conclusive proof electron microscopy was employed with several of the images collected shown in Figure 85. Electron microscopy confirmed the cubic morphology of the particles further supports the presence of zeolite A (Figure 85). Each image contains regions of lower contrast; these correspond to the zeolite itself. The higher contrast regions are the metal oxide particles randomly distributed through the zeolitic particles. This provided further confirmation the digestion had been successful. The metal oxide and zeolite content were confirmed by EDX analysis when the SEM images were captured. Further analysis of image c) (1.5M NaOH) showed several different shaped particles had developed alongside the standard zeolite A cubes. This suggested this concentration of NaOH had led to a morphology change rather than a change in formation as a secondary phase was not seen in Figure 84. For this reason, a concentration of 1.25M was chosen for the digestion and synthesis of the new zeolite A hybrids.

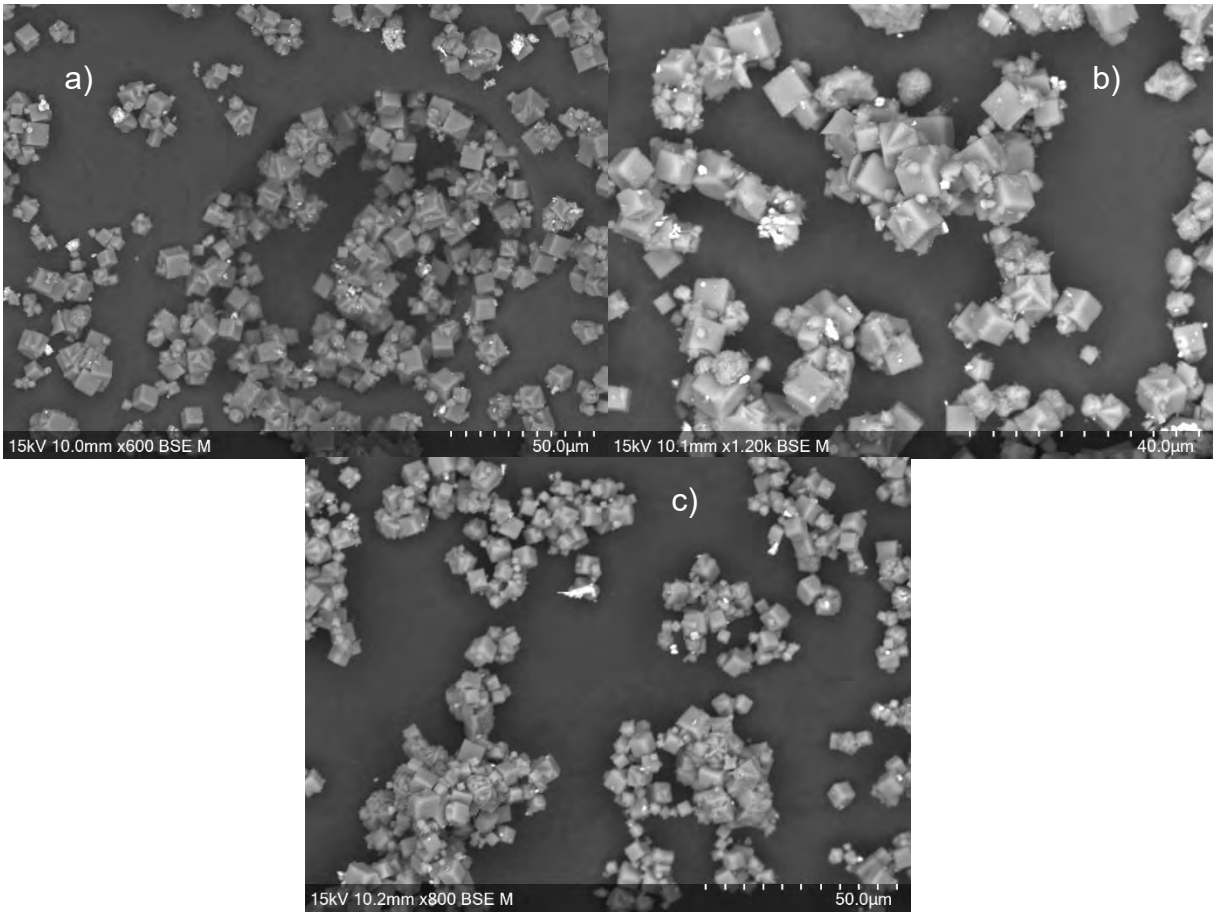


Figure 85 SEM images of zeolite A created using a magnetic matrix digested at different NaOH concentrations. a) 1M, b) 1.25M and c) 1.5M.

Although the SEM images confirmed a greater distribution of the magnetic particles throughout the zeolite, there were still regions that sparsely contained magnetic material. This suggested that the magnetic content could be increased further, improvement was to be expected as the synthesis only used 20% matrix content (0.2:1). The next set of experiments explored the possibility of increasing the magnetic capability of the zeolite by increasing the matrix content from 20% to 50%, 100% and 200% (0.2:1, 0.5:1, 1:1 and 2:1 respectively) alongside the standard synthesis reagents. SEM images and XRD patterns of the zeolite made using a 2:1 matrix content suggested zeolite formation had been inhibited similar to using the aluminosilicate matrix without digestion (appendix section 5.0.). Therefore, the

maximum loading was found to be possible by using a 1:1 matrix content alongside the standard reagents. This equated to a magnetic loading of ~21 wt% which is significantly more than 4.7 wt% which was the maximum achieved via the other magnetisation methods.[1,2] The XRD patterns of the remaining ratios are shown in Figure 86. Figure 86 showed that when the lowest matrix loading was used the differences to standard zeolite A are subtle. Further inspection of the 0.2:1 XRD pattern showed an additional peak at 28˚; this is a reflection produced by hematite. The patterns in Figure 86 are produced using a Fe(II)Fe(III) matrix which had significantly more hematite present than the other matrices presented and would explain why this reflection is seen. Additional peaks produced by hematite seen at 38, 48, 51 and 58˚ have been denoted by an asterisk. As the metal content is increased more differences were observed; an increase in the intensity of the iron oxides and changes in relative intensities but the overall zeolite structure remained.

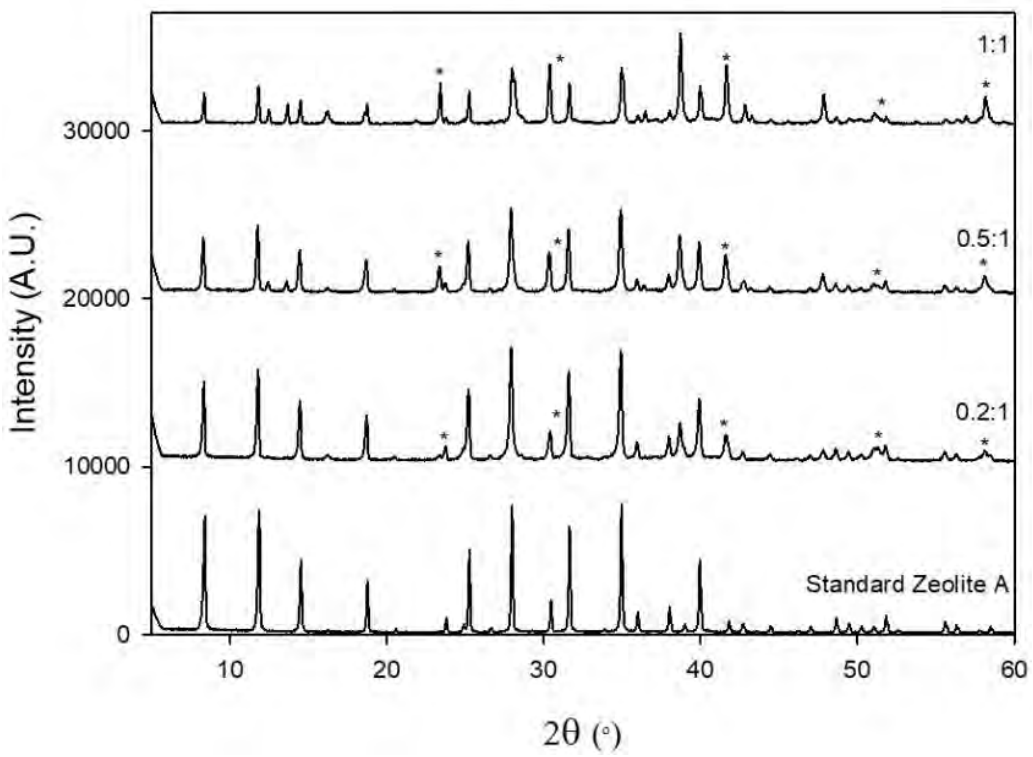


Figure 86 Powder X-ray diffraction patterns of superparamagnetic zeolite A hybrids made using different amounts of magnetic matrix. A standard form of zeolite A has been added for comparison.

Electron microscopy was again used to investigate the surface and topology of the zeolite A hybrids, shown in Figure 87 through to Figure 89. This confirmed that the topology had been maintained even at the highest loading (1:1 or 100% matrix content) as had been suggested by the XRD patterns. The figures showed that as the matrix content increased so did the number of high contrast regions in the image. This visually confirmed a more homogeneous distribution of the magnetic material across all of the zeolite particles. However, it was unknown if the magnetic particles were attached to the surface of the zeolite or if the zeolite had developed around them. Both options have their advantages and disadvantages, if zeolite has grown around the spinel, it will increase the mechanical strength which may be advantageous given the application.

However, doing so may disrupt the zeolitic channels, therefore, affecting ion exchangeability. To provide this information STEM was used to probe the sample, Figure 90 contains several images that were taken of the Fe(II)Fe(III) hybrid zeolite A.

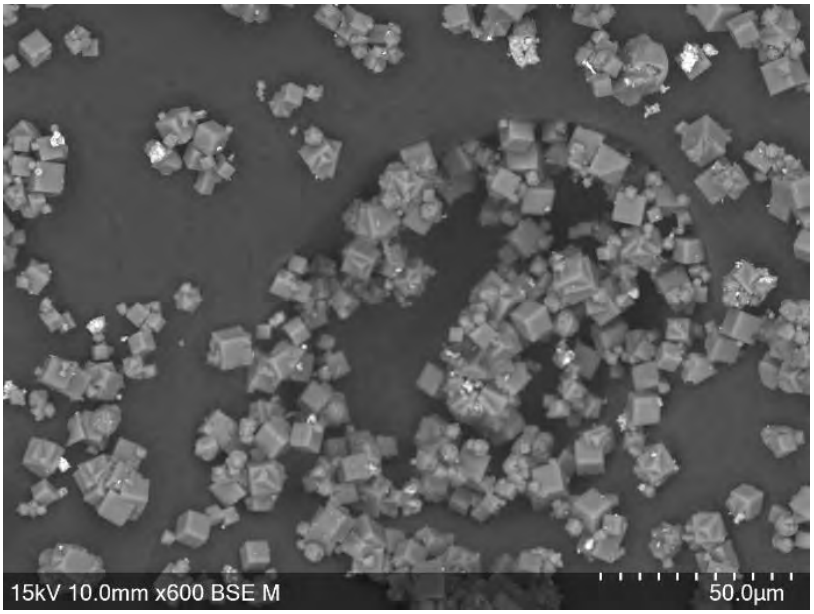


Figure 87 SEM back scattered image to investigate the topology and metal oxide distribution of zeolite A made using 20% (0.2:1)matrix content alongside standard reagents.

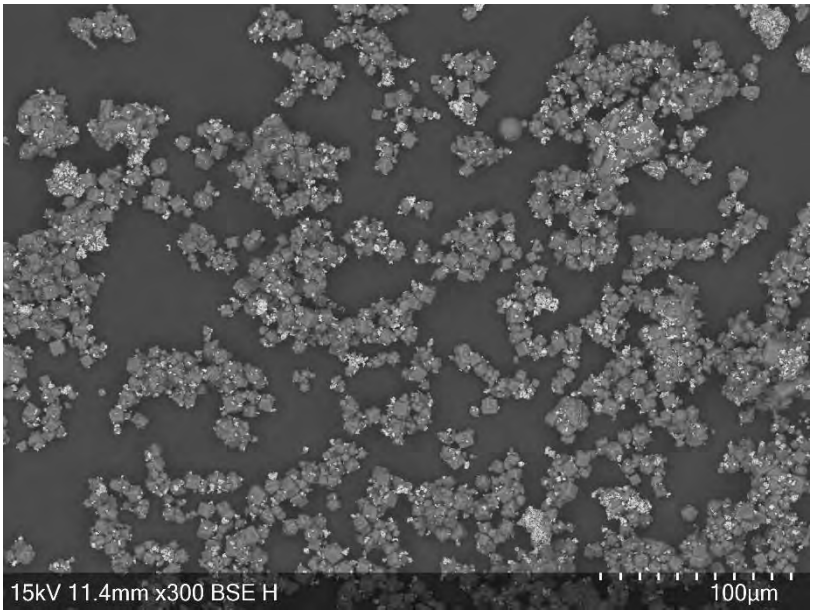


Figure 88 SEM back scattered image to investigate the topology and metal oxide distribution of zeolite A made using 50% (0.5:1)matrix content alongside standard reagents.

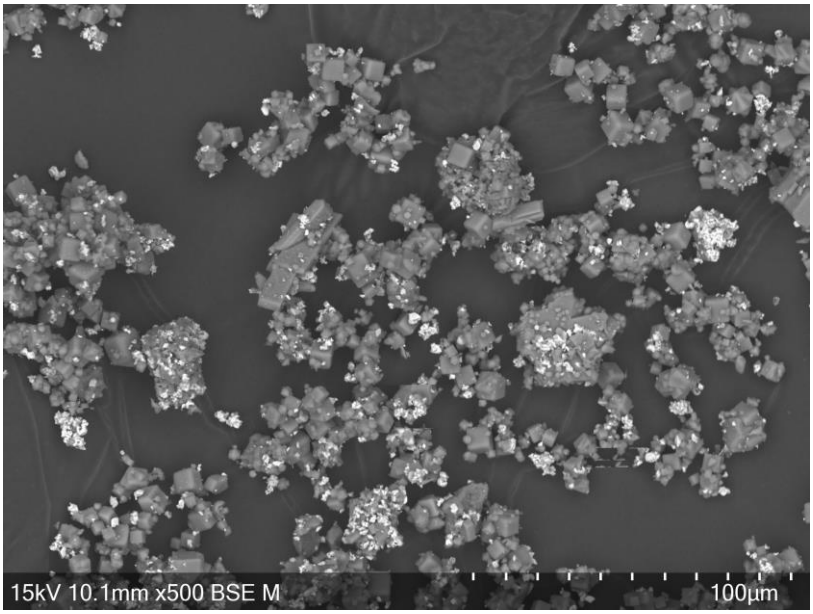


Figure 89 SEM back scattered image to investigate the topology and metal oxide distribution of zeolite A made using 100% (1:1)matrix content alongside standard reagents.

The image at the top of Figure 90 contains red letters to display points at which EDX was performed. EDX was used to identify regions of interest before elemental mapping. EDX confirmed that Fe was found alongside Si, Al, O and Na in the high contrast region A but is absent in the lower contrast region D. This suggested the zeolite contained magnetic material whilst also confirming the whole surface of the zeolite was not completely covered with the magnetic spinel implying that it will still be useful as an ion-exchange material.

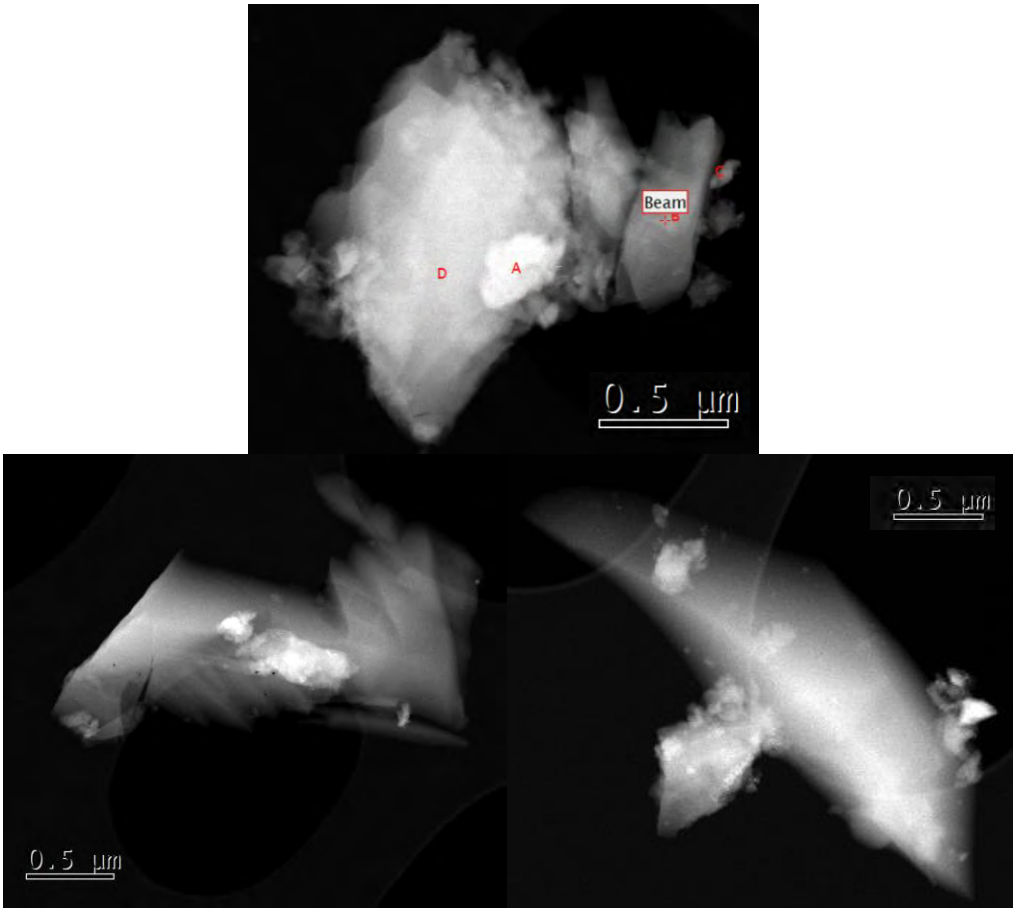


Figure 90 A selection a STEM images of zeolite A formed using a Fe(II) Fe(III) matrix. One containing red letters to depict points at which EDX analysis was performed to identify regions of interest.

After identifying a region of interest an elemental map was captured as shown in Figure 91. The box in the top left of Figure 91 is the initial STEM image, it contains a region highlighted by ‘spectrum image’. This shows the region over which the elemental map was taken. The elemental mapping images again confirmed that iron oxide was present, this can be seen in the red and light blue boxes. It shows that the iron oxide is present over the whole of the higher contrast region in the highlighted area. However, sodium is less present below the spinel which may suggest that the iron oxide is embedded in the framework. This is depicted by the lighter shading of green. This suggests that the oxide could be chemically bound which provides greater mechanical strength than merely precipitating on the surface of the zeolite. This has been the preferred method of creating magnetic zeolites previously.

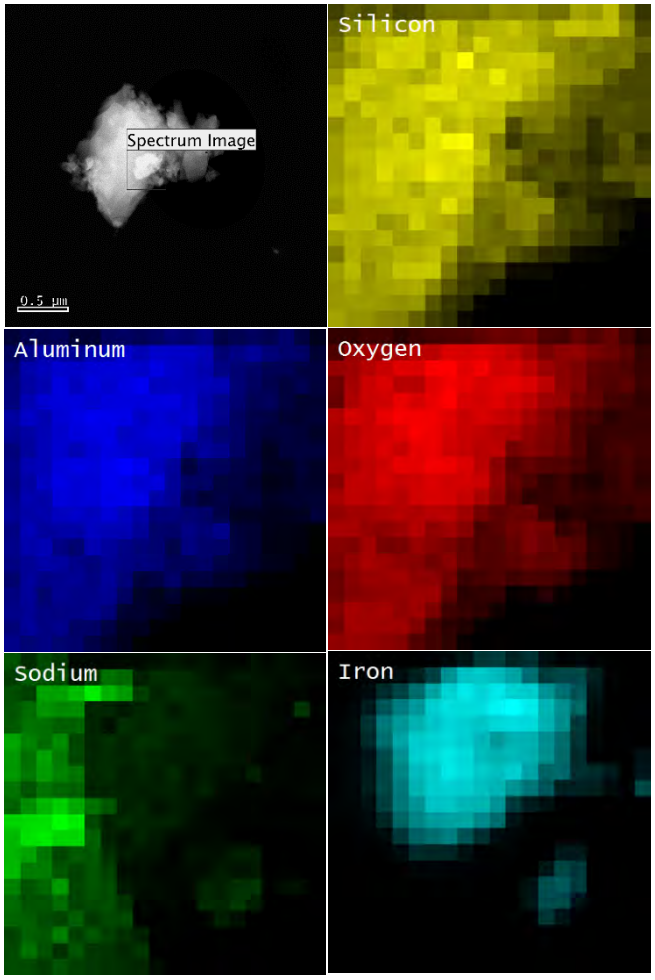


Figure 91 STEM image of 1:1 zeolite A hybrid with the EDX spectrum area highlighted with the corresponding elemental compositions.

However, it remained unknown how the incorporation might affect the zeolite, particularly the ion exchange behaviour. TGA/DTA analysis shown in Figure 92 was completed on the hybrid material to compare it to the parent zeolite (appendix section 5.1). The DTA showed similar structural changes but with an additional phase change at 750˚C which could be related to in the metal oxides of the matrix material. Interestingly, the hybrid zeolite had a weight loss of ~8% which is significantly less than the ~18% calculated for the parent zeolite. It is proposed the difference is due to a reduced zeolite content in the hybrid material compared to the parent zeolite, therefore, less water is present in the hybrid material.

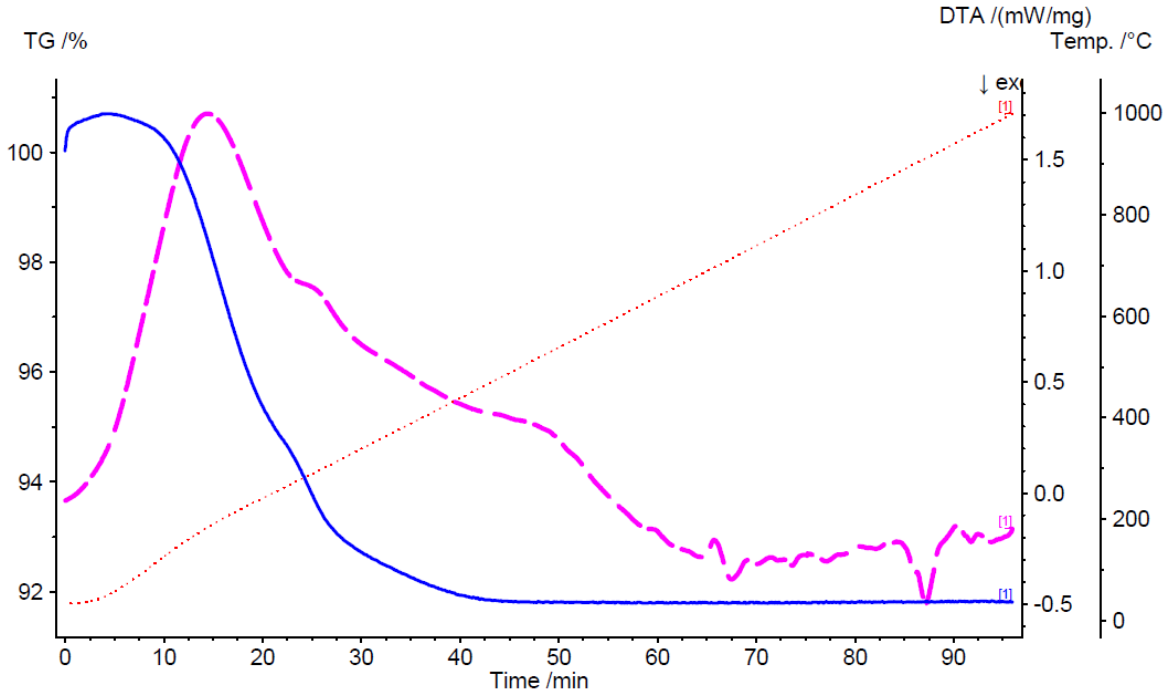


Figure 92 TGA and DTA curves of a zeolite A hybrid with maximum magnetic loading. The blue curve relates to TG% (mass loss), the purple to DTA and red corresponds to temperature.

Unfortunately BET measurements of the surface area could not be obtained to characterise the pore network. Therefore, the ion exchange behaviour alone will be used to determine the impact of the incorporation.

5.3. Magnetic characterisation of zeolite A hybrids

Electron microscopy and XRD confirmed the synthesis of a new hybrid form of zeolite A with magnetic particles incorporated. Therefore, the magnetic behaviour of the new material was investigated to determine if the superparamagnetic behaviour of the matrix had transferred to the new zeolite and if the magnetic moment was high enough to be suitable for the aqueous waste separation as had been intended.

Results presented in chapter 4 showed an aluminosilicate matrix containing manganese(II) and iron(III) had the greatest magnetic moment, therefore, these materials were expected to create strongest form of magnetic zeolite A. The magnetic results that are shown in Figure 93 are from hybrid forms of zeolite A, which were made using different amounts of this matrix. They used the matrix content notation described earlier, i.e. the 0.2:1 notation means that this sample was synthesised using 20% matrix content. This is not referring to the synthesis ratio at which the material was made as it was during Chapter 4. This notation provides a simplistic method to compare the magnetic behaviour to the magnetic content within each material.

Figure 93 showed that there was a positive correlation between the amount of matrix and the magnetic moment. This was expected based upon the increase in high contrast regions in SEM images shown previously (Figure 87 to Figure 89). All the materials measured continued to display superparamagnetism and achieved moments of up to 12.2 emu/g. These values, however, cannot be directly compared to the aluminosilicate matrix alone, as the units in Chapter 4 account for the amount of magnetic material present, and this type of analysis is not applicable here. However, they can be directly compared to other magnetic zeolites and the magnetic moments

achieved are similar to values recorded by zeolites made via the coprecipitation method[1,2,7,8]. The new method is proposed to be superior to coprecipitation as the products are thought to have a more accessible surface area due to the nature of the synthesis. Although 12.2 emu/g was the strongest moment recorded for zeolite A, the data for the remaining zeolite hybrids are presented in Table 24.

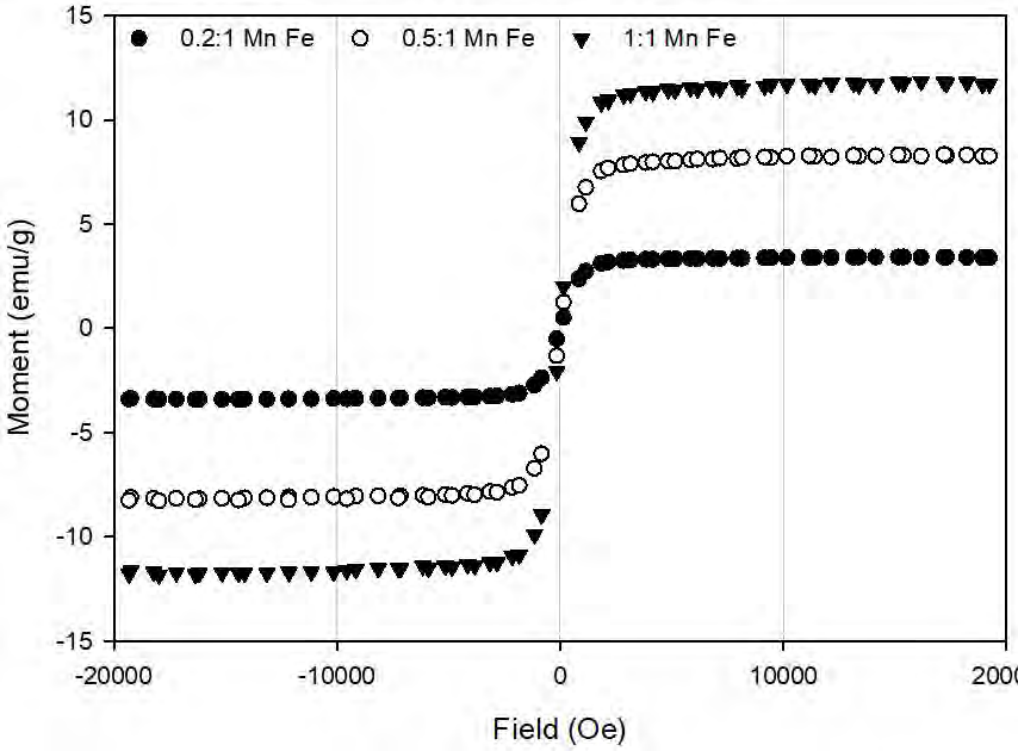


Figure 93 Magnetic response of the hybrid zeolite A using different manganese(II)-iron(III) matrix to product loadings.

Table 24 also showed a positive correlation for the other matrix materials investigated; both nickel(II)-iron(III) and iron(II)-iron(III) maintained their superparamagnetic behaviour. It is presumed that cobalt(II)-iron(III) did not maintain the behaviour seen in (4.6.2.) due to issues during synthesis rather than the zeolite synthesis altering the behaviour. The iron(II)-iron(III) system produced materials with the lowest moments, this is because during the synthesis of materials containing iron(II) it is very difficult to prevent the formation of hematite. However, depending upon the application and flow

of the solution they could be used if one of the stronger candidates could not. The two strongest hybrids were from the nickel(II)-iron(III) and manganese(II)iron(III) systems. As nickel is carcinogenic the use of manganese would be preferable as it has fewer risks to the user and the environment. Therefore, the manganese(II)-iron(III) hybrid version of zeolite would be chosen as the best option to create a readily exchangeable superparamagnetic form of zeolite A. Upon comparing these values to its competitors made using the gel based method it displays significantly stronger moments and is more similar to the moments recorded by magnetic zeolites made via coprecipitation.[1,2,7,8]

Table 24 A summary of the magnetic moments for the zeolite A hybrid materials.

Sample	Magnetic moment (emu/g)	Superparamagnetic (Y/N)
0.2:1 Fe(II) Fe(III)	0.87	Y
0.5:1 Fe(II) Fe(III)	1.27	Y
1:1 Fe(II) Fe(III)	1.94	Y
0.2:1 Co(II) Fe(III)	1.36	N
0.5:1 Co(II) Fe(III)	1.64	N
1:1 Co(II) Fe(III)	9.86	N
0.2:1 Ni(II) Fe(III)	4.35	Y
0.5:1 Ni(II) Fe(III)	6.68	Y
1:1 Ni(II) Fe(III)	10.06	Y
0.2:1 Mn(II) Fe(III)	3.70	Y
0.5:1 Mn(II) Fe(III)	8.31	Y
1:1 Mn(II) Fe(III)	12.2	Y

5.5. Zeolite A Hybrids and their ion exchange capabilities

Powder XRF analysis of each sample was performed to check the Si/Al ratios. The 0.2:1 and 0.5:1 samples were approximately 1 but increased to ~1.05 at 1:1 which is in the expected region. The expected ratio for a non-magnetised form of zeolite A made using a similar method was 1.10. This confirms there would be the expected number of sodium cations for exchange.

To confirm that the hybrid was suitable for the remediation applications, Cs^{+} and Sr^{2+} ion exchanges were performed to compare the uptake of the non-magnetic form of zeolite A to the new hybrid form. The hybrid zeolite A with different amounts of aluminosilicate matrix incorporated were tested to determine if the incorporation of the matrix had affected the ion exchangeability. To investigate this the zeolite was dispersed in a 10ppm stock solution of either Cs^{+} or Sr^{2+} and shaken until equilibrium was achieved (24 hours). The Cs^{+} and Sr^{2+} cations were kept separate as comparing uptake was the premise of the experiment as opposed to investigating selectivity with competing cations present. The experiment involved two separate sets of exchanges: in one set the amount of active zeolite was scaled to account for the matrix, thus the uptake would be comparable, and the second set was unscaled. An example of the scaling is Fe(II) zeolite A made using a 0.2:1 ratio had approximately 10.3% magnetic material based on XRF analysis. Therefore, by scaling the zeolite mass by this amount (0.03g to 0.0331g) will result in the amount of active material being comparable between exchanges. Performing a scaled and unscaled ion exchange will demonstrate the effect (if any) the magnetic content has.

A comparison of the Cs^+ uptake is shown in Figure 94. Although Cs^+ uptake is known to be unfavourable in zeolite A, Figure 94 showed approximately a 92.2% uptake. Both the scaled and unscaled had uptake values greater than 92%. For the scaled experiment this is to be expected as there could have been more active zeolite present than had been accounted for. This is likely to be the same reasoning for the unscaled zeolites appearing to take up more than the parent zeolite as it is unlikely that the incorporation of the spinel has improved uptake. Overall Figure 94 showed that the incorporation of the magnetic material does not appear to negatively impact the uptake of Cs^+ in zeolite A. Usually the adsorption decreases with an increase in magnetic content but, in this case the magnetic content is shown to not affect adsorption and this demonstrates how the new method is clearly superior to its predecessors.[1]

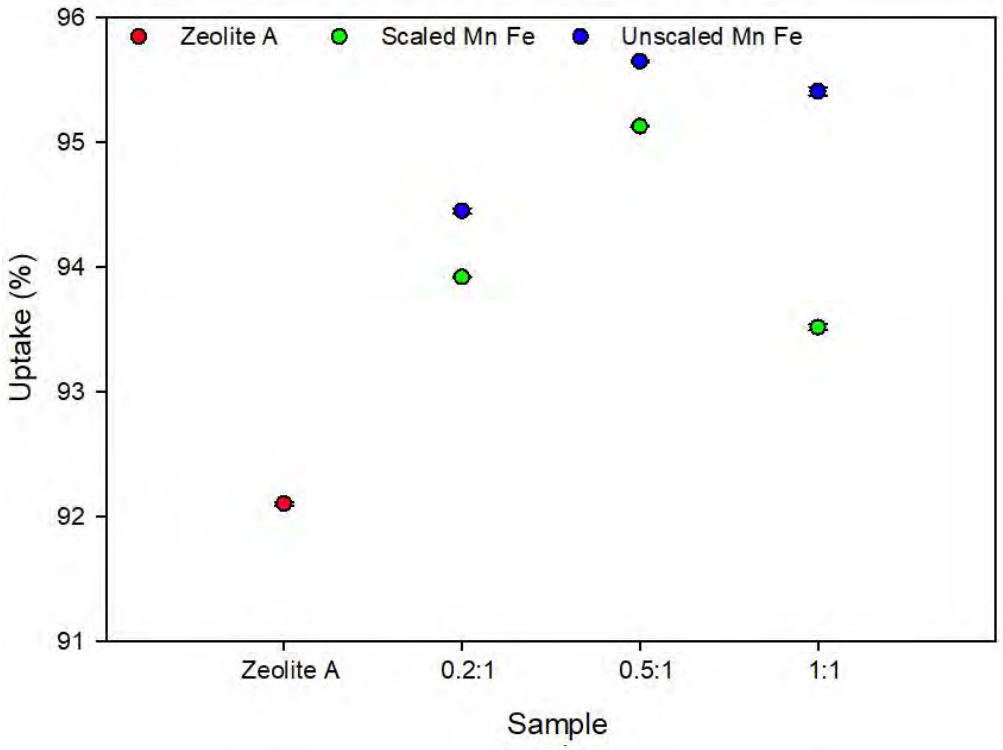


Figure 94 A comparison of the Cs^+ uptake in the magnetised and un-magnetised forms of zeolite A when using a Mn(II) Fe(III) matrix. RSDs are included but are too small to be seen.

After confirming the success of Cs^{+} uptake in the manganese(II)iron(II) hybrid zeolite A, Sr^{2+} uptake was then investigated, results are shown in Figure 95. Figure 95 showed almost complete uptake was achieved after 24 hours regardless of the host zeolite. The scaled and unscaled values were almost identical for the 0.5:1 and 1:1 hence the points are stacked on top of one another. This again suggested that the incorporation did not negatively influence uptake.

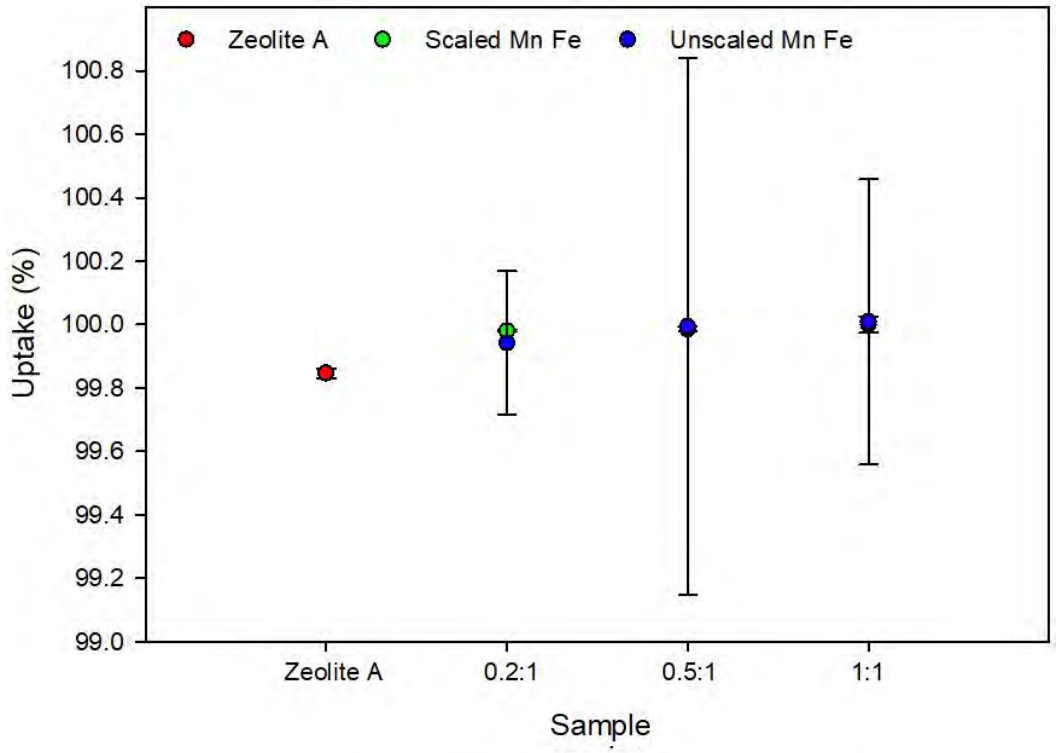


Figure 95 A comparison of the Sr^{2+} uptake in the magnetised and un-magnetised forms of zeolite A when using a Mn(II) Fe(III) matrix.

The uptake experiments were also carried out on the iron(II)-iron(III) form of zeolite A to reinforce that incorporation does not negatively affect ion exchange. The results are summarised in Table 25. Table 25 confirms that the same behaviour was seen for this hybrid material as for the manganese(II)-iron(III) system. Therefore, this confirms that the proposed synthesis method is successful in synthesising hybrid zeolites that have

unaffected ion exchange abilities and therefore, are new magnetic ion exchange materials for waste remediation or solid-liquid separations.

Table 25 A comparison of Cs^{+} and Sr^{2+} uptake in the magnetised and non-magnetised forms of zeolite A.

Sample		Cs^{+} uptake (%)	Sr^{2+} uptake (%)
Zeolite A		92.15	99.84
0.2:1 Fe Fe	Scaled	95.47	99.13
	Unscaled	99.99	99.98
0.5:1 Fe Fe	Scaled	96.10	99.98
	Unscaled	99.99	99.99
1:1 Fe Fe	Scaled	96.82	99.99
	Unscaled	99.99	100.00

5.6. Synthesis and characterisation of zeolite X hybrids

Having demonstrated the success in the formation of magnetic hybrids of zeolite A, a similar method was applied to the zeolite X system. Initial experiments focused on incorporation without any pretreatment. Unfortunately, the same problems arose with the zeolite not properly developing or the zeolites that did form being unmagnetised. Therefore, to overcome this, a digestion was again employed. Commonly zeolite X is synthesised in a HDPE bottle. However, as the synthesis included a digestion step the whole synthesis was transferred into a steel autoclave. This solved several of the synthesis issues related to overpressure where it caused the HDPE bottles to burst. Various digestion and synthesis conditions were used. The respective hybrid zeolites were analysed using XRD and SEM with results summarised in Table 26. All initial testing used 25% matrix content (0.25:1).

Table 26 showed that when the liquor was kept after the digestion, if the NaOH concentration was ≥1.25 M, then zeolite A formation was favoured, with zeolite X merely an impurity up to 2 M. After which the synthesis was hampered resulting in the formation of SiO_2. However, at 1 M NaOH, zeolite X was the dominant phase with a small zeolite A impurity. Although appearing successful SEM showed the matrix did not appear to be well incorporated with most of the zeolite unmagnetised. Conversely when the liquor was replaced by water, zeolite X was the main phase up to 2 M where the synthesis was disrupted. However, at a NaOH concentration ≥1.25 M the morphology of the particles changed from spheres to fibrous particles.

Table 26 Experimental digestion and subsequent synthesis conditions to produce zeolite X hybrid materials.

Digestion concentration	Digestion liquor kept (or replaced by water) Y/N	Synthesis result	SEM analysis showed?
1M	Y	Zeolite X/ zeolite A impurity	Rounded edged cubes. No contrast differences. Zeolite appeared unmagnetised.
1.25M	Y	Zeolite A/ zeolite X impurity	N/A
1.5M	Y	Zeolite A/ zeolite X impurity	N/A
2M	Y	SiO_2	N/A
1M	N	Zeolite X only	Small sphere type particles. Regions of higher contrast. Low loading resulted in the zeolite appearing mostly unmagnetised
1.25M	N	Zeolite X/ zeolite A impurity	Zeolite appeared as fibrous particles as well as large aggregates. Less cohesion between magnetic phase and the zeolite.
1.5M	N	Zeolite X/ zeolite A impurity	See 1.25M result
2M	N	SiO_2	N/A

Although Table 26 showed that digestion had limited success in synthesizing zeolite X, at a NaOH concentration of 1M with water as the solvent, SEM analysis showed that the zeolite appeared mostly unmagnetised due to the matrix appearing to have larger particles than that of those completed in stronger base. However, a typical zeolite X synthesis does not require the use of NaOH. The presence of this in greater concentrations was changing the pH significantly and therefore causing zeolite A formation either as the dominant phase or as an impurity. To circumvent this the digestion step was removed although the digestion was shown to be required in the synthesis of zeolite A hybrids due to the larger aggregates disrupting the synthesis. To overcome this issue the matrix material was ball milled at 150 rpm using ZrO_2 grinding media in a RETSCH XRD-Mill McCrone before being combined with the metasilicate and aluminate solutions. A XRD pattern of zeolite X made using milled material is shown in Figure 96, which confirmed that milling enabled zeolite nucleation to occur with the matrix present, but the zeolite formed was poorly crystalline.

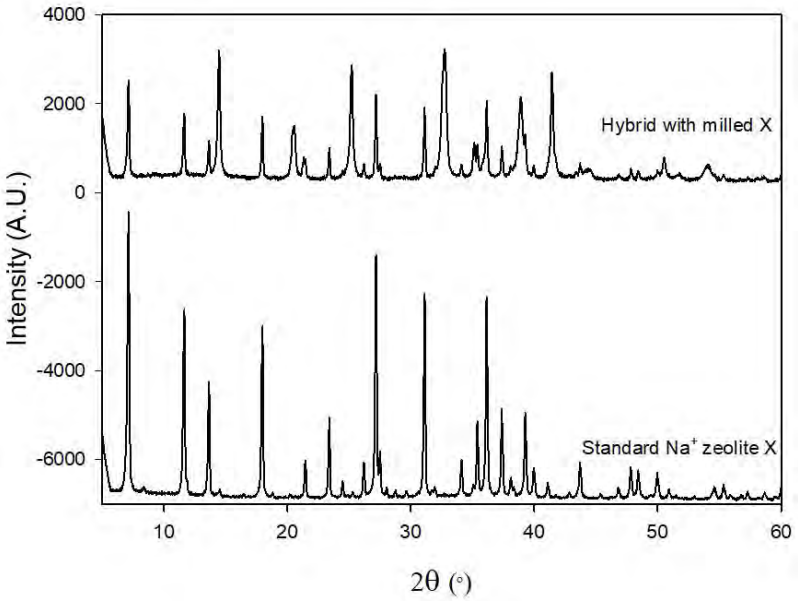


Figure 96 XRD pattern of zeolite X made using a milled matrix. A pattern of Na-X has been included for comparison.

SEM images in Figure 97 confirmed that milling of the matrix reduced the particle size sufficiently to allow for uninhibited formation of the zeolite. The particle size reduction allowed for a more uniform distribution throughout the zeolite compared to that seen when using a NaOH digestion at the same level of loading. Although Figure 97 was created using the lowest matrix loading there were several areas that contained the high contrast particles. EDX analysis confirmed these particles contained iron and Mn in the correct ratios expected for $MnFe_2O_4$.

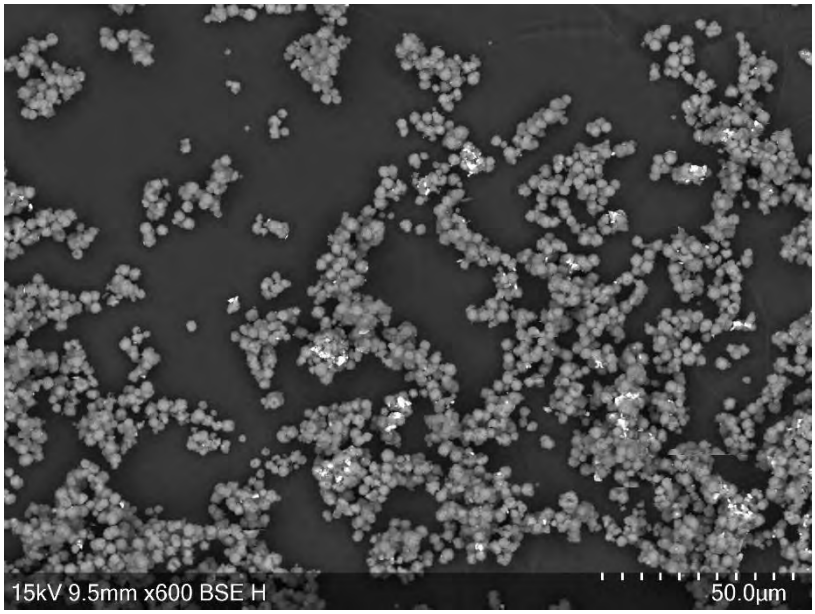


Figure 97 An SEM image of a zeolite X hybrid made using milled matrix in a 0.25:1 ratio under standard synthesis conditions.

After confirming that the synthesis method proposed above produced repeatable results, an investigation into the optimal metal loading was started. Initial testing used a 0.25:1 matrix content (25%), this was increased to 0.5:1, 1:1 and 1.5:1 with the XRD patterns relating to this shown in Figure 98. Any ratio greater than 1.5:1 under current conditions disrupted the synthesis (appendix section 5.2.1). Each of the patterns in Figure 98 contained a small peak at 8˚; this is an indication of a zeolite A. Zeolite A commonly forms during the synthesis of zeolite X due to the closeness in their Si/Al ratios and structure. Both comprise of beta cages but in zeolite A these are joined by D4R, whereas in zeolite X they are joined by D6R. Therefore, if there are regions of slight Si deficiency, due to poor mixing for example, this favours the formation of zeolite A. However, as zeolite A reflections have low intensities, most of the framework was FAU(X). Figure 98 showed that the intensity in the reflections related to the spinel increased with metal content. This suggested that greater amount of the spinel was incorporated. This was again confirmed using electron microscopy to detect areas of

higher and lower contrast as was completed for the zeolite A hybrids. However, conversely to zeolite A, in the highest loading (1.5:1) the magnetic component did not completely disperse uniformly to magnetise individual zeolites particles and instead magnetised the larger clusters. However, this still facilitated solid-liquid magnetic separation. The incomplete dispersion suggested that the loading would need to be increased if a greater magnetic moment was needed or if magnetisation of individual zeolites was required. The Si/Al ratios of these hybrids ranged from ~1.13 to ~1.14; a non-magnetised form of zeolite X synthesised during this project typically had a ratio of 1.15. Therefore, these new materials have an expected Si/Al ratio.

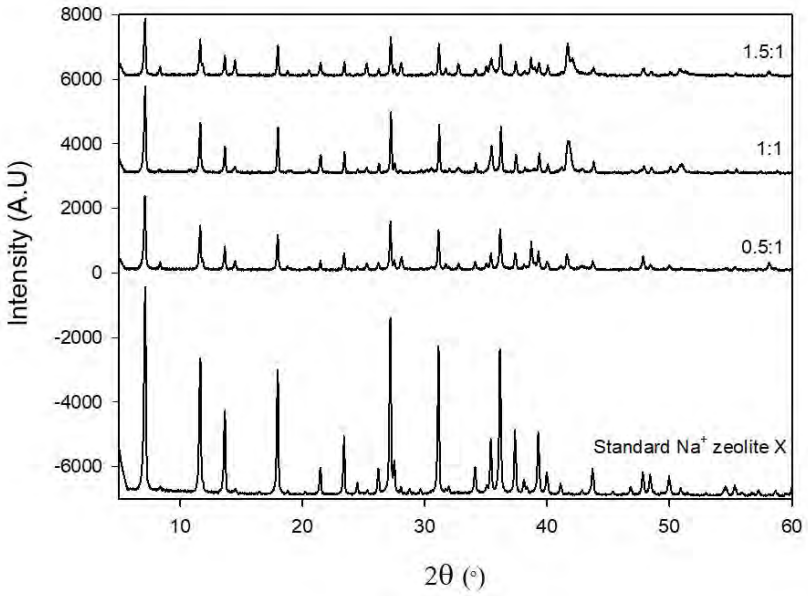


Figure 98 XRD patterns of zeolite X hybrids made using different amounts of matrix content. A standard form of zeolite X has been added for comparison.

5.7. Magnetic characterisation of zeolite X hybrids

Initial magnetic testing with an Nd bar magnet found that all the zeolite was attracted regardless of the loading used. Therefore, all the magnetic products would be analysed by VSM. Unfortunately, it was not possible to collect a complete set of VSM for every system. Of the two systems that were measured; nickel(II)-iron(III) and manganese(II)-iron(III), the best magnetic moments were displayed by the nickel(II)-iron(III) system (Figure 99). The manganese(II)-iron(III) data are included in the appendix section 5.2.2.

Similarly to the zeolite A hybrids, Figure 99 showed a positive correlation between the amount of matrix and the magnetic moment. Analysis of SEM images expected this, as more spinel was distributed throughout the zeolite as the amount of spinel was increased. All the materials measured were again superparamagnetic with a maximum moment of 8.57 emu/g. The values achieved were slightly less than was achieved by the hybrids of zeolite A, however, the SEM images of the 1.5:1 ratio suggested more of the aluminosilicate matrix could be incorporated if desired. However, it remained unknown how this current level of loading has affected the ion exchange behaviour and this level of magnetism is considered sufficient for the application therefore, no further loading was attempted.

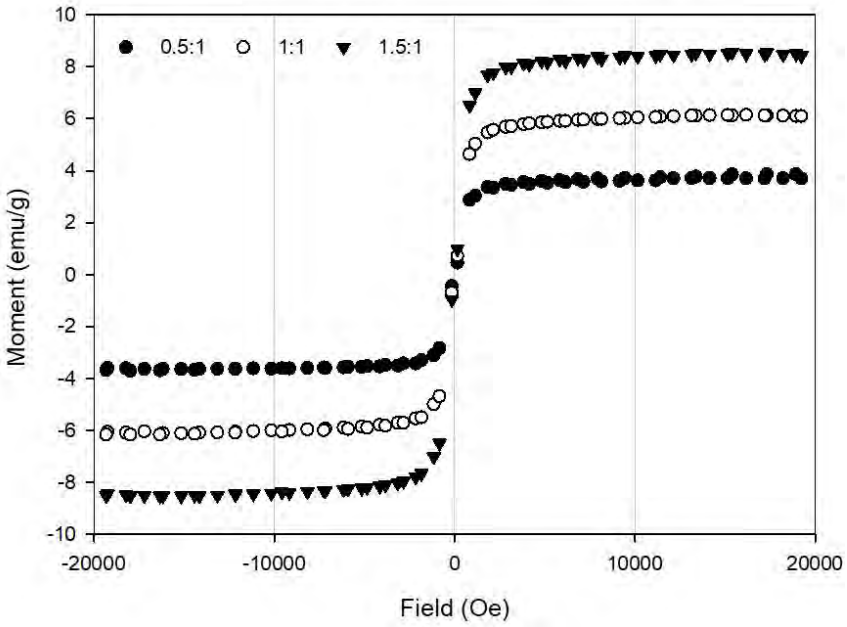


Figure 99 Magnetic response of the hybrid zeolite X using different amounts nickel(II)-iron(III) matrix alongside standard synthesis reagents.

5.8. Ion exchange capabilities of zeolite X hybrids

The ion exchange behaviour of the X hybrids was investigated to confirm that the hybrid was suitable for the remediation application. The ion exchanges that were completed compared the uptake of the non-magnetic form of zeolite X to the new hybrid form. The hybrid zeolite X with different amounts of aluminosilicate matrix incorporated were tested to determine if the incorporation of the matrix had affected the ion exchange capability. The method was kept the same as described previously. A comparison of the Cs^+ uptake in nickel(II)-iron(III)-X (NiFe-X) is shown in Figure 100.

Cs^+ uptake has been reported to be favourable in zeolite X in the absence of competing cations.[9] Figure 100 showed that the standard sodium form had a ~90.2% uptake. Both the scaled and unscaled had uptake values greater than 90.2%. The scaled exchanges plateaued at ~96% for both the 1:1 and 1.5:1 which suggests this was the upper bound of the exchange. It is currently unknown how the matrix incorporation changes the size and shape of the pores and channels but Figure 100 suggests there is not any negative effects. After confirming the success of Cs^+ uptake, Sr^{2+} uptake was then investigated, results are shown in Figure 101.

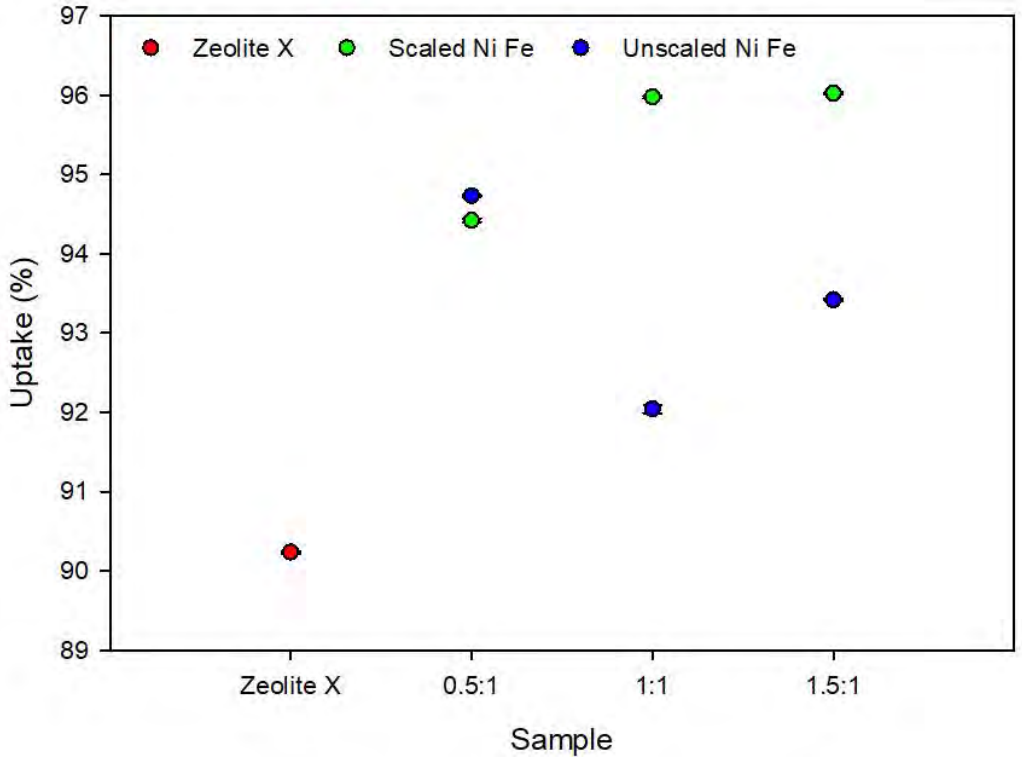


Figure 100 A comparison of the Cs+ uptake in the magnetised and un-magnetised forms of zeolite X when using a Ni(II) Fe(III) matrix. RSDs are included but are too small to be seen.

Figure 101 showed almost complete uptake was achieved after 24 hours regardless of the host zeolite. The scaled and unscaled values were identical with several points stacked on top of one another. Results presented again suggested that the incorporation did not negatively influence Sr^{2+} uptake. Therefore, this confirms that the zeolite X hybrid zeolites are possible as new ion exchange materials for magnetic separation. Given that these hybrids had presented with similar levels of exchange to those presented for the zeolite A hybrids, the application environment would influence the hybrid of choice i.e. the acidity of the waste stream.

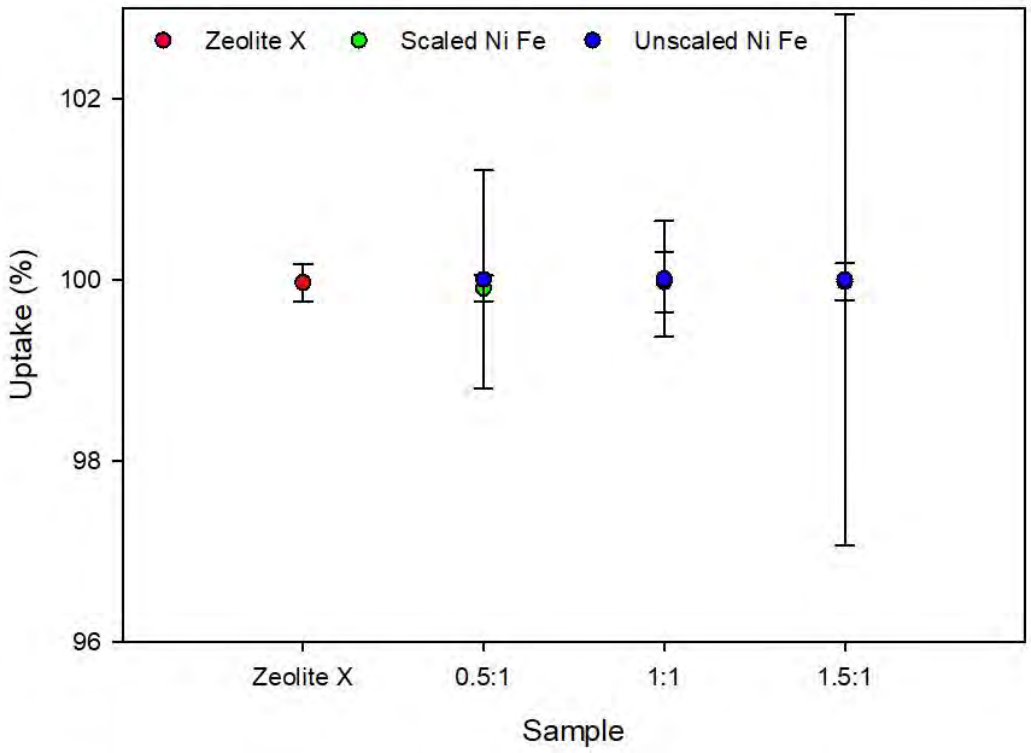


Figure 101 A comparison of the Sr^{2+} uptake in the magnetised and un-magnetised forms of zeolite X when using a Ni(II) Fe(III) matrix.

5.9. Synthesis and characterisation of zeolite Y and chabazite hybrids

Hybrid versions of zeolite Y and chabazite were also made as the parent zeolites are reported to be effective Cs^+ exchangers. Zeolite Y required extensive grinding of the aluminosilicate matrix to allow for incorporation. Whereas chabazite preferred digestion but using KOH instead of NaOH. Chabazite was synthesised using the ammonium form of zeolite Y, which was broken down using KOH and then slowly recrystallised into chabazite. The presence of Na^+ from a digestion pretreatment disrupted the recrystallisation process entirely hence KOH was used instead. Both systems were subjected to the same SEM and STEM analysis procedures outlined previously and were also found to have chemically bound to their respective zeolite hosts. The magnetic loading was optimised for each system with their magnetic responses compiled in Table 27. Due to restrictions only two systems could be fully characterised. All data presented in Table 27 exhibited superparamagnetism. Hybrid versions of these zeolites used the same matrix notation as described previously. XRD patterns relating to the magnetisation optimisation for both zeolite systems can be found in the appendix section 5.8.

Table 27 showed that the synthesis method of both systems had some degree of success in terms of incorporation. The iron(II)-iron(III) matrices of both systems appeared to be the weakest except for CHA-Fe(II)Fe(III)-1.5:1 which had the greatest moment of all hybrid zeolites presented. This suggested that difference in the batches used to magnetise the zeolites was significant. These hybrid syntheses required the use of a 23ml autoclave. The amount of matrix required to magnetise this amount of

material was significant, and as the matrix materials were synthesised in a tube furnace, there was a limit on how much could be made each time. As the formation of the iron(II)-iron(III) matrix was the most delicate, regardless of the zeolite system, due to how readily hematite formation occurred, this was then reflected in the variation of the magnetic moments recorded. The nickel(II)-iron(III) matrix in both systems showed the linear trend seen previously for the A and X hybrids. This suggested that the synthesis method had been successful, and the issues presented for the synthesis of the iron(II)-iron(III) matrices was related to their own synthesis as opposed to failure to incorporate to create the hybrid material.

Table 27 The magnetic moments of zeolite Y and Chabazite hybrid materials synthesised with different magnetic loadings.

Hybrid zeolite and matrix used	Moment measured at given matrix content (emu/g)		
Zeolite Y	**0.5:1**	**1:1**	**1.5:1**
Iron(II) iron(III)	0.5	1.16	0.86
Nickel(II) iron(III)	1.39	7.28	11.19
Chabazite	**0.5:1**	**1:1**	**1.5:1**
Iron(II) iron(III)	0.8	0.8	15.1
Nickel(II) iron(III)	4.63	6.53	6.02

After confirming the chabazite and Y hybrids had sufficient levels of magnetism the ion exchange behaviour was investigated with the results summarised in Table 28 and Table 29. Both hybrids displayed the same behaviour as the other hybrids investigated in that magnetisation did not negatively impact their ion exchange properties.

Table 28 A comparison of Cs^+ and Sr^{2+} uptake in the magnetised zeolite Y hybrids and their non-magnetised counterpart.

Sample		Cs^+ uptake (%)	Sr^{2+} uptake (%)
Zeolite Y		95.94	99.86
0.5:1 Ni Fe	Scaled	96.95	99.88
	Unscaled	96.54	99.96
1:1 Ni Fe	Scaled	98.88	99.96
	Unscaled	98.84	99.91
1.5:1 Ni Fe	Scaled	97.45	99.87
	Unscaled	97.62	99.93

Table 29 A comparison of Cs^+ and Sr^{2+} uptake in the magnetised chabazite hybrids and their non-magnetised counterpart.

Sample		Cs^+ uptake (%)	Sr^{2+} uptake (%)
Chabazite		97.06	99.57
0.5:1 Ni Fe	Scaled	96.94	99.95
	Unscaled	97.98	99.88
1:1 Ni Fe	Scaled	97.34	99.91
	Unscaled	97.98	99.86
1.5:1 Ni Fe	Scaled	98.44	99.95
	Unscaled	98.18	99.82

5.10. Conclusion

This chapter has shown the development of several new synthesis methods to create superparamagnetic forms of zeolite A, X, Y and chabazite. It has shown issues related to creating these hybrids and possible methods of overcoming them, through a digestion or milling. Use of SEM was able to confirm that dissolution of the vitreous aluminosilicate matrix reduced particle size. In the formation of zeolite X hybrids, milling provided an equally successful alternative. STEM was able to confirm that the magnetic particles were embedded within all the hybrid zeolites. This provides a greater mechanical strength than merely precipitating on the surface which was known to be an issue with the predecessor. TGA data from the zeolite A hybrid suggested the incorporation did not affect the thermal stability of the zeolite. VSM analysis showed there was a positive correlation between the magnetic moment and matrix loading regardless of the zeolite system. VSM measurements confirmed that the hybrids displayed suitable magnetic moments for their applications, whilst the Cs^{+} and Sr^{2+} comparison exchanges confirmed that the inclusion of the magnetic particles does not affect the materials ion exchange capabilities. This confirmed that the novel synthetic methods presented create new magnetically separating ion exchange materials with superior exchange properties than alternative methods at similar levels of magnetisation.

5.11 References

1 J. Cao, X.-W. Liu, R. Fu and Z. Tan, *Sep. Purif. Technol.*, 2008, **63**, 92–100.

2 H. Liu, S. Peng, L. Shu, T. Chen, T. Bao and R. L. Frost, *Chemosphere*, 2013, **91**, 1539–1546.

3 L. C. A. Oliveira, D. I. Petkowicz, A. Smaniotto and S. B. C. Pergher, *Water Res.*, 2004, **38**, 3699–3704.

4 I. W. Nah, K. Y. Hwang, C. Jeon and H. B. Choi, *Miner. Eng.*, 2006, **19**, 1452–1455.

5 J. Dong, Z. Xu and S. M. Kuznicki, *Adv. Funct. Mater.*, 2009, **19**, 1268–1275.

6 H. Park, S. K. Terhorst, R. K. Bera and R. Ryoo, *Carbon N. Y.*, 2019, **155**, 570–579.

7 D. Feng, C. Aldrich and H. Tan, *Hydrometallurgy*, 2000, **56**, 359–368.

8 H. Faghihian, M. Moayed, A. Firooz and M. Iravani, *Comptes Rendus Chim.*, 2014, **17**, 108–117.

9 P. K. Sinha, P. K. Panicker, R. V. Amalraj and V. Krishnasamy, *Waste Manag.*, 1995, **15**, 149–157.

Chapter 6. Summary and further work

6.1. Summary

The first aim of this research was to optimise the aqueous ion exchange of transition metals (TMs) in zeolites A, X and Y to achieve exchange levels that are usually observed after multiple exchanges. After successfully ion exchanging the TM into the zeolite, the next aim was to develop magnetic nanoparticles to create an ion exchanging zeolite with superparamagnetic separation capabilities.

The aqueous ion exchange chapter of this thesis and respective sections of the appendix have thoroughly explored the one-step aqueous exchange of several TMs in zeolites A, X and Y, with optimised conditions determined. The work presented in certain cases achieved exchange levels which have previously only been obtained through multiple exchanges. The levels were found to vastly exceed what is expected during the exchange of a divalent cation which has suggested that there is an additional process occurring alongside ion exchange. The anion of the exchange salt was shown to have a negligible effect on the level of exchange.

The time-based studies found that the degree of over-exchange was shown to be related to the cation itself, with iron(II) favouring over-exchange. This was proposed to be due to how readily iron(II) oxidises. This results in large amounts of iron oxide on the surface of the zeolite resulting in greater amounts of iron detected. This was seen to a lesser extent in the other octahedrally coordinating cations, cobalt(II) and nickel(II), due to slower oxidisation. Manganese(II) exchange was also found to result in over-exchange but this was proposed to be due to the monovalent $Mn(OH)^{+}$ forming at the

pH used. Due to its smaller hydrated radius, it can result in a higher quantity of manganese bound to the zeolite than would be expected from ion exchange alone. For the time-based exchanges, zinc was the only system found to not over-exchange, this series of exchanges were carried out at the least acidic pH which suggests that over-exchange could be related to pH. At the pH used it is proposed that zinc exists as the monovalent $[Zn(OH)]^{+}$, ionic pair $[Zn(OH_2)]^{0}$ or as ZnO clusters. Absorption of these species results in lower mobility, ultimately disabling the ion exchange. Due to the issues relating to zinc/sodium determination, WD-XRF analysis alone does not provide conclusive evidence to determine whether zinc over exchange occurs.

The investigation into the effects of temperature and concentration in these aqueous exchanges found that the exchange of manganese(II) and zinc(II) is unaffected by temperature. This was proposed to be due to manganese having the lowest hydration energy (-1845 kJ mol^{-1}) and therefore the process did not require additional energy provided by the increase in temperatures to remove the hydration shell. Instead, the outward exchange of sodium into the external solution was the limiting factor, thus the more concentrated solutions had a greater sodium content. Regarding zinc, it was thought that the adsorption is disabled therefore temperature cannot affect the level of exchange. The exchange levels for the three remaining cations; iron, cobalt and nickel were affected by both concentration and temperature. Using a more concentrated solution was shown to negatively affect uptake regardless of the cation used. This has been proposed to be due to pore blocking; this effectively disables the exchange process because there are too many cations present in solution. In contrast, temperature was shown to positively affect the levels of ion exchange. Temperature directly relates to the kinetic energy of the metal cations. By increasing the temperature

there is additional kinetic energy given to the cations, thereby increasing the rate of diffusion. Altering the temperature will also affect the equilibrium absorption capacity of the adsorbent for the metal cations. In a more general view, an increase in temperature results in higher levels of exchange. This is proposed to be due to the zeolite exhibiting a higher affinity for the metal cations and/or an increase in the number of active sites on the surface of the zeolite. At elevated temperatures, it has been shown that the energy of the system facilitates the attachment of metals on its surface. These factors explain why an increase in metal exchange was observed. However, it does not explain why exchange levels are greater than would be expected for a divalent cation. Surface deposition of an oxide or oxyhydroxide are the most plausible species. Neither of these were detected except in the case of iron(II)-A where hematite was detected by Raman spectroscopy. At the pH used for exchanges dissolution is expected as opposed to precipitation. However, it is possible for these species to occur within the pores as there is separate intrapore chemistry compared to that in the exchange solution. It is difficult to determine the reason for the over-exchange as the ion exchanges being studied are not considered a clean exchange of a divalent metal for sodium, there is additional chemistry occurring or over-exchange would not happen.

Chapter 4 focused around using the TM-exchanged zeolites to create a magnetic zeolite. However, it was found that under the conditions used, the zeolite broke down up to 400˚C earlier than expected. This was thought to be caused by the acidity of the reaction mixture created by the exchange salts during the melting stage. Therefore, instead of developing magnetic particles within a zeolite framework, they were trapped within an aluminosilicate matrix which had formed from the zeolite after degradation. It was proposed that due to the Si/Al content of the matrix materials, it could be

incorporated into a synthesis of a new zeolite which would then be capable of ion exchange. Therefore, the optimisation of the synthesis was explored. The anion was found to affect the phase formed, with a nitrate salt favouring the formation of hematite regardless of the divalent cation. In contrast, the chloride anion favoured the development of a spinel phase alongside hematite. The presence of hematite as an impurity was an issue, and it was suggested that it was caused by an oxidation reaction. To minimise the oxidation, the synthesis was performed under a nitrogen atmosphere, this significantly reduced hematite formation therefore promoting the formation of the desired phase.

The identity of the spinel phase was unknown, to determine its identity Raman spectroscopy was employed as vibrational modes of the possible products are different. The Raman spectrum collected on the cobalt(II)-iron(III) matrix produced a spectrum that matched closely to that of $CoFe_2O_4$. However, the iron(II)-iron(III) matrix produced a spectrum that only matched to hematite. This was proposed to be caused by the hematite forming on the surface with the secondary phase trapped within the bulk. As Raman spectroscopy is a surface-based technique it did not have the required penetration depth. ^{57}Fe Mössbauer spectroscopy was used instead as it is more sensitive to identification of magnetically ordered phases as there is a difference in the magnitude of their magnetic hyperfine fields. Mössbauer spectroscopy also removed the surface limitations of Raman spectroscopy as it probes the bulk of the sample. It confirmed the formation of magnetite and $CoFe_2O_4$ in the iron(II)-iron(III) and cobalt(II)-iron(III) matrices respectively.

Although the identity of the secondary phase had been determined, the reaction pathway had not been established. To explore this TGA/DTA was used to identify regions of interest which could be focused on during VT-XRD analysis. Unfortunately, equipment limitations meant that phase formation was unable to be captured. However, VT-XRD provided proof that use of a slower ramp to high temperatures favoured the formation of hematite. This suggested that the hypothesis that higher temperatures promoted greater mixing to develop greater amounts of the desired phase was plausible. With this knowledge the optimised process was applied to the remaining TM-exchanged zeolites.

Given the application in magnetic remediation, the best method to determine the optimal conditions was by comparing the magnetic behaviour. It was found that use of a synthesis temperature of 1000˚C at a 2:1 M(II):Fe(III) produced the greatest magnetic moment. Increasing or decreasing this ratio was found to significantly reduce the magnetic moment, as the formation of alternate phases was favoured. VSM confirmed that 4 out of 5 (4/5) systems were magnetic for zeolite A and 4/5, 3/5 for zeolites X and Y respectively. The largest magnetic moment was recorded by Mn(II)-Fe(III)-A at 65.78 emu/g of magnetic material. All but the cobalt(II) based systems were superparamagnetic. The cobalt(II) systems instead required a 1:1 ratio. The ferromagnetism displayed by the 2:1 system was thought to be caused by the size of the particles exceeding 10 nm.

After establishing that these materials could be made in two-steps, a one-step process was explored. This involved the addition of the di- and trivalent cations simultaneously. This method was also found to generate magnetic particles, however, as there were still additional cations present, new phases began to develop. This however did not

appear to impact the magnetic moment of the cobalt(II)-iron(III) system as a moment of 61.4 emu/g of magnetic material was measured. The one-step procedure was not as successful in the iron(II)-iron(III) system, and this was thought to be due to how readily the iron oxidises, therefore it favoured the formation of hematite. Based upon this only the cobalt(II)-iron(III) system made in one-step was taken forward to magnetise a new form of zeolite.

The initial synthesis of zeolite A hybrids focused around using the aluminosilicate matrix directly in a standard zeolite A synthesis, however this was unsuccessful. The large matrix aggregates inhibited the zeolite nucleation around the particles. In the regions where the synthesis was uninhibited, unmagnetised zeolite particles were formed. An increase in the crystallisation time from 5 to 24 hours was shown to significantly increase the crystallinity of the zeolite when the matrix material was used.

The failure to incorporate the matrix material was thought to stem from differences in in solubility between the aluminosilicate matrix and the reagents commonly used in zeolite synthesis and the size of the particles. The aluminosilicate matrix was digested in NaOH to help reduce the particle size and overcome the differences in solubility. A range of concentrations were used with 1.25 M found to be optimal. Typically, the digestions were only partial, but there was always a reduction in particle size and the differences in solubilities were alleviated.

SEM images suggested there were regions of the hybrid that remained unmagnetised at a 20% matrix content. Therefore, the amount of magnetic material loaded into the hybrid was increased to 50%, 100% and 200% (0.5:1, 1:1 and 2:1 respectively). The hybrid made using a 200% matrix content showed signs that nucleation had been

inhibited similar to using undigested aluminosilicate matrix. Therefore, the maximum loading was found to be a 100% matrix content alongside the standard reagents. This equated to a magnetic loading of ~21 wt%, which was significantly more than the predecessors that achieved a maximum of 4.7 wt%.

Use of electron microscopy and elemental mapping suggested that the matrix particles were embedded within the zeolite framework. This suggested that the particles were chemically bound to the zeolite which provides greater mechanical strength than precipitating on the surface of the zeolite.

The magnetic behaviour of the hybrid materials showed that there was a linear relationship between the matrix content and the size of the magnetic moment. All of the zeolite A hybrids maintained the superparamagnetic behaviour of the parent materials, and 12.2 emu/g was the strongest moment recorded. This level of magnetism is similar to that created by coprecipitation but was proposed to have a more accessible surface area due to the absence of surface fouling.

In the absence of BET measurements, the impact of incorporation was determined by the ion exchange behaviour alone. The scaled and unscaled exchanges for both Cs^{+} and Sr^{2+} showed there was no negative impact in uptake compared to the unmagnetised form regardless of the matrix content. Usually, adsorption decreases with an increase in magnetic content, therefore this demonstrated how this novel method is superior to its predecessors.

The formation of zeolite X, Y and chabazite hybrids was also shown to be successful. The synthesis of these materials encountered similar solubility and particle size issues as the zeolite A hybrids. Zeolite X and Y used milling and extensive grinding whereas

chabazite required a KOH digestion to combat this. VSM measurements confirmed that the hybrids displayed suitable magnetic moments for their applications. The optimal loading was again determined for each system and those hybrid materials were exposed to Cs^{+} and Sr^{2+} solutions to determine the impact of incorporation. This again showed there was no negative impact in uptake compared to their respective unmagnetised form regardless of the matrix content. Therefore, the results confirmed that all the novel synthetic methods presented created new magnetically separating ion exchange materials with superior exchange properties.

6.2. Further work

Work in this thesis suggested that increasing the iron(III) content was unsuccessful in zeolites that contained iron(II), however, preliminary testing for the zeolites that contained the other TMs was started towards the end of the PhD. Hybrids made at a 3:1 Fe^{3+}:Mn^{2+} ratio recorded higher magnetic moments than had been observed previously at 67.84 and 51.30 (emu/g of magnetic material) for Mn(II)-Fe(III)-A and Ni(II)-Fe(III)-A respectively.

This suggests that an improvement on the magnetic moments of the hybrid materials is possible. Further synthesis would explore increasing the iron content for the other zeolites that do not contain iron(II). Although further optimisation is thought to be possible, developing greater understanding of the reaction pathway could improve the process further. For an in-situ phase formation to be captured an advanced setup is required as the synthesis requires a high temperature, N_2 gas and X-rays from a synchrotron radiation source.

The ion exchange of manganese and zinc were completed at a less acidic pH compared to the other metals. Further work could explore the adjustment of the ion exchanges solutions prior to the addition of the zeolite.

Having successfully created these new materials the next step would be to deploy them on a small scale, an example system that was built is given in Figure 102. This system was comprised of 3 separate containers. Container 1 has magnetised zeolite immersed in liquid effluent which is mixed using a mechanical overhead stirrer. After reaching the required exchange time the contents of container 1 is pumped through line one into container 2 using a peristaltic pump. Container 2 is surrounded by Nd bar magnets that attracts the magnetised zeolite allowing for solid-liquid separation. The ion exchanged liquid effluent is then pumped through line two into container 3. Container 3 contains the decontaminated solution with the exchanged zeolite remaining in container 2.

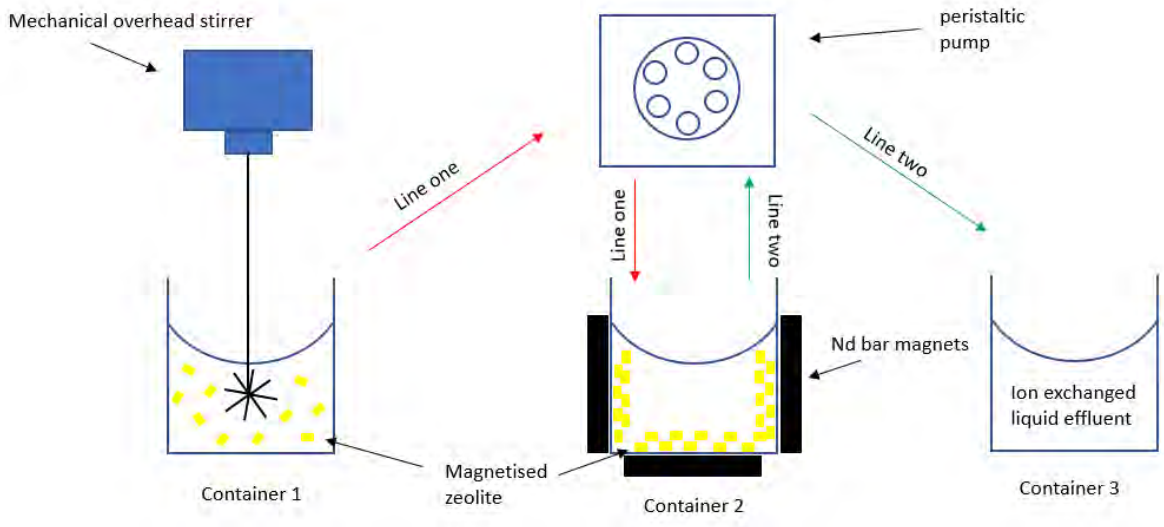


Figure 102 A diagram of an example flow system trialled using the novel exchange materials.

This system used a peristaltic pump equipped with 2.73 mm diameter tubing which allowed a flow rate of up to 12340 µl/min at 60 rpm. Although this provided a steady flow a more powerful pump would generate a more efficient system. Further work would require collaboration with academia or industry to investigate alternative flow system configurations and different types of pumps to determine an optimal small scale setup.

Appendix

Contents

Chapter 3 _____ 3

3.1. Zeolite A XRD pattern ion exchange comparisons _____ 3

3.2. Zeolite A temperature and concentration based ion exchanges _____ 6

3.3. Zeolite X time-based ion exchanges _____ 25

3.4. Zeolite X temperature and concentration based ion exchanges _____ 30

3.5. Zeolite Y time-based ion exchanges _____ 44

3.6. Zeolite Y temperature and concentration based ion exchanges _____ 48

Chapter 4 _____ 59

4.1 Zeolite X & Y synthesis XRD patterns _____ 59

4.1.1 Zeolite X _____ 59

4.1.2 Zeolite Y _____ 60

4.2 Matrix magnetic data _____ 62

4.2.1 Zeolite A _____ 62

4.2.2 Zeolite X _____ 63

4.2.3 Zeolite Y _____ 65

Chapter 5 _____ 67

5.0. Zeolite A hybrid XRD _____ 67

5.1 TGA _____ 68

5.2 Zeolite X hybrids _____69

5.2.1 Zeolite X hybrid synthesis XRD _____69

5.2.2 Magnetic characterisation of zeolite X Mn(II)Fe(III) hybrid _____70

5.3 Magnetic characterisation of zeolite Y hybrids _____71

5.4 Magnetic characterisation of chabazite hybrids _____72

5.5 Electron microscopy of zeolite X hybrids _____74

5.6 Electron microscopy of zeolite Y hybrids _____77

5.7 Electron microscopy of chabazite hybrids _____79

5.8 Hybrid zeolite Y and chabazite XRD patterns _____83

Chapter 3

3.1. Zeolite A XRD pattern ion exchange comparisons

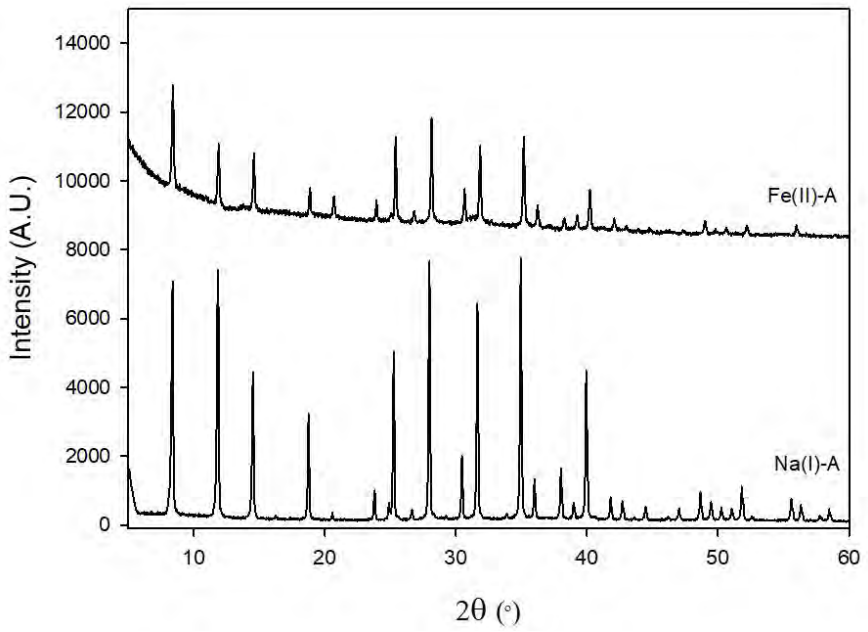


Figure 1 Comparison of the Na^{+} and Fe^{2+} zeolite A X-ray diffraction patterns before optimisation. The pattern for Fe(II)-A has been offset by 8000 counts.

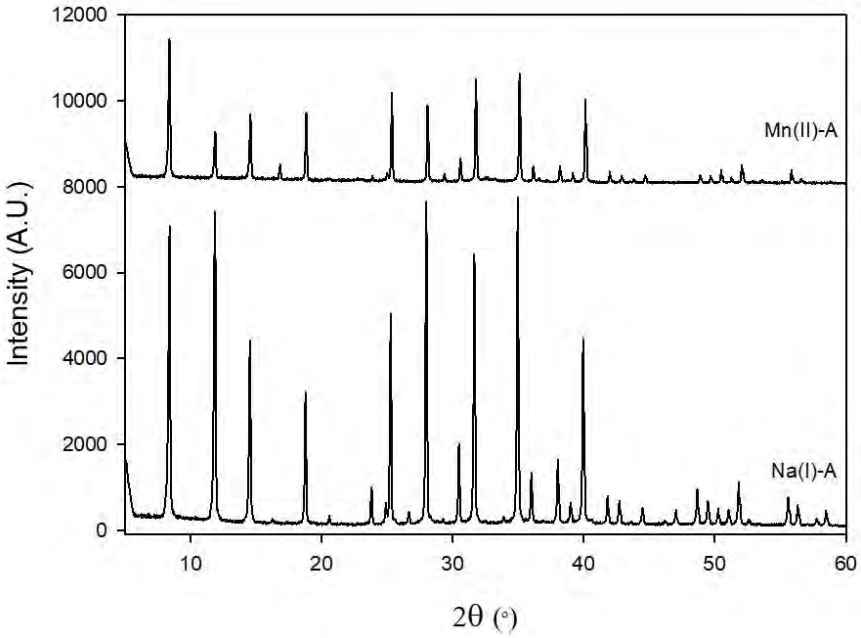


Figure 2 Comparison of the Na^{+} and Mn^{2+} zeolite A X-ray diffraction patterns before optimisation. The pattern for Mn(II)-A has been offset by 8000 counts.

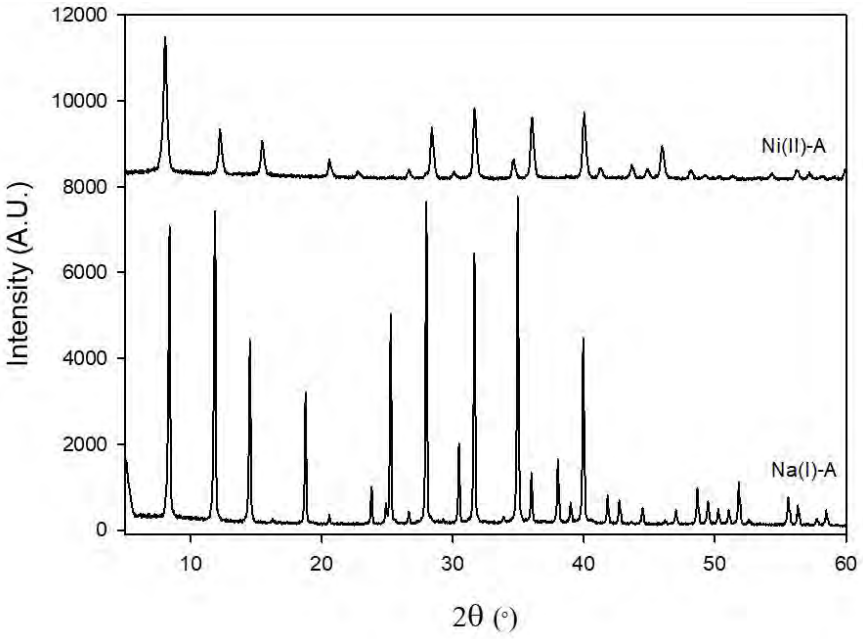


Figure 4 Comparison of the Na^{+} and Ni^{2+} zeolite A X-ray diffraction patterns before optimisation. The pattern for Ni(II)-A has been offset by 8000 counts.

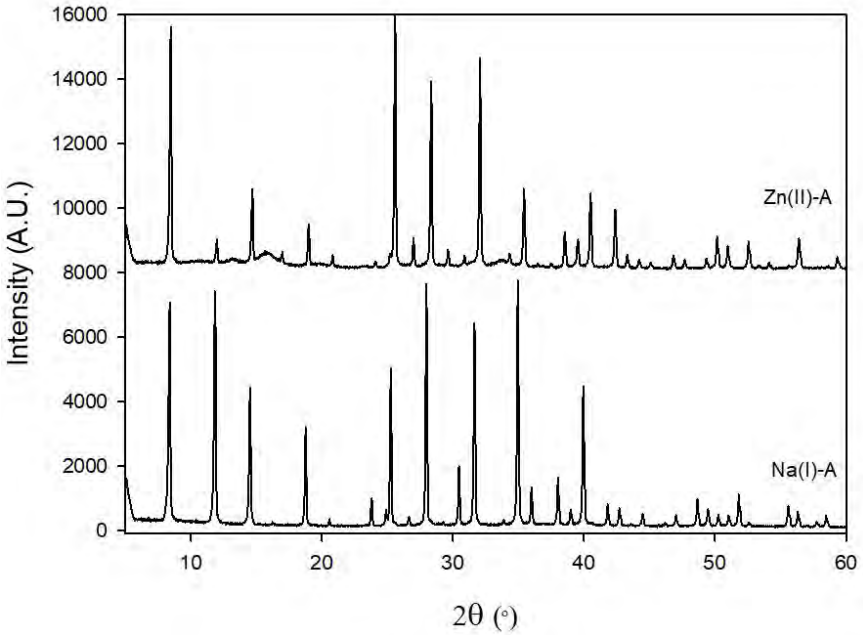


Figure 5 Comparison of the Na^{+} and Zn^{2+} zeolite A X-ray diffraction patterns before optimisation. The pattern for Co(II)-A has been offset by 8000 counts.

3.2. Zeolite A temperature and concentration based ion exchanges

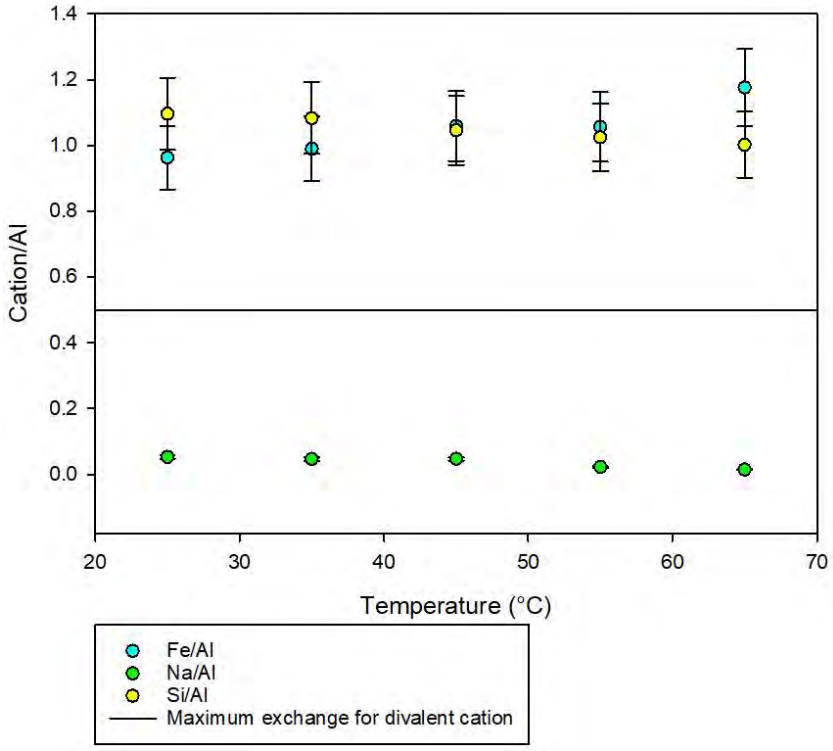


Figure 7 The effect of temperature at a concentration of 0.25 M of iron(II) chloride on Fe(II) cation exchange in zeolite A. Element ratios are calculated from WD-XRF data from dried powders in pellet form. The size of the error bars reflects a 10% error commonly associated with XRF of pellets.

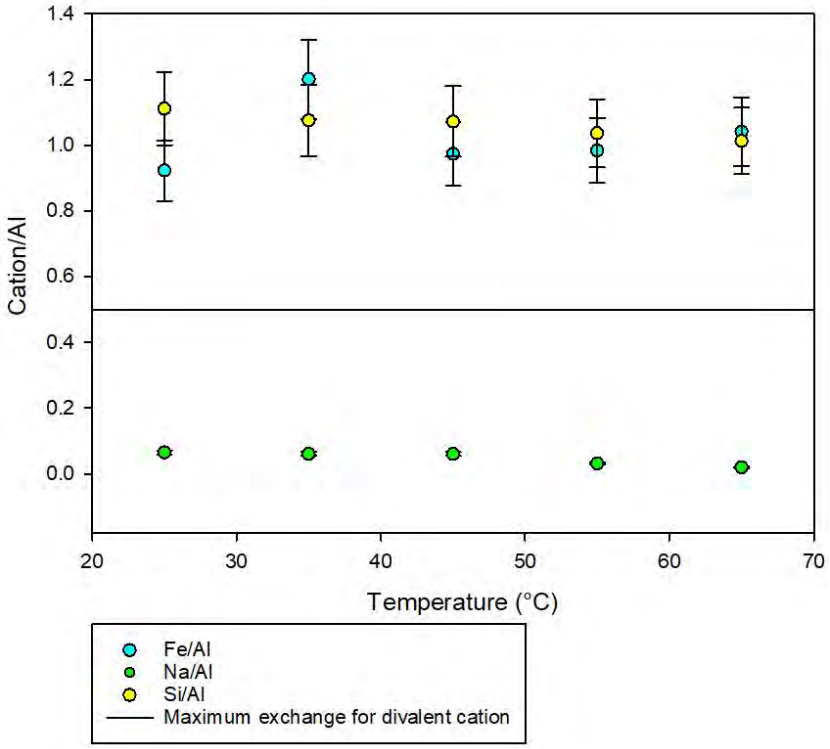


Figure 9 The effect of temperature at a concentration of 0.5 M of iron(II) chloride on Fe(II) cation exchange in zeolite A. Element ratios are calculated from WD-XRF data from dried powders in pellet form. The size of the error bars reflects a 10% error commonly associated with XRF of pellets.

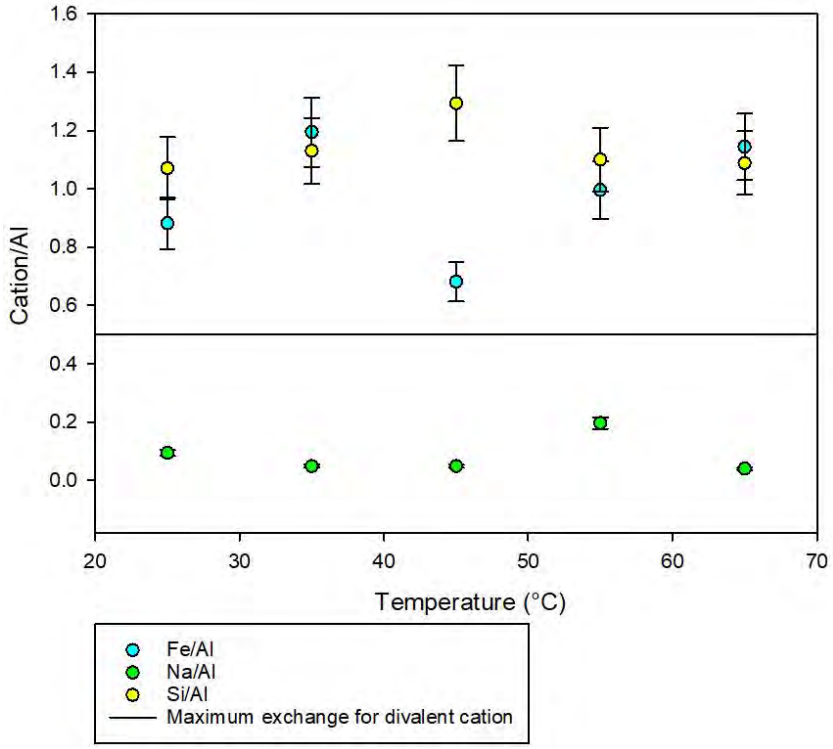


Figure 11 The effect of temperature at a concentration of 1 M of iron(II) chloride on Fe(II) cation exchange in zeolite A. Element ratios are calculated from WD-XRF data from dried powders in pellet form. The size of the error bars reflects a 10% error commonly associated with XRF of pellets.

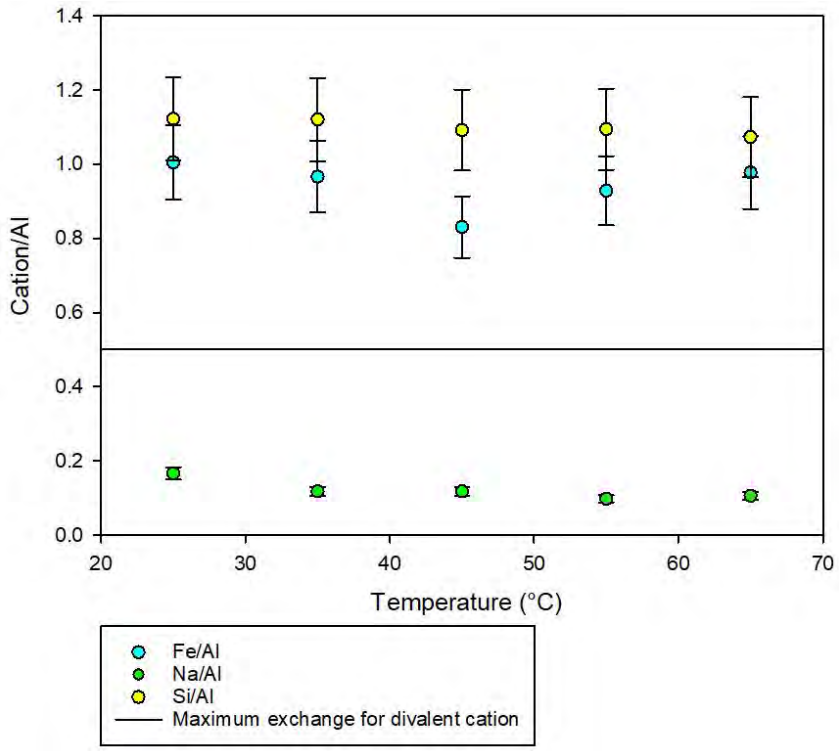


Figure 13 The effect of temperature at a concentration of 2 M of iron(II) chloride on Fe(II) cation exchange in zeolite A. Element ratios are calculated from WD-XRF data from dried powders in pellet form. The size of the error bars reflects a 10% error commonly associated with XRF of pellets.

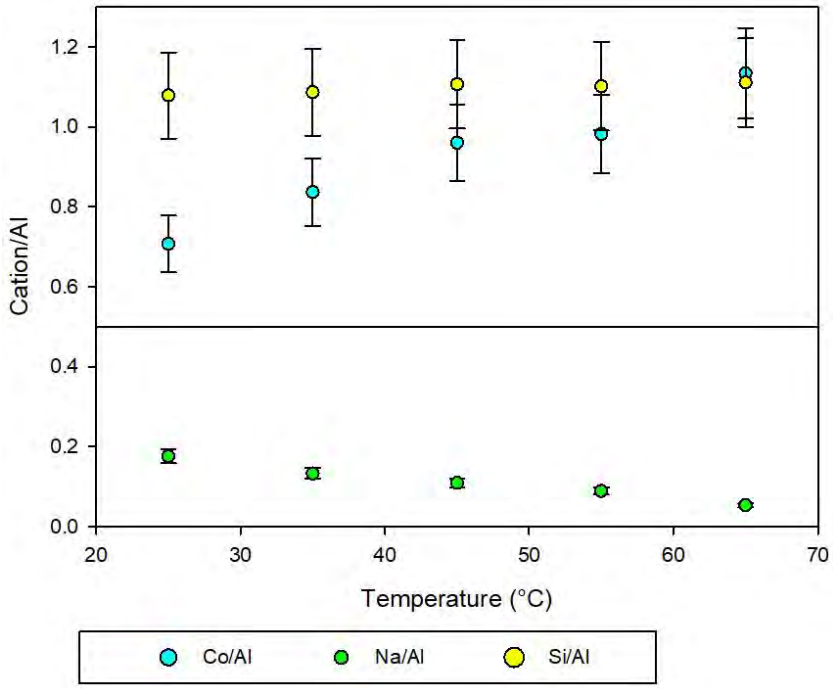


Figure 17 The effect of temperature at a concentration of 0.25 M of cobalt(II) nitrate on Co(II) cation exchange in zeolite A. Element ratios are calculated from WD-XRF data from dried powders in pellet form. The size of the error bars reflects a 10% error commonly associated with XRF of pellets.

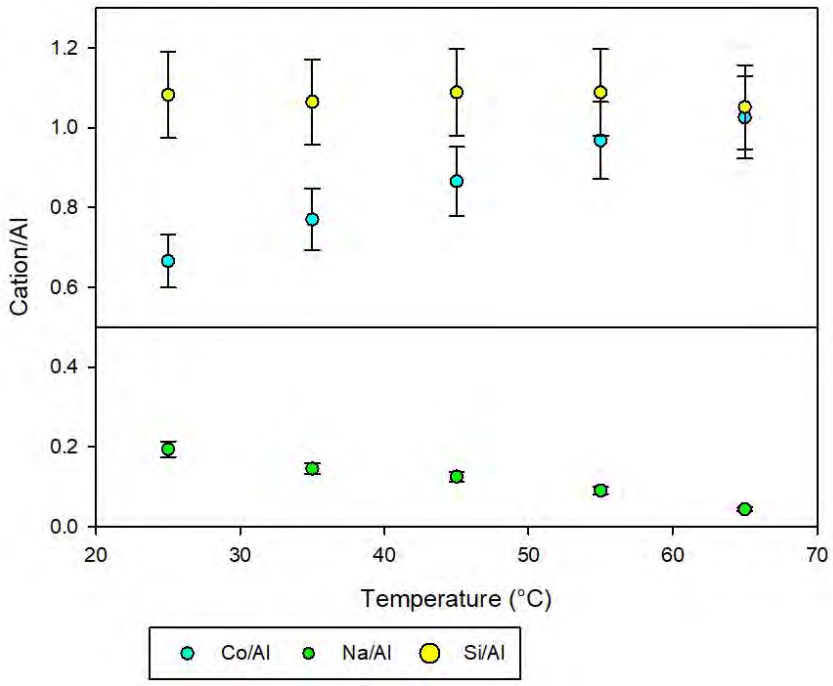


Figure 15 The effect of temperature at a concentration of 0.5 M of cobalt(II) nitrate on Co(II) cation exchange in zeolite A. Element ratios are calculated from WD-XRF data from dried powders in pellet form. The size of the error bars reflects a 10% error commonly associated with XRF of pellets.

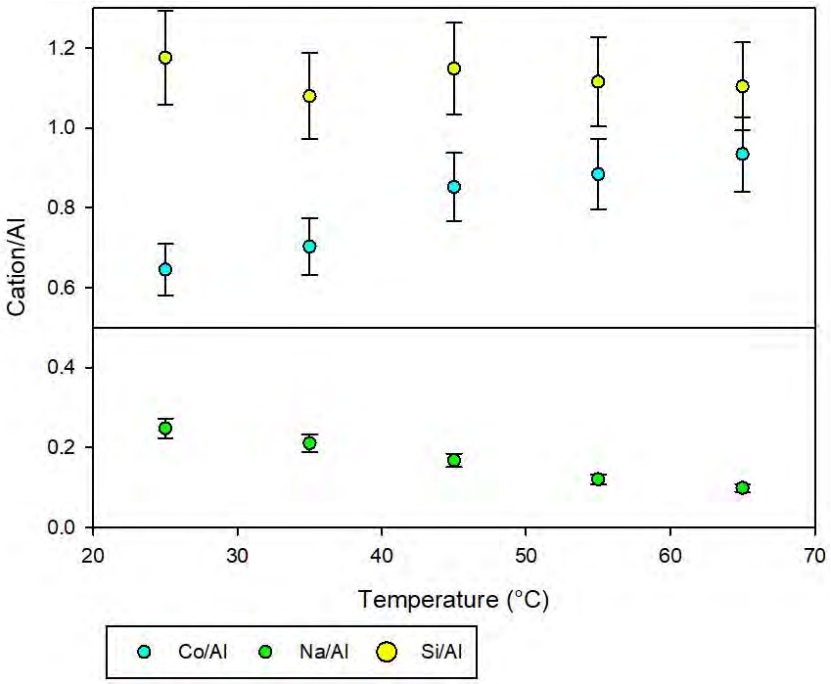


Figure 21 The effect of temperature at a concentration of 1 M of cobalt(II) nitrate on Co(II) cation exchange in zeolite A. Element ratios are calculated from WD-XRF data from dried powders in pellet form. The size of the error bars reflects a 10% error commonly associated with XRF of pellets.

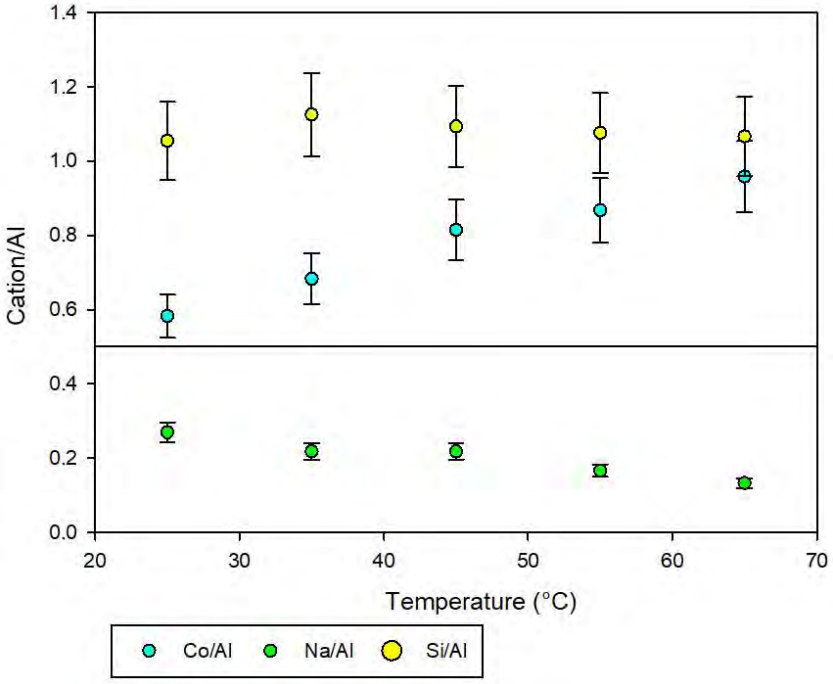


Figure 19 The effect of temperature at a concentration of 2 M of cobalt(II) nitrate on Co(II) cation exchange in zeolite A. Element ratios are calculated from WD-XRF data from dried powders in pellet form. The size of the error bars reflects a 10% error commonly associated with XRF of pellets.

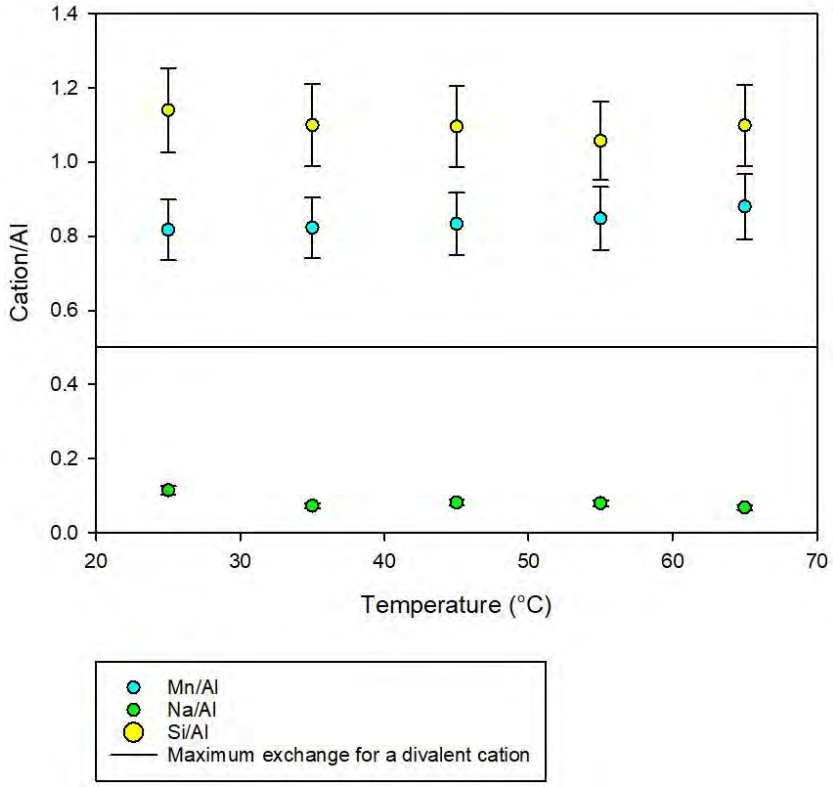


Figure 23 The effect of temperature at a concentration of 0.25 M of manganese(II) chloride on Mn(II) cation exchange in zeolite A. Element ratios are calculated from WD-XRF data from dried powders in pellet form. The size of the error bars reflects a 10% error commonly associated with XRF of pellets.

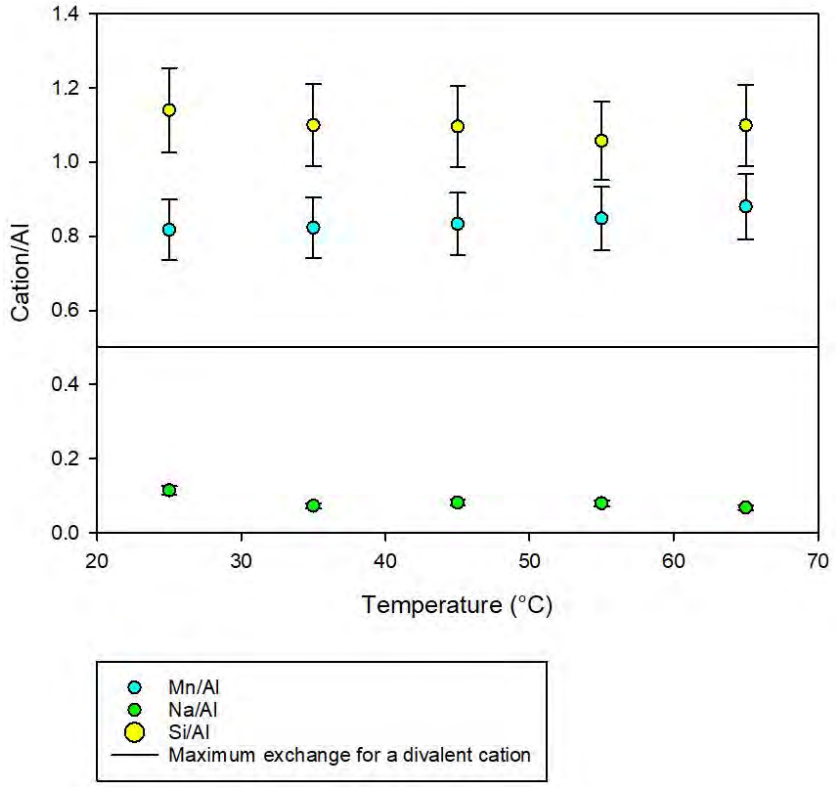


Figure 25 The effect of temperature at a concentration of 0.5 M of manganese(II) chloride on Mn(II) cation exchange in zeolite A. Element ratios are calculated from WD-XRF data from dried powders in pellet form. The size of the error bars reflects a 10% error commonly associated with XRF of pellets.

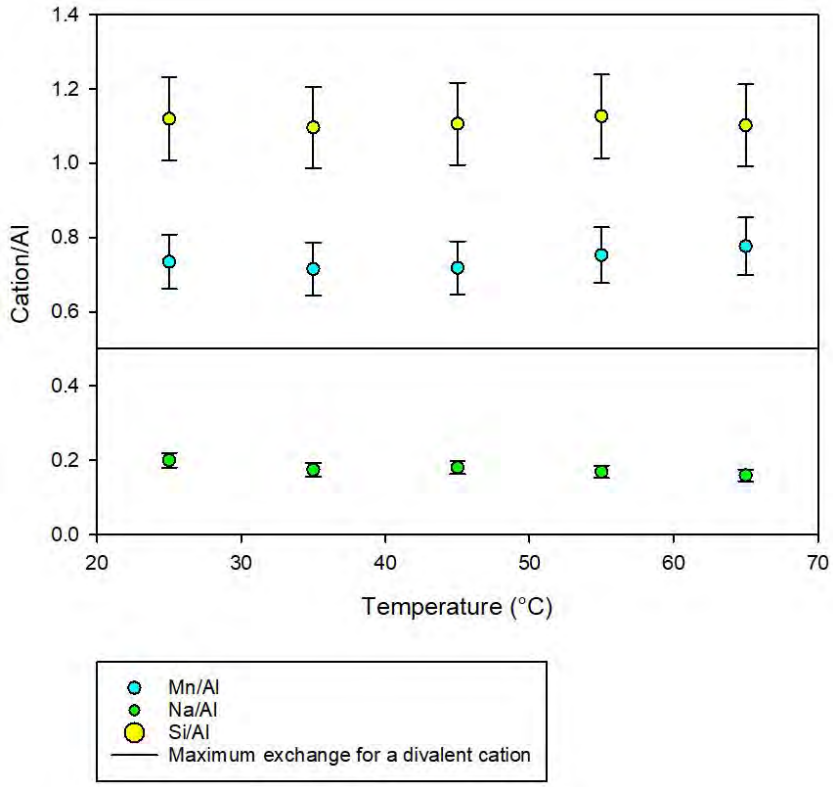


Figure 27 The effect of temperature at a concentration of 1 M of manganese(II) chloride on Mn(II) cation exchange in zeolite A. Element ratios are calculated from WD-XRF data from dried powders in pellet form. The size of the error bars reflects a 10% error commonly associated with XRF of pellets.

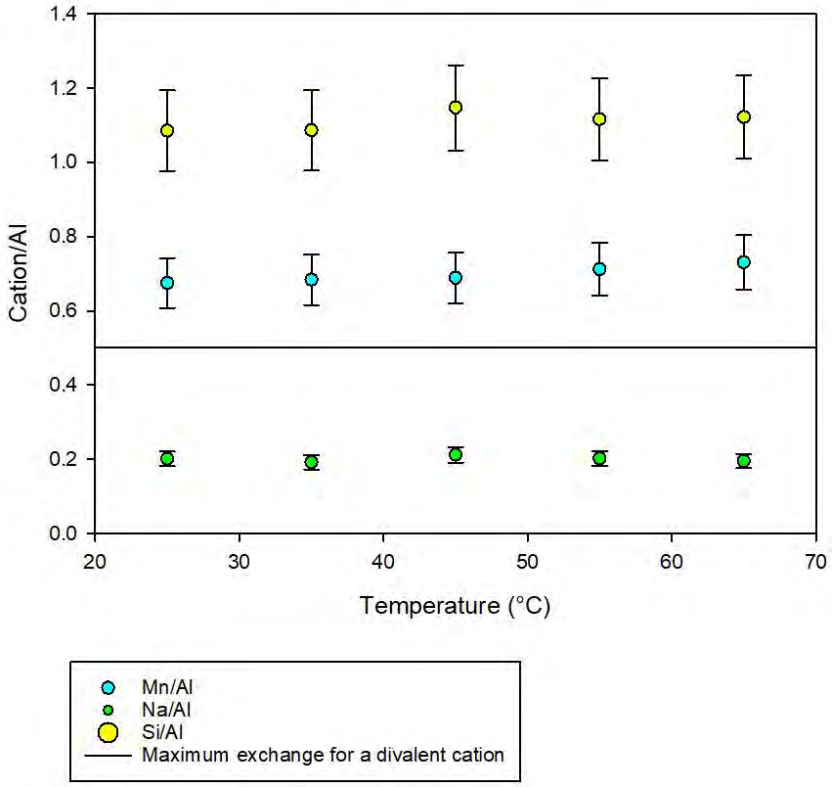


Figure 29 The effect of temperature at a concentration of 2 M of manganese(II) chloride on Mn(II) cation exchange in zeolite A. Element ratios are calculated from WD-XRF data from dried powders in pellet form. The size of the error bars reflects a 10% error commonly associated with XRF of pellets.

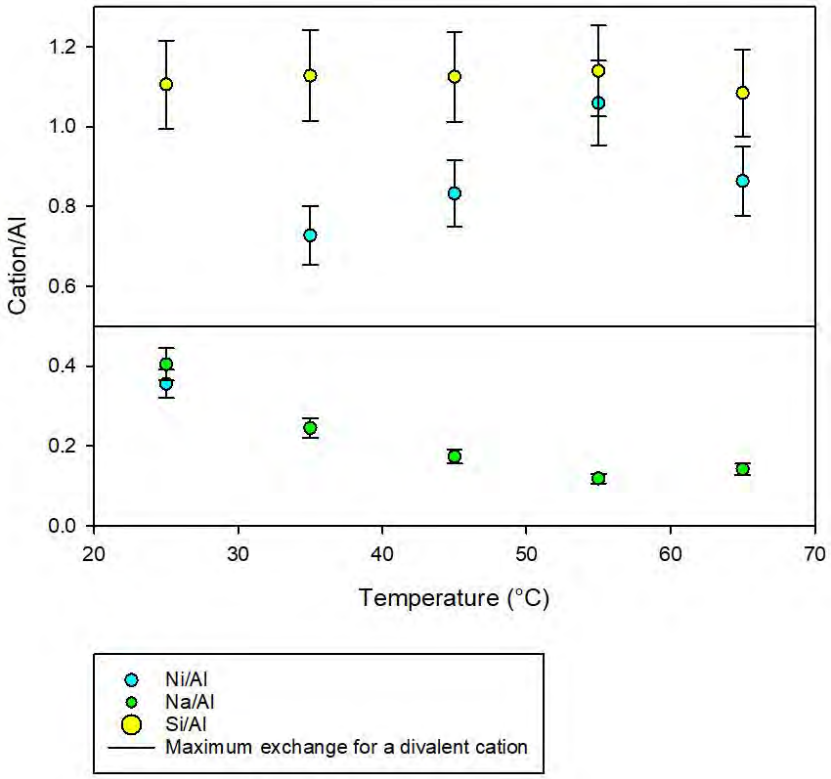


Figure 31 The effect of temperature at a concentration of 0.25 M of nickel(II) nitrate on Ni(II) cation exchange in zeolite A. Element ratios are calculated from WD-XRF data from dried powders in pellet form. The size of the error bars reflects a 10% error commonly associated with XRF of pellets.

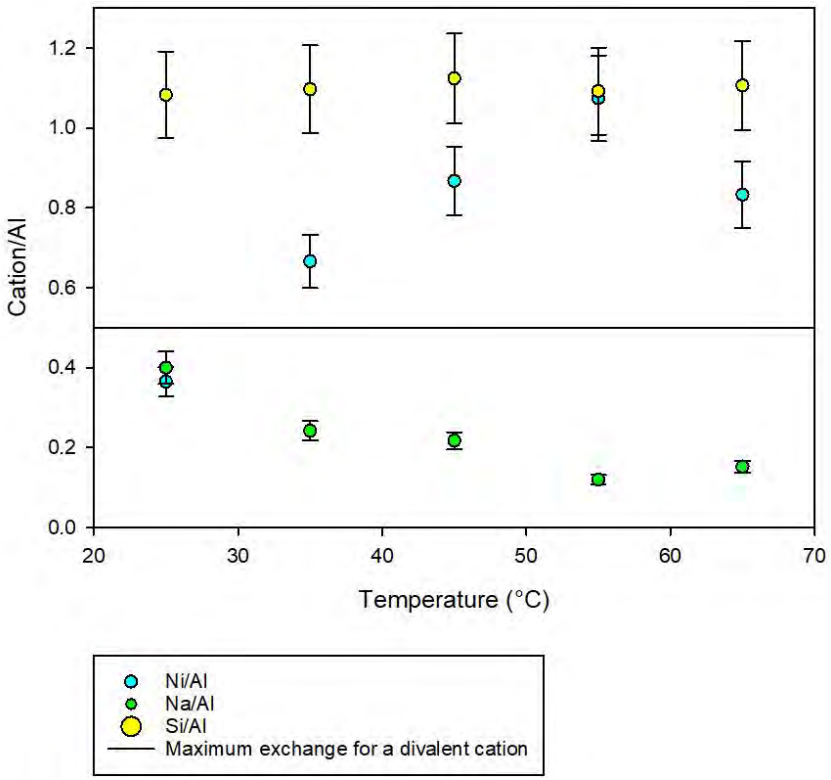


Figure 33 The effect of temperature at a concentration of 0.5 M of nickel(II) nitrate on Ni(II) cation exchange in zeolite A. Element ratios are calculated from WD-XRF data from dried powders in pellet form. The size of the error bars reflects a 10% error commonly associated with XRF of pellets.

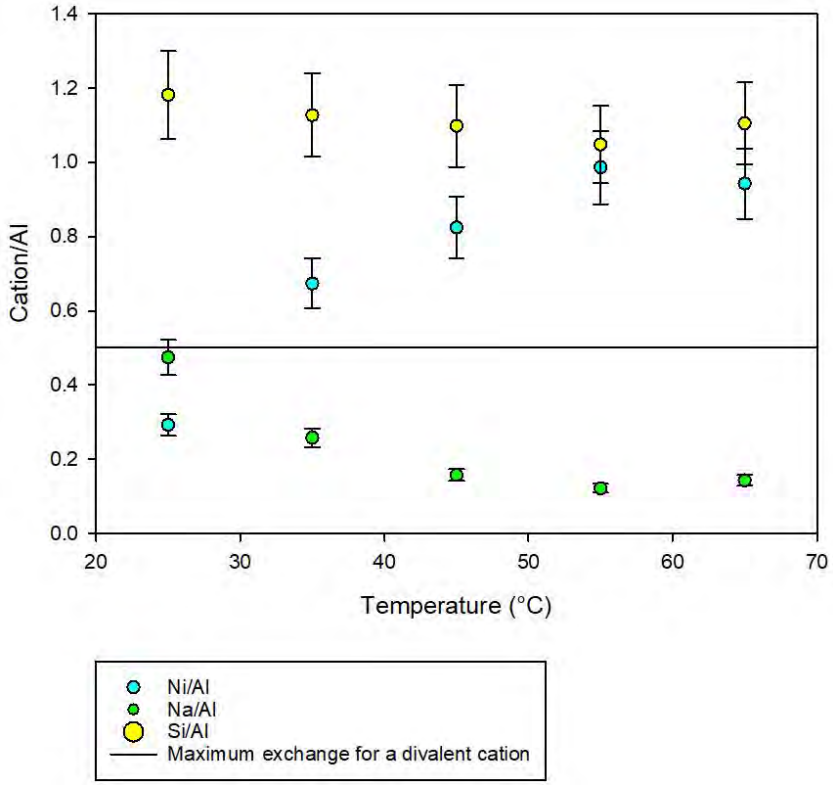


Figure 35 The effect of temperature at a concentration of 1 M of nickel(II) nitrate on Ni(II) cation exchange in zeolite A. Element ratios are calculated from WD-XRF data from dried powders in pellet form. The size of the error bars reflects a 10% error commonly associated with XRF of pellets.

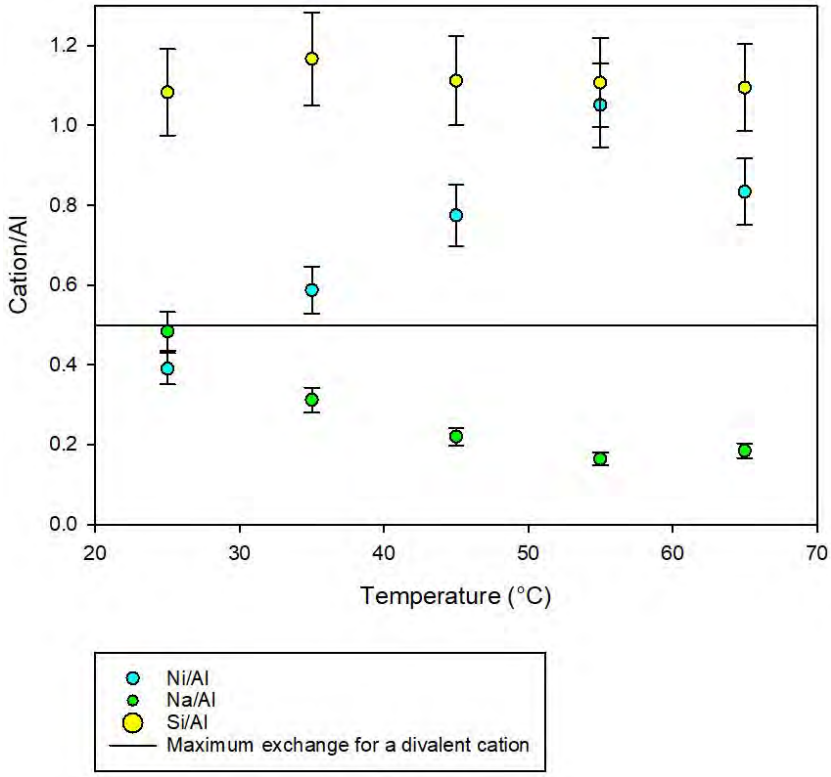


Figure 37 The effect of temperature at a concentration of 2 M of nickel(II) nitrate on Ni(II) cation exchange in zeolite A. Element ratios are calculated from WD-XRF data from dried powders in pellet form. The size of the error bars reflects a 10% error commonly associated with XRF of pellets.

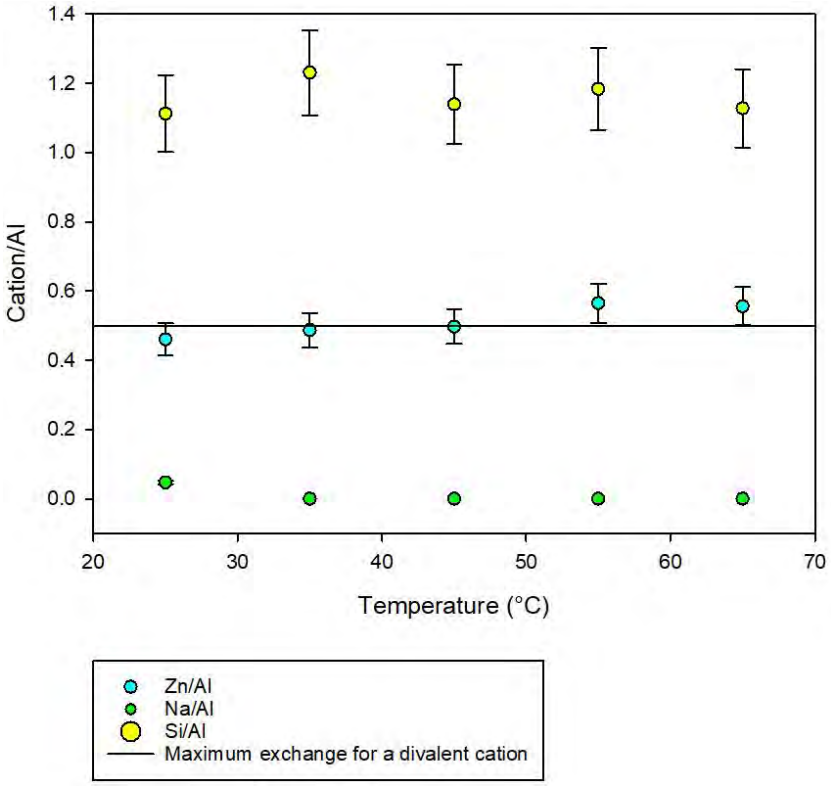


Figure 39 The effect of temperature at a concentration of 0.25 M of zinc(II) chloride on Zn(II) cation exchange in zeolite A. Element ratios are calculated from WD-XRF data from dried powders in pellet form. The size of the error bars reflects a 10% error commonly associated with XRF of pellets.

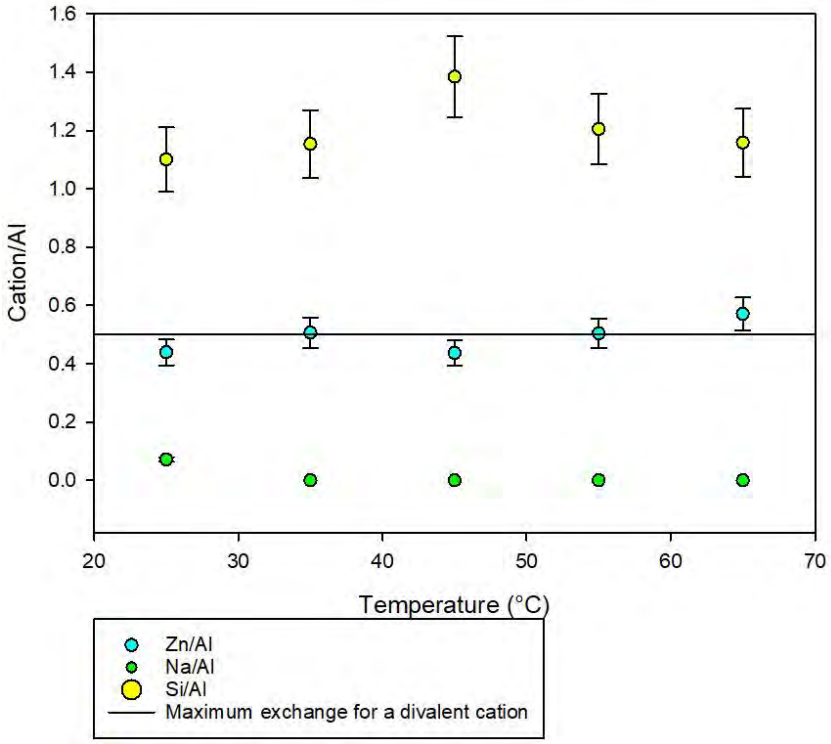


Figure 41 The effect of temperature at a concentration of 0.5 M of zinc(II) chloride on Zn(II) cation exchange in zeolite A. Element ratios are calculated from WD-XRF data from dried powders in pellet form. The size of the error bars reflects a 10% error commonly associated with XRF of pellets.

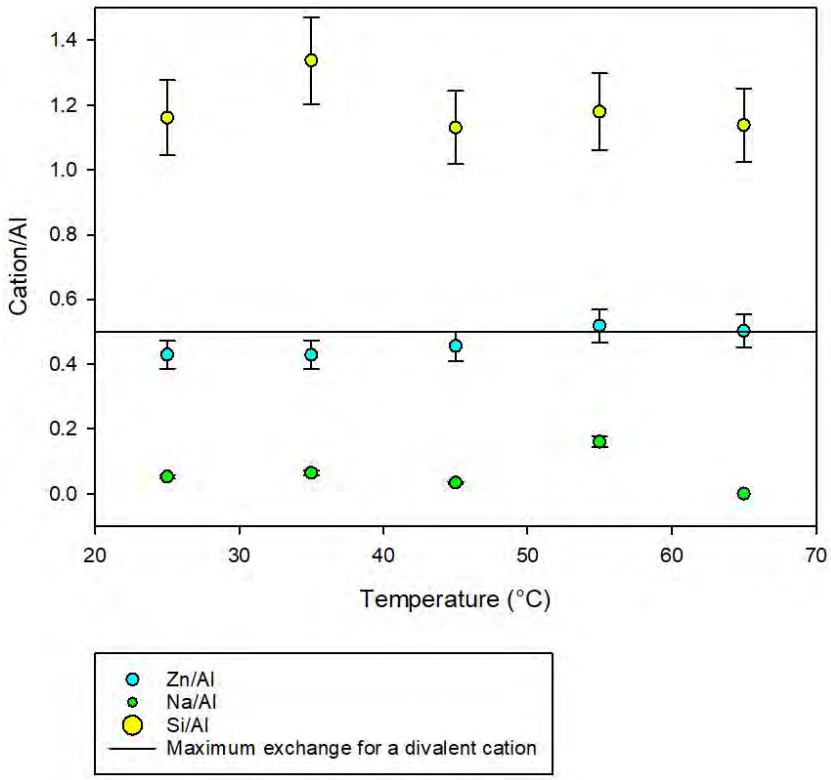


Figure 43 The effect of temperature at a concentration of 1 M of zinc(II) chloride on Zn(II) cation exchange in zeolite A. Element ratios are calculated from WD-XRF data from dried powders in pellet form. The size of the error bars reflects a 10% error commonly associated with XRF of pellets.

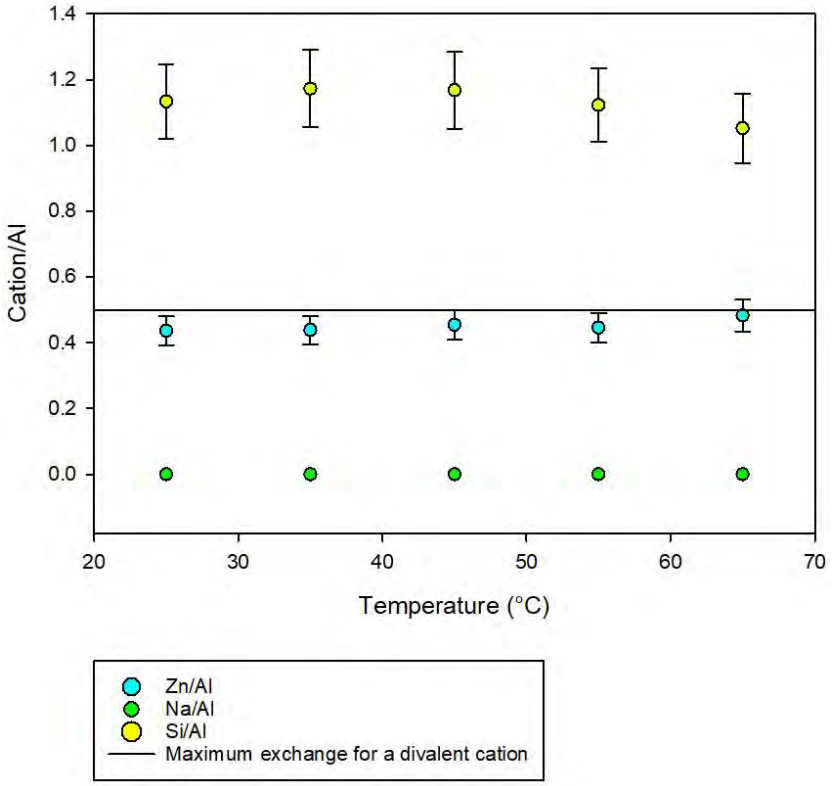


Figure 45 The effect of temperature at a concentration of 2 M of zinc(II) chloride on Zn(II) cation exchange in zeolite A. Element ratios are calculated from WD-XRF data from dried powders in pellet form. The size of the error bars reflects a 10% error commonly associated with XRF of pellets.

3.3. Zeolite X time-based ion exchanges

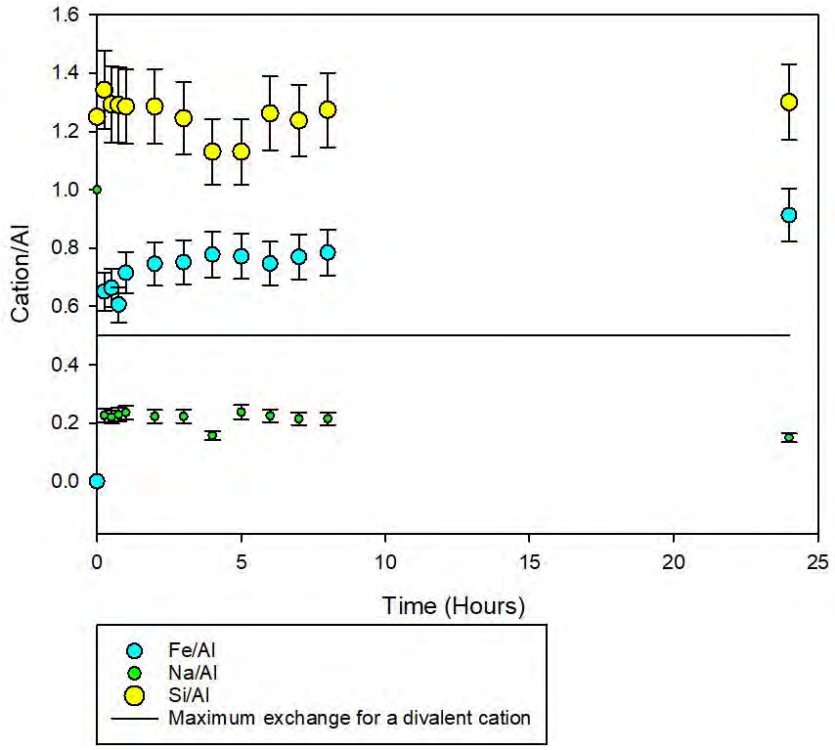


Figure 47 Time based uptake kinetics of Fe(II) in zeolite X using 0.25 M iron(II) chloride at 25˚C over a 24-hour time frame. Element ratios are calculated from WD-XRF data from dried powders in pellet form. The size of the error bars reflects a 10% error commonly associated with XRF of pellets.

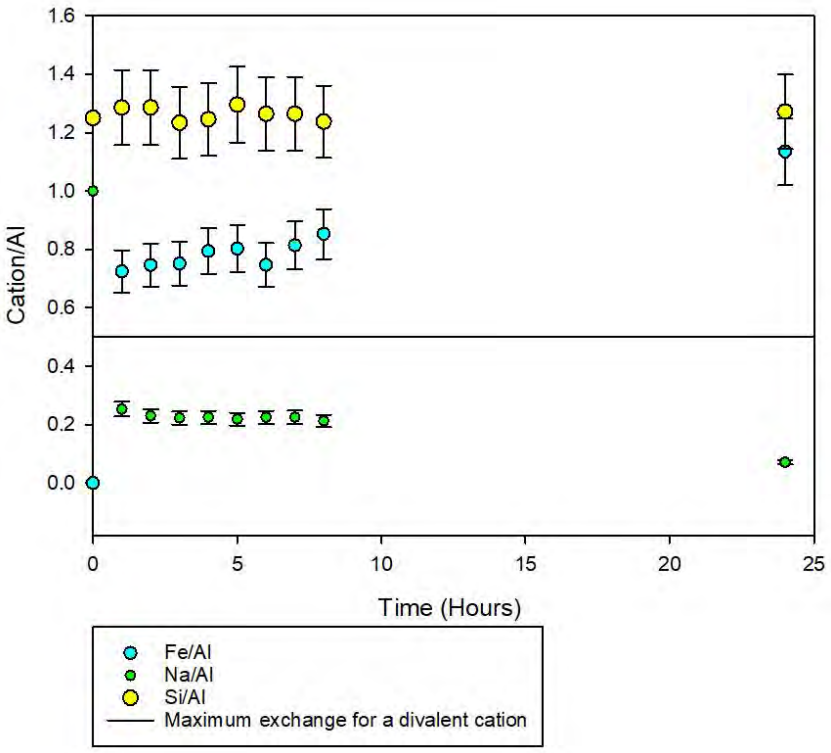


Figure 48 Time based uptake kinetics for zeolite X using 0.25 M iron(II) sulphate at 25˚C over a 24-hour time frame. Element ratios are calculated from WD-XRF data from dried powders in pellet form. The size of the error bars reflects a 10% error commonly associated with XRF of pellets.

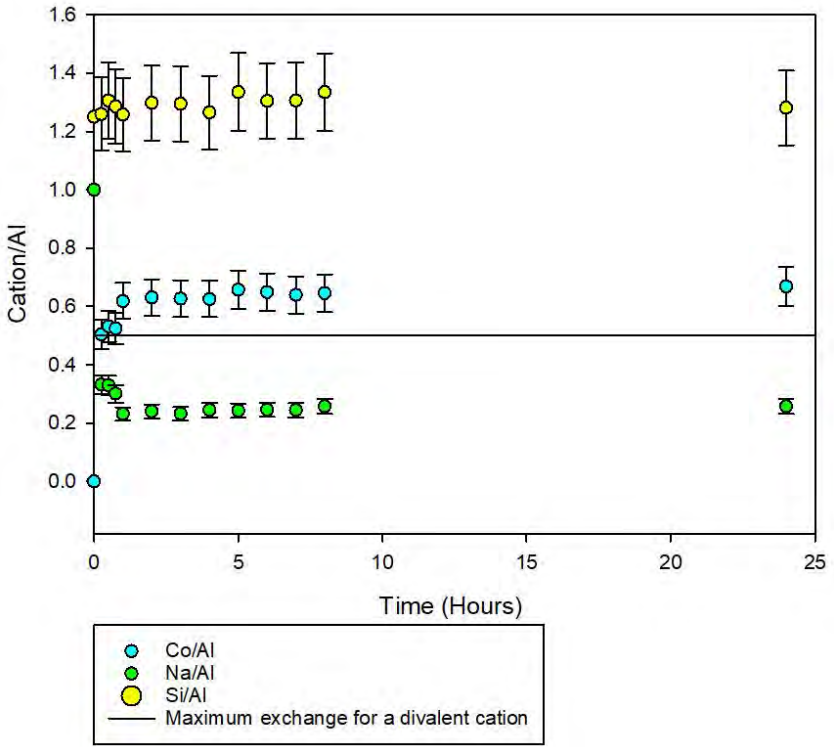


Figure 49 Time based uptake kinetics of Co(II) in zeolite X using 0.25 M co(II) nitrate at 25˚C over a 24-hour time frame. Element ratios are calculated from WD-XRF data from dried powders in pellet form. The size of the error bars reflects a 10% error commonly associated with XRF of pellets.

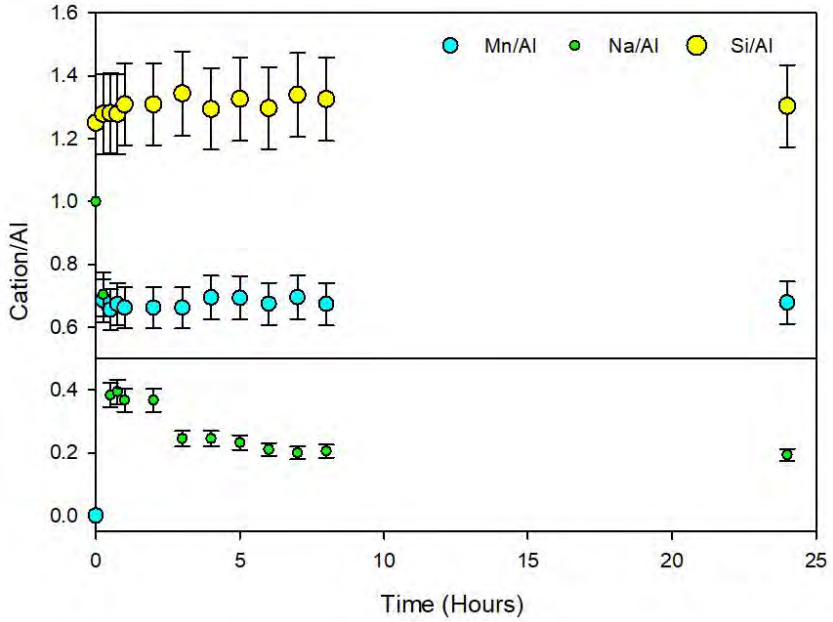


Figure 50 Time based uptake kinetics of Mn(II) in zeolite X using 0.25 M manganese(II) chloride at 25˚C, over a 24-hour timeframe. Element ratios are calculated from WD-XRF data from dried powders in pellet form. The size of the error bars reflects a 10% error commonly associated with XRF of pellets.

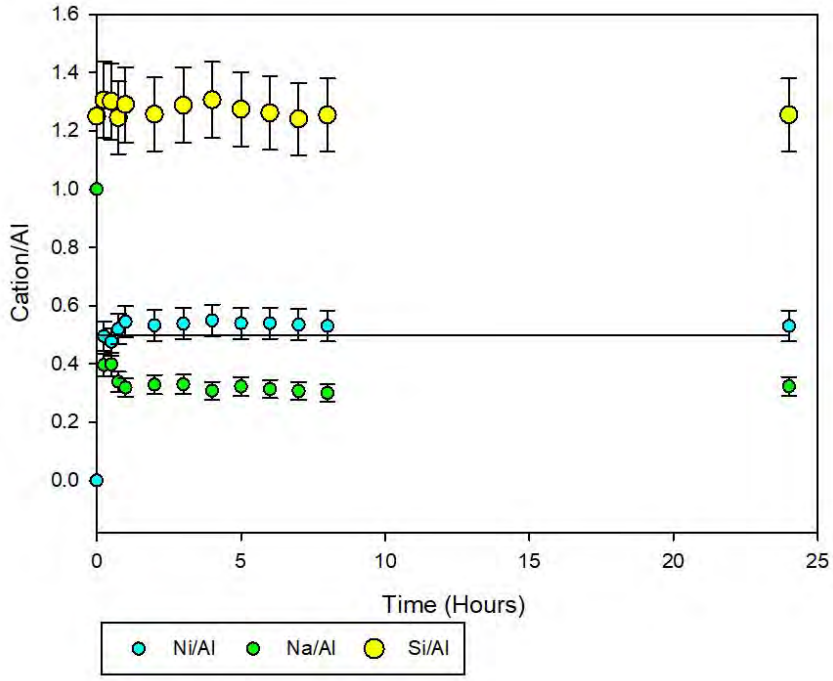


Figure 52 Time based uptake kinetics for Ni(II) in zeolite X using 0.25 M nickel(II) nitrate solution at 25˚C over a 24-hour time frame. Element ratios are calculated from WD-XRF data from dried powders in pellet form. The size of the error bars reflects a 10% error commonly associated with XRF of pellets.

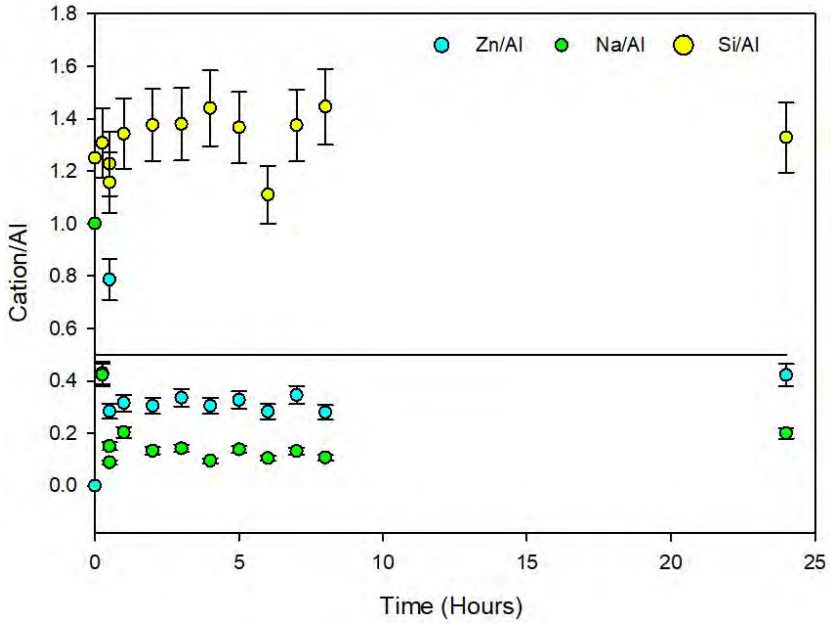


Figure 54 Time based uptake kinetics for Zn(II) in zeolite X using 0.25 M zinc(II) chloride solution at 25˚C over a 24-hour time frame. Element ratios are calculated from WD-XRF data from dried powders in pellet form. The size of the error bars reflects a 10% error commonly associated with XRF of pellets.

3.4. Zeolite X temperature and concentration based ion exchanges

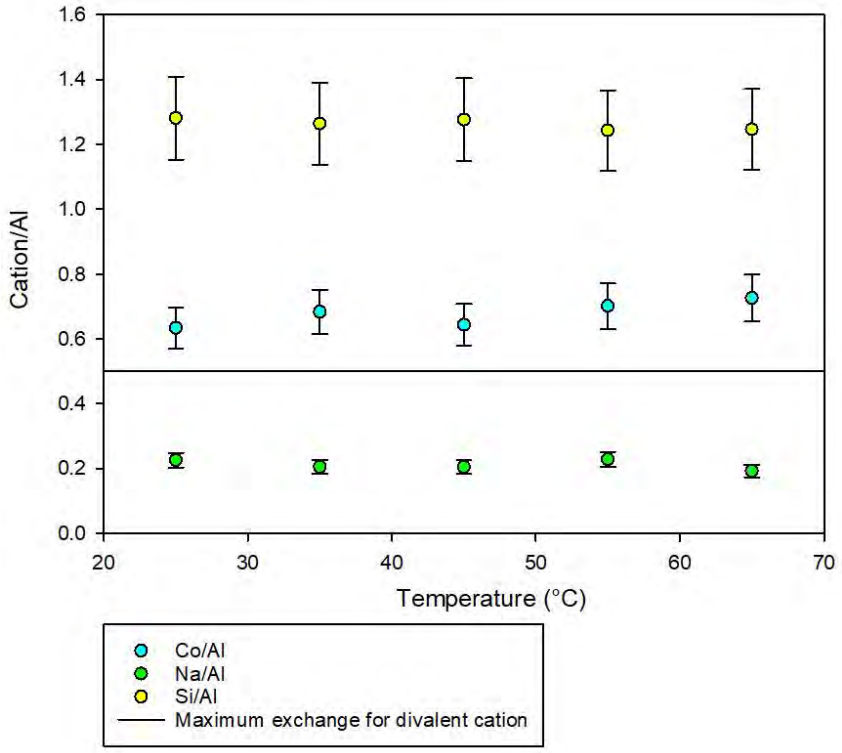


Figure 56 The effect of temperature at a concentration of 0.25 M of cobalt(II) nitrate on Co(II) cation exchange in zeolite X. Element ratios are calculated from WD-XRF data from dried powders in pellet form. The size of the error bars reflects a 10% error commonly associated with XRF of pellets.

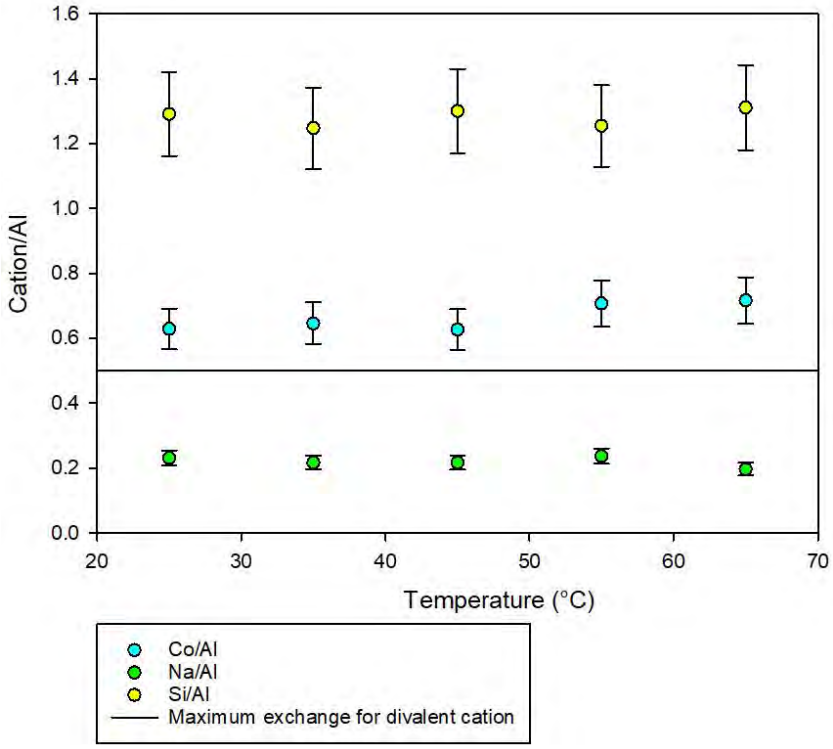


Figure 58 The effect of temperature at a concentration of 0.5 M of cobalt(II) nitrate on Co(II) cation exchange in zeolite X. Element ratios are calculated from WD-XRF data from dried powders in pellet form. The size of the error bars reflects a 10% error commonly associated with XRF of pellets.

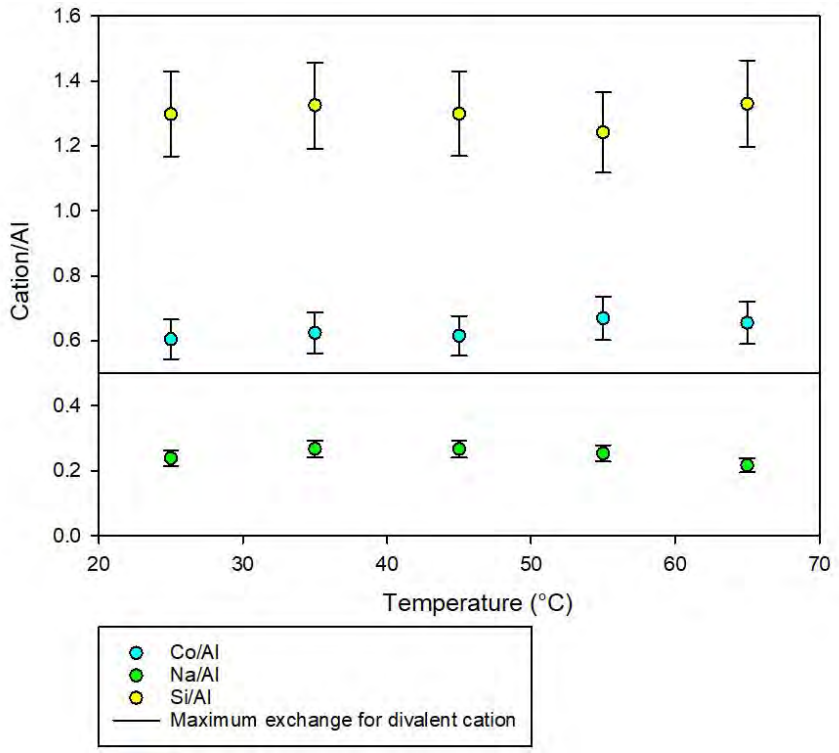


Figure 60 The effect of temperature at a concentration of 1 M of cobalt(II) nitrate on Co(II) cation exchange in zeolite X. Element ratios are calculated from WD-XRF data from dried powders in pellet form. The size of the error bars reflects a 10% error commonly associated with XRF of pellets.

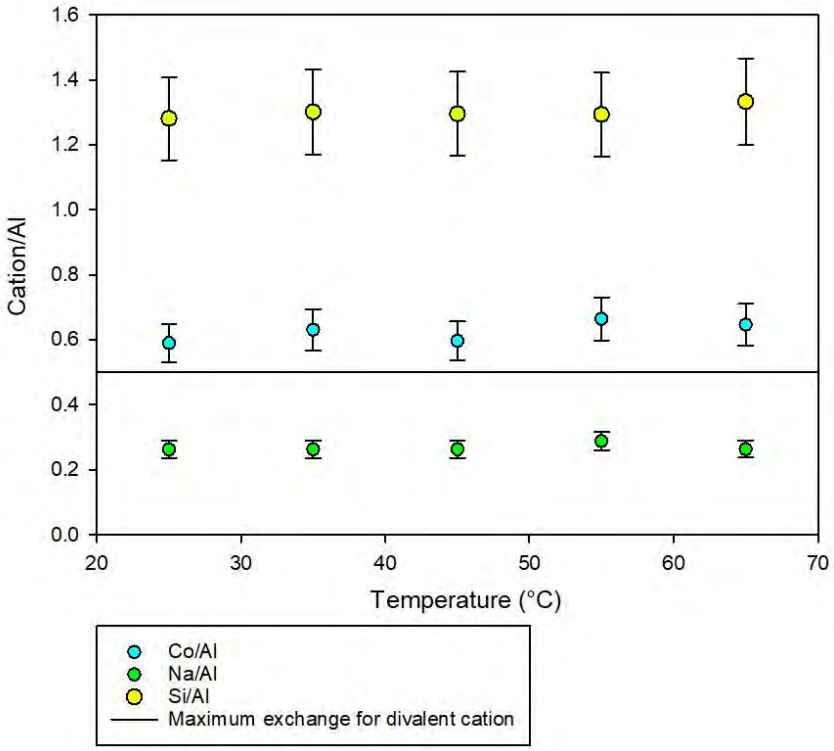


Figure 62 The effect of temperature at a concentration of 2 M of cobalt(II) nitrate on Co(II) cation exchange in zeolite X. Element ratios are calculated from WD-XRF data from dried powders in pellet form. The size of the error bars reflects a 10% error commonly associated with XRF of pellets.

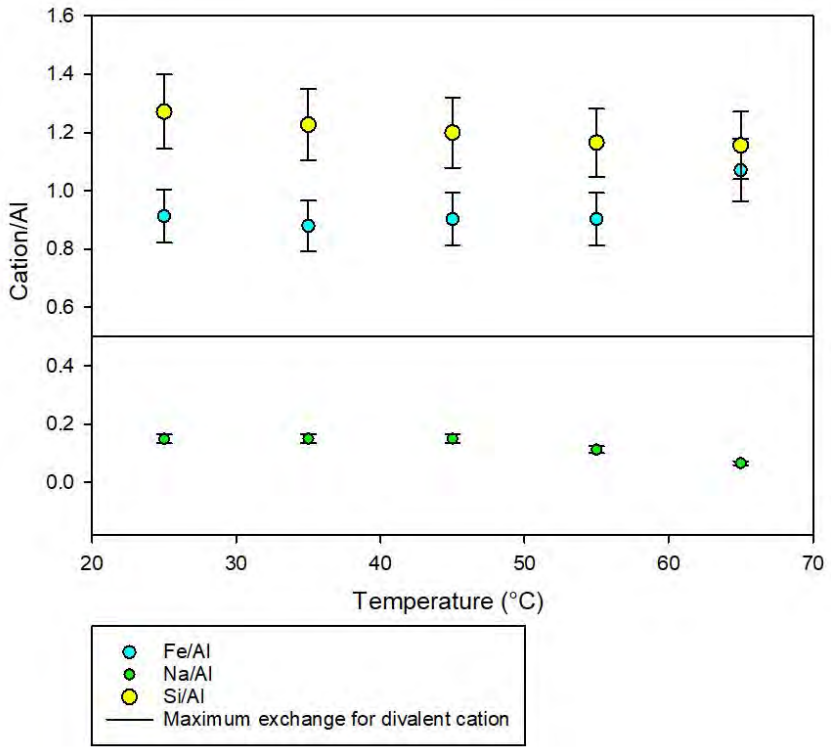


Figure 64 The effect of temperature at a concentration of 0.25 M of iron(II) chloride on Fe(II) cation exchange in zeolite X. Element ratios are calculated from WD-XRF data from dried powders in pellet form. The size of the error bars reflects a 10% error commonly associated with XRF of pellets.

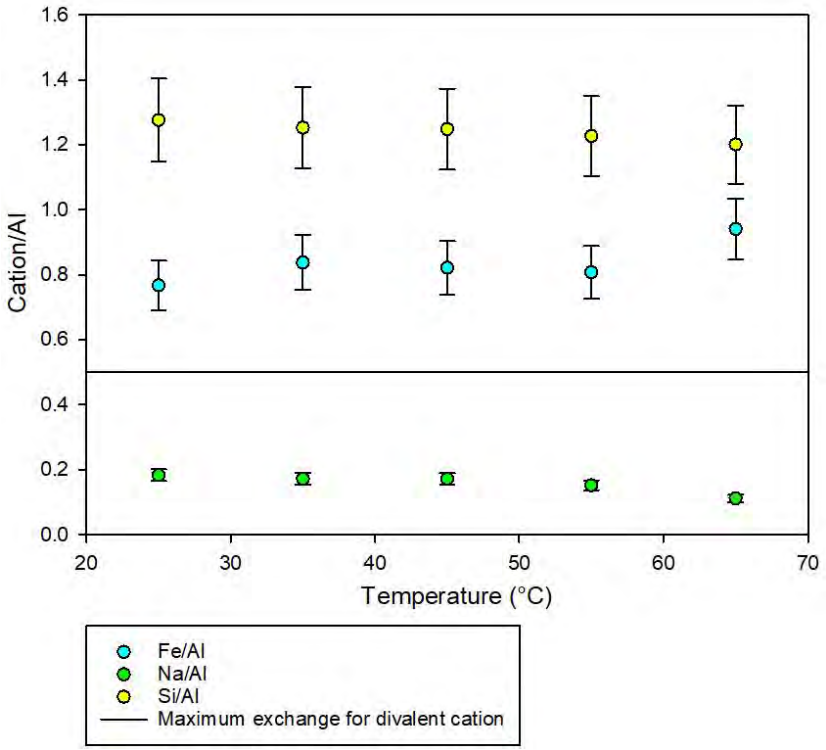


Figure 66 The effect of temperature at a concentration of 0.5 M of iron(II) chloride on Fe(II) cation exchange in zeolite X. Element ratios are calculated from WD-XRF data from dried powders in pellet form. The size of the error bars reflects a 10% error commonly associated with XRF of pellets.

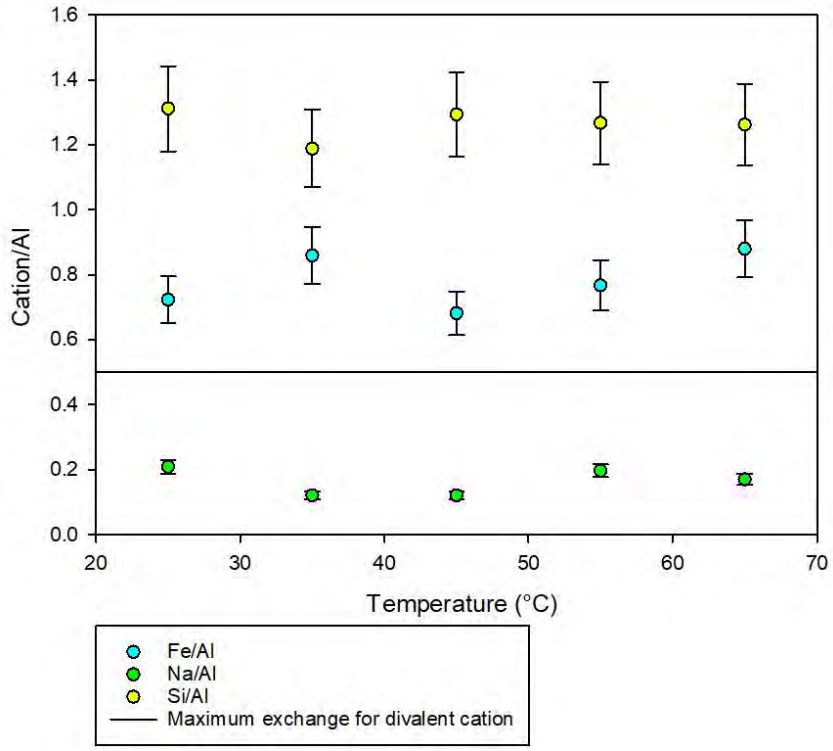


Figure 68 The effect of temperature at a concentration of 1 M of iron(II) chloride on Fe(II) cation exchange in zeolite X. Element ratios are calculated from WD-XRF data from dried powders in pellet form. The size of the error bars reflects a 10% error commonly associated with XRF of pellets.

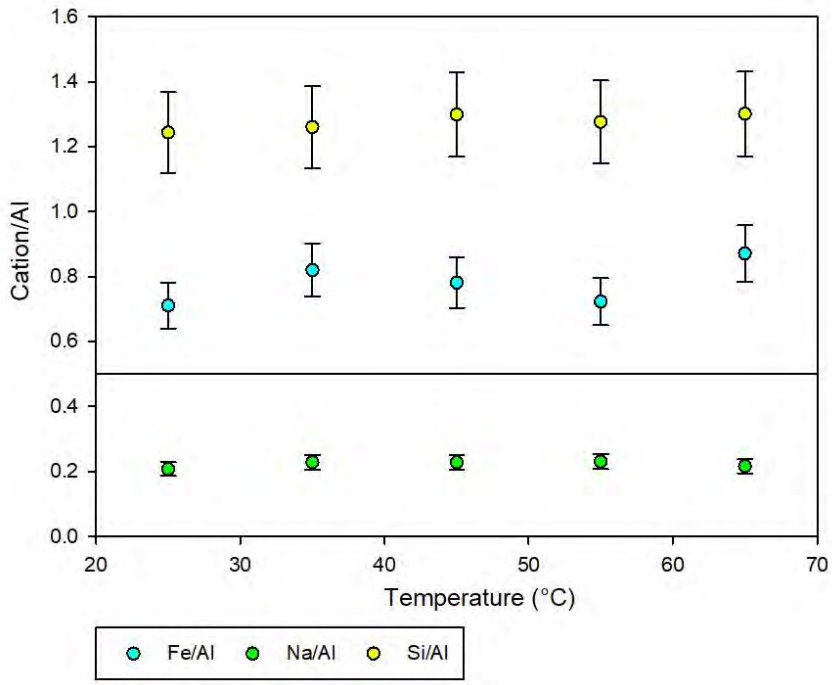


Figure 70 The effect of temperature at a concentration of 2 M of iron(II) chloride on Fe(II) cation exchange in zeolite X. Element ratios are calculated from WD-XRF data from dried powders in pellet form. The size of the error bars reflects a 10% error commonly associated with XRF of pellets.

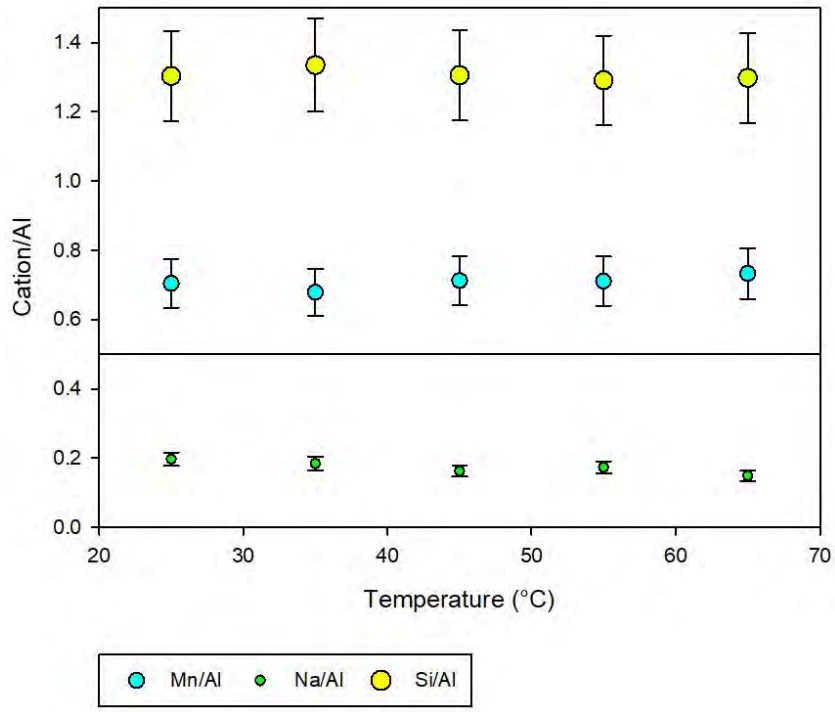


Figure 72 The effect of temperature at a concentration of 0.25 M of manganese(II) chloride on Mn(II) cation exchange in zeolite X. Element ratios are calculated from WD-XRF data from dried powders in pellet form. The size of the error bars reflects a 10% error commonly associated with XRF of pellets.

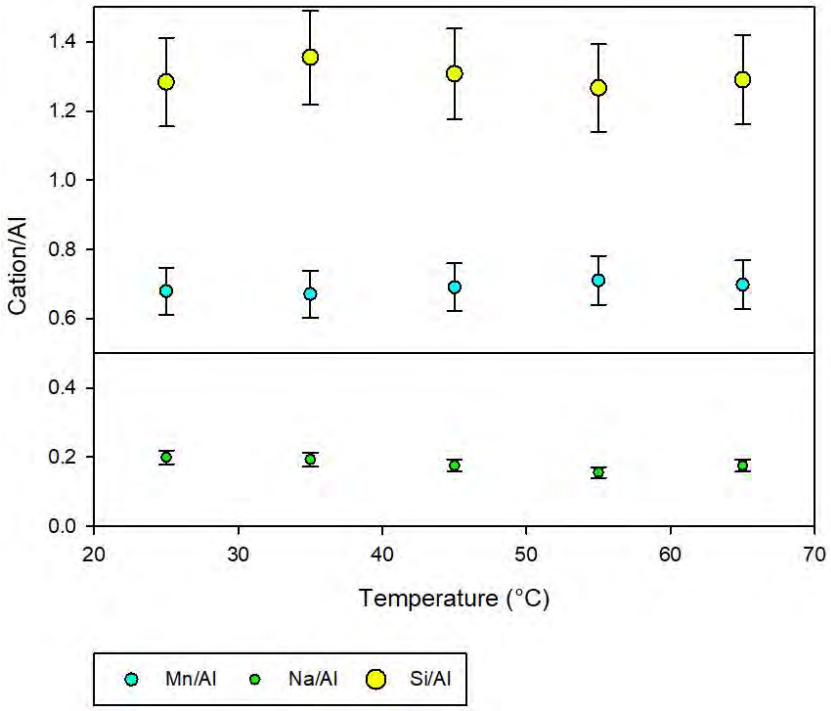


Figure 74 The effect of temperature at a concentration of 0.5 M of manganese(II) chloride on Mn(II) cation exchange in zeolite X. Element ratios are calculated from WD-XRF data from dried powders in pellet form. The size of the error bars reflects a 10% error commonly associated with XRF of pellets.

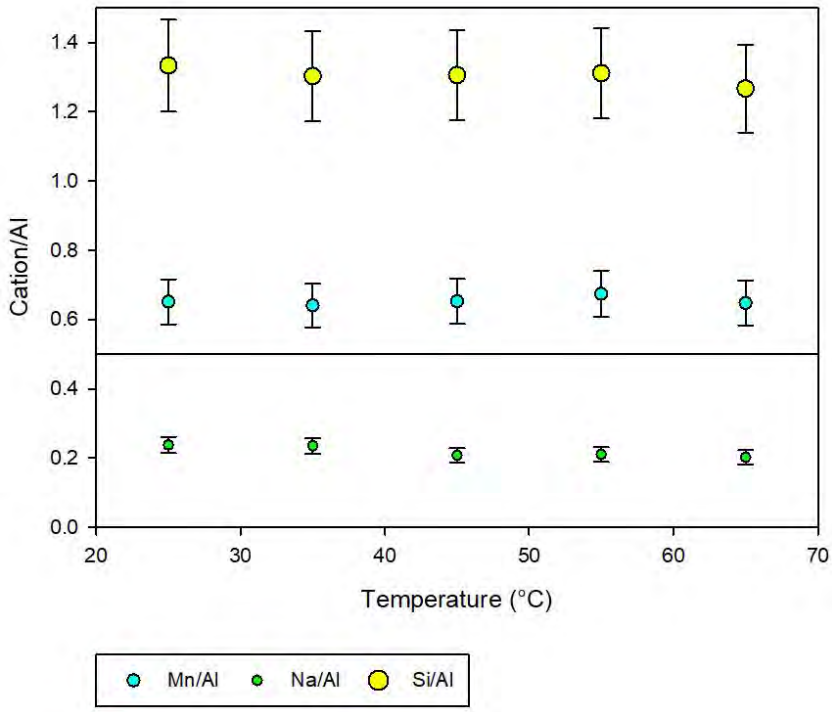


Figure 76 The effect of temperature at a concentration of 1 M of manganese(II) chloride on Mn(II) cation exchange in zeolite X. Element ratios are calculated from WD-XRF data from dried powders in pellet form. The size of the error bars reflects a 10% error commonly associated with XRF of pellets.

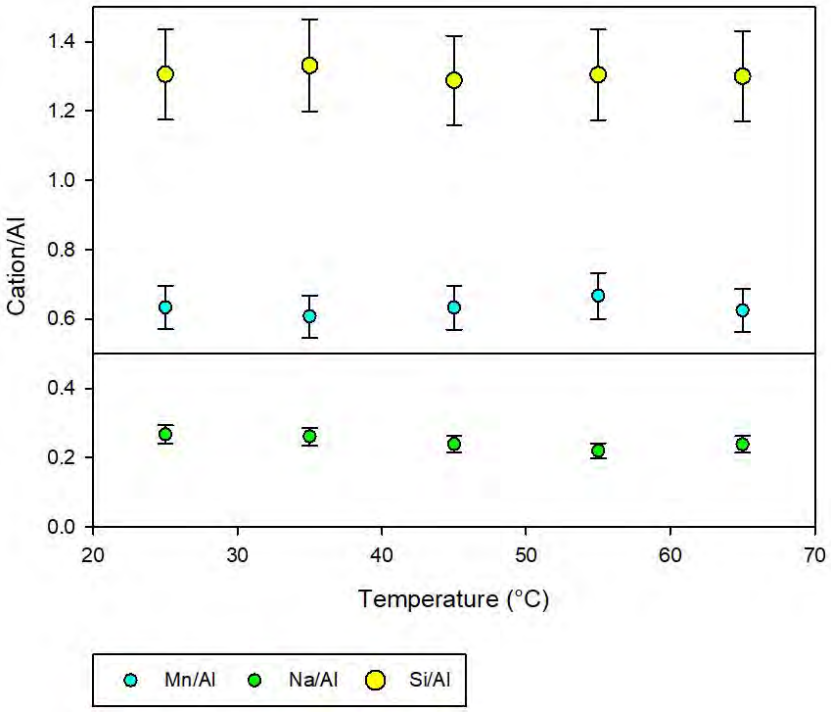


Figure 78 The effect of temperature at a concentration of 2 M of manganese(II) chloride on Mn(II) cation exchange in zeolite X. Element ratios are calculated from WD-XRF data from dried powders in pellet form. The size of the error bars reflects a 10% error commonly associated with XRF of pellets.

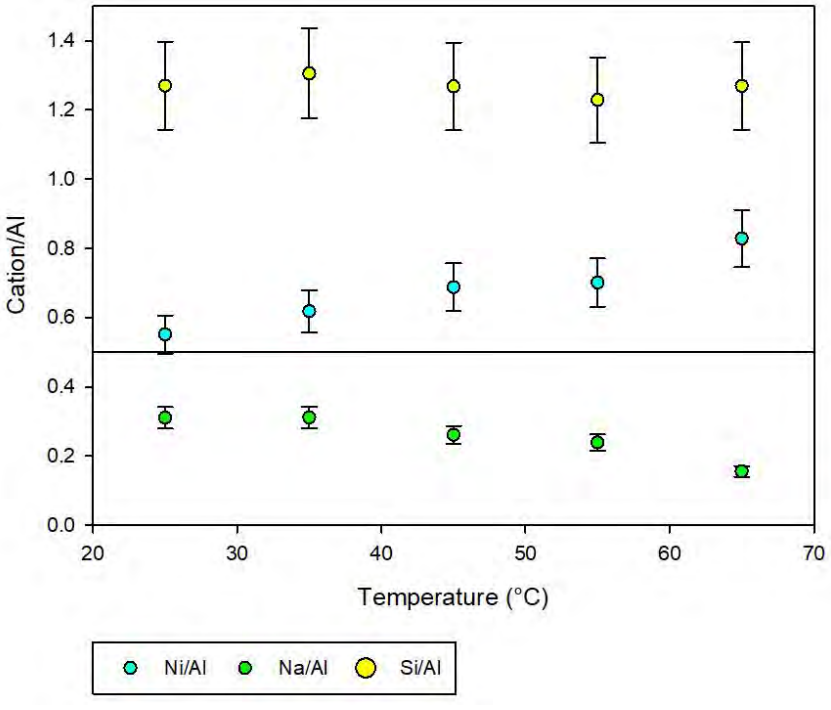


Figure 80 The effect of temperature at a concentration of 0.25 M of nickel(II) nitrate on Ni(II) cation exchange in zeolite X. Element ratios are calculated from WD-XRF data from dried powders in pellet form. The size of the error bars reflects a 10% error commonly associated with XRF of pellets.

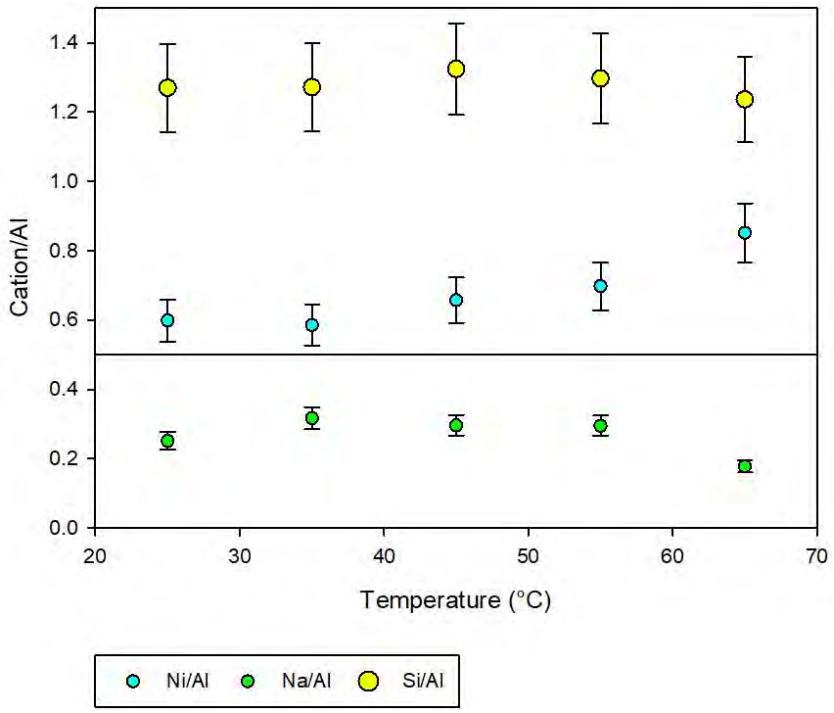


Figure 82 The effect of temperature at a concentration of 0.5 M of nickel(II) nitrate on Ni(II) cation exchange in zeolite X. Element ratios are calculated from WD-XRF data from dried powders in pellet form. The size of the error bars reflects a 10% error commonly associated with XRF of pellets.

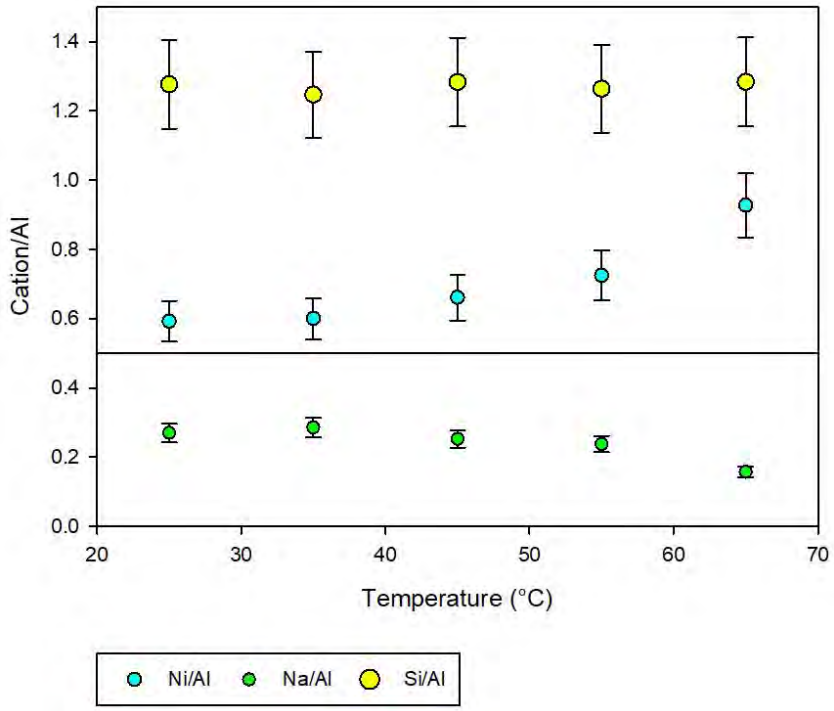


Figure 84 The effect of temperature at a concentration of 1 M of nickel(II) nitrate on Ni(II) cation exchange in zeolite X. Element ratios are calculated from WD-XRF data from dried powders in pellet form. The size of the error bars reflects a 10% error commonly associated with XRF of pellets.

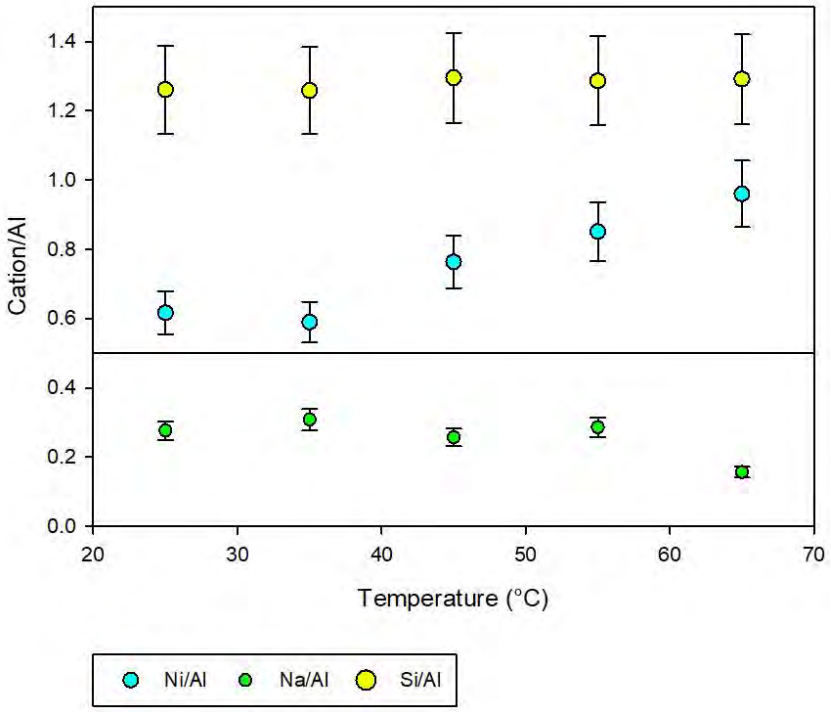


Figure 86 The effect of temperature at a concentration of 2 M of nickel(II) nitrate on Ni(II) cation exchange in zeolite X. Element ratios are calculated from WD-XRF data from dried powders in pellet form. The size of the error bars reflects a 10% error commonly associated with XRF of pellets.

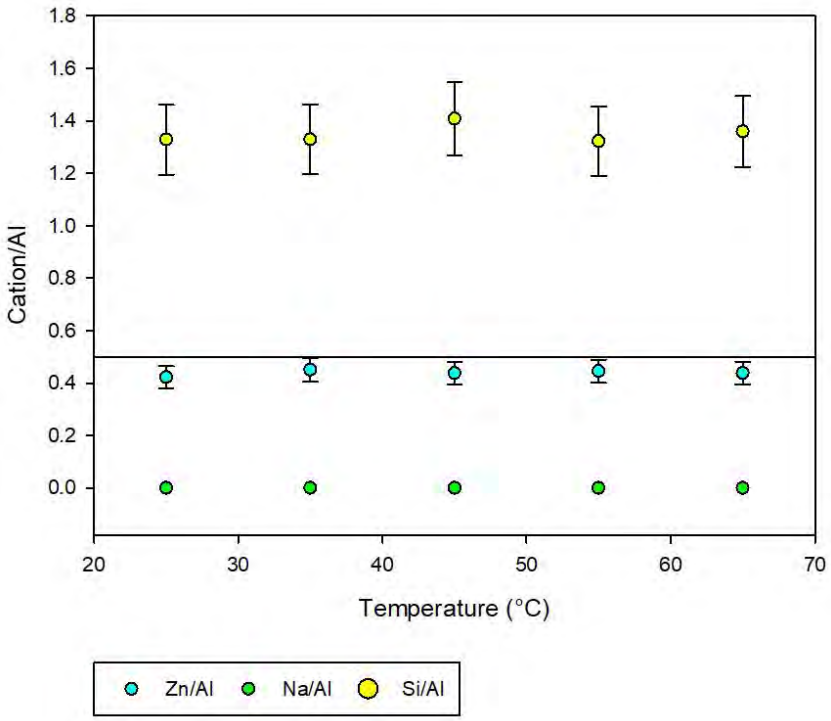


Figure 88 The effect of temperature at a concentration of 0.25 M of zinc(II) chloride on Zn(II) cation exchange in zeolite X. Element ratios are calculated from WD-XRF data from dried powders in pellet form. The size of the error bars reflects a 10% error commonly associated with XRF of pellets.

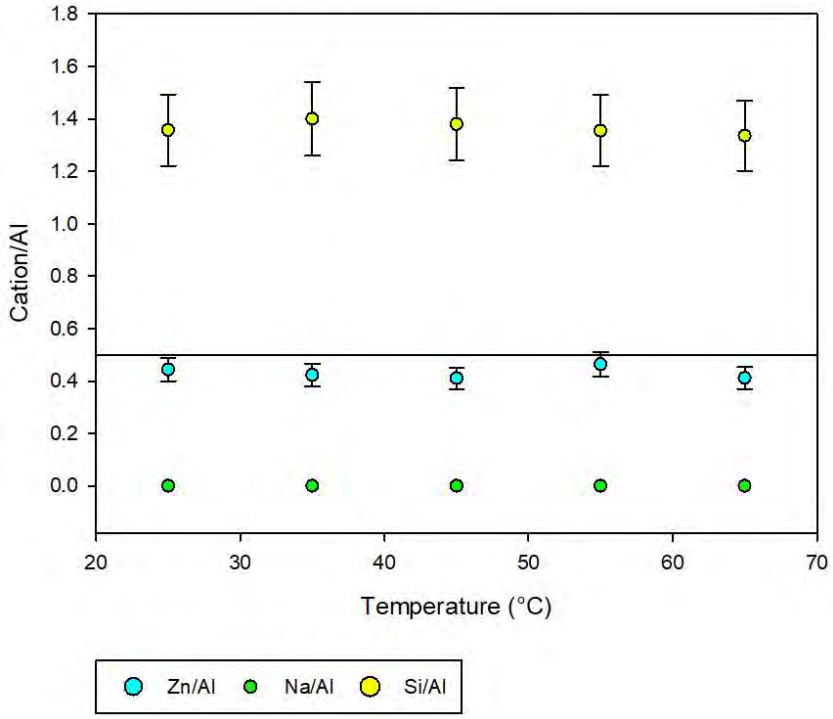


Figure 90 The effect of temperature at a concentration of 0.5 M of zinc(II) chloride on Zn(II) cation exchange in zeolite X. Element ratios are calculated from WD-XRF data from dried powders in pellet form. The size of the error bars reflects a 10% error commonly associated with XRF of pellets.

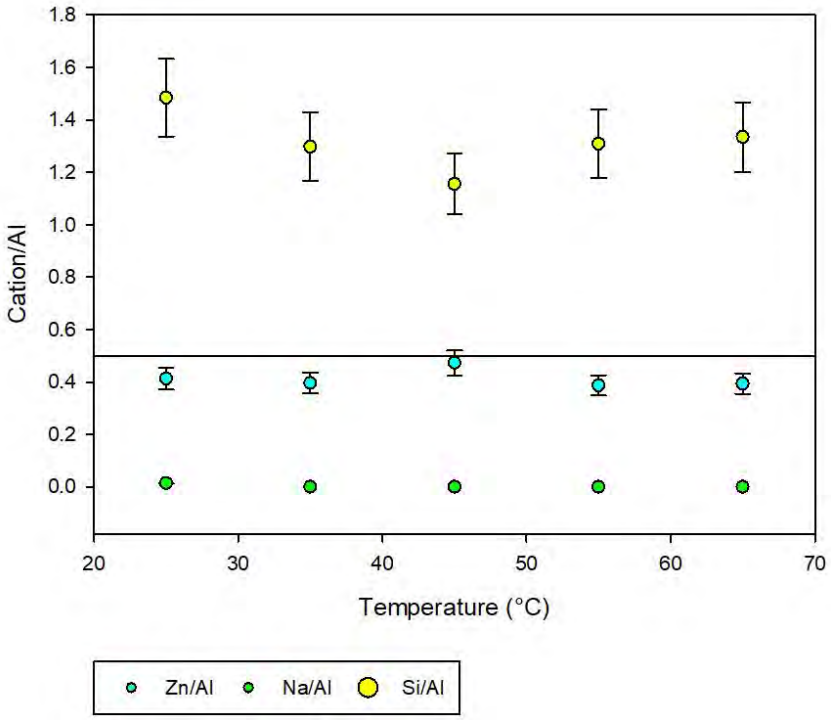


Figure 92 The effect of temperature at a concentration of 1 M of zinc(II) chloride on Zn(II) cation exchange in zeolite X. Element ratios are calculated from WD-XRF data from dried powders in pellet form. The size of the error bars reflects a 10% error commonly associated with XRF of pellets.

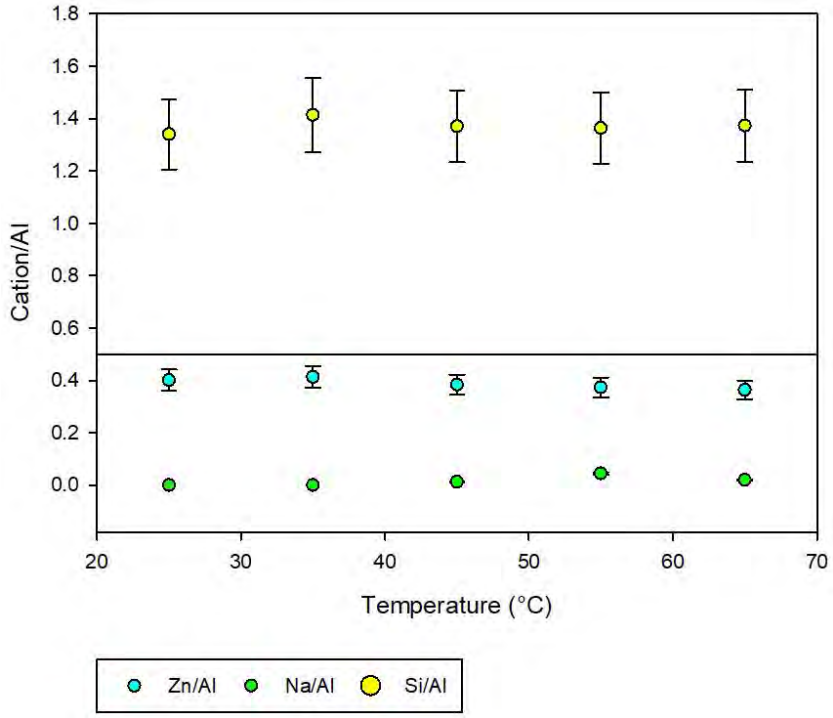


Figure 94 The effect of temperature at a concentration of 2 M of zinc(II) chloride on Zn(II) cation exchange in zeolite X. Element ratios are calculated from WD-XRF data from dried powders in pellet form. The size of the error bars reflects a 10% error commonly associated with XRF of pellets.

3.5. Zeolite Y time-based ion exchanges

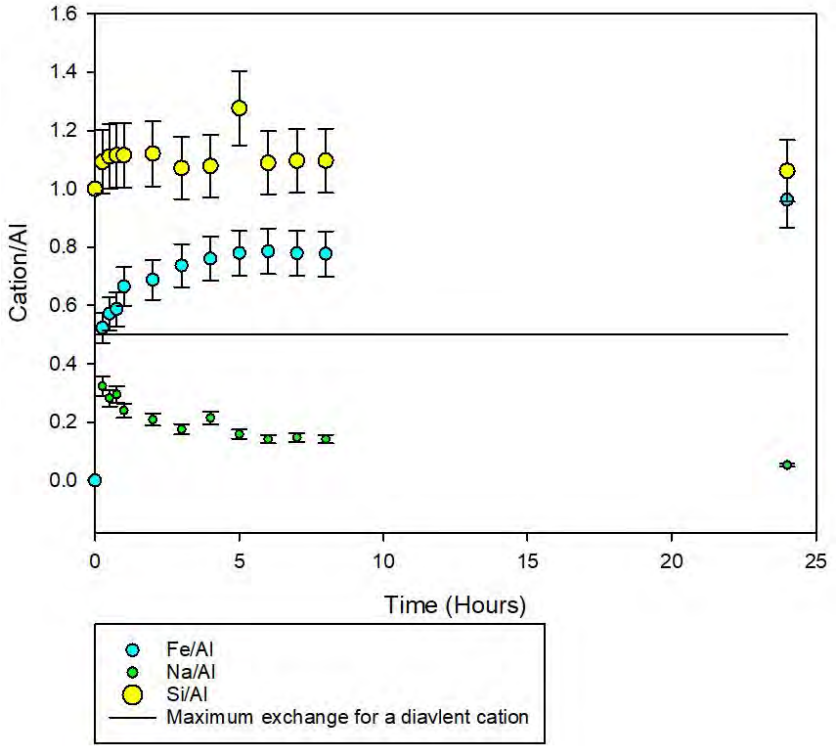


Figure 96 Time based uptake kinetics of Fe(II) in zeolite Y using 0.25 M iron(II) chloride at 25˚C over a 24-hour time frame. Element ratios are calculated from WD-XRF data from dried powders in pellet form. The size of the error bars reflects a 10% error commonly associated with XRF of pellets.

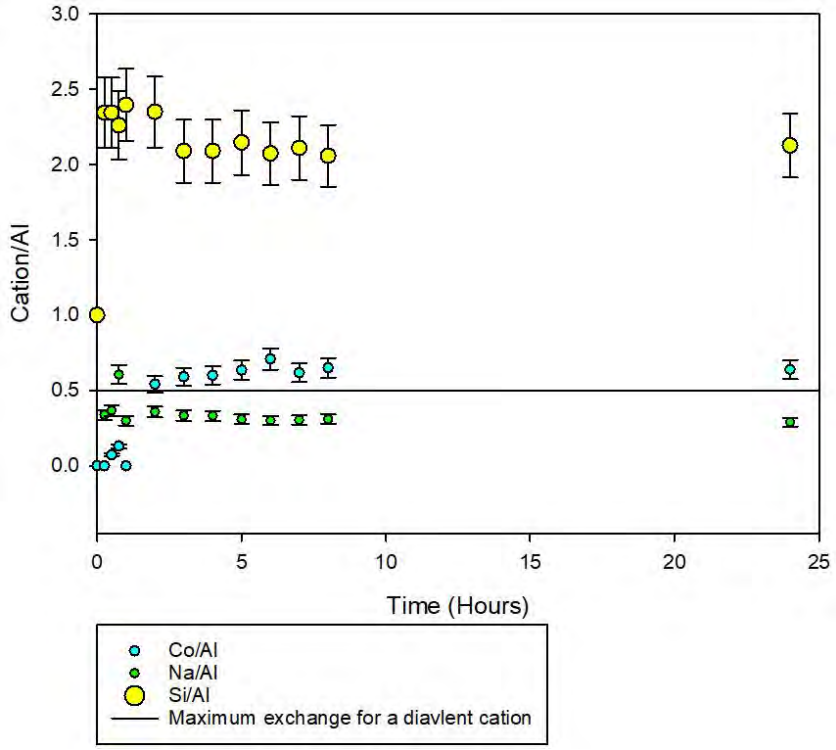


Figure 98 Time based uptake kinetics of Co(II) in zeolite Y using 0.25 M co(II) nitrate at 25˚C over a 24-hour time frame. Element ratios are calculated from WD-XRF data from dried powders in pellet form. The size of the error bars reflects a 10% error commonly associated with XRF of pellets.

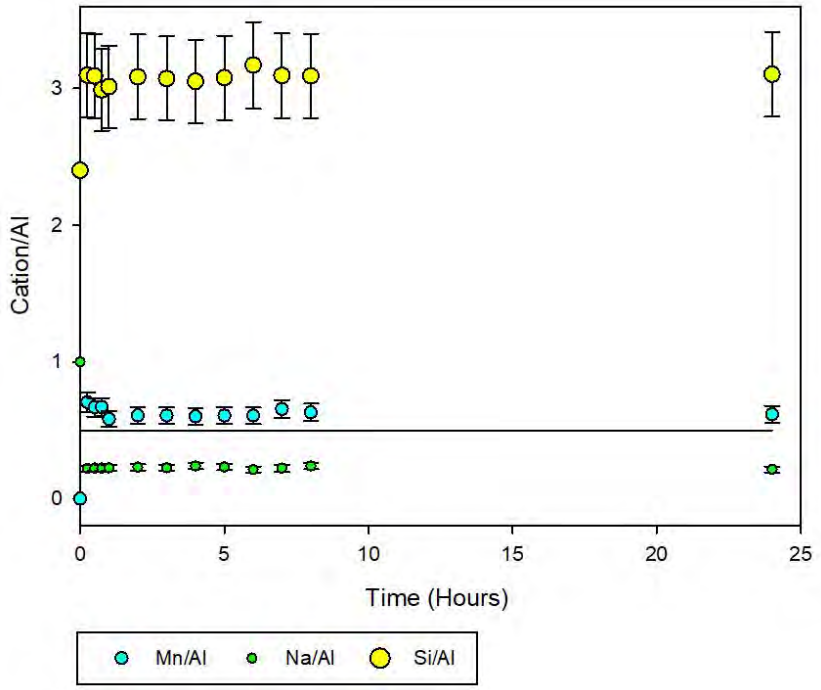


Figure 100 Time based uptake kinetics of Mn(II) in zeolite Y using 0.25 M manganese(II) chloride at 25˚C, over a 24-hour timeframe. Element ratios are calculated from WD-XRF data from dried powders in pellet form. The size of the error bars reflects a 10% error commonly associated with XRF of pellets.

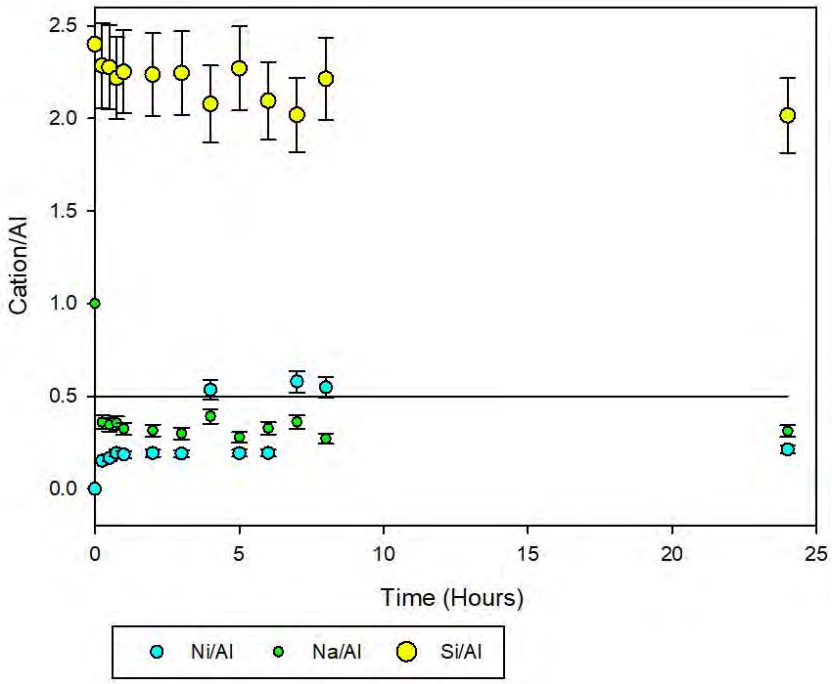


Figure 102 Time based uptake kinetics for Ni(II) in zeolite Y using 0.25 M nickel(II) nitrate solution at 25˚C over a 24-hour time frame. Element ratios are calculated from WD-XRF data from dried powders in pellet form. The size of the error bars reflects a 10% error commonly associated with XRF of pellets.

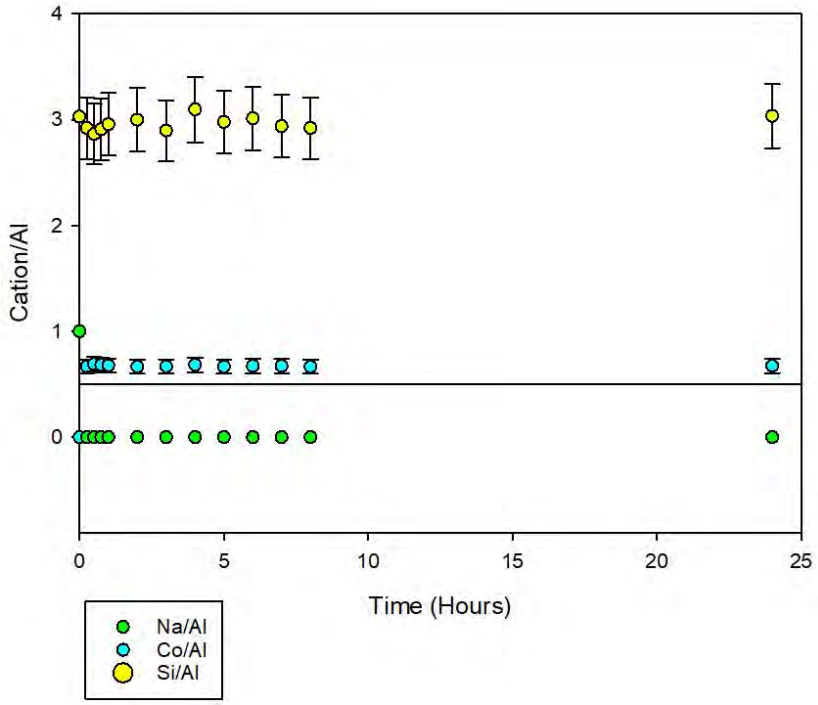


Figure 104 Time based uptake kinetics for Zn(II) in zeolite Y using 0.25 M zinc(II) chloride solution at 25˚C over a 24-hour time frame. Element ratios are calculated from WD-XRF data from dried powders in pellet form. The size of the error bars reflects a 10% error commonly associated with XRF of pellets.

3.6. Zeolite Y temperature and concentration based ion exchanges

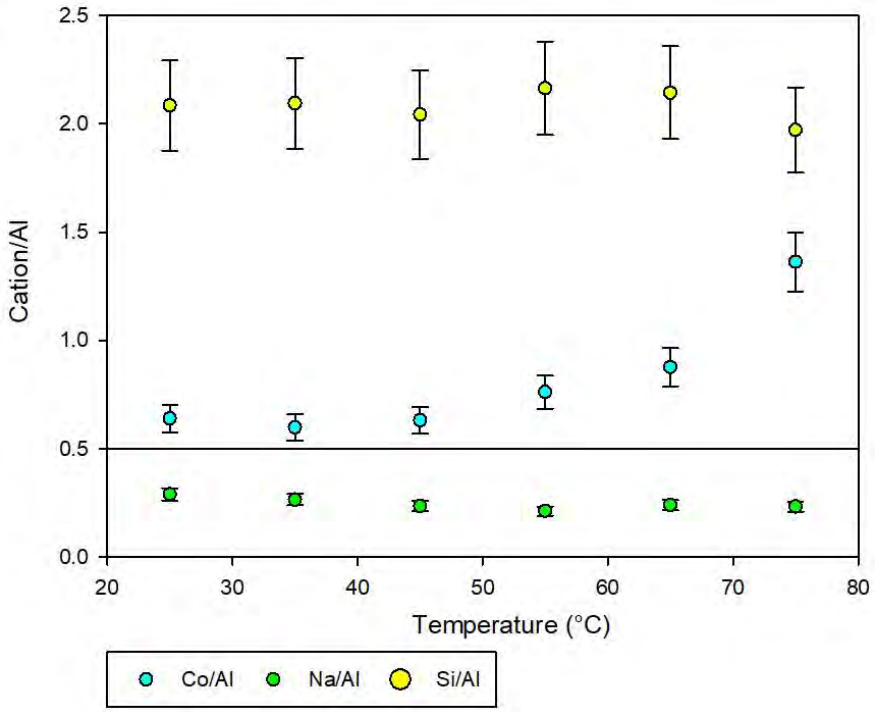


Figure 106 The effect of temperature at a concentration of 0.25 M of cobalt(II) nitrate on Co(II) cation exchange in zeolite Y. Element ratios are calculated from WD-XRF data from dried powders in pellet form. The size of the error bars reflects a 10% error commonly associated with XRF of pellets.

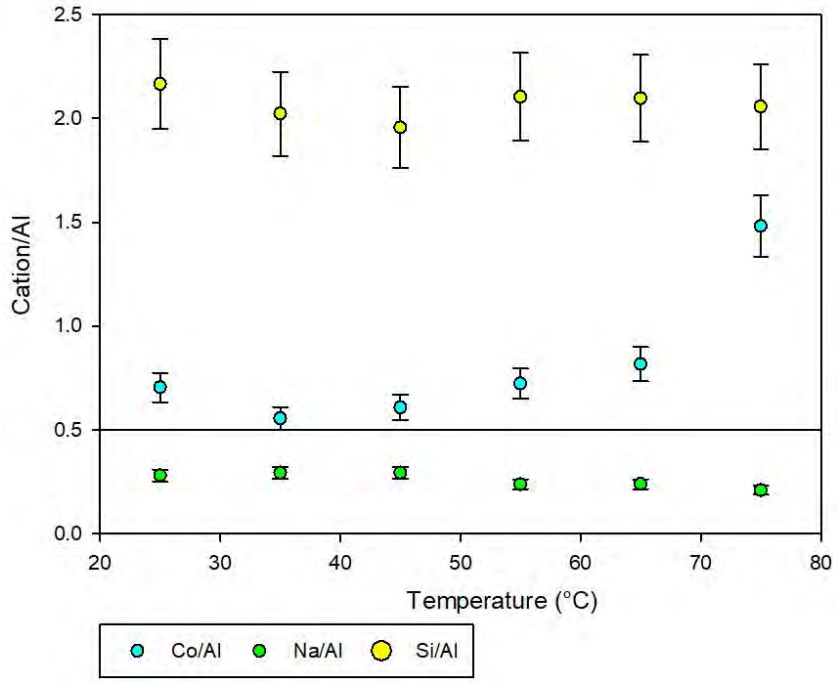


Figure 108 The effect of temperature at a concentration of 0.5 M of cobalt(II) nitrate on Co(II) cation exchange in zeolite Y. Element ratios are calculated from WD-XRF data from dried powders in pellet form. The size of the error bars reflects a 10% error commonly associated with XRF of pellets.

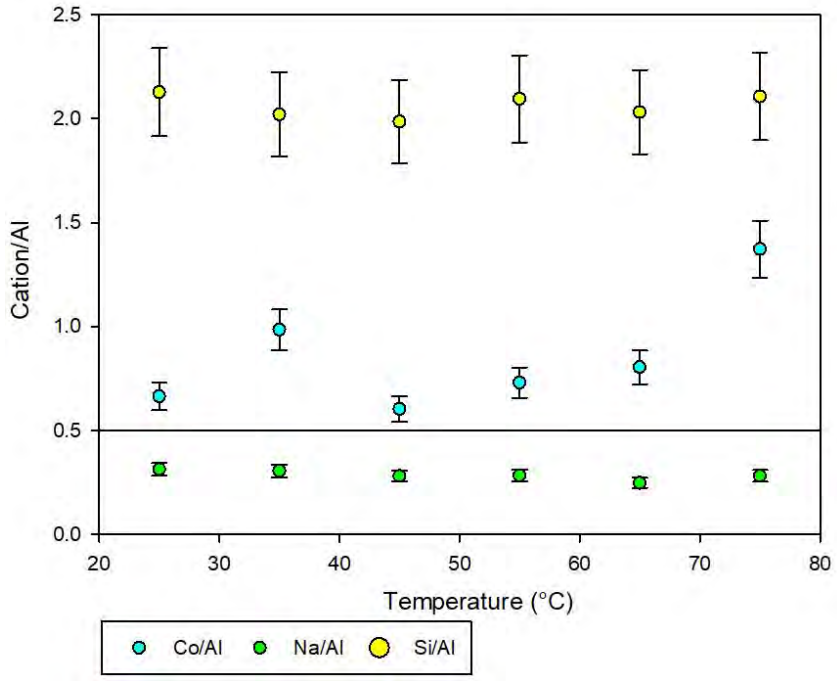


Figure 110 The effect of temperature at a concentration of 1 M of cobalt(II) nitrate on Co(II) cation exchange in zeolite Y. Element ratios are calculated from WD-XRF data from dried powders in pellet form. The size of the error bars reflects a 10% error commonly associated with XRF of pellets.

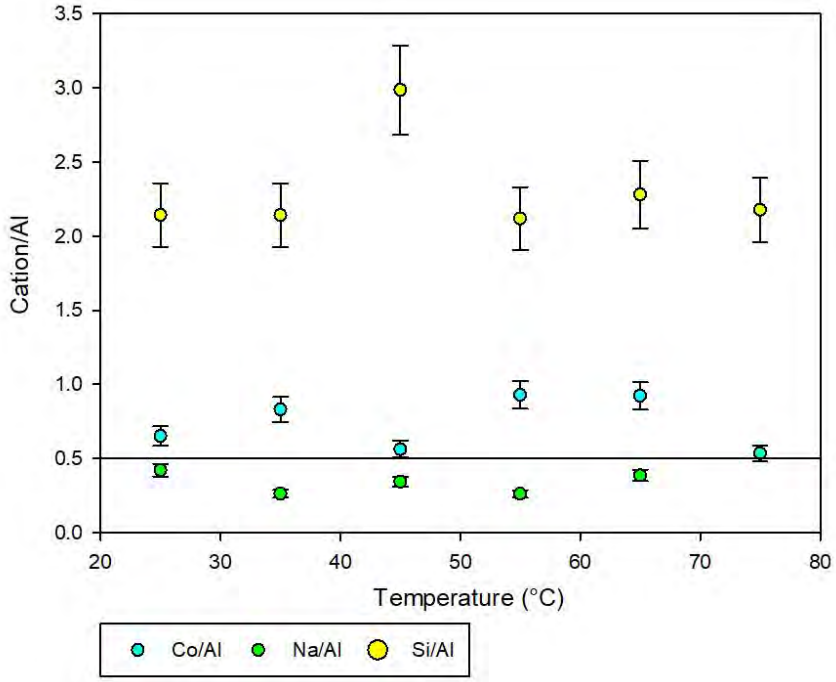


Figure 112 The effect of temperature at a concentration of 2 M of cobalt(II) nitrate on Co(II) cation exchange in zeolite Y. Element ratios are calculated from WD-XRF data from dried powders in pellet form. The size of the error bars reflects a 10% error commonly associated with XRF of pellets.

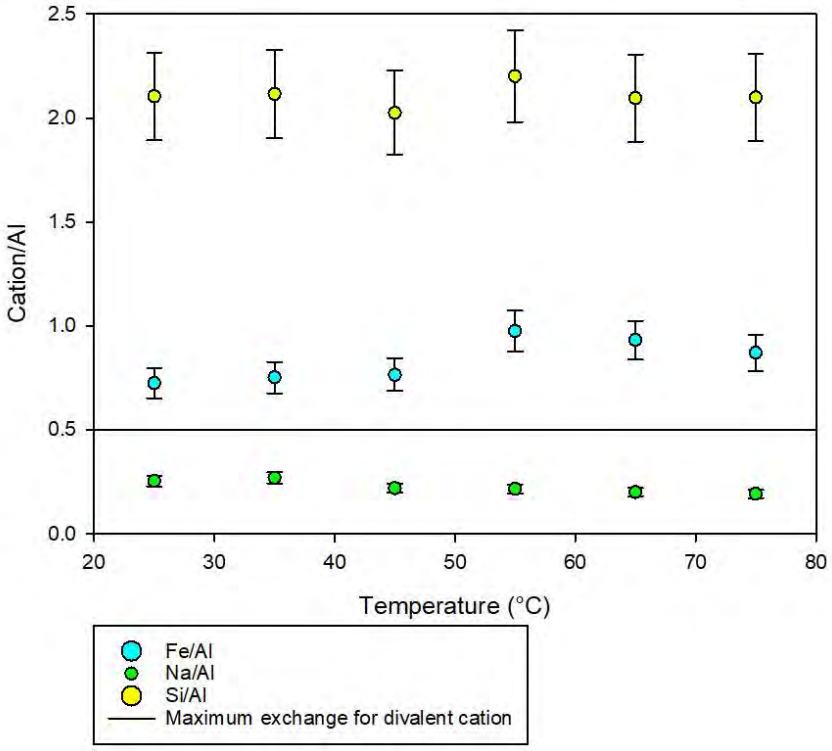


Figure 114 The effect of temperature at a concentration of 0.25 M of iron(II) chloride on Fe(II) cation exchange in zeolite Y. Element ratios are calculated from WD-XRF data from dried powders in pellet form. The size of the error bars reflects a 10% error commonly associated with XRF of pellets.

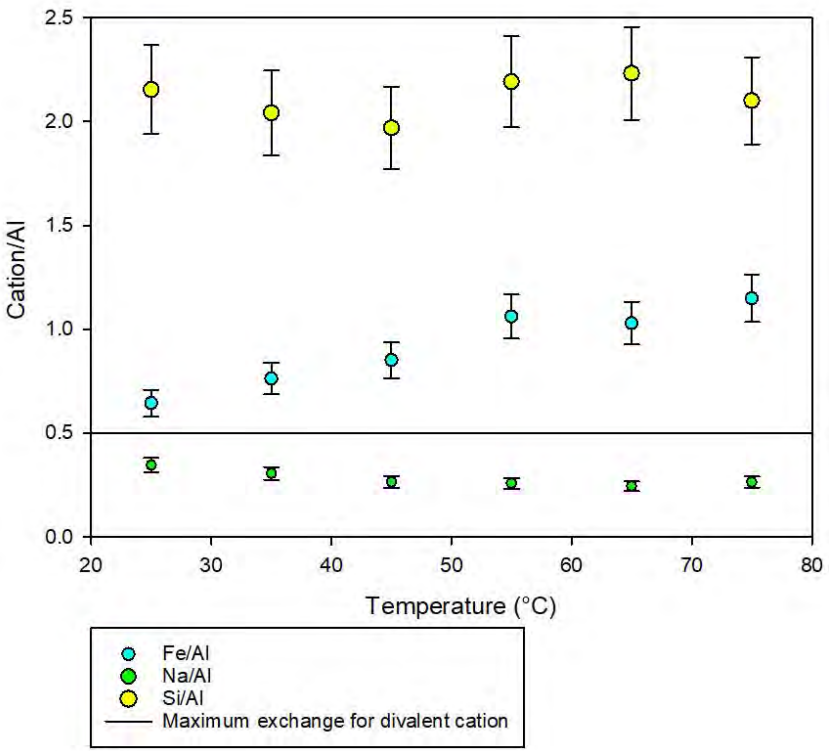


Figure 116 The effect of temperature at a concentration of 0.5 M of iron(II) chloride on Fe(II) cation exchange in zeolite Y. Element ratios are calculated from WD-XRF data from dried powders in pellet form. The size of the error bars reflects a 10% error commonly associated with XRF of pellets.

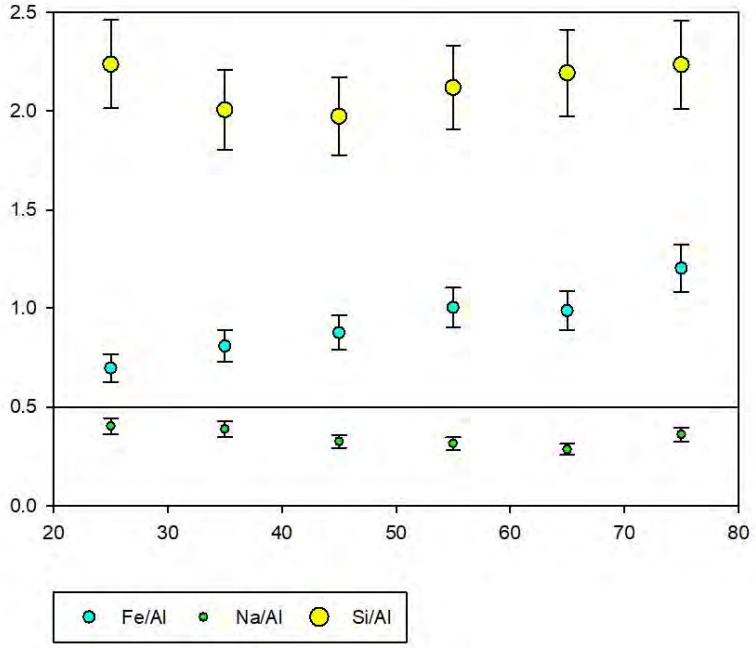


Figure 118 The effect of temperature at a concentration of 1 M of iron(II) chloride on Fe(II) cation exchange in zeolite Y. Element ratios are calculated from WD-XRF data from dried powders in pellet form. The size of the error bars reflects a 10% error commonly associated with XRF of pellets.

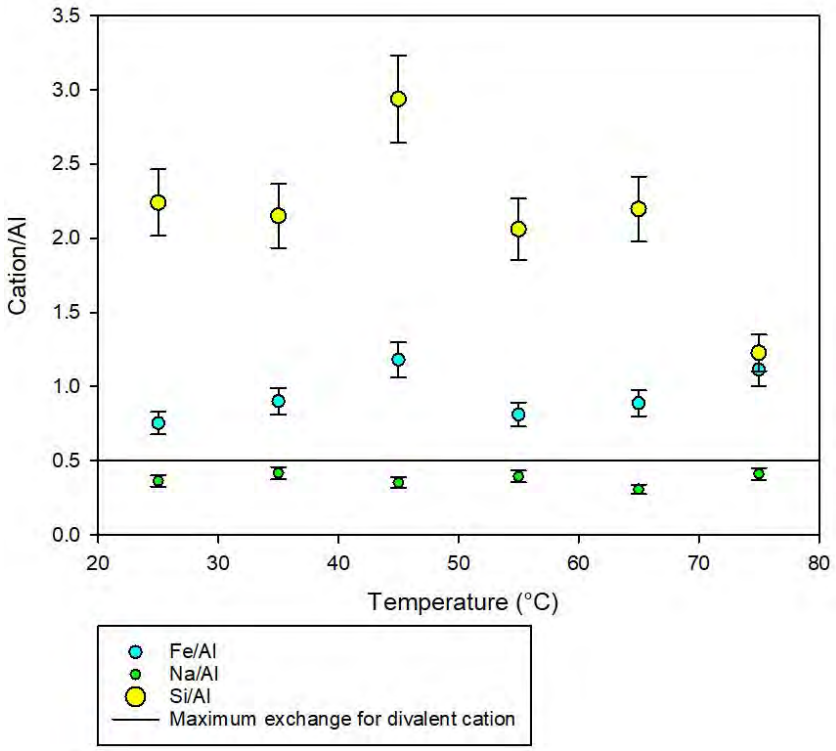


Figure 120 The effect of temperature at a concentration of 2 M of iron(II) chloride on Fe(II) cation exchange in zeolite Y. Element ratios are calculated from WD-XRF data from dried powders in pellet form. The size of the error bars reflects a 10% error commonly associated with XRF of pellets.

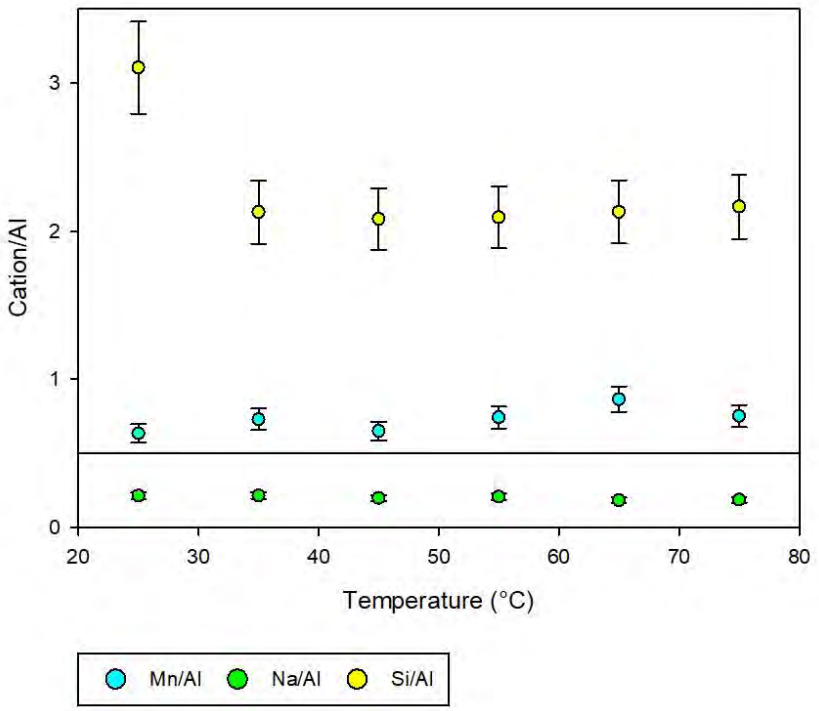


Figure 122 The effect of temperature at a concentration of 0.25 M of manganese(II) chloride on Mn(II) cation exchange in zeolite Y. Element ratios are calculated from WD-XRF data from dried powders in pellet form. The size of the error bars reflects a 10% error commonly associated with XRF of pellets.

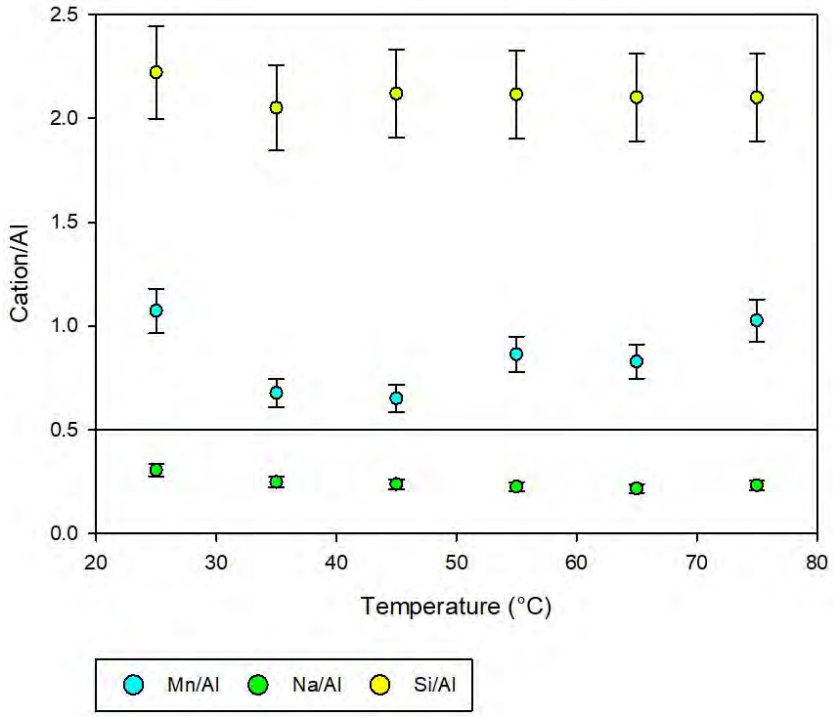


Figure 124 The effect of temperature at a concentration of 0.5 M of manganese(II) chloride on Mn(II) cation exchange in zeolite X. Element ratios are calculated from WD-XRF data from dried powders in pellet form. The size of the error bars reflects a 10% error commonly associated with XRF of pellets.

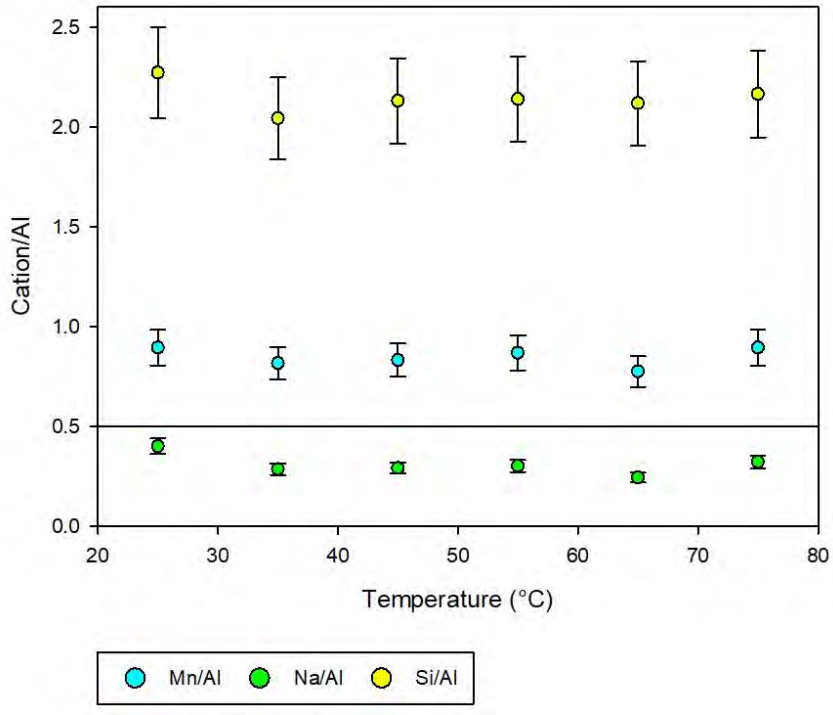


Figure 126 The effect of temperature at a concentration of 1 M of manganese(II) chloride on Mn(II) cation exchange in zeolite X. Element ratios are calculated from WD-XRF data from dried powders in pellet form. The size of the error bars reflects a 10% error commonly associated with XRF of pellets.

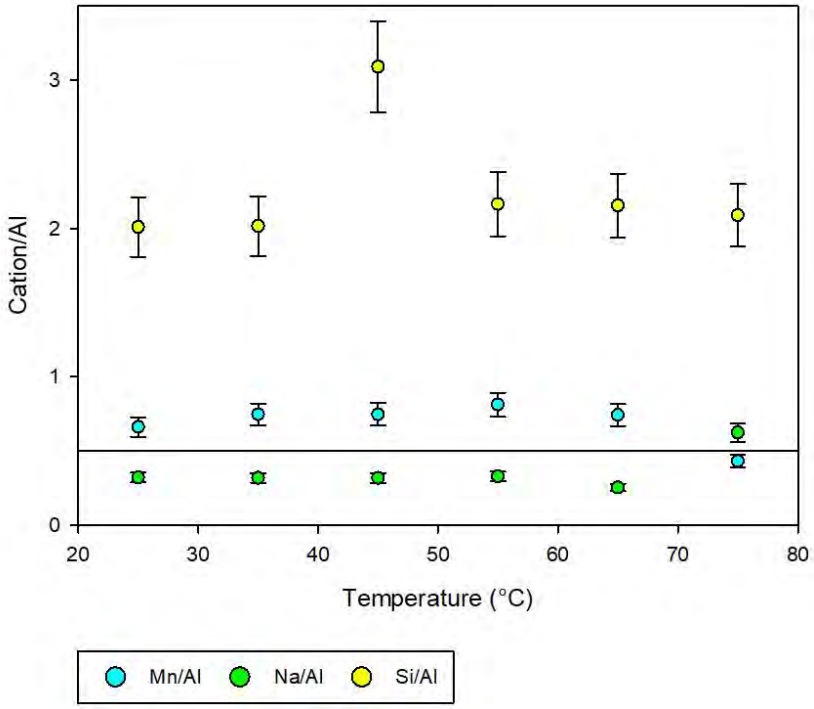


Figure 128 The effect of temperature at a concentration of 2 M of manganese(II) chloride on Mn(II) cation exchange in zeolite X. Element ratios are calculated from WD-XRF data from dried powders in pellet form. The size of the error bars reflects a 10% error commonly associated with XRF of pellets.

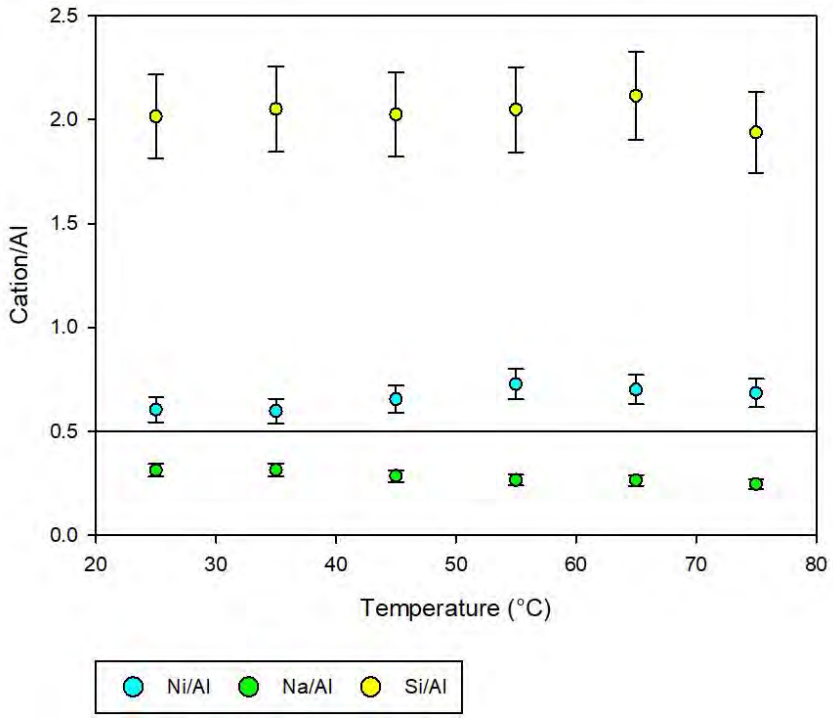


Figure 130 The effect of temperature at a concentration of 0.25 M of nickel(II) nitrate on Ni(II) cation exchange in zeolite Y. Element ratios are calculated from WD-XRF data from dried powders in pellet form. The size of the error bars reflects a 10% error commonly associated with XRF of pellets.

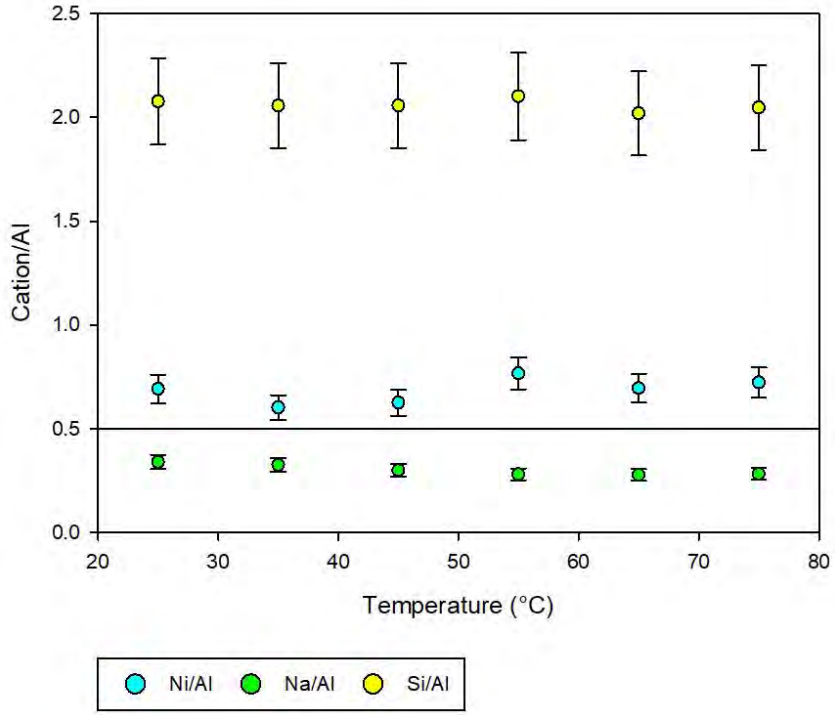


Figure 132 The effect of temperature at a concentration of 0.5 M of nickel(II) nitrate on Ni(II) cation exchange in zeolite Y. Element ratios are calculated from WD-XRF data from dried powders in pellet form. The size of the error bars reflects a 10% error commonly associated with XRF of pellets.

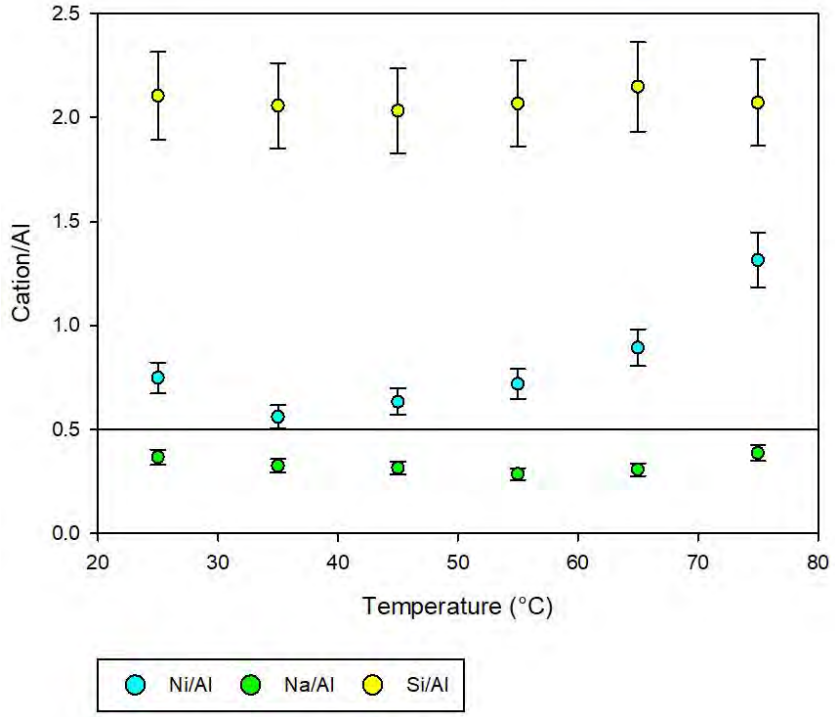


Figure 134 The effect of temperature at a concentration of 1 M of nickel(II) nitrate on Ni(II) cation exchange in zeolite Y. Element ratios are calculated from WD-XRF data from dried powders in pellet form. The size of the error bars reflects a 10% error commonly associated with XRF of pellets.

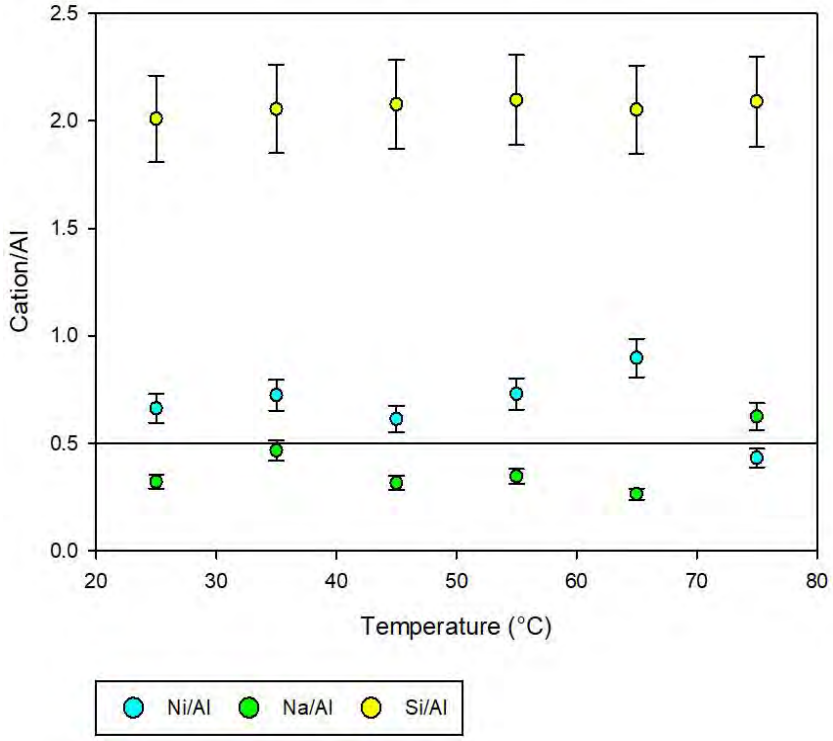


Figure 136 The effect of temperature at a concentration of 2 M of nickel(II) nitrate on Ni(II) cation exchange in zeolite Y. Element ratios are calculated from WD-XRF data from dried powders in pellet form. The size of the error bars reflects a 10% error commonly associated with XRF of pellets.

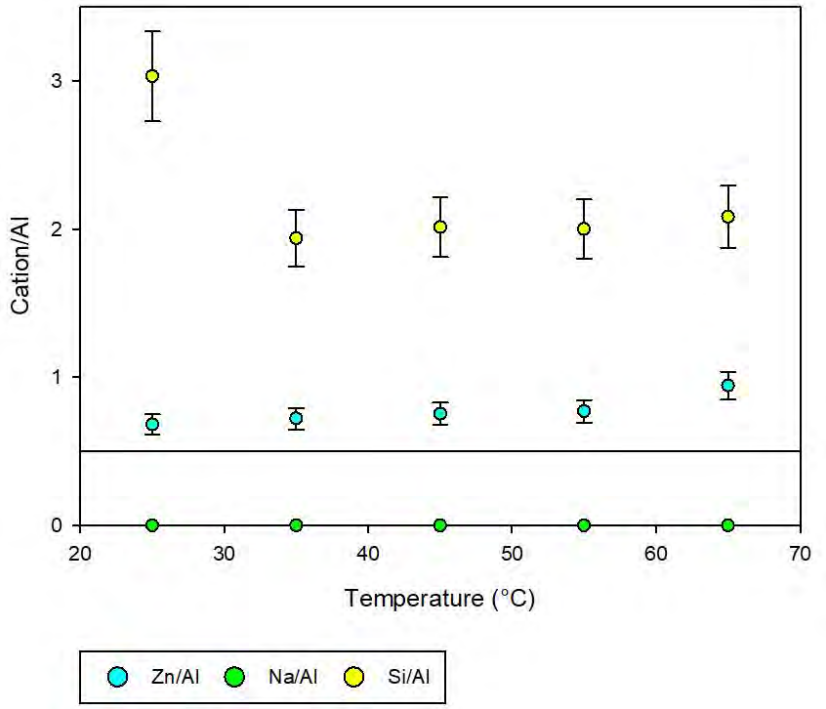


Figure 138 The effect of temperature at a concentration of 0.25 M of zinc(II) chloride on Zn(II) cation exchange in zeolite Y. Element ratios are calculated from WD-XRF data from dried powders in pellet form. The size of the error bars reflects a 10% error commonly associated with XRF of pellets.

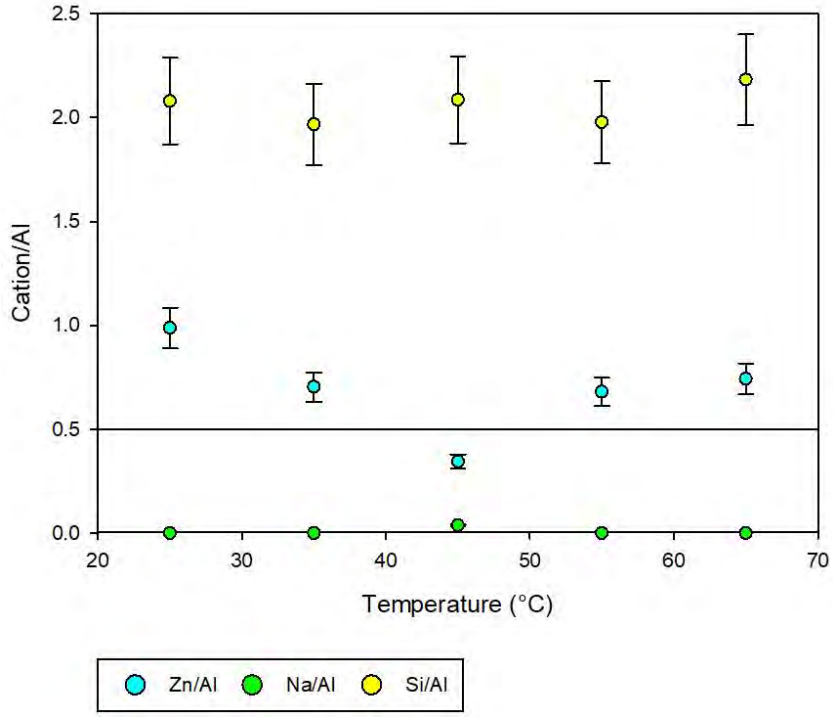


Figure 140 The effect of temperature at a concentration of 0.5 M of zinc(II) chloride on Zn(II) cation exchange in zeolite Y. Element ratios are calculated from WD-XRF data from dried powders in pellet form. The size of the error bars reflects a 10% error commonly associated with XRF of pellets.

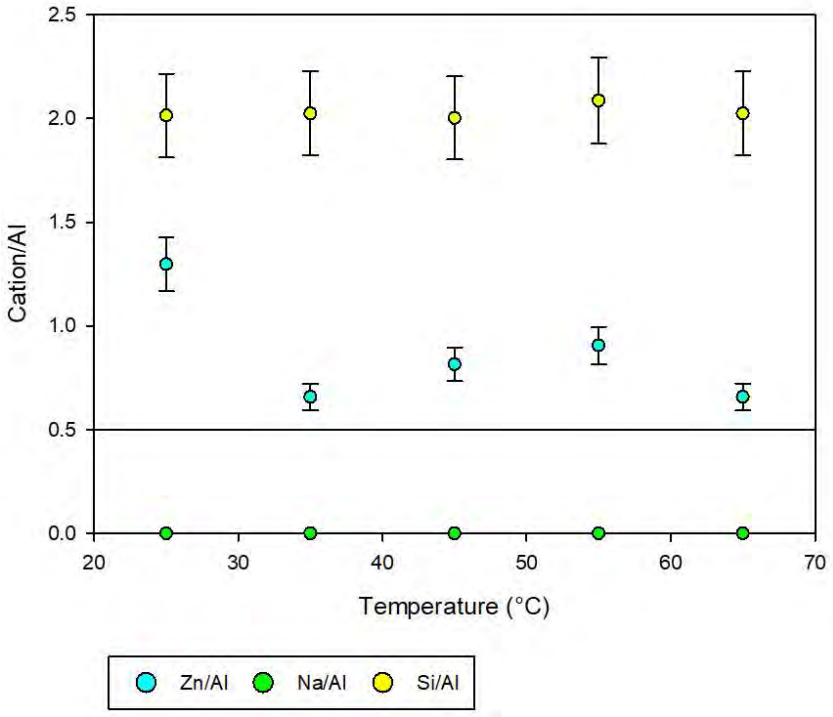


Figure 142 The effect of temperature at a concentration of 1 M of zinc(II) chloride on Zn(II) cation exchange in zeolite Y. Element ratios are calculated from WD-XRF data from dried powders in pellet form. The size of the error bars reflects a 10% error commonly associated with XRF of pellets.

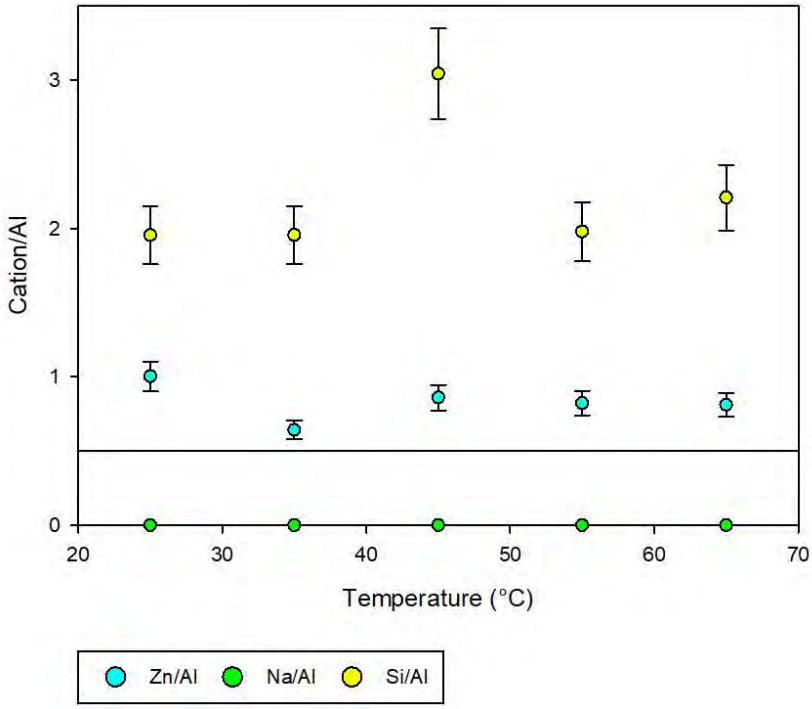


Figure 144 The effect of temperature at a concentration of 2 M of zinc(II) chloride on Zn(II) cation exchange in zeolite Y. Element ratios are calculated from WD-XRF data from dried powders in pellet form. The size of the error bars reflects a 10% error commonly associated with XRF of pellets.

Chapter 4

4.1 Zeolite X & Y synthesis XRD patterns

4.1.1 Zeolite X

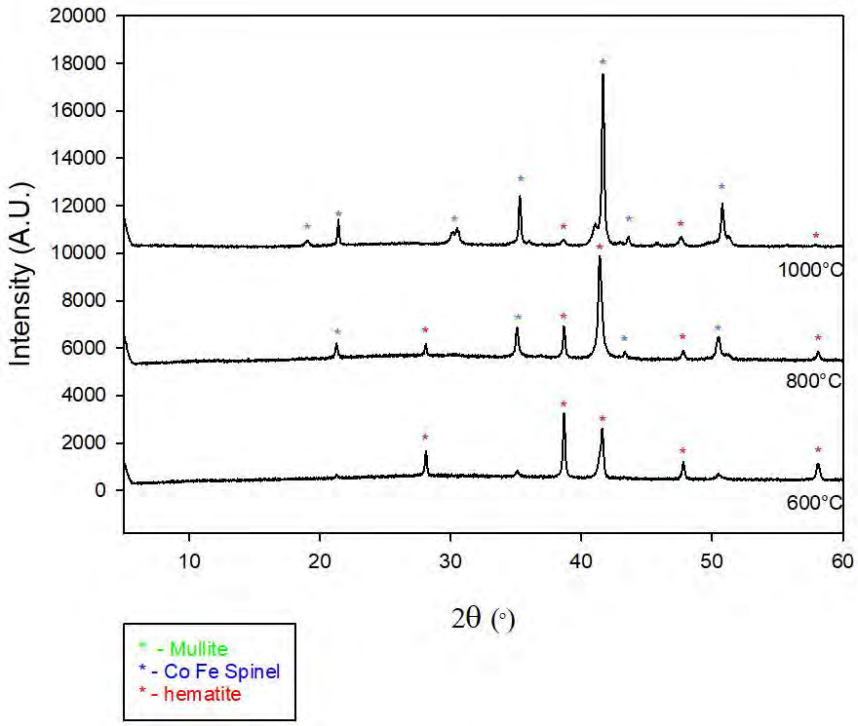


Figure 146 XRD patterns of cobalt(II)-X and iron(III) chloride in a 2:1(Fe^{3+}:Co^{2+}) ratio heated at 1000˚C under a nitrogen atmosphere.

4.1.2 Zeolite Y

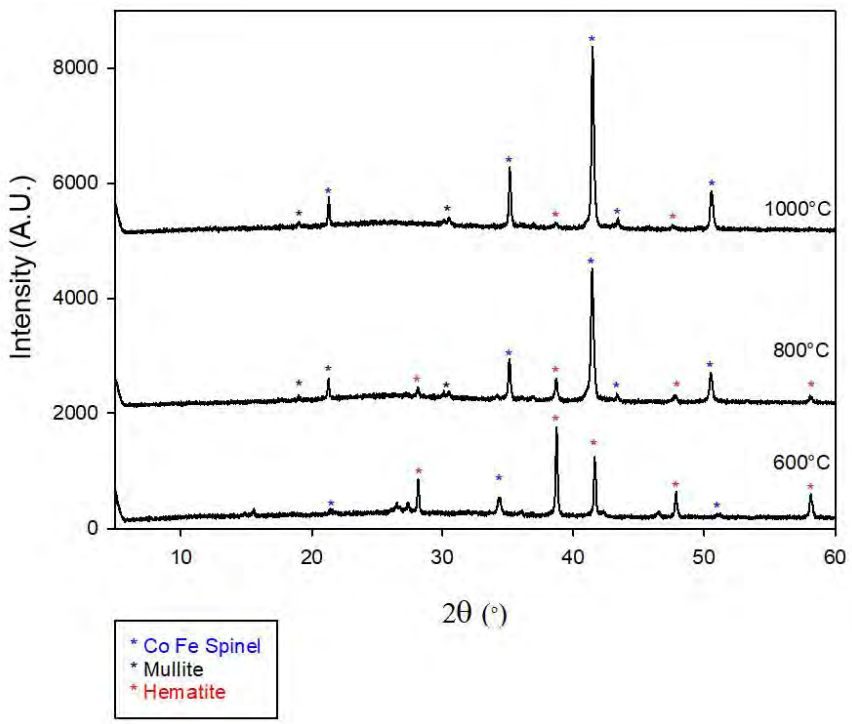


Figure 148 XRD patterns of cobalt(II)-Y and iron(III) chloride in a 2:1(Fe^{3+}:Co^{2+}) ratio heated at 1000˚C under a nitrogen atmosphere.

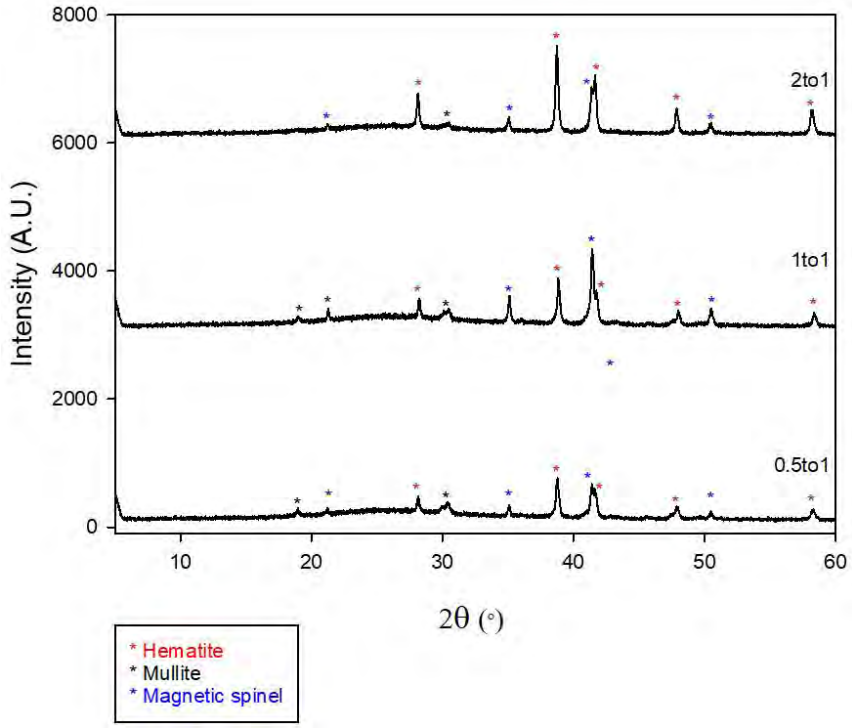


Figure 150 XRD patterns of iron(II)-Y and iron(III) chloride in a 2:1(Fe^{3+}:Co^{2+}) ratio heated at 1000˚C under a nitrogen atmosphere.

4.2 Matrix magnetic data

4.2.1 Zeolite A

Table 1 contains the magnetic responses of the products from the reaction between cobalt(II)-A and iron(III) chloride in different ratios and at different synthesis temperatures

Co(II)Fe(III)-A	0.5:1	1:1	2:1
600˚C	2.62	5.31	14.7
800˚C	2.81	16.9	19.90
1000˚C	16.82	18.7	35.6

Table 2 contains the magnetic responses of the products from the reaction between manganese(II)-A and iron(III) chloride in different ratios and at different synthesis temperatures

Mn(II)Fe(III)-A	0.5:1	1:1	2:1
600˚C	1.49	1.53	1.52
800˚C	12.19	28.65	25.4
1000˚C	8.96	29.76	65.78

Table 3 contains the magnetic responses of the products from the reaction between nickel(II)-A and iron(III) chloride in different ratios and at different synthesis temperatures

Ni(II)Fe(III)-A	0.5:1	1:1	2:1
600˚C	3.04	3.09	9.92
800˚C	6.03	19.72	20.24
1000˚C	9.88	13.43	26.43

4.2.2 Zeolite X

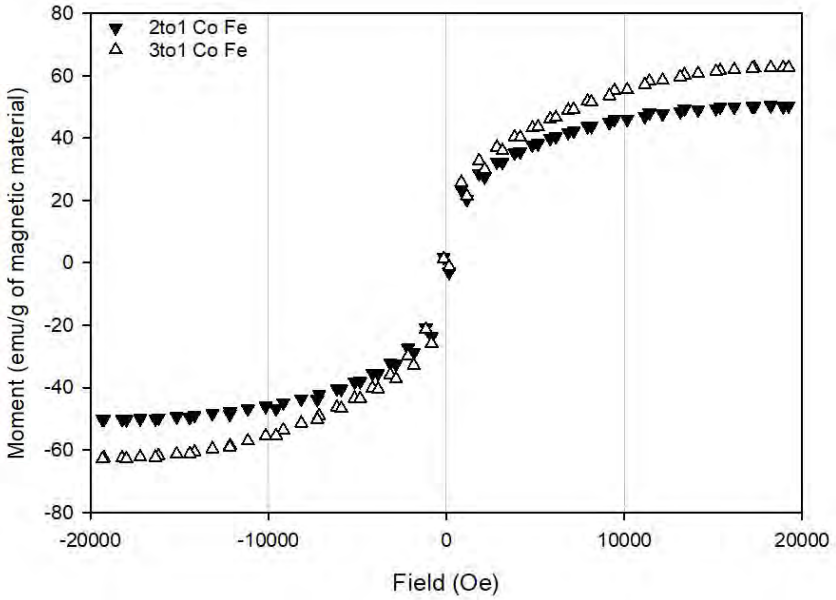


Figure 152 The magnetic responses produced by the occlusion products when using iron(III) chloride to cobalt(II) zeolite X ratios of 2:1 and 3:1 using a synthesis temperature of 1000˚C. Black triangles represent the data from the 2:1 ratio and the white triangles 3:1

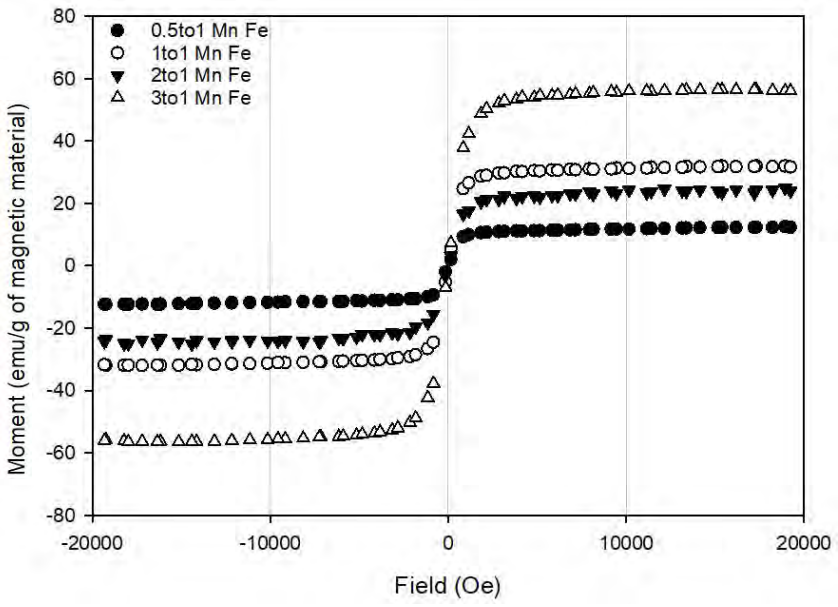


Figure 154 The magnetic responses produced by the occlusion products when using iron(III) chloride to manganese(II) zeolite X ratios of 0.5:1,1:1, 2:1 and 3:1 using a synthesis temperature of 1000˚C. Black circles represent the data from the 0.5:1 ratio, white circles 1:1, black triangles 2:1 and white triangles 3:1.

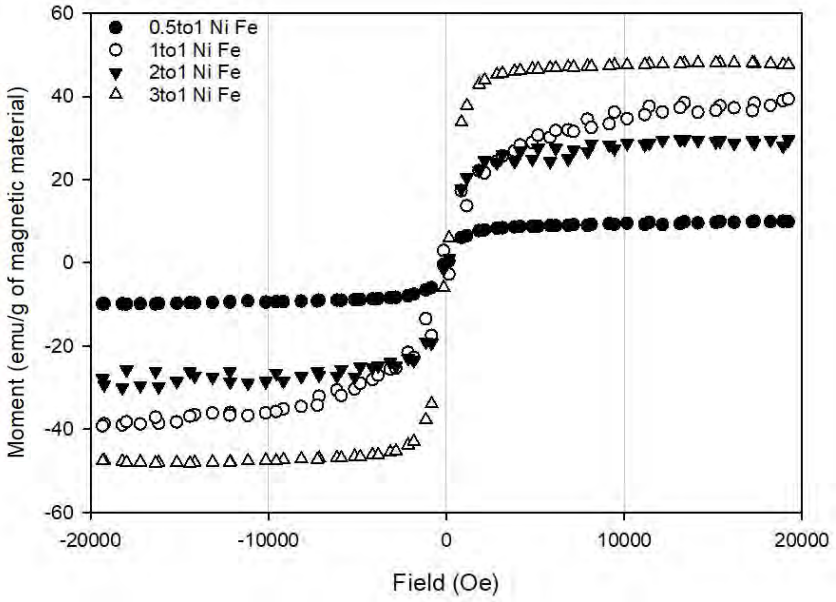


Figure 156 The magnetic responses produced by the occlusion products when using iron(III) chloride to nickel(II) zeolite X ratios of 0.5:1,1:1, 2:1 and 3:1 using a synthesis temperature of 1000˚C. Black circles represent the data from the 0.5:1 ratio, white circles 1:1, black triangles 2:1 and white triangles 3:1.

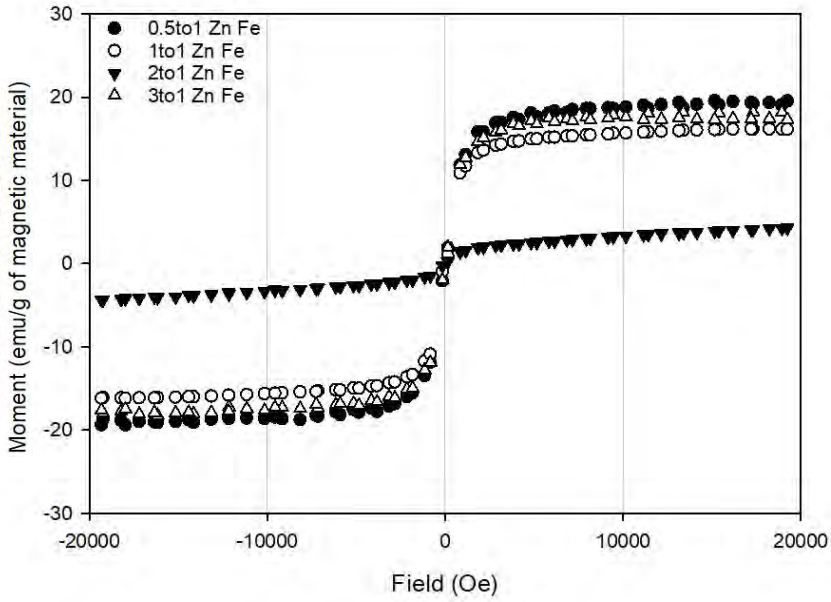


Figure 158 The magnetic responses produced by the occlusion products when using iron(III) chloride to zinc(II) zeolite X ratios of 0.5:1,1:1, 2:1 and 3:1 using a synthesis temperature of 1000˚C. Black circles represent the data from the 0.5:1 ratio, white circles 1:1, black triangles 2:1 and white triangles 3:1.

4.2.3 Zeolite Y

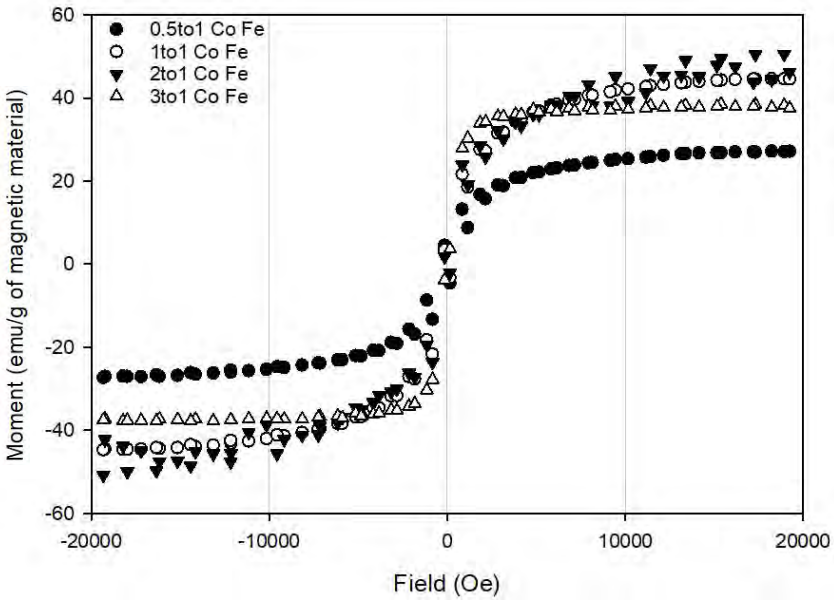


Figure 160 The magnetic responses produced by the occlusion products when using iron(III) chloride to cobalt(II) zeolite Y ratios of 0.5:1,1:1, 2:1 and 3:1 using a synthesis temperature of 1000˚C. Black circles represent the data from the 0.5:1 ratio, white circles 1:1, black triangles 2:1 and white triangles 3:1.

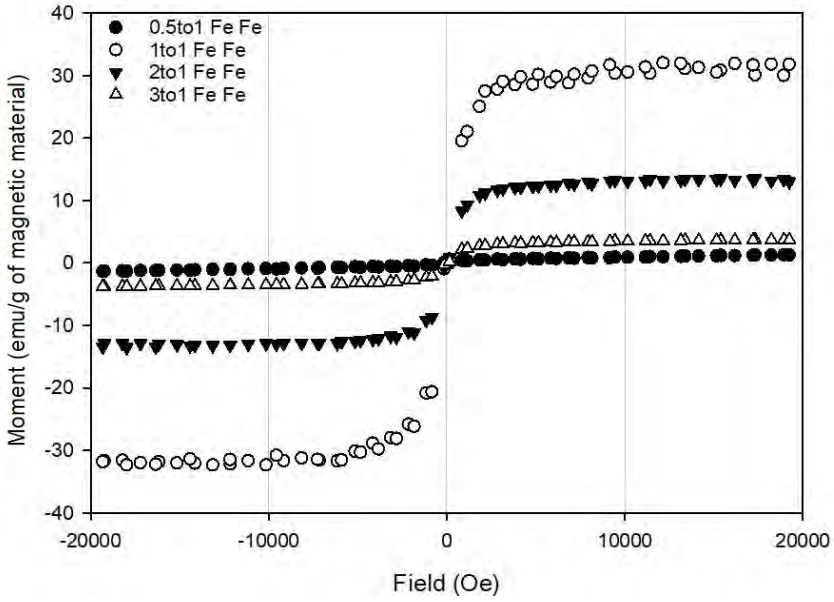


Figure 162 The magnetic responses produced by the occlusion products when using iron(III) chloride to iron(II) zeolite Y ratios of 0.5:1,1:1, 2:1 and 3:1 using a synthesis temperature of 1000˚C. Black circles represent the data from the 0.5:1 ratio, white circles 1:1, black triangles 2:1 and white triangles 3:1.

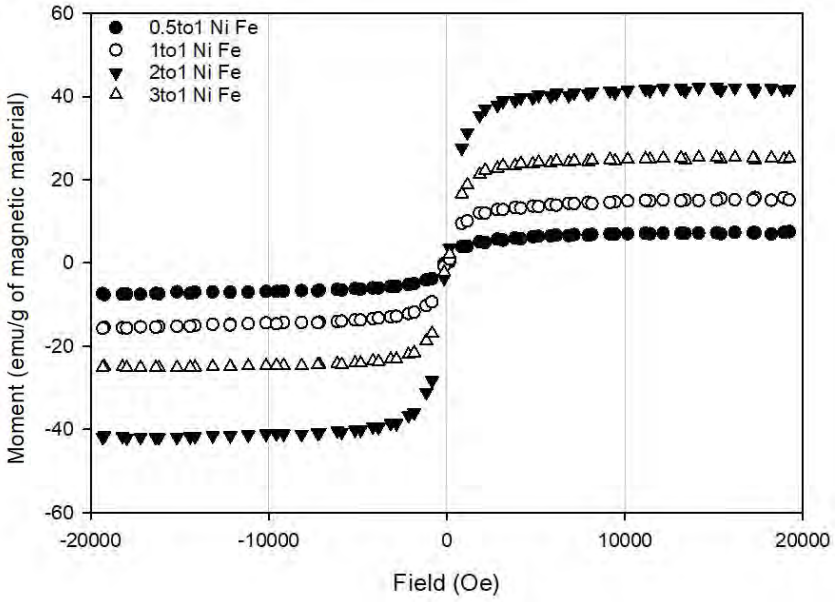


Figure 164 The magnetic responses produced by the occlusion products when using iron(III) chloride to cobalt(II) zeolite Y ratios of 0.5:1,1:1, 2:1 and 3:1 using a synthesis temperature of 1000˚C. Black circles represent the data from the 0.5:1 ratio, white circles 1:1, black triangles 2:1 and white triangles 3:1.

4.3 Example refinement

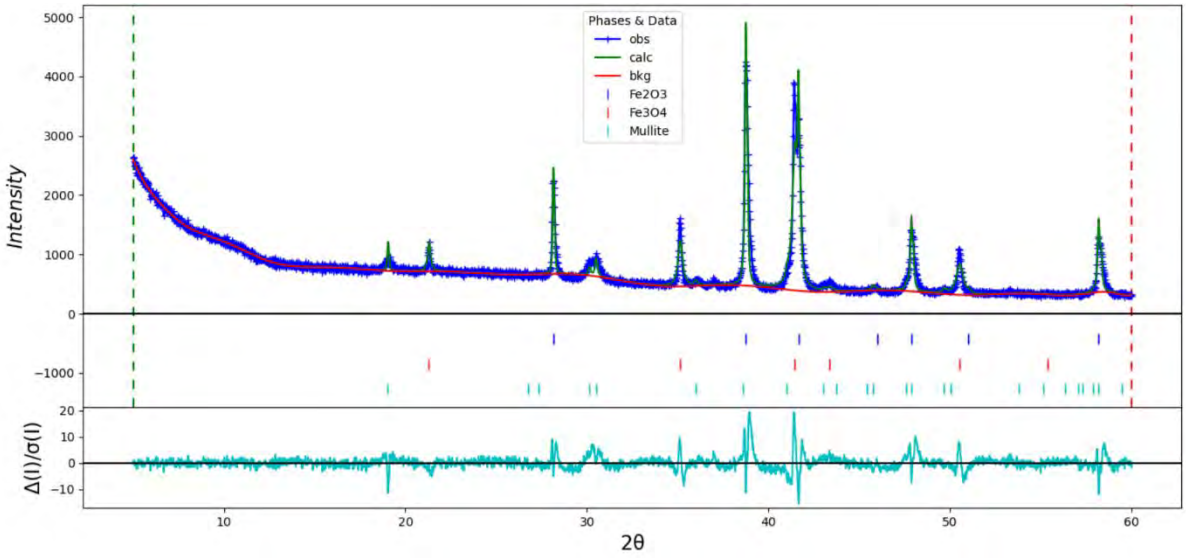


Figure 110 An example GSAS refinement for determining hematite to magnetite ratio.

Chapter 5

5.0. Zeolite A hybrid XRD

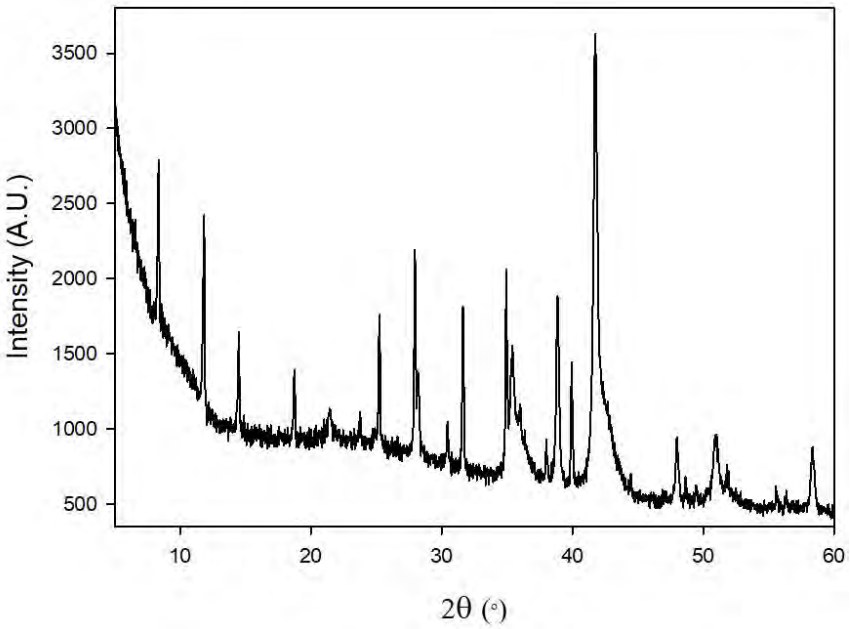


Figure 166 Powder X-ray diffraction patterns of superparamagnetic zeolite A hybrids made using 200% matrix content.

5.1 TGA

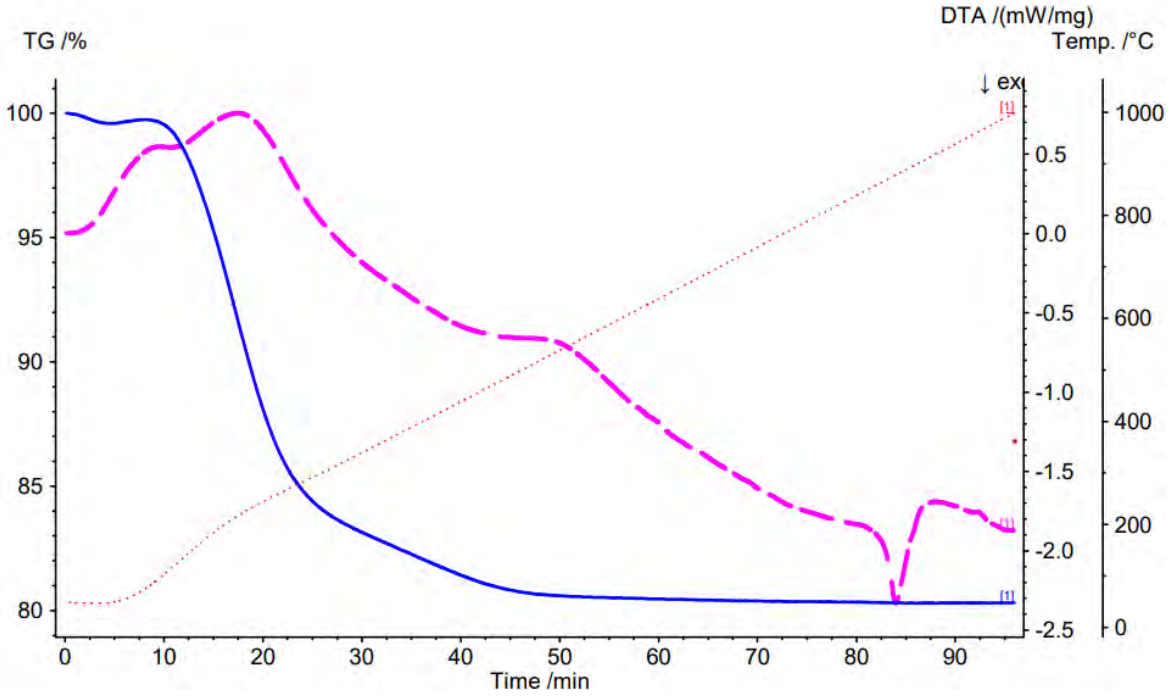


Figure 168 TGA and DTA curves of a standard Na^+ form of zeolite A. The blue curve relates to TG% (mass loss), the purple to DTA and red corresponds to temperature.

5.2 Zeolite X hybrids

5.2.1 Zeolite X hybrid synthesis XRD

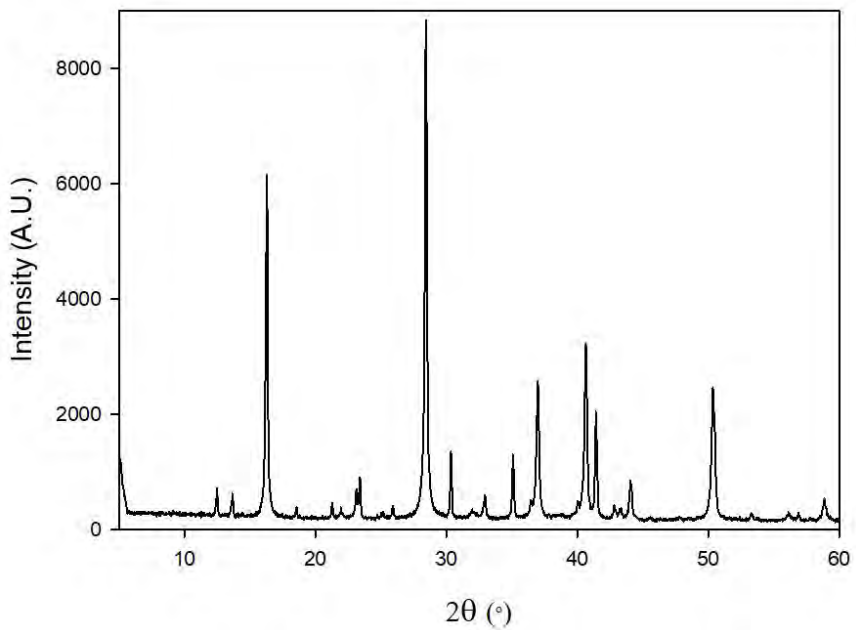


Figure 170 XRD patterns of zeolite X hybrids made using a 200% matrix content alongside standard synthesis regents.

5.2.2 Magnetic characterisation of zeolite X Mn(II)Fe(III) hybrid

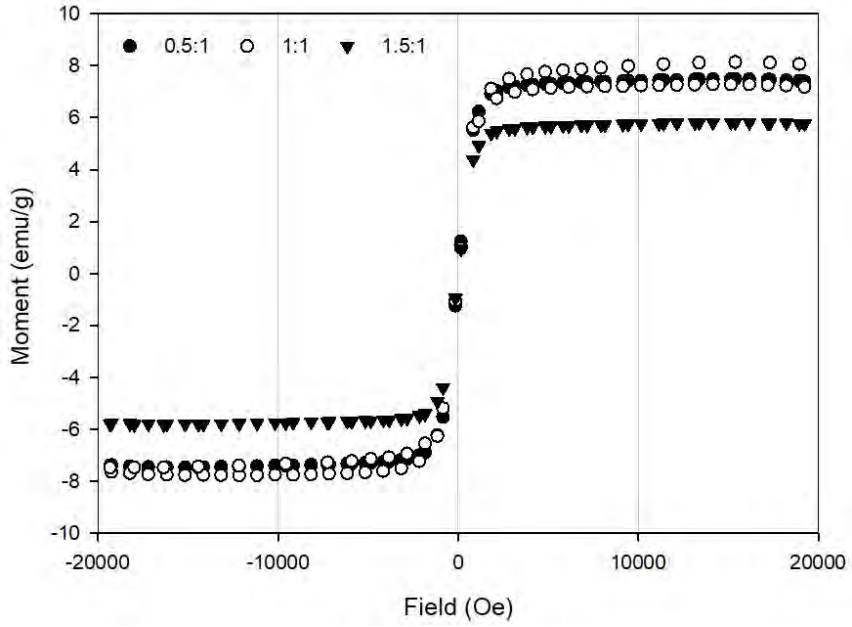


Figure 172 Magnetic response of the hybrid zeolite X using different amounts manganese(II)-iron(III) matrix alongside standard synthesis reagents.

5.3 Magnetic characterisation of zeolite Y hybrids

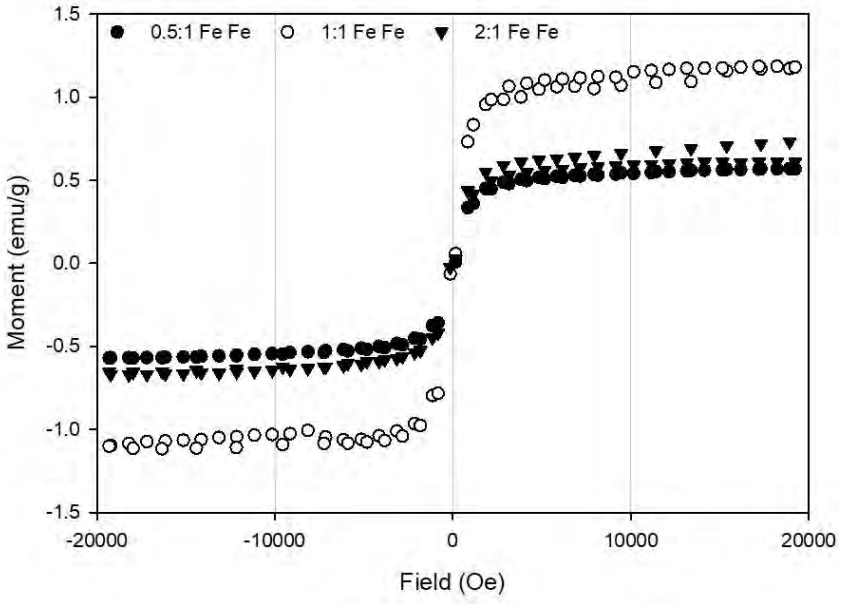


Figure 174 Magnetic response of the hybrid zeolite Y using different amounts iron(II)-iron(III) matrix alongside standard synthesis reagents.

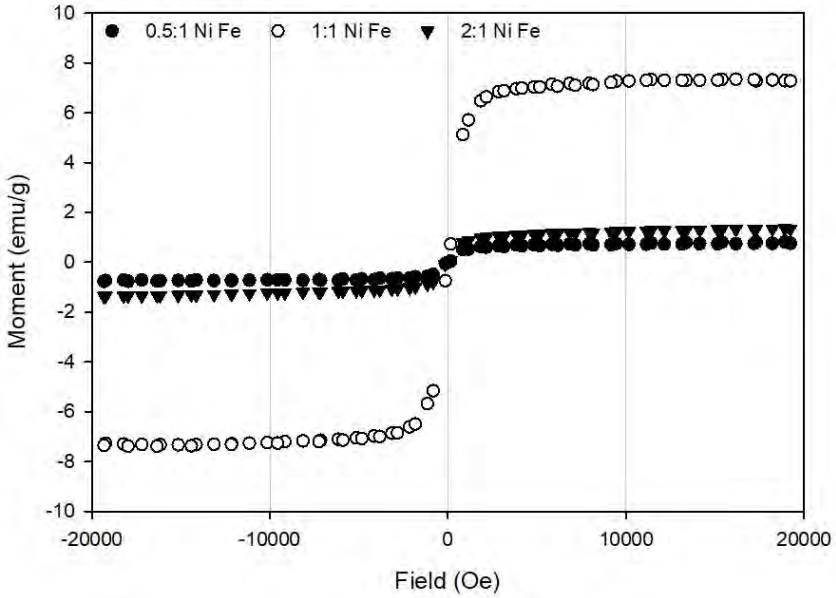


Figure 176 Magnetic response of the hybrid zeolite Y using different amounts nickel(II)-iron(III) matrix alongside standard synthesis reagents.

5.4 Magnetic characterisation of chabazite hybrids

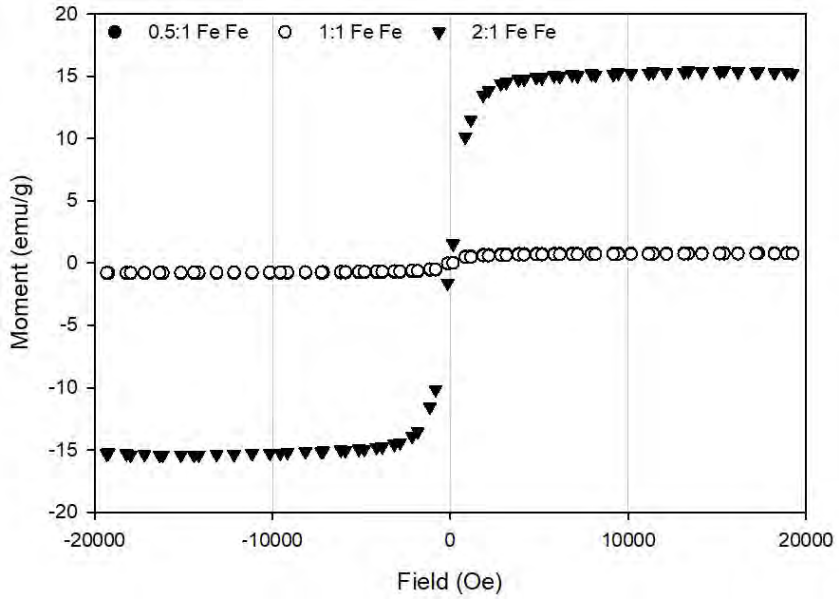


Figure 178 Magnetic response of the hybrid chabazite using different amounts iron(II)-iron(III) matrix alongside standard synthesis reagents.

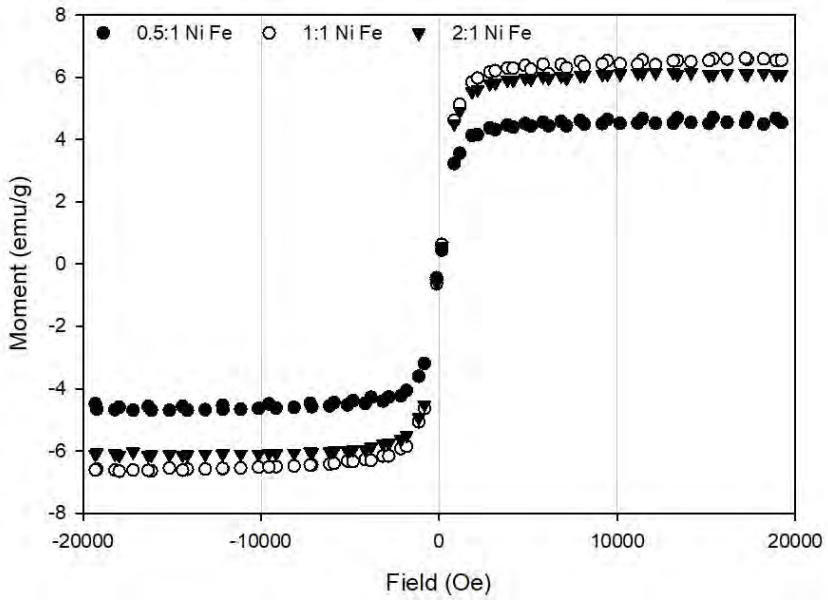


Figure 180 Magnetic response of the hybrid chabazite using different amounts nickel(II)-iron(III) matrix alongside standard synthesis reagents.

5.5 Electron microscopy of zeolite X hybrids

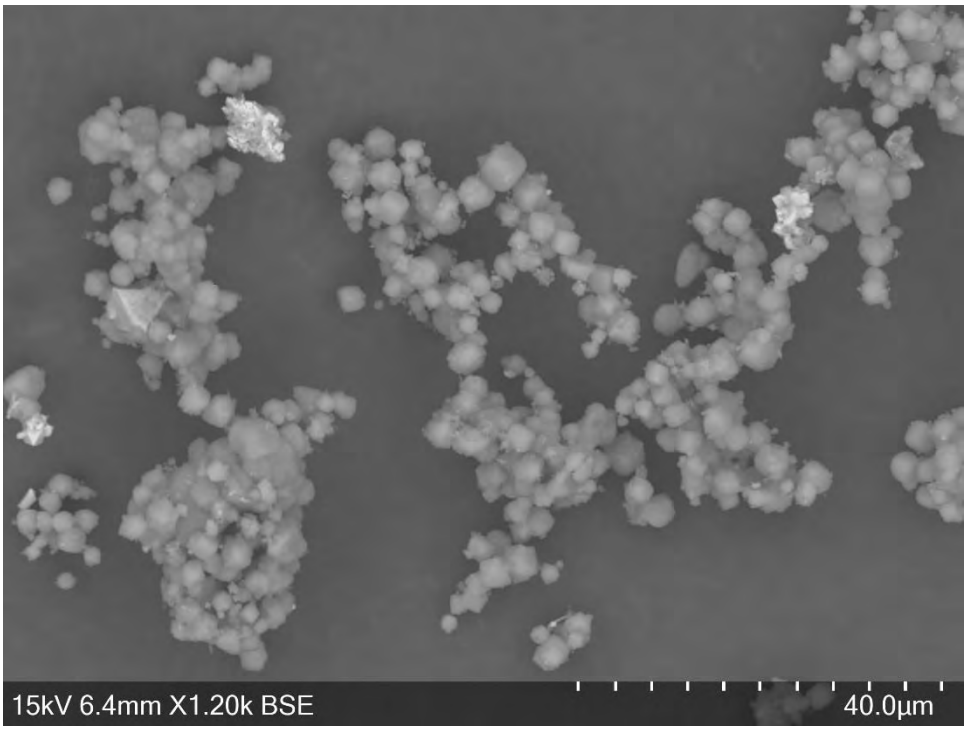


Figure 182 An SEM image of a zeolite X hybrid made using milled matrix in a 0.5:1 ratio under standard synthesis conditions.

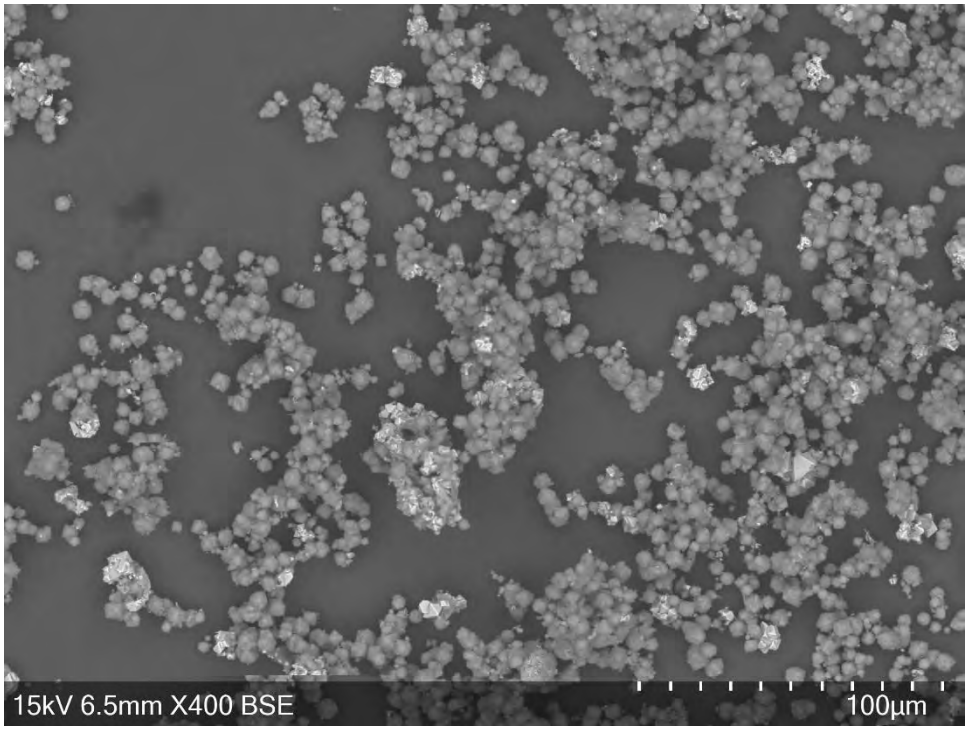


Figure 184 An SEM image of a zeolite X hybrid made using milled matrix in a 1:1 ratio under standard synthesis conditions.

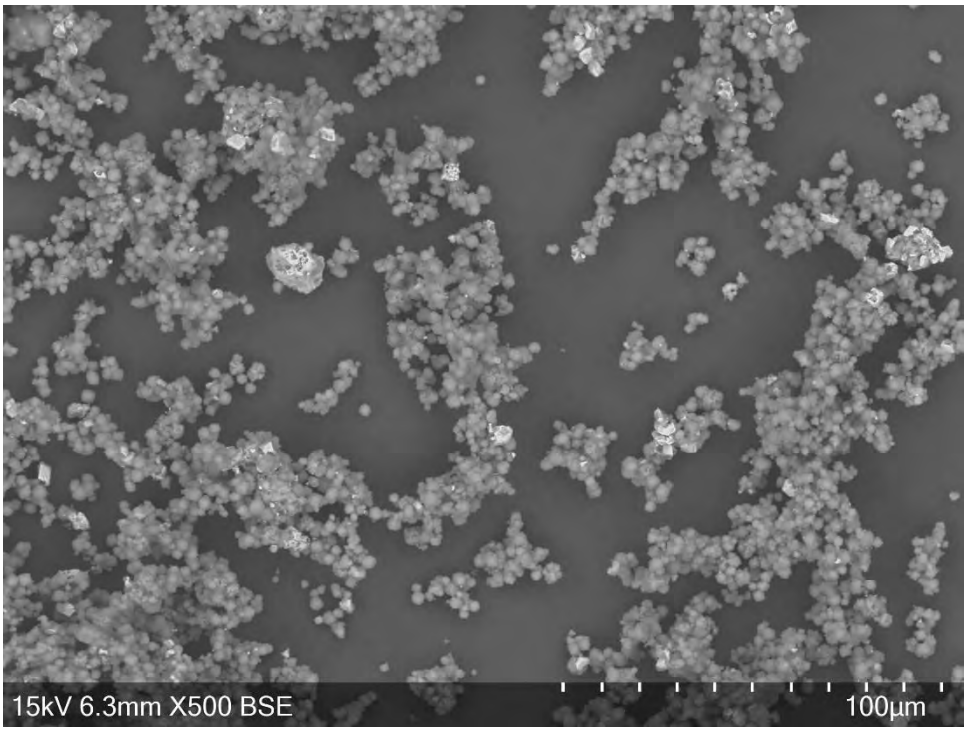


Figure 186 An SEM image of a zeolite X hybrid made using milled matrix in a 1.5:1 ratio under standard synthesis conditions.

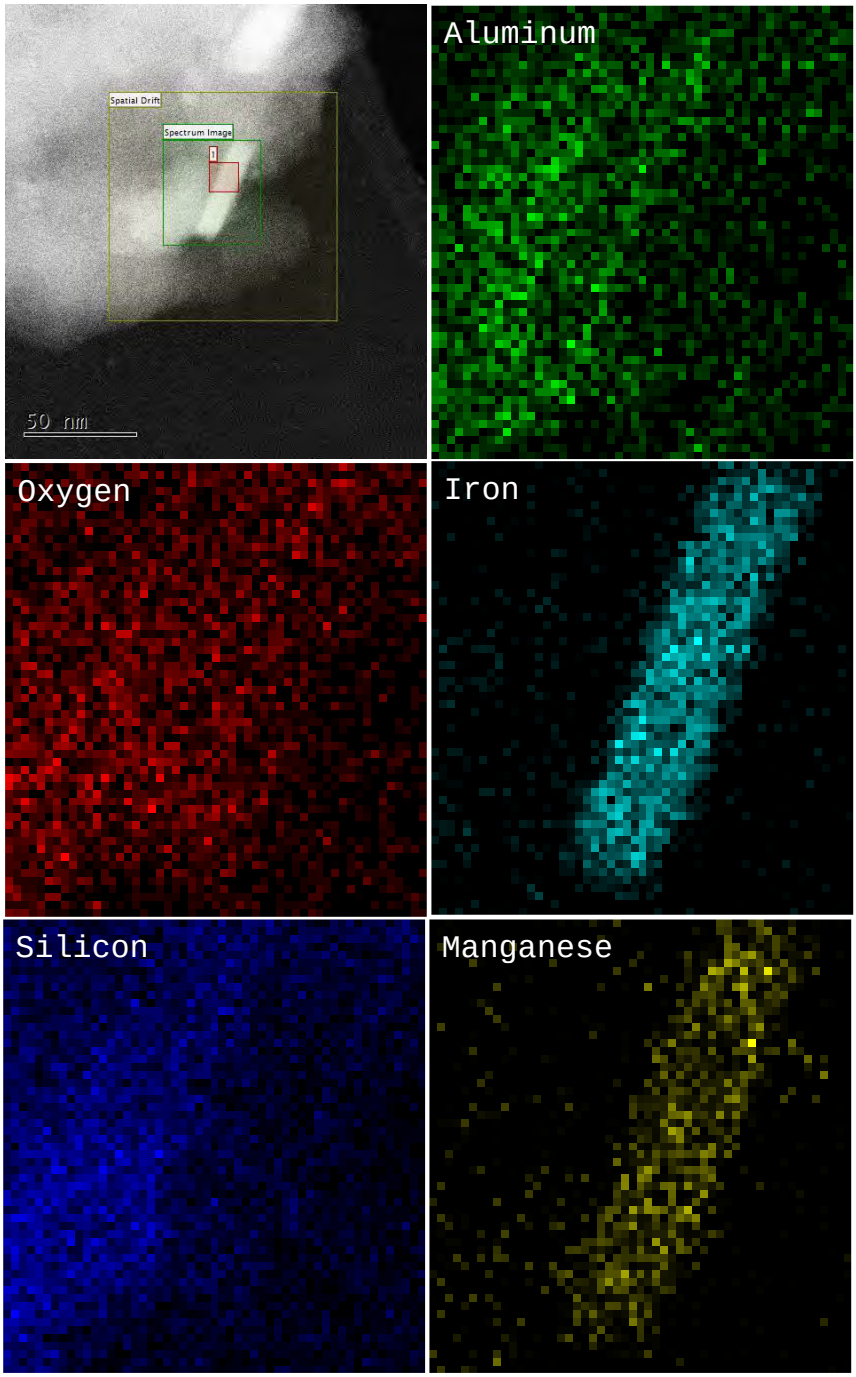


Figure 188 STEM image of 1.5:1 zeolite X hybrid with the EDX spectrum area highlighted with the corresponding elemental imaging.

5.6 Electron microscopy of zeolite Y hybrids

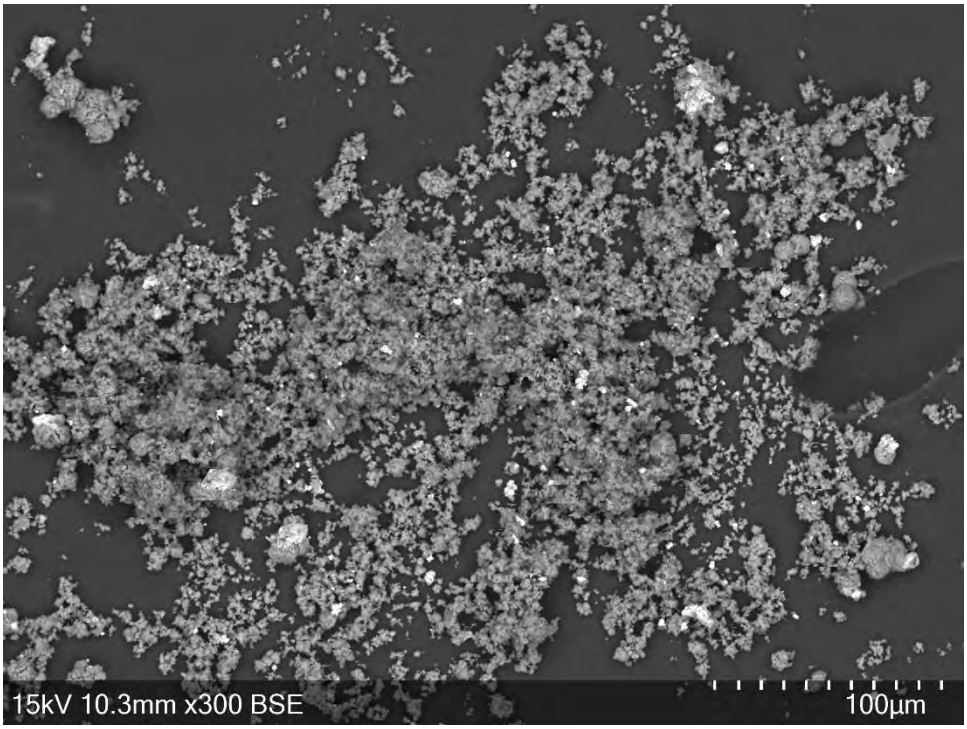


Figure 190 An SEM image of a zeolite Y hybrid made using milled matrix in a 1:1 ratio under standard synthesis conditions.

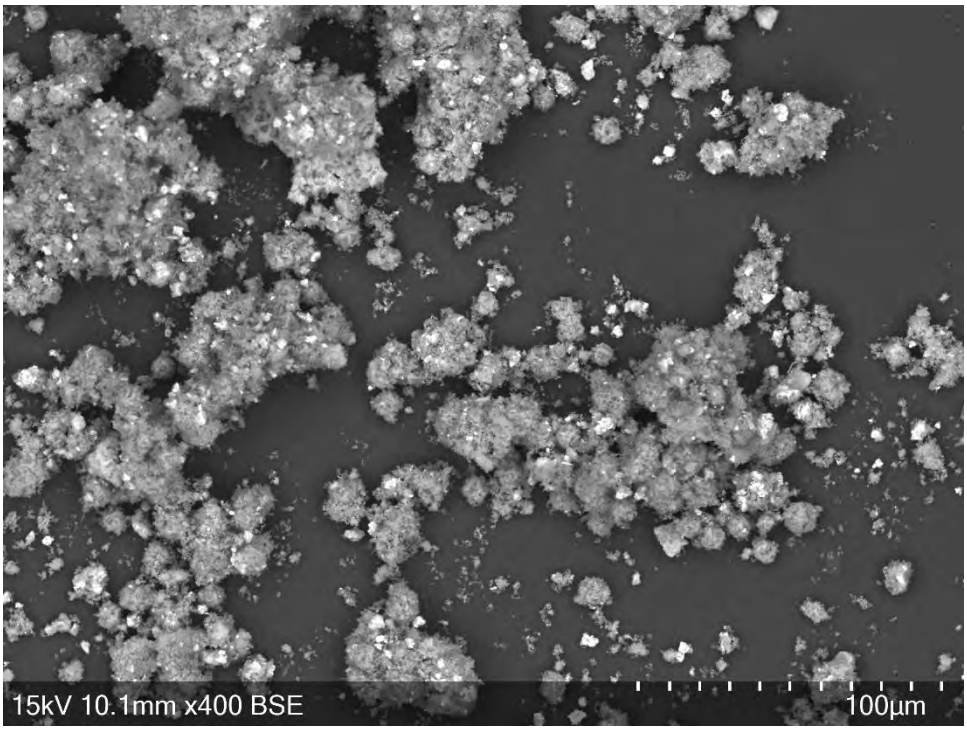


Figure 192 An SEM image of a zeolite Y hybrid made using milled matrix in a 1.5:1 ratio under standard synthesis conditions.

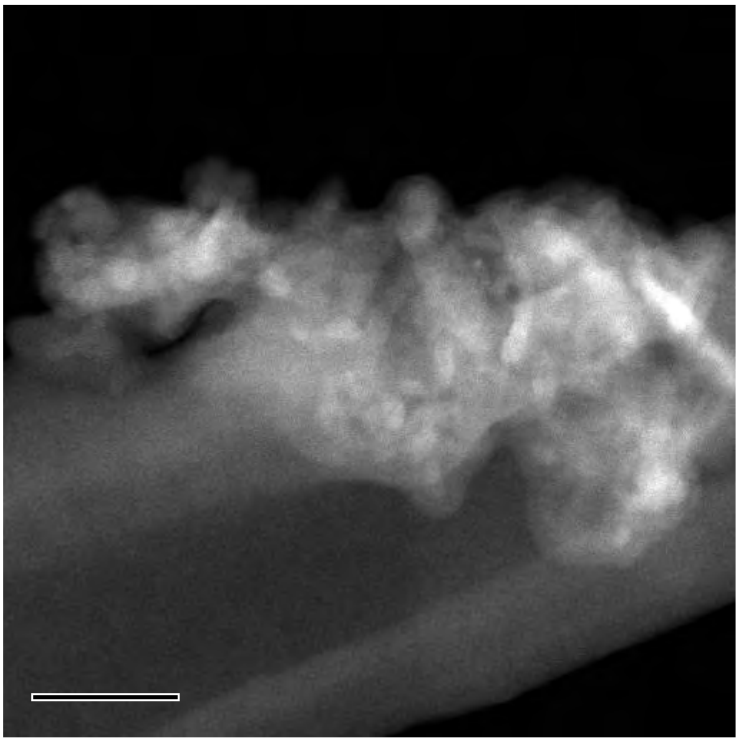


Figure 194 A high resolution STEM image of a zeolite Y hybrid made using milled matrix in a 1.5:1 ratio under standard synthesis conditions.

5.7 Electron microscopy of chabazite hybrids

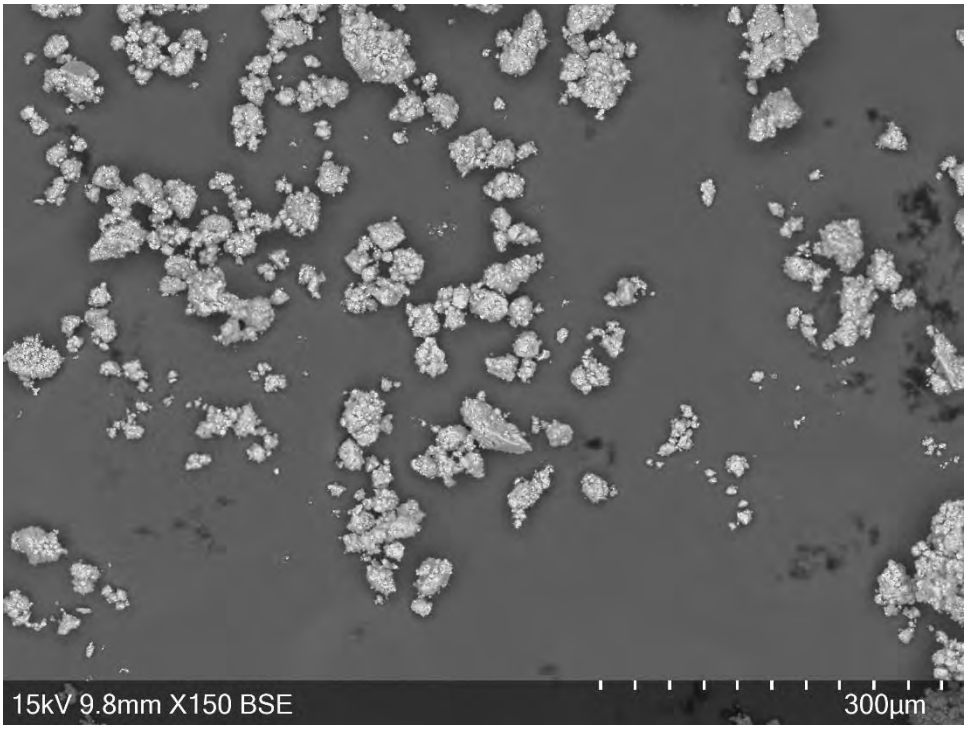


Figure 196 An SEM image of a chabazite hybrid made using matrix in a 1:1 ratio under standard synthesis conditions.

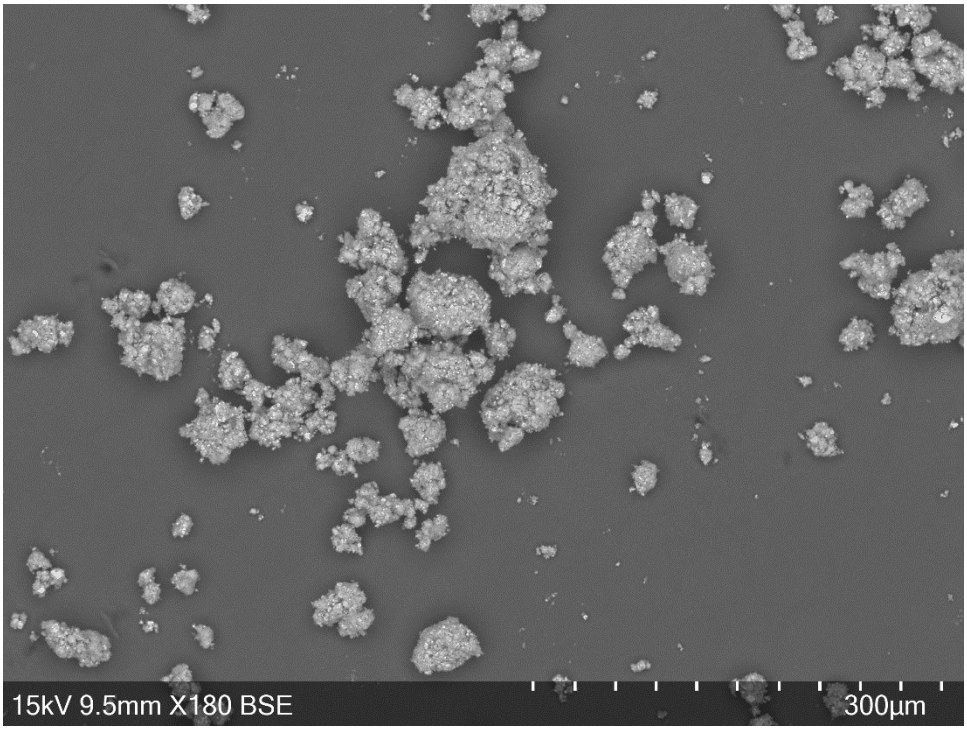


Figure 198 An SEM image of a chabazite hybrid made using matrix in a 1.5:1 ratio under standard synthesis conditions.

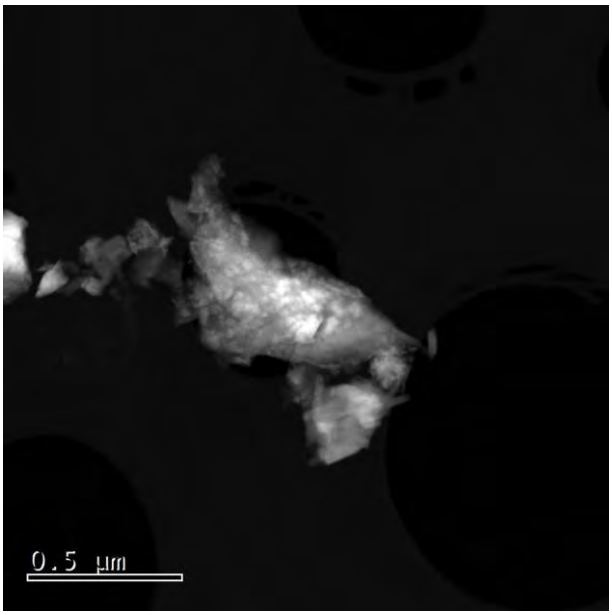


Figure 200 High resolution STEM image of chabazite using matrix in a 1.5:1 ratio under standard synthesis conditions.

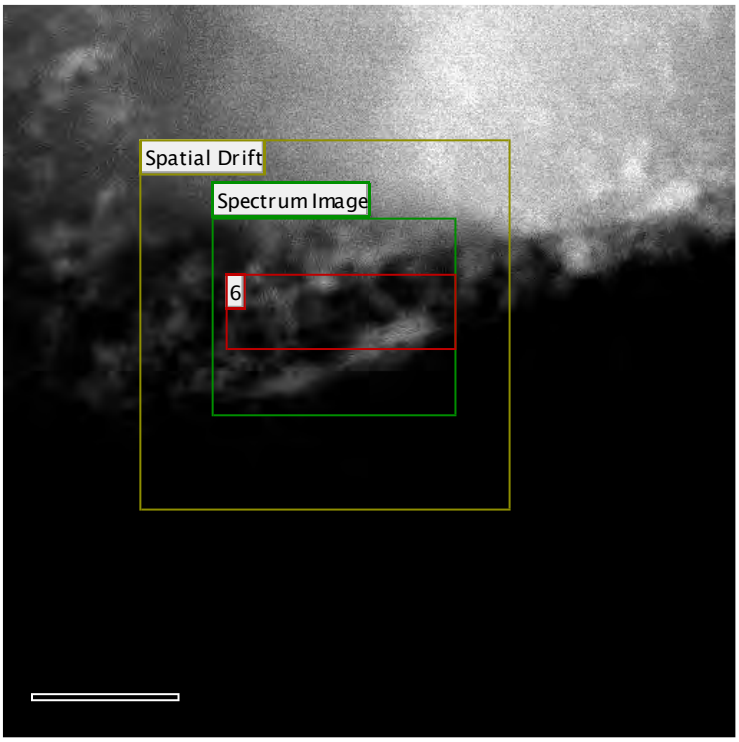


Figure 202 STEM image of 1.5:1 chabazite hybrid with the EDX spectrum area highlighted.

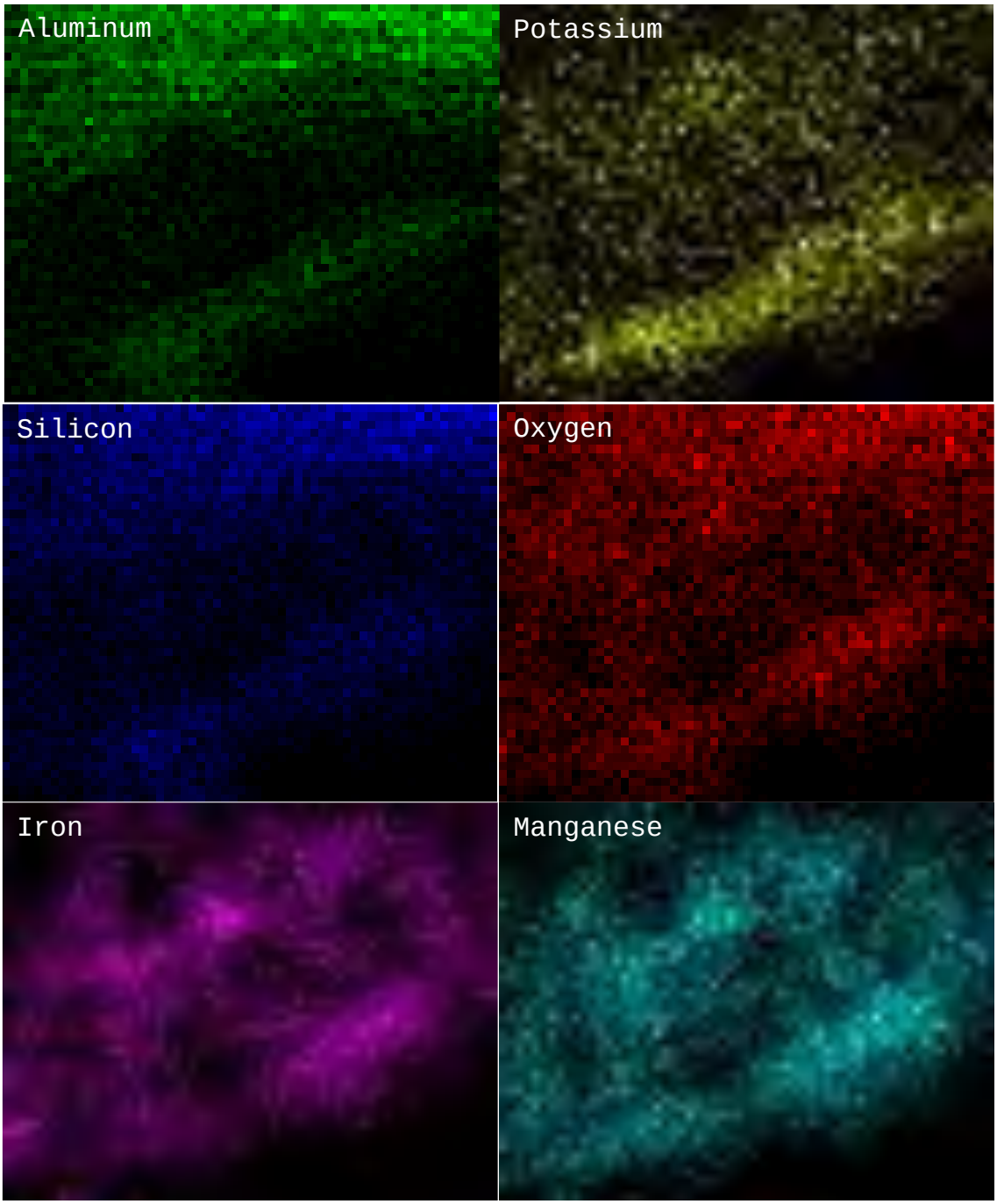


Figure 204 Elemental images taken of 1.5:1 chabazite hybrid shown in figure 101.

5.8 Hybrid zeolite Y and chabazite XRD patterns

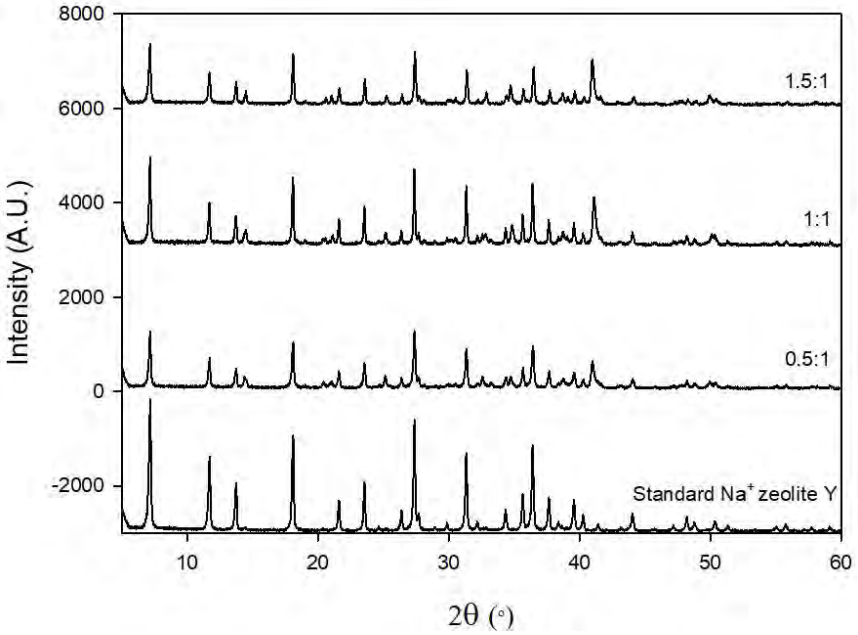


Figure 206 XRD patterns of zeolite Y hybrids made using different amounts of matrix content. A standard form of zeolite Y has been added for comparison.

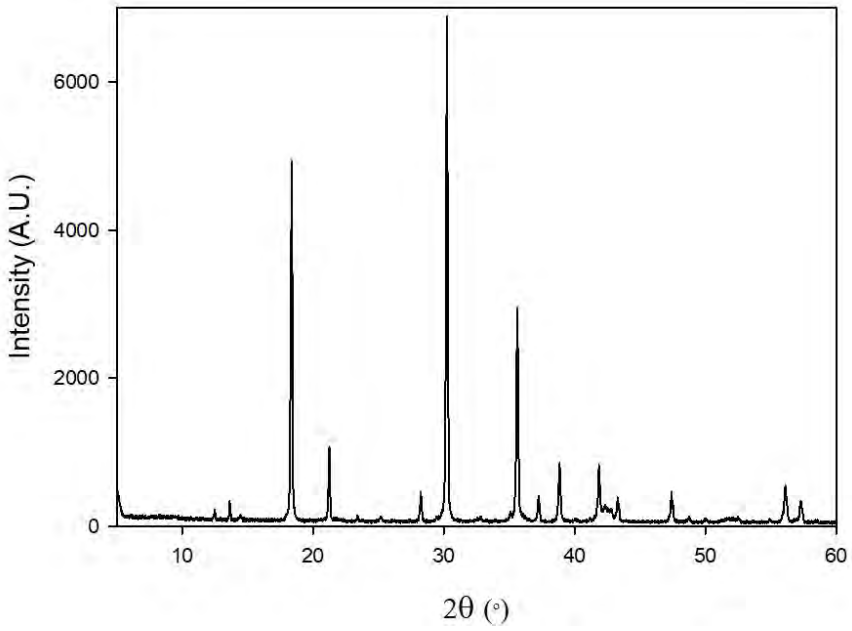


Figure 208 XRD pattern of zeolite Y hybrid made using 200% matrix content alongside standard synthesis reagents.

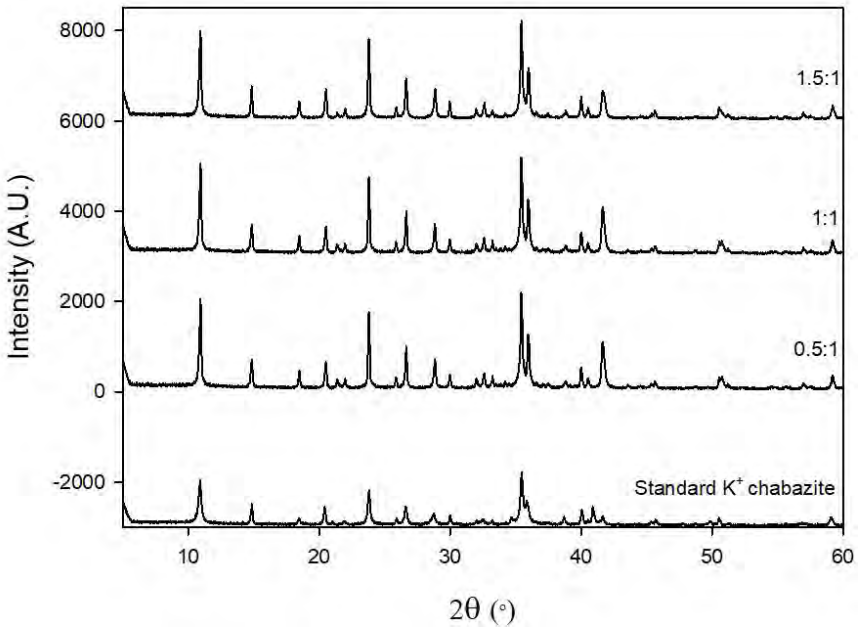


Figure 210 XRD patterns of chabazite hybrids made using different amounts of matrix content. A standard form of chabazite has been added for comparison.

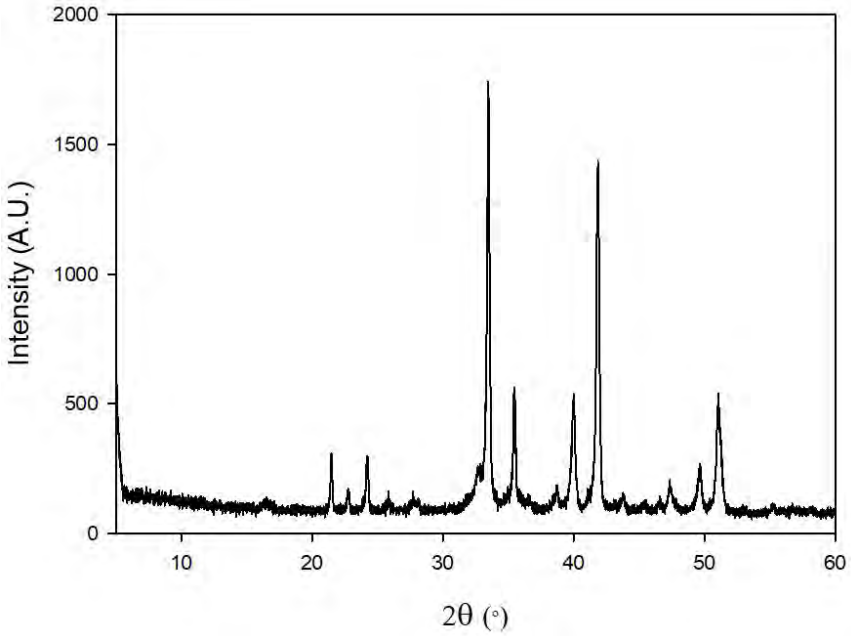


Figure 212 XRD pattern of chabazite hybrid made using 200% matrix content alongside standard synthesis reagents.